



Experimental Investigations on the Effects of Grid-screen, Sand Bed, and Nozzle Orientation on the Dynamics of Bubble Plumes

by

Arsalan Behzadipour

A thesis submitted to the Faculty of Graduate Studies and Research

in partial fulfillment of the requirements for the degree of

Doctor of Philosophy

in

Civil Engineering

Department of Civil Engineering

Winter 2023

Thunder Bay, Ontario

Advisor: Dr. Amir H. Azimi

Author's Declaration Page

I hereby declare that I am the sole author of this thesis document. This is a true copy of this document, including any required revisions as accepted by my supervisor.

Abstract

A bubble plume is defined as a column of air that flows through a liquid ambient due to the density difference between air and the ambient liquid. Bubble plumes have been utilized in wastewater treatment and oxygen transfer in civil and environmental engineering projects. Based on the injection pressure of air flow, bubble plumes can be converted to jet plumes or bubbly jets. A bubble plume is generated by the injected pressurized air/gas, and a bubbly jet is generated by injection of gas-liquid mixture in the ambient. In addition, bubble plumes can be generated by injecting air through a nozzle, airborne stone, or a group of diffusers into the ambient water. Bubble plumes are classified as two-phase air-liquid flow in which the ambient hydrodynamics and initial conditions dictate the motion of air bubbles and their sizes. Bubble plumes are extensively used in civil, environmental, and chemical engineering fields in many different industrial applications (Beutel et al., 2008). In recent years, there has been an increasing interest in using bubble plumes for mixing or aeration in lakes to improve water quality by adding oxygen.

Lakes and reservoirs management is an important component in the climate and environmental issues (Beutel et al., 2008; 2006; Stefan, 1992). As a result, air injection is a major area of interest within the field of wastewater treatment and reservoir management. The separation of suspended particles from the liquid phase is of great importance in water and wastewater treatment. The Dissolved Air Flotation (DAF) is a separation technique in which the flotation process is used to remove a wide range of suspended solids and emulsions such as oil and grease in wastewater treatment plants (Fanaie and Khiadani, 2020). The DAF system works by producing a stream of small bubbles that attaches to solids and lift them to the surface, where a surface scraping mechanism can remove the residuals. They are advantageous in comparison with other mechanical mixers due to their design simplicity, economical construction, and low maintenance and operation costs. The yield of bubble plumes which is the volume of the injected air for mixing air and water in comparison with other mixing techniques can minimize the cost of operation by enhancing the mixing of air bubbles in water ambient. The oxygen transfer efficiency is a major area of interest within the field of bubble plume hydrodynamics.

Although extensive research studies have been carried out on bubble plume hydrodynamics, few studies were carried out to evaluate and improve the oxygen transfer

in bubble plumes. To fill out the gap of knowledge, the present research project aims to elucidate and conduct novel methods to enhance oxygen transfer in bubble plumes. This research shows the effect of grid screens, bed sands, and different nozzle configurations on bubble plume parameters such as bubble mean velocity, bubble mean diameter, size distribution, bubble concentration, and bubble interfacial area. To improve the bubble plume performance, bubble interfacial area should be increased, and this goal is achieved by cutting bubbles into smaller sizes and reducing bubble velocity to be able to increase the residence time of the plume.

In chapter 2, a series of laboratory experiments were conducted to improve the entrainment and mixing capacity of vertically discharged bubble plumes by employing a grid screen located at different distances from the nozzle. Bubble characteristics such as bubble size, bubble size distribution, bubble concentration, and mean bubble velocity were measured using an accurate Refractive Bubble Index (RBI) probe along the plume axis, before and after the grid screen. The effects of grid screen openings and airflow discharge on variations of bubble characteristics were examined to increase the residence time of bubbles. It is assumed that by employing the grid screen, bubble size and bubble velocity are reduced and the contact time between bubbles and ambient water increases. As a result, the proposed methods of this research study can increase the air-water mixture potential, which is very important in engineering and industrial applications. Finally, the pretests results showed that the grid screen size and its distance from the nozzle decreased the vertical velocity of bubbles with an average value of 38%. Also, it is considered that dynamics of bubbles before and after the grid screen can be analyzed, and a regime classification can be proposed based on variations of the normalized bubble velocity with the distance from the nozzle. The proposed techniques enhance the bubble mixing and practical equations are proposed to estimate the elevation between different evolution regimes based on the bubble Reynolds number. Furthermore, the effect of adjusting the grid screen through the water ambient is investigated experimentally.

In Chapter 3, the effects of air discharge on bubble plume characteristics were analyzed. A series of laboratory experiments was conducted to test the effects of air flow on bubble hydrodynamics parameters by evaluating, bubble interfacial area and bubble size frequency. Four air discharges were selected (3, 6, 9, and 12 L/min) and bubble

characteristics such as bubble mean velocity, bubble concentration, bubble mean diameter, and bubble size distribution were measured with a Bubble Refractive Instrument (RBI) probe. In Chapter 4, bubble plume hydrodynamic forces were extracted from experimental data. The contributed parameters were investigated, and the screen surface tension and grid-screen forces were predicted by using multi-regression technique.

In Chapter 5, sand beds with different grain sizes are introduced to reduce bubble diameter and improve oxygen transfer as an example of sustainable and cost-effective approach. Laboratory tests were carried out to evaluate the effect of bed sands in bubble plume characteristics. Different air discharges of $Q_a = 3$ L/min, 6 L/min, 9 L/min, and 12 L/min were selected to test the effect of air discharge on the dynamics of bubbles in vertically discharged bubble plume.

In Chapter 6, the effect of nozzle configurations on oxygen transfer was studied. Also, the effect of nozzle orientation by comparing single vertical nozzle with twin inclined nozzle on bubble jet parameters was investigated. The experimental observations and extracted data were compared with the benchmark tests, including a single vertical bubbly jet with same cross-sectional area as of twin bubbly jets to study the effect of bubble interaction and coalescence due to collision of bubbles in inclined jets. The focus of study on Chapter 6 was to investigate bubble dynamics and mass transfer characteristics of bubbly jet and the aeration induced by air-water bubbly jets injected vertically and with two inclined nozzles in stagnant water.

Acknowledgments

I would like to express my sincere gratitude to my supervisor Dr. Amir Hossein Azimi for his guidance, patience, motivation, and enthusiasm. His guidance helped me throughout my research to overcome many obstacles. I would like to thank Dr. Eltayeb Eltahir Mohamedelhassan, Dr. Basel I. Ismail and Dr. Ioan Nistor who kindly agreed to evaluate the quality of my research work as my committee members and gave me valuable suggestions and advice. I am also thankful to Mr. Morgan Ellis and Mr. Brandon Trepanier for their tremendous supports for my experimental setup and willingness to help.

Finally, I would like to particularly thank my family, amazing parents (Mohammad and Masoumeh) and lovely sister (Samin) for their encouragement and being supportive of my endeavors.

Table of Contents

Chapter 1	17
Motivation and Background	17
1.1 Definitions	17
1.2 Motivations	18
1.3 Application of bubble plumes	20
1.4 Methodology	21
1.5 Goals and Novelty of the present research study	26
1.6 Overview of the present study	27
Chapter 2	32
Effect of grid-screen on bubble characteristics of vertically discharged bubble plumes	32
2.1 Introduction	32
2.2 Experimental Setup	38
2.3 Results and Discussions	44
2.3.1 Flow visualization	46
2.3.2 Time history data	47
2.3.3 Bubble characteristics	50
2.3.4 Regime classification	61
2.4 Conclusions	66
Chapter 3	69
Effects of air discharge on bubble dynamics in vertically discharged bubble plumes	69
3.1 Introduction	69
3.2 Experimental Setup	74
3.3 Results and discussion	77
3.3.1 Bubble velocity and concentration	80
3.3.2 Bubble size distribution	86
3.3.3 Bubble characteristics	88
3.3.4 Momentum and buoyancy fluxes	94
3.3.5 Bubble velocity fluctuations	100
3.4 Conclusions	103
Chapter 4	107
Hydrodynamic modifications in vertical bubble plumes by a grid-screen	107

4.1 Introduction	107
4.2 Experimental Setup	111
4.3 Results and Discussion	116
4.3.1 <i>Bubble characteristics</i>	116
4.3.2 <i>Momentum equation and force balance</i>	127
4.4 Conclusions	139
Chapter 5	143
Effect of bed sand on bubble plume configuration	143
5.1 Introduction	143
5.2 Experimental setup	148
5.3 Results and Discussions	152
5.3.1 <i>Flow visualization</i>	152
5.3.2 <i>Effect of sand bed on bubble plume characteristics</i>	155
5.4 Conclusions	175
Chapter 6	179
Bubble dynamics and coalescence in twin oblique bubble plumes	179
6.1 Introduction	179
6.2 Experimental Setup	183
6.3 Experimental Results	187
6.3.1 <i>Flow Visualization</i>	187
6.3.2 <i>Bubble diameter, concentration, and velocity</i>	190
6.3.3 <i>Bubble Reynolds number and bubble frequency</i>	196
6.4 Discussions	197
6.5 Conclusions	202
Chapter 7	205
General Conclusions and Recommendations for Future Research	205
7.1 General Conclusions	205
7.2 Recommendation for Future Research	210
7.2.1 <i>Bubble dynamics in Two-layer domain:</i>	211
7.2.2 <i>De-stratification in a reservoir mixed by bubble plumes:</i>	212
https://www.wrl.unsw.edu.au/sites/wrl/files/uploads/Projects/WRL-TR2021-17-A-review-of-artificial-destratification-techniques-for-cold-water-pollution-mitigation.pdf	213
7.2.3 <i>Numerical simulations of bubble plumes:</i>	214
7.2.4 <i>Bubble dynamics with background turbulence:</i>	215

Appendix 1	218
Air bubble dynamics in bubble plumes with a grid-screen	218
Appendix 2	232
Suggested guideline for air injection systems in industry	232
References	237

List of Tables

Table 2. 1: Experimental parameters and air flow discharges of bubbly jets and plumes from the literature.....	33
Table 2. 2: Experimental parameters and bubble characteristics of vertically discharged bubble plumes passing through a sieve.....	41
Table 3. 1: Experimental parameters and bubble characteristics of vertically discharged bubble plumes.....	75
Table 4. 1: Experimental parameters and bubble characteristics of vertically discharged bubble plumes passing through a grid-screen.....	115
Table 4. 2: The values slope and intercept of the proposed equations for prediction of the threshold air discharge, Q_{at}	126
Table 5. 1: Experimental parameters and bubble characteristics of vertically discharged bubble plumes passing through a layer of sand bed. The nozzle diameter in this study is $d_o = 3$ mm.	151
Table 6. 1: Details of experimental tests for Single Vertical (SV-series) and Twin Inclined (TI-series) with different air and water discharge configurations and nozzle sizes for the inclined angle of $\alpha = 45^\circ$	184

List of Figures

Figure 1.1: Optical Probe setup.	22
Figure 1.2: Depicting the path of light when the tip of the probe is in water (top image), and when a bubble is detected (bottom image).	23
Figure 1.3: Typical phase indication function.	24
Figure 1.4: The steps of the present study	30
Figure 2. 1: The schematic of experimental setup, image of bubbly plume passing through a grid-screen, the components of an optoelectronic unit and Refractive Bubble Instrument (RBI) optical probe tip.	40
Figure 2. 2: Time histories of the recorded voltage signals with a Refractive Bubble Instrument (RBI) optoelectronic unit: a) a sample of instantaneous voltage signals with time; b) phase identification from raw voltage signals.	44
Figure 2. 3: Time histories of the cumulative average of bubble velocity and bubble concentration with and without a grid-screen for $Q_a = 4$ L/min and at $x/d_o = 330$: a) variations of the cumulative average of bubble velocity without a grid-screen (Test No. 1); b) variations of the cumulative average of bubble velocity with a grid-screen for $d_s = 2.38$ mm, $X_s = 0.4$ m (Test No. 7); c) variations of the cumulative average of bubble concentration without a grid-screen (Test No. 1); d) variations of the cumulative average of bubble concentration with a grid-screen for $d_s = 2.38$ mm, $X_s = 0.4$ m (Test No. 7).	45
Figure 2. 4: Images of bubble plume variations with time for the plume tests without a grid-screen and for $d_o = 1$ mm. The time step between each image is two seconds: a) $Q_a = 4$ L/min, (Test No. 1); b) $Q_a = 6$ L/min (Test No. 2); c) $Q_a = 8$ L/min, (Test No. 3).	46
Figure 2. 5: Effect of grid-screen on bubble breakup at different distances from the nozzle for $Q_a = 4$ L/min, $d_o = 1$ mm: a) bubble plume without a grid-screen; b) bubble plume with a grid-screen, $d_s = 0.841$ mm, $X_s = 0.14$ m.	47
Figure 2. 6: Time-histories of bubble concentration with and without a grid-screen for $Q_a = 4$ L/min, $d_o = 1$ mm, $d_s = 2.38$ and at $x/d_o = 330$: a) bubble plume without a grid-screen, (Test No.1); b) bubble plume with a grid-screen located at $X_s = 0.14$ m, (Test No.7) ; c) bubble plume with a grid-screen located at $X_s = 0.22$ m, (Test No.8); d) bubble plume with a grid-screen located at $X_s = 0.30$ m, (Test No.9).	48
Figure 2. 7: Time-histories of bubble velocity with and without a grid-screen for $Q_a = 4$ L/min, $d_o = 1$ mm, $d_s = 2.38$ mm and at $x/d_o = 330$: a) bubble plume without a grid-screen (Test No.1); b) bubble plume with a grid-screen located at $X_s = 0.14$ m, (Test No.7); c) bubble plume with a grid-screen located at $X_s = 0.22$ m, (Test No.8); d) bubbly plume with a grid-screen located at $X_s = 0.30$ m, (Test No.9).	49
Figure 2. 8: Effects of grid-screen on the Probability Density Function (PDF) of bubble size in bubble plumes with different discharges, screen sizes, and distances from the nozzle: a) $Q_a = 4$ L/min, $d_o = 1$ mm, without a grid-screen (Test No.1); b) $Q_a = 6$ L/ min, $d_o = 1$ mm, without a grid-screen (Test No.2); c) $Q_a = 4$ L/ min, $d_o = 1$ mm, $d_s = 2.38$ mm, $X_s = 0.14$ m, (Test No.7); d) $Q_a = 6$ L/ min, $d_o = 1$ mm, $d_s = 2.38$ mm, $X_s = 0.14$ m, (Test No.10).	52
Figure 2. 9: Effects of grid-screen on the total number of bubbles detected by the RBI probe, N_b : a) $Q_a = 4$ L/min, $d_o = 1$ mm, without a grid-screen (Test No.1) and $X_s = 0.14$ m, (Test No.7); b) $Q_a = 6$ L/ min, $d_o = 1$ mm, without a grid-screen (Test No.2) and $X_s = 0.14$ m, (Test No.10).	54
Figure 2. 10: Variations of bubble size along the vertical axis of bubble plumes with different air discharges, Q_a , nozzle diameters, d_o , and grid-screen sizes, d_s , for a screen located at $X_s = 0.14$ m, 0.22 m, and 0.30 m: a) $Q_a = 4$ L/min, $d_o = 1$ mm, $Re = 5661.71$; b) $Q_a = 4$ L/min, $d_o = 3$ mm, $Re =$	

1887.23; c) $Q_a = 6$ L/min, $d_o = 1$ mm, $Re = 8492.56$; d) $Q_a = 6$ L/min, $d_o = 3$ mm, $Re = 2830.85$; e) $Q_a = 8$ L/min, $d_o = 1$ mm, $Re = 11323.42$; f) $Q_a = 8$ L/min, $d_o = 3$ mm, $Re = 33970$	56
Figure 2. 11: Variations of the normalized bubble velocity with normalized vertical distance from the nozzle in bubble plumes with different air discharges, Q_a , nozzle sizes, d_o , and grid-screen sizes, d_s . The grid-screen was located at $X_s = 0.30$ m: a) $Q_a = 4$ L/min, $d_o = 1$ mm; b) $Q_a = 4$ L/min, $d_o = 3$ mm; c) $Q_a = 6$ L/min, $d_o = 1$ mm; d) $Q_a = 6$ L/min, $d_o = 3$ mm; e) $Q_a = 8$ L/min, $d_o = 1$ mm; f) $Q_a = 8$ L/min, $d_o = 3$	59
Figure 2. 12: Snapshot images of bubbles before and after a grid-screen with $d_s = 0.841$, $X_s = 0.22$ m, $d_o = 1$ mm, and different air discharges: a) $Q_a = 4$ L/min, (Test No. 20); b) $Q_a = 6$ L/min (Test No. 23); c) $Q_a = 8$ L/min, (Test No. 26).	60
Figure 2. 13: Regime classification in bubble plumes passing through a grid-screen. The classification is defined based on bubble velocity variations and distance from the nozzle (Test No.7, BP1-4-16).....	62
Figure 2. 14: The correlation of boundary height between regimes (III) and (IV) and Nozzle Reynolds number for bubble plumes passing through a grid screen: a) $d_s = 2.38$ mm; b) $d_s = 0.841$ mm.	63
Figure 2. 15: The correlation of boundary height between regimes (III) and (IV) and Bubble Reynolds number for bubble plumes passing through a grid screen: a) $d_s = 2.38$ mm; b) $d_s = 0.841$ mm.	65
Figure 2. 16: The correlation of boundary height between regimes (III) and (IV) and Bubble Reynolds number for bubble plumes passing through a grid screen: a) $d_s = 2.38$ mm; b) $d_s = 0.841$ mm.	66
Figure 3. 1: The schematic of experimental setup, images of optoelectronic unit, and optical probe tip of the Refractive Bubble Instrument (RBI).	76
Figure 3. 2: Snapshot images of bubbles showing the effects of air discharge, Q_a , on formation of bubble plume and bubble size distribution at a certain distance from the nozzle, $x/d_o = 177$: a) $Q_a = 3$ L/min; b) $Q_a = 6$ L/min; c) $Q_a = 9$ L/min; d) $Q_a = 12$ L/min.	78
Figure 3. 3: Images of bubble plume variations with time for the plume tests with $d_o = 3$ mm. The time step between each image is 0.07 seconds: a) $Q_a = 3$ L/min; b) $Q_a = 6$ L/min; c) $Q_a = 9$ L/min; d) $Q_a = 12$ L/min.	80
Figure 3. 4: Variations of the cumulative average of bubble velocity with distance from the nozzle: a) $x/d_o = 117$ and $Q_a = 12$ L/min; b) $x/d_o = 177$ and $Q_a = 9$ L/min; c) $x/d_o = 117$ and $Q_a = 6$ L/min; d) $x/d_o = 177$ and $Q_a = 3$ L/min. The dashed lines indicate the $\pm 4\%$ variations of the time-averaged bubble velocity.	82
Figure 3. 5: Effect of air discharge, Q_a , on the time-histories of bubble velocity at $x/d_o = 117$: a) $Q_a = 12$ L/min; b) $Q_a = 9$ L/min; c) $Q_a = 6$ L/min; d) $Q_a = 3$ L/min.	83
Figure 3. 6: Time-histories of bubble concentration with different air discharges at $x/d_o = 117$: a) $Q_a = 12$ L/min; b) $Q_a = 9$ L/min; c) $Q_a = 6$ L/min; d) $Q_a = 3$ L/min.	84
Figure 3. 7: Correlations between air discharge and bubble characteristics at $x/d_o = 117$: a) variations time average bubble concentration with Q_a , b) variations of time average bubble velocity with Q_a	85
Figure 3. 8: Effects of air discharge, Q_a , on bubble size distribution: a) $x/d_o = 203$; b) $x/d_o = 177$; c) $x/d_o = 127$; d) $x/d_o = 107$	87
Figure 3. 9: Variations of bubble size distribution using the Probability Density Function (PDF) with air discharge, Q_a , at different distances from the nozzle, x/d_o : a) $x/d_o = 203$; b) $x/d_o = 177$; c) $x/d_o = 127$; d) $x/d_o = 107$	88

Figure 3. 10: Variations of the bubble hydrodynamics along the vertical axis of bubble plumes with different air discharges of $Q_a = 3, 6, 9$ and 12 L/min: a) bubble mean velocity; b) interfacial area of bubbles; c) bubble mean diameter; d) bubble frequency; e) bubble concentration; f) bubble Reynolds number. The red vertical lines show the onset of bubble dispersion stage.....	92
Figure 3. 11: Effect airflow discharge, Q_a , on the total number of bubbles, N_b , above the nozzle with $d_o = 0.003$ m. The number of bubbles was detected during the 100 seconds of measurements.	94
Figure 3. 12: Effect of airflow discharge on the normalized momentum and buoyancy above the nozzle, $d_o = 0.003$ m: a) normalized momentum flux; b) normalized buoyancy flux.	96
Figure 3. 13: Variations of non-dimensional discharge of vertical bubble plume along the vertical axis.	98
Figure 3. 14: Effect of airflow discharge on variations of normalized bubble size with bubble Reynolds number.	100
Figure 3. 15: Effect of airflow discharge on variations of bubble velocity fluctuations above the nozzle, $d_o = 0.003$ m: a) bubble velocity fluctuations with x/d_o ; b) normalized bubble velocity fluctuations with x/d_o	101
Figure 3. 16: Effect of air discharge on the distribution of bubble turbulent intensity, I at $x/d_o = 177$ a) $Q_a = 3$ L/min; b) $Q_a = 6$ L/min; c) $Q_a = 9$ L/min; d) $Q_a = 12$ L/min.	103
Figure 4. 1: The schematic of experimental setup, optoelectronic unit, and coordinate system of a vertical bubble plume passing through a grid-screen.	112
Figure 4. 2: Images of the RBI instrumentation and bubbly plume: a) RBI optoelectronic unit; b) double-tip optical fiber probe; c) vertical bubble plume passing through a grid-screen with $X_s = 0.14$ m from the nozzle. The air discharge in this image is $Q_a = 4$ L/min and screen opening is $d_s = 0.841$ mm.	114
Figure 4. 3: Effect of grid-screen on the size and shape of bubbles after the screen: a) bubble plume without a grid-screen (Benchmark test, Test No.1, BP1); b) bubble plume with a grid-screen (Test No.7, BP1-14-16).....	117
Figure 4. 4: Vertical variations of the centerline velocity of bubbles above the nozzle for $Q_a = 6$ L/min, $d_o = 1$ mm (Test No. 2, BP2) and other similar tests in the literature.....	118
Figure 4. 5: Effect of air discharge on the vertical profile of bubble concentration in bubble plumes with different nozzle sizes, d_o , and grid-screen openings, d_s . The grid-screen was located at $X_s = 0.30$ m from the nozzle: a) $Q_a = 4$ L/min, $d_o = 1$ mm; b) $Q_a = 4$ L/min, $d_o = 3$ mm; c) $Q_a = 6$ L/min, $d_o = 1$ mm; d) $Q_a = 6$ L/min, $d_o = 3$ mm; e) $Q_a = 8$ L/min, $d_o = 1$ mm; f) $Q_a = 8$ L/min, $d_o = 3$ mm.....	120
Figure 4. 6: Time history plots of bubble plume characteristics: a) bubble velocity; b) gas time; c) liquid time.	122
Figure 4. 7: Vertical profile of average gas time at different distances from the nozzle: a) $Q_a = 4$ L/min, $d_o = 1$ mm; b) $Q_a = 4$ L/min, $d_o = 3$ mm, $d_s = 2.38$ mm; c) $Q_a = 8$ L/min, $d_o = 1$ mm; d) $Q_a = 8$ L/min, $d_o = 3$ mm.....	124
Figure 4. 8: Variations of the threshold air discharge, Q_{at} , in bubble plumes with different grid-screen openings, d_s , and distances from the nozzle, X_s	126
Figure 4. 9: Schematic sketch of control volume in a bubble plume passing through a grid-screen to determine forces acting on the grid-screen.	129
Figure 4. 10: A comparison on variations of drag coefficient used for bubble plumes, C_D , with bubble Reynolds number, Re_b , with other models.	130
Figure 4. 11: Effect of grid-screen on the vertical profile of buoyancy force, F_B , at different distances from the nozzle: a) $Q_a = 4$ L/min, $d_o = 1$ mm; b) $Q_a = 4$ L/min, $d_o = 3$ mm; c) $Q_a = 6$	

L/min, $d_o = 1$ mm; d) $Q_a = 6$ L/min, $d_o = 3$ mm; e) $Q_a = 8$ L/min, $d_o = 1$ mm; f) $Q_a = 8$ L/min, $d_o = 3$ mm.	132
Figure 4. 12: Effect of grid-screen on the vertical profile of drag force, F_D , at different distances from the nozzle: a) $Q_a = 4$ L/min, $d_o = 1$ mm; b) $Q_a = 4$ L/min, $d_o = 3$ mm; c) $Q_a = 6$ L/min, $d_o = 1$ mm; d) $Q_a = 6$ L/min, $d_o = 3$ mm; e) $Q_a = 8$ L/min, $d_o = 1$ mm; f) $Q_a = 8$ L/min, $d_o = 3$ mm.	134
Figure 4. 13: Variations of forces after the grid-screen versus Reynolds number: a) added mass force, F_{AM} ; b) buoyancy force, F_B ; c) drag force, F_D	136
Figure 4. 14: Variation of surface tension force, F_{σ} , versus bubble Reynolds number in bubble plumes with a grid-screen at different distances from the nozzle.	138
Figure 4. 15: Variation of the net acting force on the grid-screen, F_S , with Reynolds number in bubble plumes with a grid-screen and at different distances from the nozzle.	139
Figure 5. 1: The schematic of experimental setup, image of bubbly plume passing through bed sand, the components of an optoelectronic unit, and the Refractive Bubble Instrument (RBI) optical probe tip.	150
Figure 5. 2: Effects of bed sand with different grain sizes on variations of bubble mean diameter in vertically discharged bubble plumes for $Q_a = 6$ L/min, $h = 0.10$ m, and $d_o = 3$ mm: a) bubble plume without bed sand (i.e., benchmark test); b) $d_s = 2.38$ mm; c) $d_s = 4.76$ mm; d) $d_s = 12.5$ mm.	153
Figure 5. 3: Images on the time-series of bubble plumes passing through sand beds with different sand bed sizes for $d_o = 3$ mm, $h = 0.10$ m, and $Q_a = 6$ L/min: a) without a sand bed (i.e., benchmark test); b) $d_s = 2.38$ mm; c) $d_s = 4.76$ mm; d) $d_s = 12.5$ mm. The time step between each image is two seconds.	155
Figure 5. 4: Effects of sand bed thickness on the bubble size distribution in bubble plumes with a sand bed size of $d_s = 4.76$ mm and a maximum air discharge of $Q_a = 12$ L/min measured at $x/d_o = 190$	157
Figure 5. 5: Effects of aggregate size on bubble size distribution of a bubble plume with an air discharge of $Q_a = 6$ L/min and $h = 0.20$ m measured at $x/d_o = 143$	158
Figure 5. 6: Time-histories of bubble centerline velocity with different sand bed sizes at $x/d_o = 190$, $Q_a = 6$ L/min, and $h = 0.20$ m: a) without a sand bed (i.e., Benchmark test); b) $d_s = 2.76$ mm; c) $d_s = 4.76$ mm; d) $d_s = 12.5$ mm.	159
Figure 5. 7: Time-histories of bubble concentration for tests with an air discharge of $Q_a = 6$ L/min, sand bed thickness of $h = 0.20$ m, and with different sand bed sizes measured at $x/d_o = 190$: a) without sand bed (Benchmark test); b) $d_s = 2.76$ mm; c) $d_s = 4.76$ mm; d) $d_s = 12.5$ mm.	161
Figure 5. 8: Effect of sand bed thickness and aggregate size on variations of the centreline bubble velocity with the vertical distance from the nozzle: a) $Q_a = 3$ L/min, $h = 0.10$ m; b) $Q_a = 3$ L/min, $h = 0.20$ m; c) $Q_a = 6$ L/min, $h = 0.10$ m; d) $Q_a = 6$ L/min, $h = 0.20$ m; e) $Q_a = 12$ L/min, $h = 0.10$ m; f) $Q_a = 12$ L/min, $h = 0.20$ m.	163
Figure 5. 9: Variations of the normalized bubble velocity with normalized vertical distance from the nozzle in bubble plumes with different air discharges, Q_a , and sand bed thicknesses, h : a) $Q_a = 3$ L/min, $h = 0.10$ m; b) $Q_a = 3$ L/min, $h = 0.20$ m; c) $Q_a = 6$ L/min, $h = 0.10$ m; d) $Q_a = 6$ L/min, $h = 0.20$ m; e) $Q_a = 12$ L/min, $h = 0.10$ m; f) $Q_a = 12$ L/min, $h = 0.20$ m.	165
Figure 5. 10: Effect of grain size in bed sand, d_s , on variations of bubble interfacial area with vertical distance from the nozzle in bubble plumes with different air discharges, Q_a and sand bed thicknesses, h : a) $Q_a = 3$ L/min, $h = 0.10$ m; b) $Q_a = 3$ L/min, $h = 0.20$ m; c) $Q_a = 6$ L/min, $h = 0.10$ m; d) $Q_a = 6$ L/min, $h = 0.20$ m; e) $Q_a = 12$ L/min, $h = 0.10$ m; f) $Q_a = 12$ L/min, $h = 0.20$ m.	167
Figure 5. 11: Effect of sand bed size, d_s , on variations of the mean bubble diameter with vertical distance from the nozzle in bubble plumes with different air discharges, Q_a , and sand bed	

thicknesses, h : a) $Q_a = 3$ L/min, $h = 0.10$ m; b) $Q_a = 3$ L/min, $h = 0.20$ m; c) $Q_a = 6$ L/min, $h = 0.10$ m; d) $Q_a = 6$ L/min, $h = 0.20$ m; e) $Q_a = 12$ L/min, $h = 0.10$ m; f) $Q_a = 12$ L/min, $h = 0.20$ m. 169

Figure 5. 12: Effects of sand bed size, d_s , on variations of bubble concentration with the vertical distance from the nozzle in bubble plumes with different air discharges, Q_a , and sand bed thicknesses, h : a) $Q_a = 3$ L/min, $h = 0.10$ m; b) $Q_a = 3$ L/min, $h = 0.20$ m; c) $Q_a = 6$ L/min, $h = 0.10$ m; d) $Q_a = 6$ L/min, $h = 0.20$ m; e) $Q_a = 12$ L/min, $h = 0.10$ m; f) $Q_a = 12$ L/min, $h = 0.20$ m. 171

Figure 5. 13: Effect of sand bed size, d_s , on variations of bubble frequency with the vertical distance from the nozzle in bubble plumes with different air discharges, Q_a , and sand bed thicknesses, h : a) $Q_a = 3$ L/min, $h = 0.10$ m; b) $Q_a = 3$ L/min, $h = 0.20$ m; c) $Q_a = 6$ L/min, $h = 0.10$ m; d) $Q_a = 6$ L/min, $h = 0.20$ m; e) $Q_a = 12$ L/min, $h = 0.10$ m; f) $Q_a = 12$ L/min, $h = 0.20$ m. Continuous lines show the correlations for the benchmark test and dashed lines show the variations for the sand bed tests. 173

Figure 5. 14: Effect of sand bed size, d_s , on variations of bubble Reynolds number with the vertical distance from the nozzle in bubble plumes with different air discharges, Q_a , and sand bed thicknesses, h : a) $Q_a = 3$ L/min, $h = 0.10$ m; b) $Q_a = 3$ L/min, $h = 0.20$ m; c) $Q_a = 6$ L/min, $h = 0.10$ m; d) $Q_a = 6$ L/min, $h = 0.20$ m; e) $Q_a = 12$ L/min, $h = 0.10$ m; f) $Q_a = 12$ L/min, $h = 0.20$ m. 175

Figure 6. 1: The schematic of experimental setup, image of twin inclined bubbly jets, components of an optoelectronic unit, and Refractive Bubble Instrument (RBI) optical probe tip. 184

Figure 6. 2: Images of time variations of single vertical bubble jet with $Q_a = 2$ L/min and $Q_w = 3$ L/min ($Q_a/Q_w = 0.67$). The time step between each image is 0.05 second: a) $d_o = 3$ mm; b) $d_o = 4.2$ mm. 187

Figure 6. 3: Time-series images of Twin-Inclined (TI-Series) bubble jets. The time step between each image is 0.05 seconds: a) Test No.14 (TI1.11D3); b) Test No.16 (TI3.33D3). 188

Figure 6. 4: Snapshot images of bubbles showing the effects of inclined nozzles on formation of bubble jet and bubble size distribution at a certain distance from the nozzle: a) Test No.14, TI1.11D3, $x/d_o = 140$; b) Test No.2, SV1.11D3, $x/d_o = 140$; c) Test No.16, TI3.33D3, $x/d_o = 117$; d) Test No.4, SV3.33D3, $x/d_o = 117$ 189

Figure 6. 5: Effect of air injection configuration on the time-histories of bubble velocity at $x/d_o = 103$ for $Q_a/Q_w = 0.67$: a) Test No.1 (SV0.67D3); b) Test No.9 (TI0.67D2.1). 190

Figure 6. 6: Variations of bubble size and velocity along the vertical axis of bubbly jet with different air-water discharges: a) variations of bubble mean velocity in Single Vertical (SV-Series) bubbly jets; b) variations of bubble mean velocity in Twin Inclined (TI-Series) bubbly jets; c) variations of bubble mean size in Single Vertical (SV-Series) bubbly jets; d) variations of bubble mean velocity in Twin Inclined (TI-Series) bubbly jets. 192

Figure 6. 7: Variations of the normalized bubble velocity with normalized vertical distance from the nozzle in bubble jet with different air–water discharges with same nozzle diameter sizes: a) Single Vertical (SV-Series) bubbly jets; b) Twin Inclined (TI-Series) bubbly jet. 193

Figure 6. 8: Variations of bubble interfacial area and concentration along the normalized vertical distance of bubbly jet with different air-water discharges: a) variations of bubble mean velocity in Single Vertical (SV-Series) bubbly jets; b) variations of bubble mean velocity in Twin Inclined (TI-Series) bubbly jets; c) variations of bubble mean size in Single Vertical (SV-Series) bubbly jets; d) variations of bubble mean velocity in Twin Inclined (TI-Series) bubbly jets. 196

Figure 6. 9: Variations of bubble Reynolds number and bubble frequency along normalized vertical distance of bubbly jet with different air-water discharges: a) variations of bubble mean velocity in Single Vertical (SV-Series) bubbly jets; b) variations of bubble mean velocity in Twin Inclined (TI-

Series) bubbly jets; c) variations of bubble mean size in Single Vertical (SV-Series) bubbly jets; d) variations of bubble mean velocity in Twin Inclined (TI-Series) bubbly jets.	197
Figure 6. 10: Effects air-water discharge ratio on variations of bubble mean velocity along the vertical axis of Single Vertical and Twin Inclined bubble jets: a) $Q_a/Q_w = 0.67$; b) $Q_a/Q_w = 1.11$; c) $Q_a/Q_w = 2.00$; d) $Q_a/Q_w = 3.33$. Set 1 has a nozzle diameter of $d_o = 2.1$ mm for SV and $d_o = 3$ mm for TI and Set 2 has a nozzle diameter of $d_o = 3$ mm for SV and $d_o = 4.2$ mm for TI.	199
Figure 6. 11: Effects of air-water discharge ratio on variations of bubble interfacial area along vertical axis in both vertical and Inclined on the bubble jet: a) $Q_a/Q_w = 0.67$; b) $Q_a/Q_w = 1.11$; c) $Q_a/Q_w = 2.00$; d) $Q_a/Q_w = 3.33$. Set 1 has a nozzle diameter of $d_o = 2.1$ mm for SV and $d_o = 3$ mm for TI and Set 2 has a nozzle diameter of $d_o = 3$ mm for SV and $d_o = 4.2$ mm for TI.	200
Figure 6. 12: Variation of drag coefficient with bubble Reynolds number: a) Single Vertical bubble jets (SV-Series, Tests No.1 to 4); b) Twin Inclined bubble jets (TI-Series, Tests No.13 to 16). ...	201
Figure 7. 1: Schematic of the two-layer domain of distilled and saline flow layers in experimental tank and the sketch of the opto-electric unit.	211
Figure 7. 2: Image of a stratification profile in a reservoir.	213
Figure 7. 3: Bubble plume de-stratification in reservoirs.	214
Figure 7. 4: Numerical modeling of grid screen in column reactor by Jain et al. (2013)	215
Figure 7. 5: Suggested experimental setup for bubble plume with background turbulence.	216

Chapter 1

Motivation and Background

1.1 Definitions

Bubbles released from a localized source of air rise through the water column and entrain with the ambient water. This upward rising mixture, driven by the buoyancy force of bubbles, constitutes a bubble plume. Many parameters control the motion of bubbles in stagnant ambient water, such as the initial momentum due to air discharge, nozzle diameter, initial buoyancy due to density difference between air and water, and turbulent diffusion due to bubble motion (Lima Neto, 2012). Air flow can be released from a single circular nozzle, porous diffusers, or a cluster of nozzles to form a bubbly jet/plume. The change in the controlling parameters results in the formation of air bubbles with different shapes and sizes. The velocity of bubbles also depends on the discharge mechanism and the magnitude of the initial air discharge. Hence, the effects of initial flow configurations such as nozzle size and air discharge are indispensable to understand, control, and simulate the motion of air bubbles in form of bubbly jet/plumes. Many laboratory experiments and numerical simulations have been carried out to address the effects of controlling parameters on the motion of bubbles (Yapa and Zheng, 1999; Socolofsky and Adams, 2002, 2003; McGinnis et al., 2004; Singleton et al., 2007; Lima Neto et al., 2008a) and yet more studies are needed to understand the effect of other design parameters such as the addition of grid-screen and bed sands on bubble dynamics. Controlling parameters directly affect the oxygen transfer performance. Oxygen transfer from bubbles to bulk water depends on the dynamics of bubble plume parameters. The lateral bubble motion associated with wake vortices in the ambient fluid depends on the bubble size and bubble concentration in bubble plumes which vary with convection and diffusion processes.

Based on the balance between the initial momentum and buoyancy in bubble plumes, a discharge of air in the ambient water can form a bubbly jet or a bubbly plume. The bubbly jet is formed when a flow is generated by a continuous source of momentum (i. e., water

injection), whereas bubbly plume is formed by a buoyancy source of air injection with relatively low initial velocity). It is possible to have both initial momentum and buoyancy in bubbly jet-plume when a mixture of air and water is injected through a nozzle. A bubbly jet-plume is also called a forced plume or a buoyant jet in which both initial momentum and buoyancy control the motion of bubbles (Lee and Chu, 2003; Lima Neto et al., 2008b). In bubbly jet plumes, bubbles move upward due to the density difference between air and water and the initial velocity is the momentum of the jet. The effect of initial momentum augments bubble motion due to air and water injection. Extensive experimental and numerical studies have been performed to understand bubble dynamics in forced plumes (Jain et al., 2013). Different analytical and numerical models were proposed to predict bubble dynamics and mixing in bubbly jets and plumes (Lima Neto et al., 2008b).

1.2 Motivations

The efficiency of oxygen transfer is a fundamental goal in design of bubble plumes. Recent developments in bubble plume hydrodynamics have emphasized the need to enhance the performance of aerators. Despite the previous studies in bubble plume dynamics (Lima Neto et al., 2008a; Niida and Watanabe, 2018), little is known about bubble plume parameters that contributed to oxygenation and aeration performance improvement in water bodies such as reservoirs and lakes. (Szekely and Themelis, 1971; Socolofsky and Adams, 2002, 2003)

The present study is motivated by the effect of different nozzle size in reducing bubble size and increasing the contact area between air and water in buoyancy-driven bubble plumes. The larger contact surfaces between air and water enhance the oxygen transfer in wastewater treatment plants and improve aerators' efficiency in natural ponds. Due to the presence of small porous media in air-stone nozzles, such nozzles are more susceptible to clogging in wastewater treatment tanks and require frequent backwash and maintenance (Lai and Socolofsky, 2019). The aim of the present research project is to provide a conceptual and practical framework based on the effect of using natural bubble size reducers such as grid screen, bed sands, and different nozzle configurations on bubble

plume parameters such as bubble mean velocity, bubble mean diameter, bubble size distribution, bubble concentration, and bubble interfacial area. To improve the bubble plume's efficiency, bubble mean velocity should be reduced which increases the residence time in bubble plumes and increases bubble interfacial area by cutting bubbles into smaller size.

A grid-screen is introduced to be placed at fixed distances from a single circular nozzle to reduce bubble size and velocity similar to an air stone nozzle. However, it is expected that the maintenance costs due to air-stone clogging with time is eliminated by the new design **proposed in this research**. In this study, two grid-screens with different opening dimensions are tested, and the grid-screens are installed at different distances from the nozzle. The variations of bubble size, bubble concentration, and velocity along the vertical axis of bubble plumes are measured for different air discharges to understand how air discharge and screen size alter the bubble characteristics and how far air bubbles remain intact after passing through a grid screen. To test the effects of controlling parameters such as nozzle size, air discharge, grid-screen openings, and the distance between grid-screen and nozzle on the efficiency of bubble plume after the grid-screen, the variations of bubble characteristics such as bubble size, bubble velocity, and its concentration with the design parameters are examined. A Refractive Bubble Index (RBI) probe is used to collect bubble properties such as bubble diameter and velocity at the centerline of bubble plumes. Finally, the variations of acting forces on bubble plumes with grid screen are discussed based on the experimental results. The contributed parameters are used to estimate the magnitude of the screen surface tension and grid-screen resistance forces, by employing momentum equations for air and water phases.

In this study, the bubble plumes generated by an air injection system and different bubble size reducers are explored experimentally. Finally, some new equations and hydrodynamic boundaries are proposed to characterize bubble plume parameters after the grid-screen. Based on the proposed boundaries, the performance of the air injection system is investigated. Some **factors** that contribute the dynamics of bubble plume are:

- 1- The air injection system is an essential apparatus for aeration improvement in engineering projects or in environment.

- 2- Some of the existing designs requires more maintenance costs and it is expected that the new design decreases the associated costs, which is a very important parameter in the design process.
- 3- The air injection system has a simple construction; however, its applications are covered vast areas like a secondary pond. Therefore, finding and proposing a new approach to improve this structure can decrease the initial cost of project.

1.3 Application of bubble plumes

Bubble plumes encompass a wide range of natural phenomena and engineering applications such as oxygen level improvement in lake management, the prevention of suspended solids depositions in natural and man-made reservoirs, and the Dissolved Air Flotation systems (DAF) in water and wastewater treatment plants. The DAF system is an alternative clarification process that uses micro air bubbles to attach and float flocculated particles and suspended solids to the water surface for removal from the system. Moreover, aeration can be applied in oxygenation of water for fishes (Colt and Watten, 1988) and chemical reactions in metallurgical vessels (Szekely and Themelis, 1971). Air entrainment in rivers, lakes, and natural streams enhance the dissolved oxygen level and consequently improve the fish habitat. Bubble plumes have also been used to mix hot and toxic fluids in chemical engineering applications (Leitch & Daines, 1989). Bubbly flows are ubiquitous in chemical engineering applications, including chemical reactors, bioreactors, nuclear reactors, heat exchangers, and oil and gas pipelines. Bubble plumes are commonly used for hypolimnetic aeration and oxygenation, which preserves the stratification of water bodies while adding oxygen to the deepest layer of water. The reduction of oxygen in the hypolimnion layer (i.e., the layer of water in a thermally stratified lake that lies below the thermocline, is non-circulating, and remains perpetually cold) in lakes and reservoirs is a detrimental global problem that negatively affects the drinking-water treatment process, cold-water fisheries, and riverine flow impacted by releases from hydropower reservoirs.

The excessive loadings of phosphorous increase the content of organic matter, which leads to an increase in oxygen demand upon decomposition of organic matter at the surface of sediments. Meanwhile, a stable stratification condition, inhibits the replenishment of

oxygen to bottom layer of water as a result of surface aeration. As a result of stratification, lower layers of water exhibit significantly lower water quality level due to low oxygen concentration. In contrast, oxygen is needed to sustain a healthy lake ecosystem and to reduce water treatment costs in drinking water supplies (Little and McGinnis, 2001). A considerable amount of literature has been produced on the consequences of oxygen depletion in lakes and reservoirs (Beutel et al., 2008; Cooke and Carlson, 1989; Gantzer et al., 2009; Huttunen et al., 2006; Stefan, 1992). Although bubble plumes can be designed to perform their role by successfully adding oxygen to the water, research studies have shown that they may increase the consumption of oxygen in presence of sediments. Besides the application of bubble plumes in lake and reservoir management that mentioned above, other air injection **systems** and bubble plumes applications are listed as:

- 1- Using in the secondary treatment mixing ponds for water refinement,
- 2- Using as a device to increase the oxygen for aquatic creatures,
- 3- Using as a nozzle to inject gases through the water for gas mixing with the ambient,
- 4- Increasing and decreasing the growth rate of the alga and other aquatic vegetation cover that are mainly formed in lakes and rivers,
- 5- Decomposition of microorganisms by air injection system
- 6- Investigate the stratification in rivers and lakes,
- 7- Air and water mixing
- 8- Prevention of vegetation growth on the water surface by gas injection.

1.4 Methodology

Several methods have been introduced to evaluate bubble plume parameters such as employing optical probes and Particle Image Velocimetry (PIV) and Particle Tracking Velocimetry (PTV) techniques. The main concept in velocimetry methods is to obtain the velocity field information by measuring the displacement of passive tracer particles from recorded photographic images at different exposures with a certain time interval. In the case that the number of particle images per unit area is small, it is possible to track individual particles to measure their displacement in a pair of images; this is referred to as

the PTV method (Keane & Adrian, 1992 and Adrian, 1991). A comparison between a Double Optical Probe such as the Refractive Bubble Index (RBI) probe and Image Analysis indicated that the RBI Optical Probe results were more accurate in bubble characteristics measurements, especially in highly unidirectional flows (Kiambi et al., 2003). In this study, an RBI optical probe is used to study the motion and concentration of bubbles in bubble plumes. A double-tip optical fiber probe system (RBI instrumentation, Meylan, France) is used during experimentation to measure the characteristics of bubbles passing by the probe's tips. The characteristics measured include the void fraction (bubble concentration), bubble frequency (i.e., the average number of bubbles passing over one minute time and it is measured at each probe position), bubble residence time, bubble interface velocity, and the Sauter mean diameter. Measurements were taken in 16 different positions in the tank's centerline exactly above the nozzle. The probe works in conjunction with the signal processing optoelectronic unit and an interface board that communicates between the optoelectronic unit and the computer (see Figure 1.1).

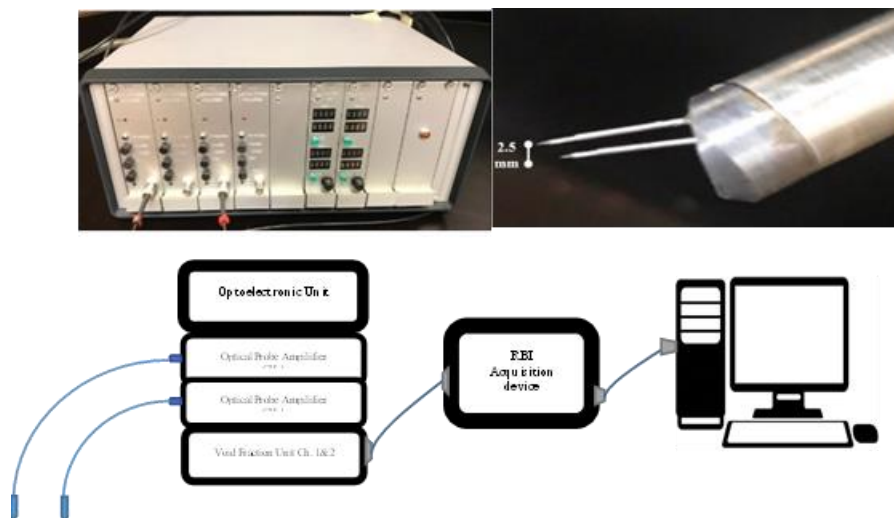


Figure 1.1: Optical Probe setup used in this study.

The optical probe detects the difference between air bubbles and water through its sophisticated mechanical properties. The optical fiber within the probe consists of crystals, which relays the signal received at the tip of the probe when in contact with either water or air. The signal is transmitted as light, which is sent from the optoelectronic unit. The light signal is refracted when the probe's tip contacts water and reflects to the optoelectronic

unit when the tip contacts air. The light reflection during the air phase occurs due to the glass within the optical fiber being of a higher index of refraction than the air. The light reflection does not occur in water because the calibration was set in the air at a threshold voltage level. The light is received by the optoelectronic unit and is interpreted as a signal that an air bubble has passed the probe. The signal has a rising edge as a bubble encounters a probe tip and a falling edge as the bubble leaves the probe tip, thereby re-submerging the tip in water.

Air bubbles are only detected if the signal is greater than or equal to the calibrated threshold voltage. Based on the length of time each of the two tips on the probe is inside an air bubble, calculation of the chord length, Sauter means diameter, and void fraction becomes possible. The optical probe is thus a powerful measurement tool when imaging techniques cannot be successfully utilized for reasons such as when a large void fraction exists, or if the apparatus is not made of a fully transparent material. During experimentation, the probe was submerged in the center of the water tank. The probe automatically moved to each of the 16 locations using an automatic measuring system. Data was collected for twenty minutes in each flow trial, in 16 different locations along the channel, for two minutes in each location. After recording concluded in one location, the probe automatically moved to its next position to begin recording another set of measurements. Once all measurements were collected for one discharge, the probe was moved to the starting position at the center of the tank to begin measurements for the subsequent discharge.

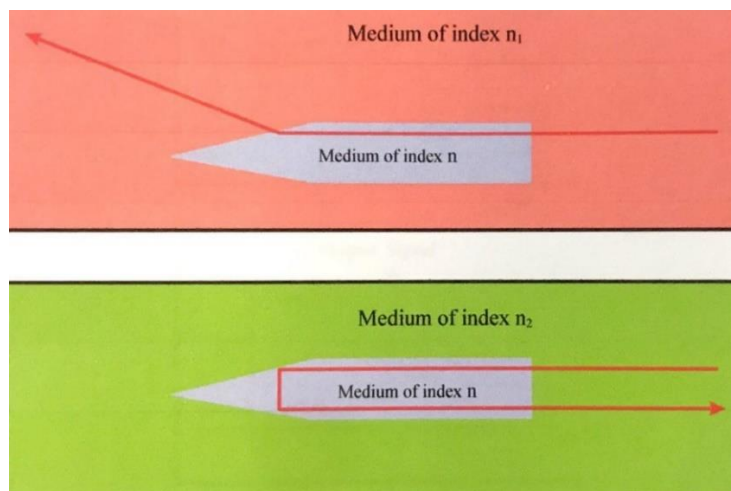


Figure 1.2: Depicting the path of light when the tip of the probe is in water (top image), and when a bubble is detected (bottom image).

After data collection, the computer software calculated several bubble parameters. The distance between the two tips on the probe of 2.5 mm must be entered into the software before parameter calculation could occur using the collected data. The void fraction (α) or bubble concentration (C_o) or more precisely the gas phase local presence ratio, is directly obtained by reducing the total presence time of the gas phase in contact with the sensitive tip of an optical probe to the whole observation time (Figure 1.3).

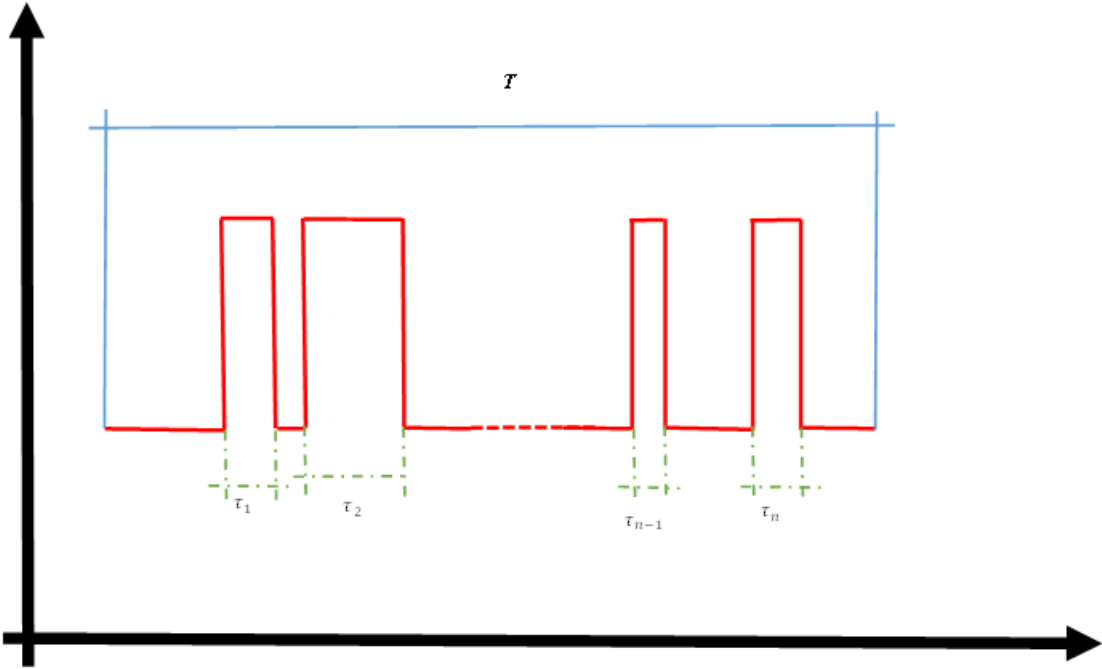


Figure 1.3: Typical phase indication function.

The void fraction is calculated by dividing the total time of air bubbles passing the probe tip by the total observation time as:

$$C = \frac{T_{gas}}{T_{acq}} = \frac{\sum_{i=1}^{i=n} \tau_i}{T} \tag{1.1}$$

where “ T_{gas} ” is the time a probe spent inside a bubble, and “ T_{aq} ” is the total acquisition time of one measurement (i.e., two minutes in this case). The probe could not provide the traditional void fraction, consisting of the total area, and the area occupied by the gas. Instead, it is a point measurement technique, where the calculated parameters are based on time. The probe recorded a count of the number of bubbles (N_b) as identified by signals from the probe tip detected at each vertical position at the centerline of the plume in the tank. The bubble interference frequency (f_b) was then calculated as:

$$f_b = \frac{N_b}{T_{acq}} \quad (1.2)$$

The time for one bubble to travel between one probe tip to the other was named the time of flight (T_{flight}), which was used to calculate the bubble interface velocity (u_b) using the following equation:

$$u_b = \frac{d}{T_{flight}} \quad (1.3)$$

where (d) corresponds to the distance between the probe tips (i.e., 2.5 mm). Since the distance between the two probe’s tips was invariable, the only factor influencing variations in the bubble interface velocity is the flighted time.

The interfacial area concentration in two-phase flow is defined as the total interface area per unit mixture volume. In the two-fluid model, this parameter specifies the geometric capability of the interfacial mass, momentum, and energy transfers because these interfacial transfers between the two phases are proportional to the available interface area. According to Ishii (1975), the definition of the local interfacial area concentration is given by:

$$a = \frac{1}{\Delta T} \sum \frac{1}{|V_i \cdot n_i|} = \frac{1}{\Delta T} \sum \frac{\Delta t}{\Delta s \cdot \cos \theta} = \frac{4N_b}{\Delta T} \cdot \frac{\Delta t}{\Delta s} \quad (1.4)$$

By using the mentioned parameters in the RBI software, bubble interfacial area, a could be shown by the following formula:

$$a = \frac{4f_{int}}{V_b} \quad (1.5)$$

Finally, the Sauter mean diameter (SMD or d_{32}), which is the average of bubble size, was calculated by considering the actual surface area, A_p and volume, V_p of bubble. It is assumed interfacial area concentration and void fraction play the same role as A_p and V_p in the RBI software as:

$$\frac{V_p}{A_p} = \frac{\frac{4}{3}\pi(\frac{d_v}{2})^3}{4\pi(\frac{d_s}{2})^2} = \frac{d_{32}}{6} \quad d_{32} = \frac{6V_p}{A_p} \quad d_b = \frac{6\alpha}{A_i} \quad (1.6)$$

1.5 Goals and Novelty of the present research study

There are several new aspects in the current study, which are briefly listed as:

- 1- Adjusting the grid-screen to increase the performance of the air injection system,
- 2- Characterizing the flow regime along the vertical bubble plume by employing the hydrodynamic parameters like bubble diameter and bubble velocity,
- 3- Considering the impacts of the contributed forces along the bubble plume with and without a grid-screen,
- 4- Measuring and testing the accuracy of experimental apparatuses like the RBI probe for future studies,
- 5- Proposing the hydrodynamic boundaries to specify the efficient distance in bubble plumes in case of increasing the aeration ratio,
- 6- **Determining** the percentage of the contributed forces in the stability of grid-screen.
- 7- Introducing the effect of bubble Reynolds number on variations of the contributed forces such as added mass, drag, and surface tension forces along the vertical bubble plume.

It should be mentioned that the experimental setup in this study was designed to attain the considered aims. The considered goals through this research are presented as follows:

- 1- Characterize the hydrodynamic parameters of bubble plumes with and without grid screen,

- 2- Define the bubble plume regimes along the vertical center line of the bubble plume based on the velocity variation,
- 3- Investigate the impacts of bubble properties such as bubble diameter and bubble velocity on performance of the air injection system with and without grid-screen.
- 4- Investigate the effect of the contributed bubble plume forces on the stability of the grid screen,
- 5- Investigate the effect of the grid-screen on the average of bubble velocity time histories of the bubble plume characteristics,
- 6- Investigate the variations of average gas time of bubble plumes at different distances from the nozzle,
- 7- Specify the threshold of flow discharge boundaries due to different grid-screen sizes and adjusted elevation, and
- 8- Investigate the variation of forces (i.e., added mass force, drag force) and study the effect of initial bubble Reynolds number.

1.6 Overview of the present study

The present study is motivated by the effect different bubble plume and nozzle configuration such as employing grid-screen, bed sand, and twin inclined nozzle in reducing bubble size and increasing the contact area between air and water in buoyancy-driven bubble plumes. The larger contact surfaces between air and water enhance the oxygen transfer in wastewater treatment plants and improve aerators' efficiency in natural ponds.

Chapter 2 of the thesis introduces a novel method to increase the oxygen transfer rate as well as reducing the maintenance cost due to clogging of air stones over time, a grid-screen is introduced to be placed at fixed distances from a single circular nozzle. In this chapter, two grid-screens with different opening dimensions are tested, and the grid-screens are installed at different distances from the nozzle. The variations of bubble size, bubble concentration, and velocity along the vertical axis of bubble plumes are measured for different airflow rates to understand how inflow rates and screen size alter the bubble characteristics and how far air bubbles remain intact after passing through a grid-screen.

To test the effects of controlling parameters such as nozzle size, airflow rates, grid-screen openings, and the distance between grid-screen and nozzle on the efficiency of bubble plume after the grid screen, the variations of bubble characteristics such as bubble size, bubble velocity, and its concentration with the design parameters are examined. Also, the bubble plume was improved by adjusting the grid-screen at the front of the enter nozzle which the air flow is injected into the ambient water. By employing the RBI probe and collecting the bubble properties, bubble diameter and velocity were measured at the centerline of the bubble plume.

In Chapter 3 of the present thesis, a series of laboratory experiments was conducted to test the effects of air discharge on bubble dynamics parameters by evaluating, bubble interfacial area and bubble size frequency. Four air discharges were selected (3, 6, 9 and 12 L/min) and bubble characteristics such as bubble mean velocity, bubble concentration, bubble mean diameter, and bubble size distribution were measured with a Bubble Refractive Instrument (RBI) probe. Linear correlations was proposed between normalized bubble diameters versus bubble Reynolds number.

In Chapter 4, the variation of the acting forces on the bubble plume with grid-screen were discussed and the forces were calculated from the experimental measurements. The effects of air discharge on the contributed parameters were investigated, and the screen surface tension force and grid-screen force were predicted by employing some formulas based on the non-line technique. Laboratory tests have been carried out to evaluate the effect of bed sands in bubble plume characteristics in Chapter 5. Different air discharges of $Q_a = 3$ L/min, 6 L/min, 9 L/min, and 12 L/min were selected to test the effect of air discharge on the dynamics of bubbles in vertically discharged bubble plumes. In this chapter, sand beds with different grain sizes are introduced to reduce bubble diameter and improve oxygen transfer as an example of sustainable and cost-effective approach.

Chapter 6 evaluates the effect of switching from single vertical nozzle to twin inclined nozzle on bubble jet parameters. The effect of nozzle configurations on rate of oxygen transfer was also studied. The experimental observations and extracted data were compared with the benchmark tests, including a single vertical bubbly jet with the same cross-sectional area as of twin bubbly jets to study the effect of bubble interaction and

coalescence due to collision of bubbles in inclined jets. The focus of this chapter was on bubble dynamics and mass transfer characteristics of bubbly jet and the aeration induced by air-water bubbly jets injected vertically and with two inclined nozzles in stagnant water.

The structure of the chapters of the present thesis are illustrated in Figure 1.4. As can be seen, the processes of the present study were shown step by step.

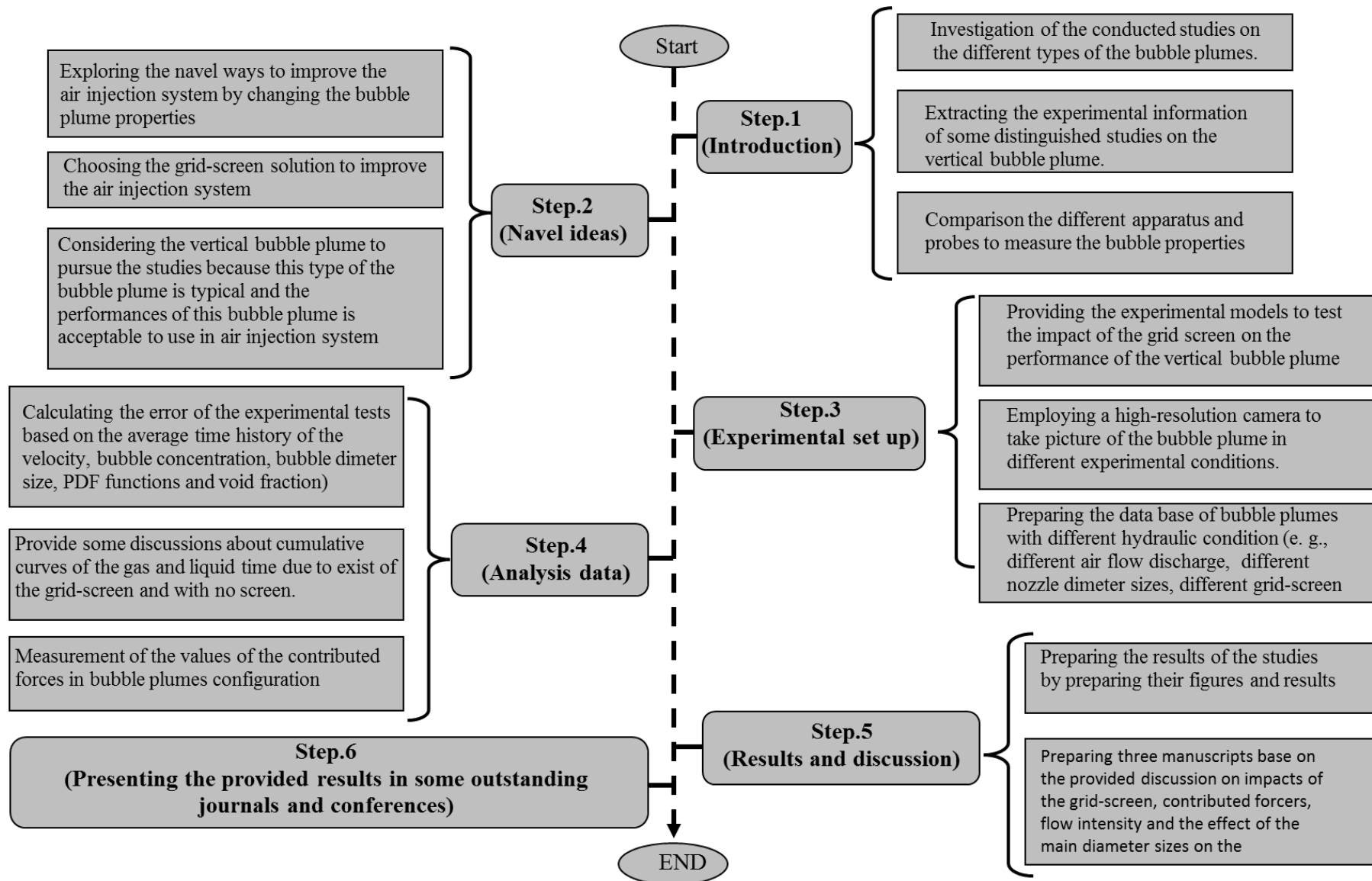


Figure 1.4: The steps of the present study

Hypotheses

Based on the results, the accuracy of the considered hypotheses are investigated. Several hypotheses that are considered through this research study are listed as:

- 1- The accuracy of the measurement by RBI probe is acceptable during the experimental test **by employing preliminary tests.**
- 2- The adjusted grid-screen directly impacts the bubble plume parameters such as bubble velocity and bubble plumes.
- 3- The grid-screen impact on the bubble velocity will be evaluated.
- 4- The size of nozzle affects the bubble plume configuration, which mainly impacts the bubble diameter.
- 5- The variation of air discharge impacts bubble characteristics such as bubble diameter and bubble velocity.
- 6- The variation of bubble velocity along the vertical axes is defined as the specified flow regimes.
- 7- The geometry parameters of the grid-screen impact on bubble plume forces such as buoyancy, Added mass, Drag, grid-screen, and surface tension forces.
- 8- Surface tension forces are determined based on the variation of the bubble Reynolds number.
- 9- The variation of the air discharge affect the flow regimes along the vertical axes of the vertical bubble plumes.
- 10- The RBI probe is reliable experimental apparatus to measure the bubble diameter and bubble velocity.
- 11- The adjusted grid-screen decreases bubble concentration at different elevations.
- 12- The probability density function can be used to show the effect of grid-screen and nozzle diameter on variation of bubble diameter and their density.
- 13- Increasing the elevation from the nozzle position decreases the bubble number, which can be deduced that due to elevation, the effect of the grid-screen was omitted, and the bubble clouds are developed through the water ambient.
- 14- The relationship between bubble diameter and vertical elevation can be characterized based on the experimental measurement.

Chapter 2

Effect of grid-screen on bubble characteristics of vertically discharged bubble plumes

2.1 Introduction

Multi-phase bubble plumes have been utilized in industrial technologies, natural water reclamation, and water quality improvement due to their capacity to induce buoyancy-driven flows and promote aeration and mixing. They have been recognized as an efficient method of enhancing air/oxygen transfer in lakes, rivers, and wastewater treatment plants (Wüest et al., 1992; Simiano et al., 2006; Funaki et al., 2009; Paerl and Otten, 2013; Aoyama et al., 2016; Ibelings et al., 2016; Yang et al., 2016). The advantages of bubble plumes over mechanical mixing systems are the simplicity of design, affordability of construction, and operation costs (Pacheco and Lima Neto, 2017; Lima and Lima Neto, 2018). Bubble plumes have been utilized in many environmental engineering problems such as oxygenation of the hypolimnion layer in lakes to reduce phosphorus release from sediments, and inhibit algal growth (Soltero et al., 1994, Moura et al., 2020). Other common applications of bubble plumes are in oxygenation of sewage in wastewater treatment plants (Schladow, 1992, 1993), in de-stratification of lakes and reservoirs (Lima Neto et al., 2016), in mixing of very hot or toxic liquids (Aoyama et al., 2016), and in destratification of lakes and reservoirs (Bormans et al., 2016). Moreover, air injection into effluent diffusers can be also an attractive alternative for artificial aeration of water bodies (Lima Neto et al., 2007).

Several mechanisms control the motion of bubbles in stagnant ambient such as initial momentum due to airflow, nozzle size, initial buoyancy due to density difference between air and water, and turbulent diffusion due to bubble motion (Lima Neto, 2012). Air is released from porous diffusers, single circular nozzles, or a cluster of nozzles to form a bubbly jet/plume, resulting in bubbles with different shapes, sizes, and velocities depending on the discharge device and the initial airflow discharge. Hence, the initial flow configurations such as nozzle size and airflow rate are indispensable to understand, control, and simulate such jets/plumes (Yapa and Zheng, 1999; Socolofsky and Adams, 2002, 2003; McGinnis et al., 2004; Singleton et al., 2007; Lima Neto et al., 2008a;

Mantripragada et al., 2021). A forced plume or a buoyant jet is formed when air and water are injected through a nozzle in which both momentum and buoyancy forces control the motion of bubbles (Lee and Chu, 2003; Lima Neto et al., 2008b). In bubbly jet-plumes, bubbles move upward due to the density difference between air and water, and bubble motion is augmented by the initial injection of air and water. Extensive experimental and numerical studies have been performed to understand bubble dynamics and different models were proposed to predict bubble dynamics and mixing in bubbly jets and plumes.

Experimental studies have shown that the geometry and initial flow rates of air/water have significant importance in the characteristics of bubble plumes (Rosso and Stenstrom, 2006; Lima Neto et al., 2008a; Laupsien et al. 2017; Lai and Socolofsky, 2019; Liu et al., 2019). Table 2.1 shows a list of experimental studies to explore the dynamics of bubble plumes for mixing improvement by testing the controlling parameters such as nozzle size, d_o , airflow rate, Q_o , mean bubble diameter, d_b , and ambient water depth, h .

Table 2. 1: Experimental parameters and air flow discharges of bubbly jets and plumes from the literature.

No.	Study	Flow	Tank Size (m) $W \times L \times H$	h	d_o	Q_o	d_b
				(m)	(mm)	(L/min)	(mm)
1	Asaeda and Imberger (1992)	Bubble plume	$1 \times 1 \times 0.75$	0.38 – 0.6	24	0.00264 – 0.768	< 4
2	Rensen and Roig (2001)	Bubble plume	$0.15 \times 0.15 \times 0.67$	0.465 0.465 0.465 0.65	Capillary tube	1.26 1.84 3.24 1.84	2.8 3 3.4 3
3	Bergman et al. (2004)	Bubble plume	$0.4 \times 0.4 \times 0.7$	0.7	Air stone	0.5, 1, 1.5	3
4	Roig and Tournemine (2007)	Bubbly jet	$0.3 \times 0.15 \times 3.1$	3.1	Capillary tube	$Q_a = 0.4 - 5$ $Q_w = 1 - 7$	1.14 – 2.38
5	Seol et al. (2007)	Bubble plume	$0.38 \times 0.38 \times 0.8$	0.6	Air stone	0.5 1 1.5	1.51 1.71 2.02

6	Lima Neto et al. (2008a)	Bubble plume	$1.2 \times 1.2 \times 0.8$	0.76	1×6 1×3 4×1.5 9×1 Air stone	2, 3	8
7	Lima Neto et al. (2008b)	Bubbly jet, Pure water jet	$1.2 \times 1.2 \times 0.8$	0.76	4, 6, 9, 13.5	$Q_a = 7.56 - 108$ $Q_w = 12$	1.14 – 2.38
8	Lima Neto et al. (2008d)	Bubbly jet	$1.8 \times 1.2 \times 0.8$	0.76	6	$Q_a = 1, 3, 5$ $Q_w = 3, 5, 7$	1.8 – 3.4
9	Seol et al. (2009)	Bubble plume	$0.38 \times 0.38 \times 0.8$	0.7	Air stone	0.1	1.2
10	Riboux et al. (2009)	Bubble plume	$0.15 \times 0.15 \times 1$	1	0.1 0.2 0.33 0.4	Not reported	1.6 2.1 2.5 2.5
11	Bryanat et al. (2009)	Bubble plume	$1 \times 2 \times 1.5$	1.5	Air stone	0.5, 1, 1.5	2
12	Funkai et al. (2009)	Bubble plume	$1 \times 1 \times 1$	1	127	Not reported	0.3 – 5.8
13	Fraga and Stoesser (20016)	Bubble plume	$2 \times 1 \times 1$	1	Air stone	0.5, 1.5	1, 2, 4
14	Ziegenhein and Lucas (2014)	Bubble plume	$0.05 \times 0.25 \times 0.6$ $0.05 \times 0.1125 \times 1.8$	0.6 1.8	0.7 – 0.9	0.6 4.81	3 – 5 7 – 8
15	Almeras et al. (2017)	Bubble plume	$0.45 \times 0.45 \times 2$	2	Capillary tube	Not reported	2 – 3.6
16	Lima and Lima neto (2018)	Bubbly jet	$0.5 \times 0.5 \times 1$	0.8	1×30 1×10 4×5 8×3.5	$Q_a = 1 - 9$ $Q_w = 11 - 30$	1.7 – 4.8
17	Niida and Watanabe (2018)	Bubble plume	$0.15 \times 0.17 \times 0.2$	0.2	0.26 0.4 1.2 1.2 1.2	0.015 0.04 0.05 0.08 0.012	2 3.2 3.6 4.2 4.9
18	Lai and Socolofsky (2019)	Bubble plume	$1 \times 1 \times 1$	1	Air stone	0.5, 1.5	1 – 4

19	Wang et al. (2019)	Bubble plume	$9.1 \times 4.6 \times 16.8$	16.8	0.4	0.25 1.2	3.8 4.1
20	Besbes et al. (2019)	Bubble plume	$0.25 \times 0.25 \times 0.3$	0.3	Sparger	850 2550 4250	4.55 4.87 4.88
21	This study	Bubble plume	$0.85 \times 1.60 \times 0.80$	0.7	1, 3	4, 6, 8	6-14

Many research studies have demonstrated the effect of air injection on the hydrodynamics of bubbles in multiphase plumes and have correlated the initial parameters such as nozzle size and air discharge on variations of bubble centerline velocity (Milgram, 1983; Socolofsky and Adams, 2003, 2005; Bombardelli, 2007; Lima Neto et al., 2008a, 2012; Wang et al., 2019; Besbes et al., 2019; Bohne et al., 2020). Fisher et al. (1979) indicated that the centerline velocity of bubbles in momentum-driven bubble plumes is a function of distance from the nozzle, x , and the initial momentum flux, M_o . In buoyancy-driven plumes (i.e., buoyant plumes) the centerline velocity of the plume is a function of distance from the nozzle, x , and the initial buoyancy flux, B_o . Recent studies have also confirmed the nonlinear correlation between the centerline velocity of bubbles and the distance from the nozzle in form of $u_b \sim x^{-1/3}$ (Bombardelli et al. 2007; Lai and Socolofsky, 2019). Bombardelli et al. (2007) provided a prediction model to estimate bubble centerline velocity, u_s , by scaling the distance from the nozzle, x , with a length scale, D , at which $D = gQ_o/4\pi\alpha^2u_s^3$ where g is the acceleration due to gravity, α is the entrainment coefficient, and u_s is the bubble slip velocity. It was found that the normalized bubble velocity can be expressed as $u_b/u_s = 1.24(x/D)^{-1/3}$.

The impact of bubble expansion as hydrostatic pressure decreases, and buoyancy variation were studied by Fanelop (1980). The centerline velocity of bubbles and its variations along with a relatively deep tank (i.e., $h = 10$ m) was measured and the effect of air discharge, ranged between 300 L/min to 1326 L/min, on bubble velocity was tested. It was found that the centerline bubble velocity decreased with distance from the nozzle, x , and the centerline velocity linearly decreased by 34% at a distance 9 m from the nozzle. A series of experimental investigations was carried out to study the effects of plume configuration on model blowout and broken gas pipelines (Milgram, 1983). Their

laboratory experiments were carried out in a 3.66 m deep tank and bubble plumes with different air discharges ranging between 12.1 L/min and 140 L/min were tested. It was found that the centerline velocity of bubbles decreased by approximately 45% at a distance 1.5 m from the nozzle and velocity variations along the vertical axis became negligible afterwards.

Experimental studies on the aeration configuration of bubble plumes have shown that the initial nozzle configuration has a negligible effect on variations of centerline bubble velocity (Lima Neto et al., 2008a). Lima Neto (2012) developed an integral model to predict bubble velocity variations and found that the centerline velocity was invariant with water depth for $x > 1.5$ m. Beyond the threshold distance, the centerline velocity of bubbles was 34% of the initial bubble velocity. Fraga and Stoesser (2016) performed a large-eddy simulation of bubble plumes. The numerical model was validated with the experimental data of vertically released bubble plumes (see Table 2.1). An adverse correlation was found between bubble size and centerline velocity. It was found that the slope of velocity decay decreased with increasing mean bubble diameter. The numerical results indicated that the centerline bubble velocity decreased far from the nozzle, and it was independent of the nozzle size.

Wang et al. (2019) developed a new theoretical study based on diffusive spreading to describe the lateral spreading of bubble plumes. The proposed theoretical study was validated with experimental data. Bubble plume characteristics such as bubble mean velocity, volume flux, momentum flux, and spreading rate of bubble plumes were predicted for buoyancy-driven (i.e., pure plume) and weak momentum-driven bubble plumes. The spreading rate of the weak momentum-driven plumes was found to be smaller than the classic buoyancy-driven pure plume. The dynamics of weak momentum-driven bubble plumes indicated that the normalized bubble velocity decreased with a distance from the nozzle in form of $u_b/u_s \sim x^{-1/2}$.

Many studies have shown the effect of plume characteristics such as nozzle diameter and airflow rate on bubble size and bubble size distributions (Clift et al., 1978; Iguchi et al., 1989; Wuest et al., 1992; Swasn and Mores, 1993; Renson and Roig, 2001; Bergman et al., 2004; Garcia and Garcia, 2006; Lima Neto et al., 2008 a, b; Bryant et al., 2009; Ziegenhein

and Lucas, 2017; Lima and Lima Neto, 2018; Niida and Watanabe, 2018). Laboratory experiments indicated that bubble breakup occurs at a threshold Reynolds number of $Re = 8000$. For $Re > 8000$, large bubbles break up into smaller bubbles and produce a relatively uniform bubble size distribution (Lima Neto et al., 2008b; Laupsien et al., 2021). It was found that bubble velocity was independent of nozzle size, but bubble size decreased by approximately 20% to 50% for bubble plumes generated from porous air-stone instead of single circular nozzles.

Recent laboratory experiments have confirmed the effect of porous diffusers on altering the variations of centerline bubble velocity with depth (Li et al., 2020). The numerical simulations of Li et al. (2020) have revealed that bubble size distribution ranged between 1 mm and 1.5 mm at the center of the plume and bubble sizes increased from 1.5 mm to 2.5 mm along the axis of the plume. Relatively larger bubbles (i.e., $2.5 \text{ mm} < d_b < 3 \text{ mm}$) were observed on the boundary of the plume. The experimental study of Ziegnehein and Lucas (2017) showed an adverse correlation between bubble size and airflow rate. It was reported that bubble plumes with high flow rates generated a more uniform bubble size distribution. The recent study of Bohne et al. (2020) confirmed the adverse correlation between bubble size and airflow rate.

A novel Micro Structured Bubble Column reactor (MSBC) was designed by using a wire mesh structure inserted in a pseudo-2D bubble column reactor (Sujatha et al., 2015). Different bubbly flow configurations passing through the wire mesh were tested by employing visual observations. The experimental results identified three different regimes named as bubble cutting, bubble cutting followed by re-coalescence, and gas pocket formation. The superficial gas velocities for different mesh sizes ranged from 5 to 50 mm/s. In addition to image analysis, an ultrafast X-ray tomography technique was employed to study the effect of wire mesh on bubble size reduction (Sujatha, 2016).

The performance of Micro Structured Bubble Column on bubble dynamics was investigated numerically (Jain et al., 2013). The results of validated numerical model to simulate MSBC indicated that the wire meshing is able to cut the bubbles, increases the interfacial area of bubbles, and enhances the interface dynamics. The effects of single layer and double layers of mesh on bubble dynamics were tested by employing optical

measurements and Particle Image Velocimetry (PIV) techniques (Chen et al., 2021). A comparison between one and two layers of mesh with the benchmark tests indicated that the bubble size decreased by 22.7% and 29.7%, the gas hold up increased by 5.7% and 9.7%, and the interfacial area increased by 34.8% and 43.5%, respectively.

The present study is motivated by the effect of porous air-stone devices in reducing bubble size and increasing the contact area between air and water in buoyancy-driven bubble plumes. The larger contact surface between air and water enhances the oxygen transfer between air and water, which is beneficial in improving effluent quality in wastewater treatment plants and can improve the efficiency of aerators in natural water bodies (Muller et al., 2002). Due to presence of small porous media in air-stone nozzles, such devices are more susceptible to clogging in wastewater treatment tanks and require frequent backwash and maintenance. To reduce the operation cost because of significant head losses in porous nozzles and the maintenance costs due to clogging of air-stones over time, a grid-screen is introduced which is installed at fixed distances from a single circular nozzle.

In this study, two grid-screens with different opening dimensions are tested and the grid-screens are installed at three different distances from the nozzle. The variations of bubble size, bubble concentration, and velocity along the vertical axis of the bubble plumes are measured for different air discharges to understand how air discharge and screen size affect bubble characteristics and how far air bubbles remain intact after passing through a grid-screen. To test the effects of controlling parameters such as nozzle size, airflow rates, grid-screen openings, and the distance between grid-screen and nozzle on the efficiency of bubble plume after the grid-screen, the variations of bubble characteristics such as size, velocity, and concentration with the design parameters are examined.

2.2 Experimental Setup

A series of laboratory experiments were conducted in the Multiphase Flow Research Laboratory (MFRL) at Lakehead University to study the effects of air discharge and grid-screen on variations of bubble characteristics. The experiments were performed in a glass-walled tank of 1.60 m long, 0.85 m wide, and 0.80 m deep as shown in Figure 2.1. The

tank was filled up with tap water at $20^{\circ}\text{C} \pm 1^{\circ}\text{C}$ to a depth of 0.70 m. An air pipeline provided compressed air with a pressure of $P = 4$ atm. Different airflow rates of $Q_a = 4$ L/min, 6 L/min, and 8 L/min were selected for this study. The airflow rates were measured with an accurate rotameter (LZM series Zyia OEM, Zhejiang, China) with an accuracy of $\pm 4\%$. Two different circular nozzles with the inner diameters of $d_o = 1$ mm and 3 mm were chosen and the nozzles were placed at the center of the tank and at 100 mm above the bottom (see Figure 2.1). Standard grid-screens with sieve openings of $d_s = 0.841$ mm (i.e., sieve number #20) and $d_s = 2.380$ mm (i.e., sieve number #16) were employed. The grid-screen was installed at three different elevations from the nozzle, $X_s = 0.14$ m, 0.22 m, and 0.30 m.

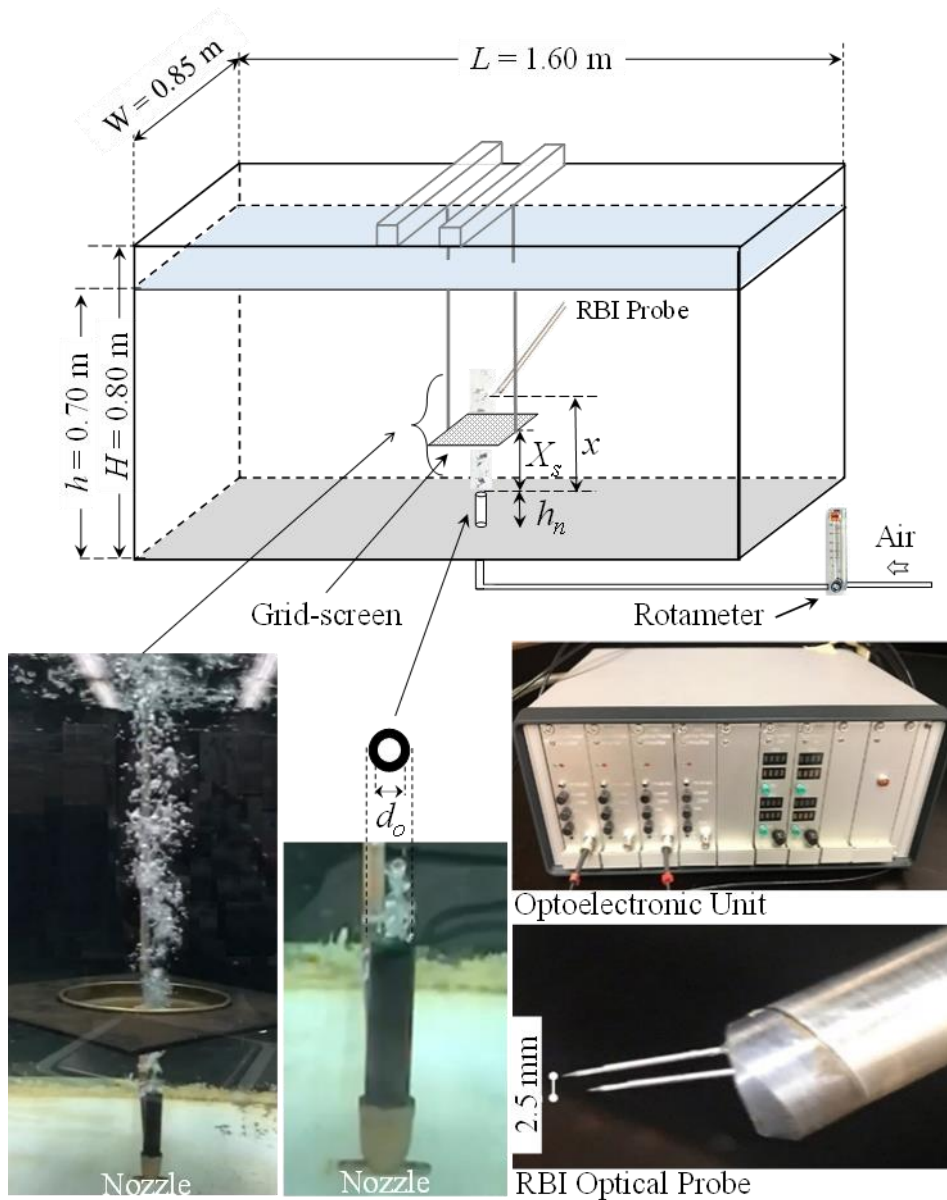


Figure 2. 1: The schematic of experimental setup **used in this study**, image of bubbly plume passing through a grid-screen, the components of an optoelectronic unit and Refractive Bubble Instrument (RBI) optical probe tip.

Overall, 36 experiments were carried out to test the effects of nozzle size, d_o , air discharge, Q_a , grid-screen size, d_s , and the distance between grid-screen and the nozzle, X_s (see Table 2.2). Benchmark tests (i.e., bubble plumes without a grid-screen) were performed to evaluate the performance of grid-screens on bubble size and velocity reduction. The optical probe was placed at the centerline of the nozzle and measurements were taken in a vertical

axis from the nozzle to the water surface with an increment of 30 mm. The experimental parameters, bubble characteristics, and the associated non-dimensional parameters are listed in Table 2.2. The time averaged bubble velocity and concentration were calculated from the analog voltage signals by the RBI software. In Table 2.2, u_b is the bubble velocity, d_a is the bubble size, C_b is the concentration factor, and Re is the Reynolds number at the nozzle in which $Re = u_o d_o / \nu_{air}$, where u_o is the initial bubble velocity, d_o is the nozzle diameter, and ν_{air} is the kinematic viscosity of air.

Table 2. 2: Experimental parameters and bubble characteristics of vertically discharged bubble plumes passing through a sieve.

Test NO.	Test.	X	d_o	Q_a	Sieve No/size		X/d_o	u_b	d_b	C_b	Re
	symbol	(mm)	(mm)	(L/min)	No.	(mm)		(m/s)	(mm)	(%)	(-)
1	BP1-4	0	1	4	-	-	-	0.855	8.94	3.98	5661.71
2	BP1-6	0	1	6	-	-	-	0.96	10.57	4.74	8492.56
3	BP1-8	0	1	8	-	-	-	1.085	10.4	9.05	11323.42
4	BP3-4	0	3	4	-	-	-	0.76	9.22	3.67	1887.23
5	BP3-6	0	3	6	-	-	-	0.846	10.32	4.59	2830.85
6	BP3-8	0	3	8	-	-	-	1.12	13.64	5.85	33970
7	BP1-4-16	14	1	4	16	2.38	3.50	0.734	7.63	4.02	5661.71
8	BP1-4-16	22	1	4	16	2.38	5.50	0.68	7.56	3.27	5661.71
9	BP1-4-16	30	1	4	16	2.38	7.50	0.66	7.43	2.89	5661.71
10	BP1-6-16	14	1	6	16	2.38	2.33	0.797	7.68	5.46	8492.56
11	BP1-6-16	22	1	6	16	2.38	3.67	0.73	7.24	4.37	8492.56
12	BP1-6-16	30	1	6	16	2.38	5.00	0.698	7.26	4.19	8492.56
13	BP3-4-16	14	3	4	16	2.38	3.50	0.688	6.82	3.94	1887.23
14	BP3-4-16	22	3	4	16	2.38	5.50	0.65	6.9	3.38	1887.23
15	BP3-4-16	30	3	4	16	2.38	7.50	0.62	6.8	3.36	1887.23
16	BP3-6-16	14	3	6	16	2.38	2.33	0.769	7.36	5.24	2830.85

17	BP3-6-16	22	3	6	16	2.38	3.67	0.727	7.12	4.63	2830.85
18	BP3-6-16	30	3	6	16	2.38	5.00	0.67	6.86	4.1	2830.85
19	BP1-4-20	14	1	4	20	0.841	3.50	0.676	7.42	2.64	5661.71
20	BP1-4-20	22	1	4	20	0.841	5.50	0.61	7.22	1.965	5661.71
21	BP1-4-20	30	1	4	20	0.841	7.50	0.54	6.45	1.64	5661.71
22	BP1-6-20	14	1	6	20	0.841	2.33	0.78	7.57	4.49	8492.56
23	BP1-6-20	22	1	6	20	0.841	3.67	0.73	7.56	3.99	8492.56
24	BP1-6-20	30	1	6	20	0.841	5.00	0.65	7.03	3.24	8492.56
25	BP1-8-20	14	1	8	20	0.841	1.75	0.89	7.63	7.01	11323.42
26	BP1-8-20	22	1	8	20	0.841	2.75	0.86	7.86	7.24	11323.42
27	BP1-8-20	30	1	8	20	0.841	3.75	0.78	7.34	6.34	11323.42
28	BP3-4-20	14	3	4	20	0.841	3.50	0.73	7.22	3.7	1887.23
29	BP3-4-20	22	3	4	20	0.841	5.50	0.58	6.65	1.86	1887.23
30	BP3-4-20	30	3	4	20	0.841	7.50	0.5	5.96	1.54	1887.23
31	BP3-6-20	14	3	6	20	0.841	2.33	0.81	7.67	5.03	2830.85
32	BP3-6-20	22	3	6	20	0.841	3.67	0.67	6.99	3.42	2830.85
33	BP3-6-20	30	3	6	20	0.841	5.00	0.62	6.84	3.22	2830.85
34	BP3-8-20	14	3	8	20	0.841	1.75	0.89	8.16	6.48	33970
35	BP3-8-20	22	3	8	20	0.841	2.75	0.77	7.65	5.38	33970
36	BP3-8-20	30	3	8	20	0.841	3.75	0.67	7.96	5.34	33970

The experimental tests started with BP, which stands for Bubble Plume, and the numbers after BP are the nozzle size in millimeter, air discharge in L/min, and sieve number. For example, the test BP1-4-20 belongs to a bubble plume with a nozzle diameter of $d_o = 1$

mm, air discharge of $Q_a = 4$ L/min, and the sieve number of #20. In this study, bubble characteristics such as bubble size, bubble velocity, and void fraction are measured.

A high-resolution camera (Prosilica GT 1910c CCD, Germany) with a speed of 20 frames per second was placed perpendicular to the tank with 1.4 m from the tank to capture images of bubble plumes and break-up/coalescence of bubbles before and after the grid-screen. A snapshot of bubble plume after the grid-screen is shown in Figure 2.1. The camera was fitted with either a 90-mm Kowa F 1.8 (Kowa, Japan) or an 18–55 mm AF-Sinkkor, 13.5–5.6 GII (Nikon, Japan) lens. A double-tip optical fiber probe system (RBI instrumentation, Meylan, France) was used to measure bubble characteristics such as bubble size, bubble velocity, and bubble concentration. A module emits infrared light via two fiber-optic cables to the tips of the probe. The probes' tips are 15 mm long, 2.5 mm apart, and two sapphire crystals were installed at the end of the probe tips (see Figure 2.1). The emitted light is refracted when the probe tip is in water and is reflected in the module when the probe tip is in the air (i.e., inside a bubble). The reflected light passes through a semi-transparent mirror combined with a prism towards a photosensitive diode in the module. The light transmission system enables the probe to acquire voltage signals with a sampling rate of 1 MHz (RBI User Manual, Meylan, France).

The raw signals are directly amplified and detected through a threshold technique method (ISO Lite Software, RBI Optical probe, France) and the analog signals are converted to a two-state signal corresponding to the phases of air and water as shown in Figure 2.2. Figure 2.2 shows a sample of a two-stage voltage signal during 30 seconds of data acquisition and a sketch of the phase identification. By analyzing digital voltage signals, the double-tip optical fiber probe is capable of measuring bubble size, void fraction (i.e., bubble concentration), and bubble frequency. In addition, bubble velocities are calculated by cross-correlation of voltage signals from both probe tips. The RBI double-tip optical fiber probe has been successfully employed in many studies. The accuracy and robustness of the system have been verified in measuring bubble characteristics in two-phase gas-liquid flows (Rensen and Roig, 2001; Boes and Hager, 2003; Kiambi et al., 2003; Chaumat et al., 2005; Murzyn et al., 2005; Lima Neto et al., 2008a, b, c). However, the RBI double-tip optical fiber probe has limitation in size determination of very oblong bubbles. A

careful observation of the images in the present study indicated that the bubbles were mostly semi-spherical.

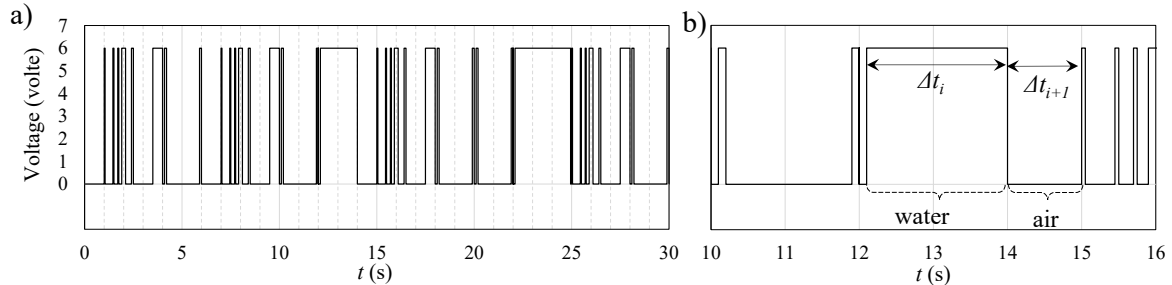


Figure 2. 2: Time histories of the recorded voltage signals with a Refractive Bubble Instrument (RBI) optoelectronic unit: a) a sample of instantaneous voltage signals with time; b) phase identification from raw voltage signals.

A number of research papers evaluated the performance of Double Optical Probe over other measurement techniques such as Passive Acoustics, Inverted Funnel, and Image Analysis (Vazquez et al., 2005; Kiambi et al., 2003). Vazquez et al. (2005) investigated the performance of three measurement techniques for bubble size determination in the quiescent water. The Passive Acoustic method performed within an accuracy between 97% and 99% in comparison with the Inverted Funnel method having an accuracy range between 88% and 96%. Furthermore, a comparison between Double Optical Probe and Image Analysis indicated that the RBI Optical Probe results were more accurate in bubble characteristics measurements especially in highly unidirectional flows where the bubble translations and rotations effects are minimized by the ambient flow (Kiambi et al., 2003).

2.3 Results and Discussions

Figure 2.3 shows the time histories of the cumulative averages for bubble velocity and bubble concentration for Tests No. 1 and No. 7 (i.e., bubble plumes with and without a grid-screen). A recording time duration of 120 seconds was selected for all experiments to ensure reaching suitable average values of bubble characteristics. The black dashed lines show the time averaged bubble velocity and concentration at 120 seconds from the

beginning of measurements. The red dashed lines show the $\pm 5\%$ variations from the averaged bubble velocity and concentration for 120 seconds of data. For bubble plumes without a grid-screen, the averaged bubble velocity and concentration after 120 seconds duration of data were 0.791 m/s and 3.917%, respectively. The cumulative average values of bubble velocity and concentration for bubble plumes with a grid-screen indicated that the bubble velocity and bubble concentration decreased by 12.5 % and 7.5%, respectively.

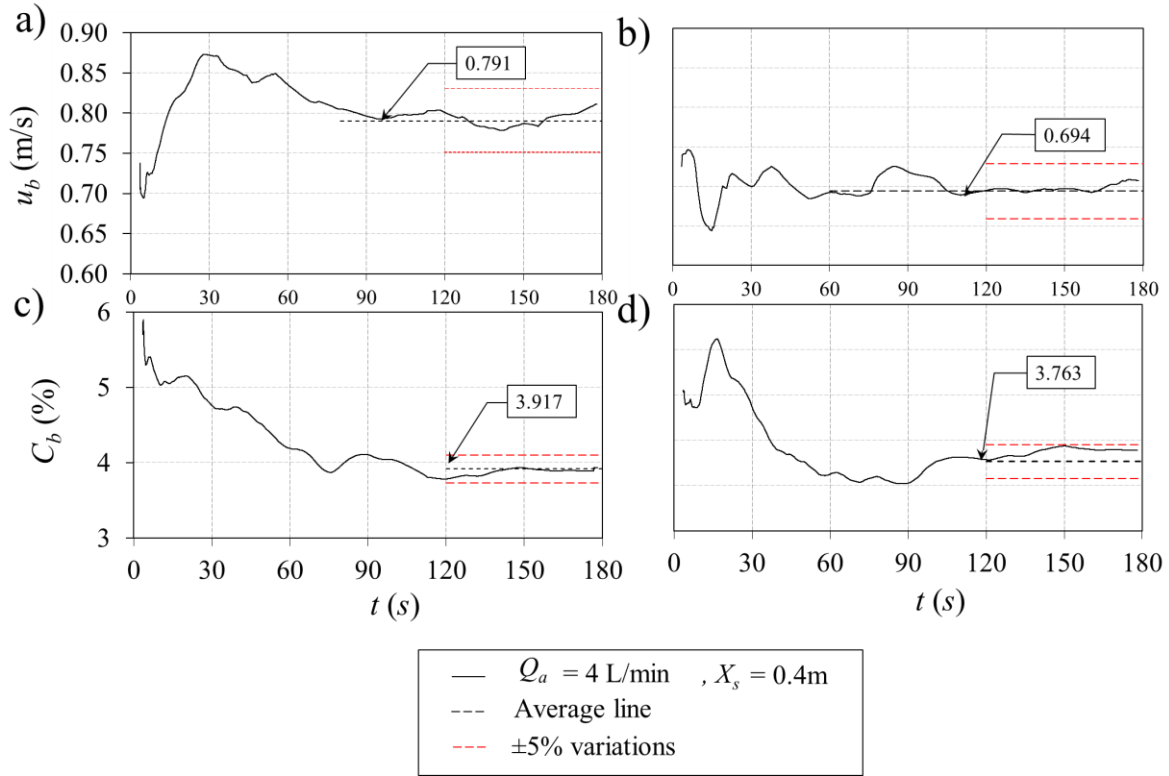


Figure 2. 3: Time histories of the cumulative average of bubble velocity and bubble concentration with and without a grid-screen for $Q_a = 4$ L/min and at $x/d_o = 330$: a) variations of the cumulative average of bubble velocity without a grid-screen (Test No. 1); b) variations of the cumulative average of bubble velocity with a grid-screen for $d_s = 2.38$ mm, $X_s = 0.4$ m (Test No. 7); c) variations of the cumulative average of bubble concentration without a grid-screen (Test No. 1); d) variations of the cumulative average of bubble concentration with a grid-screen for $d_s = 2.38$ mm, $X_s = 0.4$ m (Test No. 7).

To ensure the repeatability of results, the test with $Q_a = 8$ L/min, $d_o = 3$ mm, and the test with $Q_a = 8$ L/min, $d_o = 1$ mm were repeated three times. The bubble size and normalized bubble velocity had the measurement uncertainty of +1.5% and -2.5 %, respectively. Moreover, the same method was applied to find the uncertainty for boundary height and

normalized bubble diameter between regimes (III) and (IV) with the measurement uncertainty of +3.4% and -4.3 %, respectively.

2.3.1 Flow visualization

Figure 2.4 shows the snapshot images of bubble plumes without a grid-screen for different airflow discharges. The time interval between each consecutive image is two seconds. As the airflow discharge increased from 4 L/min to 8 L/min, a cloud of bubbles was developed and large air pockets were formed due to the wake effect behind the frontier air cloud, which reduces the rate of oxygen transfer along the vertical axis of the plume.

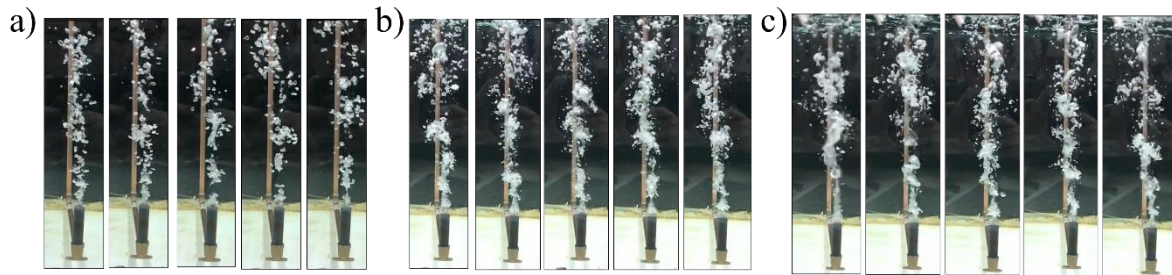


Figure 2. 4: Images of bubble plume variations with time for the plume tests without a grid-screen and for $d_o = 1$ mm. The time step between each image is two seconds: a) $Q_a = 4$ L/min, (Test No. 1); b) $Q_a = 6$ L/min (Test No. 2); c) $Q_a = 8$ L/min, (Test No. 3).

Figure 2.5 shows a comparison between the images from bubble plumes with and without a grid-screen for $Q_a = 4$ L/min and $d_o = 1$ mm. The grid-screen has an opening size of 0.841 mm, and it was located 0.14 m above the nozzle. Figure 2.5a shows a snapshot image of a bubble plume without a grid-screen and Figure 2.5b shows the snapshot image of the same bubble plume with a grid-screen. Five close-up images were selected along the vertical axis of the bubble plume to compare the effect of grid-screen on the shape and size of the air pockets. As can be seen in the close-up images, the air pockets in bubble plume with a grid-screen break up into a cluster of smaller bubbles which the clusters of small bubbles increase the air-water contact surfaces and, as a result, enhances the oxygen transfer.



Figure 2. 5: Effect of grid-screen on bubble breakup at different distances from the nozzle for $Q_a = 4$ L/min, $d_o = 1$ mm: a) bubble plume without a grid-screen; b) bubble plume with a grid-screen, $d_s = 0.841$ mm, $X_s = 0.14$ m.

2.3.2 Time history data

Figure 2.6 shows the effect of grid-screen on the time-history of bubble concentration at the plume centerline and at $x/d_o = 330$, where x is the distance from the nozzle to the point of measurement. The dashed line in Figure 2.6 shows the time averaged concentration for a period of three minutes. The nozzle diameter and air discharges were 1 mm and 4 L/min, respectively. A comparison between the bubble plume without a grid-screen (Figure 2.6a) and the plumes with grid-screens (Figures 2.6b-2.6d) indicated that the installation of a grid-screen increased the bubble concentration at the plume centerline. The maximum difference between the time averaged bubble concentration with and without a grid-screen occurred for $X_s = 0.30$ m (see Figure 2.6d) indicating 21% higher time-averaged bubble concentration than the test without a grid-screen. The grid-screen divides large air bubbles into smaller bubbles once they pass through a grid-screen. Consequently, the number of bubbles detected by the RBI probe increased and bubble concentration increased accordingly. Furthermore, the time-averaged bubble concentration was correlated with the

distance from the grid-screen, X_s . A comparison of bubble plumes with and without a grid-screen indicated that the centerline time-averaged bubble concentration increased from 10% to 18% as X_s increased from 0.22 m to 0.30 m (see Figure 2.6). The fluctuations of bubble concentration were also calculated for plumes with and without a grid-screen. The averaged concentration fluctuations for plumes without a grid-screen was 31.5% of the average bubble concentration. The grid-screen reduced concentration fluctuations by 10% and the values of concentration fluctuations were independent of X_s . Implementing a grid-screen in bubble plumes also reduced the RMS values of bubble concentration from 1.04 for plumes without a grid-screen and with a grid-screen at the elevation $X_s = 0.22$ m.

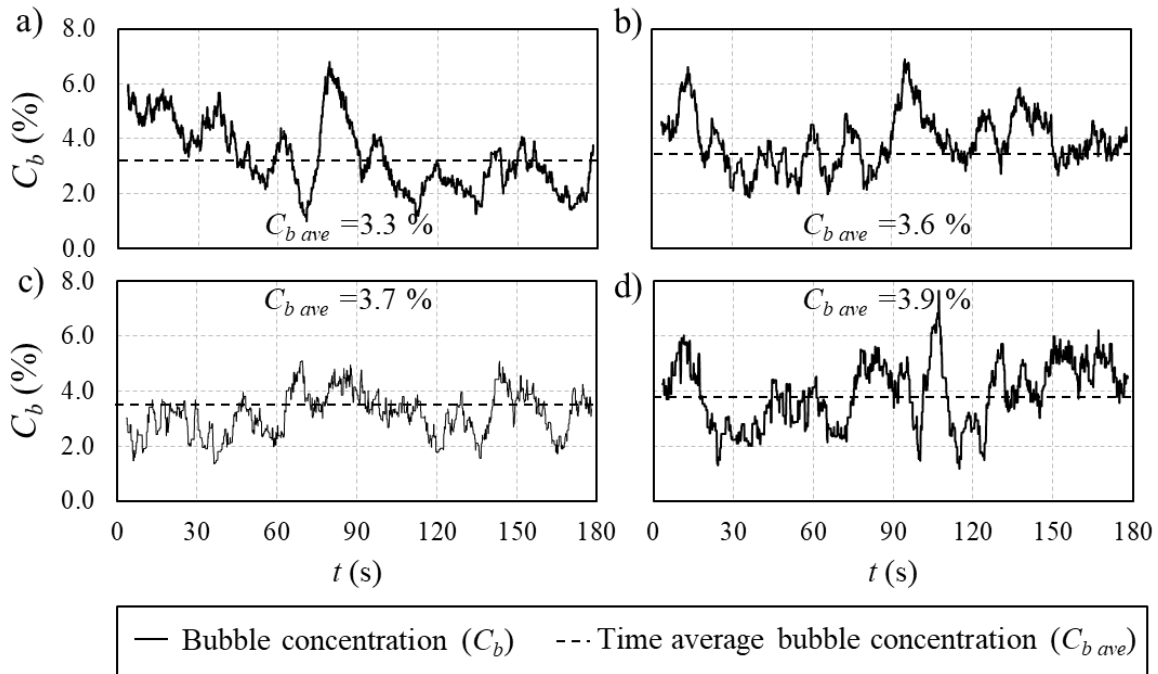


Figure 2. 6: Time-histories of bubble concentration with and without a grid-screen for $Q_a = 4$ L/min, $d_o = 1$ mm, $d_s = 2.38$ and at $x/d_o = 330$: a) bubble plume without a grid-screen, (Test No.1); b) bubble plume with a grid-screen located at $X_s = 0.14$ m, (Test No.7) ; c) bubble plume with a grid-screen located at $X_s = 0.22$ m, (Test No.8); d) bubble plume with a grid-screen located at $X_s = 0.30$ m, (Test No.9).

Figure 2.7 shows the effects of grid-screen on the time history of bubble velocity at the plume centerline and at $x/d_o = 330$. The time-history of bubble velocity was recorded for 180 seconds and the time-averaged bubble velocity, u_{bave} , was calculated and shown by the

dotted lines in Figure 2.7. The nozzle diameter and air discharge were the same as the bubble plumes presented in Figure 2.6. Figure 2.7a shows the time-history of bubble velocity for a bubble plume without a grid-screen and Figures 2.7b-2.7d show the time-histories of bubble velocities after passing through a grid-screen with different distances from the nozzle, $X_s = 0.14$ m, 0.22 m, 0.3 m, respectively.

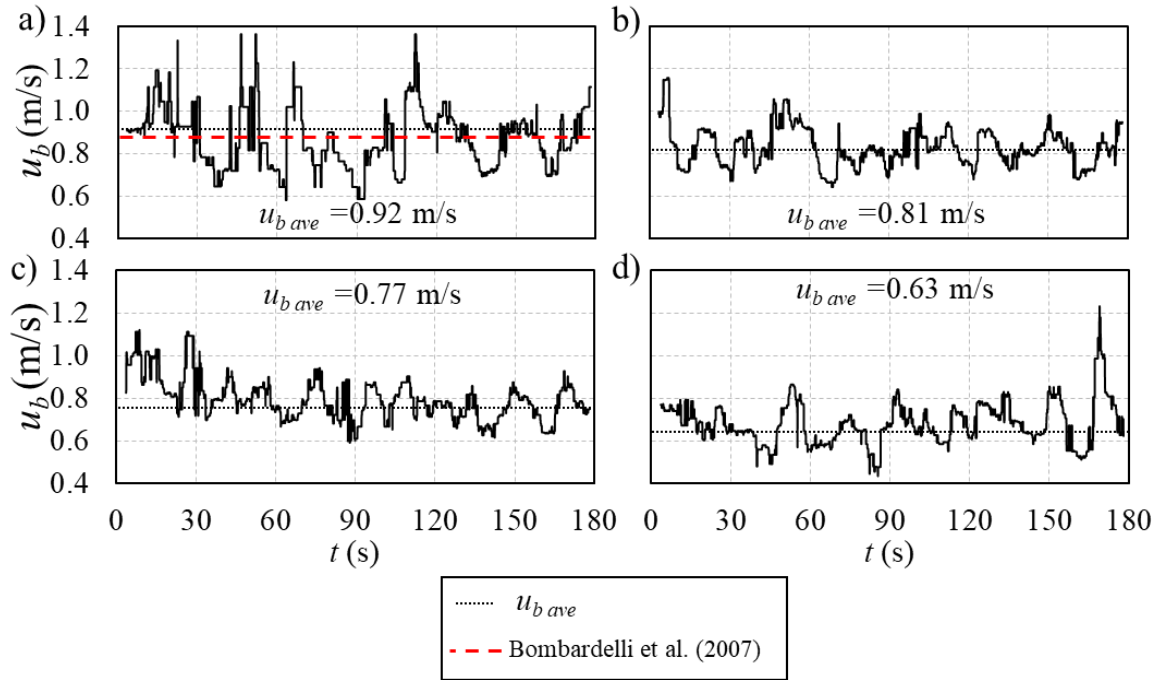


Figure 2. 7: Time-histories of bubble velocity with and without a grid-screen for $Q_a = 4$ L/min, $d_o = 1$ mm, $d_s = 2.38$ mm and at $x/d_o = 330$: a) bubble plume without a grid-screen (Test No.1); b) bubble plume with a grid-screen located at $X_s = 0.14$ m, (Test No.7); c) bubble plume with a grid-screen located at $X_s = 0.22$ m, (Test No.8); d) bubbly plume with a grid-screen located at $X_s = 0.30$ m, (Test No.9).

The time-averaged bubble velocity predicted by Bombardelli et al. (2007) was also included in the bubble plume test without a grid-screen (see Figure 2.7a) indicating a good correlation between the measured and predicted bubble velocity with only 2.2% difference. A comparison of the time-averaged bubble velocities after the grid-screen indicated that the position of the screen decreased the time-averaged bubble velocity by approximately 24%. The velocity fluctuations were calculated for both cases of with and without grid-

screen. The Root-Mean-Square (RMS) values of bubble velocity reduced from 0.116 to 0.076 for bubble plumes without grid-screen and with a grid-screen at $X_s = 0.3$ m, respectively. As shown in Figure 2.7, the time-averaged bubble velocity decreased by approximately 31% due to the presence of a grid-screen located at $X_s = 0.3$ m. It was found that the bubble velocity fluctuations are correlated with the distance between the grid-screen and the nozzle, X_s . The average velocity fluctuations for bubble plumes without a grid-screen was 13.3% and it decreased to 8.6% in the presence of a grid-screen at $X_s = 0.14$ m. Bubble velocity fluctuations increased as the distance between grid-screen and nozzle increased to 9.5% and 11.3% for $X_s = 0.22$ m and 0.3 m, respectively.

The experimental study of Lima Neto et al. (2008a) indicated that the effect of nozzle size is negligible on variations of bubble velocity. Our experimental results indicated that not only bubble size decreased (i.e., bubble concentration increased) but also the velocity of bubbles decreased after the presence of a grid-screen. Bubble size, interfacial area, a , and bubble velocity influence the rate of oxygen transfer from bubbles to the ambient water. Muller et al. (2002) reported an equation derived from Fick's law to show the relationship between bubble characteristics and oxygen transfer rate as:

$$\frac{dC}{dt} = K_L a (C_s - C) \quad (2.1)$$

where C is dissolved oxygen (DO) concentration in the ambient water; C_s is the saturation concentration of dissolved oxygen, and K_L is mass transfer coefficient or liquid film coefficient. The interfacial area of bubbles is directly correlated with the number of bubbles, bubble size, and bubble velocity. The rate of oxygen transfer increases as a result of bubble velocity reduction and increasing the residence time of bubbles (Clift et al., 1978).

2.3.3 Bubble characteristics

To study the effect of grid-screen on oxygen transfer enhancement, bubble size distribution on the plume axis and after the grid-screen were measured with the RBI probe. The Probability Density Function (PDF) of bubble size was calculated based on the time-series

of bubble size measurements with the RBI probe to identify the most probable bubble size and its distribution for different experiments. The bubble dimeters were measured for 120 seconds and different ranges of bubble sizes from 0.1 mm to 25 mm were sorted after the measurements. The percentage of bubbles in relatively narrow bonds of 0.1 mm thickness were calculated based on the total number of bubbles to generate bubble size distribution curves.

Figure 2.8 shows the most probable bubble size and bubble size distribution for bubble plumes with a grid-screen and with an opening size of 2.38 mm for two different air discharges of $Q_a = 4$ and 6 L/min. The PDF of bubble sizes for a bubble plume without a grid-screen (see Figure 2.8a and 2.8b) was also calculated for comparison. The grid-screens were installed at $X_s = 0.14$ m and bubble size distributions were measured for a distance from the nozzle ranging from 0.16 m to 0.5 m (i.e., $1.15 \leq x/X_s \leq 3.6$). The magnitude of the most probable bubble size provides an insight in uniformity of bubble size after the grid-screen. In addition, the PDF data show the effects of air discharge and grid-screen size on bubble size distribution at different distances from the nozzle. Each subplot shows the probability of bubble size in percentage from the smallest to the largest measured bubbles. A comparison of the calculated PDF for bubble plume without and with a grid-screen at $x = 0.16$ m (see Figures 2.8a and 2.8c) indicated the repeatability of the bubble size measurements since the measurement in Figure 2.8c was taken before the grid-screen. The most probable bubble size was $6.1 \text{ mm} \pm 2 \text{ mm}$ and the PDF of bubble size varied by $\pm 8.2\%$.

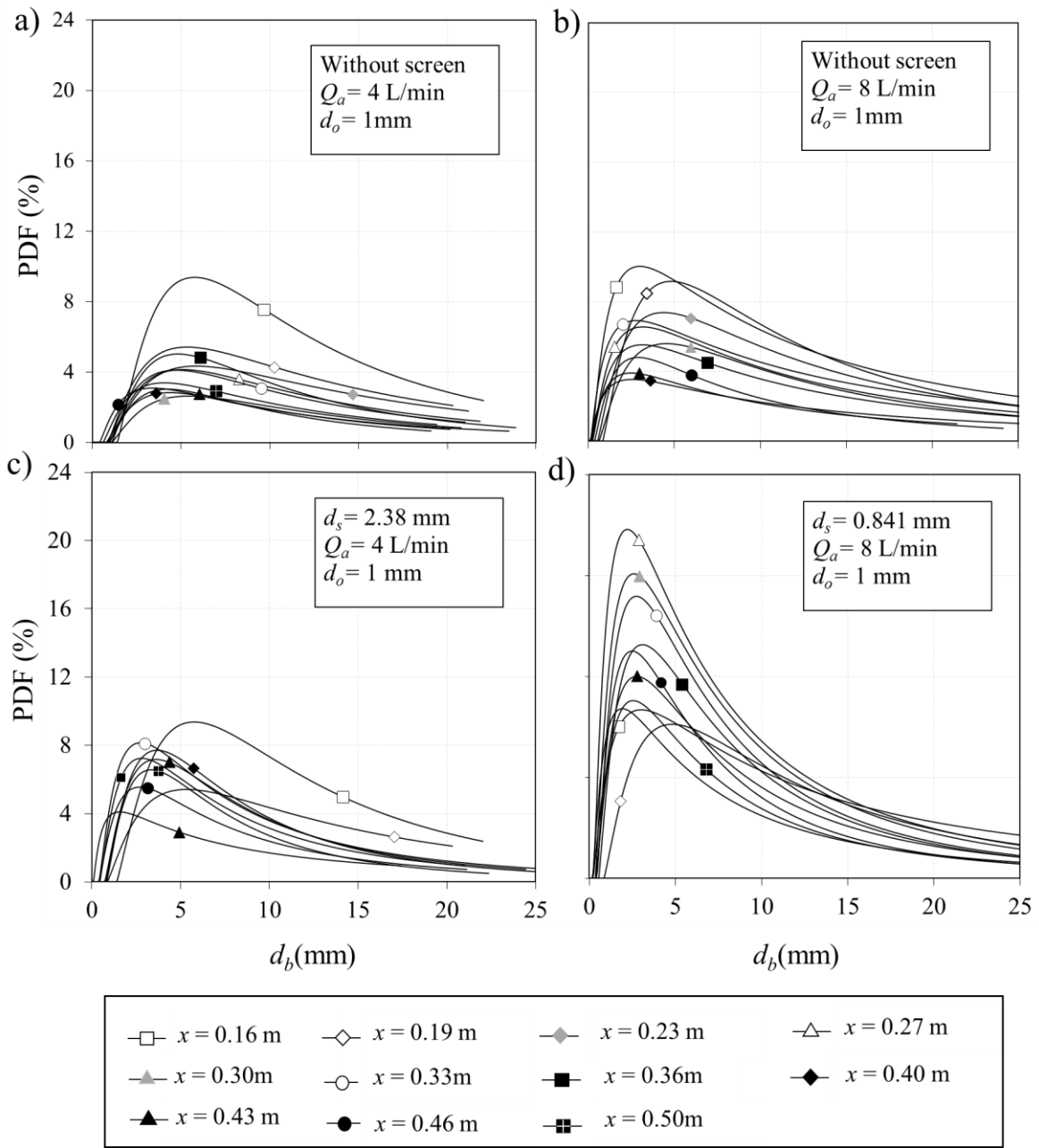


Figure 2. 8: Effects of grid-screen on the Probability Density Function (PDF) of bubble size in bubble plumes with different discharges, screen sizes, and distances from the nozzle: a) $Q_a = 4$ L/min, $d_o = 1$ mm, without a grid-screen (Test No.1); b) $Q_a = 6$ L/min, $d_o = 1$ mm, without a grid-screen (Test No.2); c) $Q_a = 4$ L/min, $d_o = 1$ mm, $d_s = 2.38$ mm, $X_s = 0.14$ m, (Test No.7); d) $Q_a = 6$ L/min, $d_o = 1$ mm, $d_s = 2.38$ mm, $X_s = 0.14$ m, (Test No.10).

From the results presented in Figure 2.8, it can be concluded that the most probable bubble size after the grid-screen decreased as all peak values of the PDF shifted toward the lower values of d_b . This indicates more uniform bubble size distribution and smaller bubble diameters due to the placement of grid-screens. The peak values in probability curves increased after the grid-screen indicating that the resulted bubbles became uniform. The distributions of bubble size before a grid-screen were in good agreement with the observations of Lima Neto et al. (2008a). Their results showed that by replacing a single nozzle with an air-stone, bubble diameters decreased by approximately 50% and the size distribution curves became sharper that indicates the formation of relatively uniform bubble size distribution. A comparison between Figures 2.8a and 2.8c shows that the most probable bubble size in bubble plumes without a grid-screen decreased from 5 mm to 3.7 mm. Due to installation of a grid-screen the peak probability range increased from 2.5% - 5% to 4% - 7%. Experimental results indicated that by installation of grid-screen not only bubble size decreased but also more uniform bubbles were formed.

Figures 2.8b and 2.8d show the effect of grid-screen in bubble plumes with higher airflow rate. A comparison between Figure 2.8a and 2.8b shows the effect of airflow discharge on bubble size and its distribution. As can be seen bubble size decreased by increasing airflow rate and the peak bubble size for $x = 0.3$ m decreased by 19% as the airflow discharge doubled. Our results on variations of the most probable bubble size and bubble size distribution were consistent with the recent studies in the literature (Zeigenhein and Lucas, 2017; Bohne et al., 2020). A comparison between bubble plumes with and without grid-screen in higher air discharges (see Figures 2.8c and 2.8d) indicated that the peak probability of bubbles at $x = 0.33$ m increased from 8% to approximately 15%.

Figure 2.9 shows the effect of grid-screen on the total number of bubbles, N_b , that were detected by the RBI probe at each point. In order to compare the effect of grid-screen on bubble characteristics, two tests were shown based on the presence of grid-screen placed at $X_s = 0.14$ m above the nozzle and the benchmark test without a grid-screen. Figure 2.9a shows the variations of the total number of bubbles along the axis of the bubble plume for a constant air discharge of $Q_a = 4$ L/min. The number of bubbles decreased almost linearly with normalized distance from the nozzle. As can be seen, the effect of grid-screen on the

total number of bubbles is insignificant for small air discharge and the total number of bubbles increased by approximately 6% in presence of a grid-screen. Figure 2.9b shows the variations of N_b with x/d_o for higher air discharge of $Q_a = 6$ L/min. As can be seen, the total number of bubbles increased by approximately 30% in presence of a grid-screen for relatively higher air discharge.

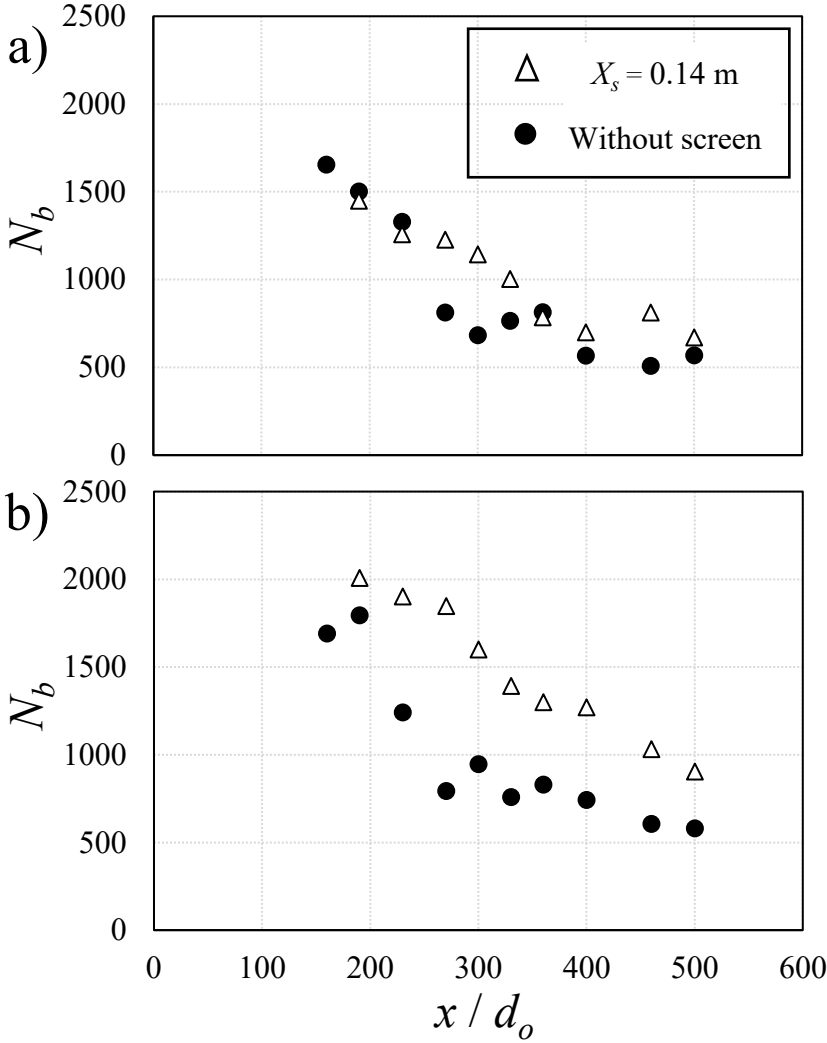


Figure 2. 9: Effects of grid-screen on the total number of bubbles detected by the RBI probe, N_b : a) $Q_a = 4$ L/min, $d_o = 1$ mm, without a grid-screen (Test No.1) and $X_s = 0.14$ m, (Test No.7); b) $Q_a = 6$ L/ min, $d_o = 1$ mm, without a grid-screen (Test No.2) and $X_s = 0.14$ m, (Test No.10).

Due to constant air discharge of 4 L/min, a comparison between the tests with and without a grid-screen indicated that by increasing the elevation from the nozzle, the number of bubbles decreased which indicated no significant variations between the number of bubbles with and without grid-screen. However, by increasing the air discharge to 6 L/min (see Figure 2.9b), the number of bubbles raised significantly after the grid-screen.

The effects of grid-screen on bubble characteristics of bubble plumes are investigated by comparing the variations of bubble size and bubble velocity along the vertical axis of the bubble plume. The variations of bubble size along the vertical axis of the plume, x , were measured in the centerline of the plume and the results were plotted for bubble plumes with different airflow discharges (see Figure 2.10). Figures 2.10a and 2.10b show the bubble size variations for $Q_a = 4$ L/min, and Figures 2.10c-2.10d and 2.10e-2.10f show the bubble size variations for $Q_a = 6$ L/min and 8 L/min, respectively. The left and right subplots in Figure 2.10 show the bubble size variations for $d_o = 1$ mm and 3 mm, respectively. The horizontal lines show the locations of grid-screens at different levels of $X_s = 0.14$ m, 0.22 m, and 0.3 m. All data points for bubble plumes without a grid-screen are shown by solid circle symbols. The white and grey symbols represent the data for the grid-screen opening of $d_s = 2.38$ mm and 0.841 mm, respectively. The uncertainty overbars for measuring bubble size are added in Figure 2.10. Similar uncertainty ranges with an average value of $\pm 1.5\%$ were found for other tests.

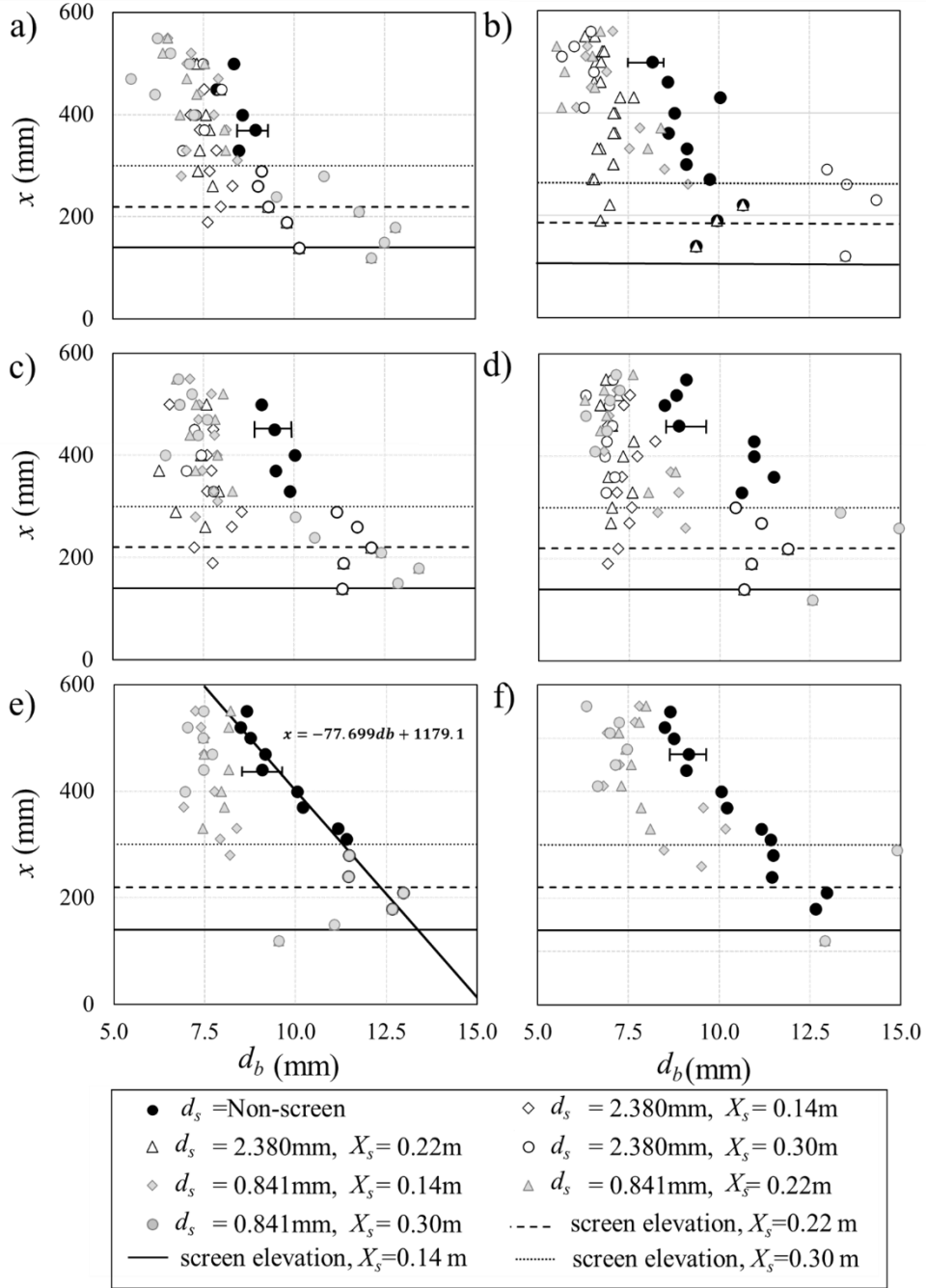


Figure 2. 10: Variations of bubble size along the vertical axis of bubble plumes with different air discharges, Q_a , nozzle diameters, d_o , and grid-screen sizes, d_s , for a screen located at $X_s = 0.14\text{ m}$, 0.22 m , and 0.30 m : a) $Q_a = 4\text{ L/min}$, $d_o = 1\text{ mm}$, $Re = 5661.71$; b) $Q_a = 4\text{ L/min}$, $d_o = 3\text{ mm}$, $Re = 1887.23$; c) $Q_a = 6\text{ L/min}$, $d_o = 1\text{ mm}$, $Re = 8492.56$; d) $Q_a = 6\text{ L/min}$, $d_o = 3\text{ mm}$, $Re = 2830.85$; e) $Q_a = 8\text{ L/min}$, $d_o = 1\text{ mm}$, $Re = 11323.42$; f) $Q_a = 8\text{ L/min}$, $d_o = 3\text{ mm}$, $Re = 33970$.

A comparison between the bubble plumes with and without a grid-screen indicated that the grid-screen significantly reduced the bubble size after the grid-screen. It was found that the bubble size reduction was independent of the screen size or the location of grid-screen. The vertical variations of bubble size in bubble plumes without a grid-screen show that the bubble diameter decreased almost linearly with vertical distance from the nozzle with an average slope of $d(d_b)/dx = -77.7$. Figure 2.10 shows that the grid-screens decreased the averaged bubble size right above the grid-screen by approximately 45 percent. However, the effect of nozzle size on variations of bubble size was limited to $\pm 4.6\%$. The effect of grid-screen size on variations of bubble size became important in bubble plume with the lowest Reynolds number, $Re = 5662$ (see Figure 2.10a). The average bubble size after the grid-screen with $d_s = 2.38$ mm was 7.5 mm and it decreased to 5 mm as the screen openings decreased from 2.38 mm to 0.84 mm. Such bubble sizes are useful for aeration and de-stratification of tropical reservoirs (Sahoo and Luketina, 2006). In bubble plumes with higher Reynolds number, the effect of screen opening became insignificant. This is consistent with the results of Lima Neto et al. (2008b), in which bubble breakup prevailed for $Re > 8000$, producing smaller bubbles and a more uniform bubble size distribution.

The effect of air discharge on variation of bubble size was studied by comparing the results presented in Figures 2.10a, 2.10c, and 2.10e. The effect of grid-screen on bubble size reduction was more pronounced in bubble plumes with higher air discharge (i.e., $Q_a = 8$ L/min). The bubble diameter ranged between 5.8 mm and 7.2 mm in bubble plume with $Q_a = 4$ L/min and bubble sizes increased to a range between 6.7 mm and 8.4 mm by increasing air discharge from 4 L/min to 6 L/min. The effect of grid-screen on bubble size distribution was noticeable in relatively lower air discharge (i.e., $Q_a = 4$ L/min) and far from the nozzle (i.e., $x/d_o = 550$). At $x/d_o = 550$, the average bubble size decreased by 32% as grid-screen size, d_s , reduced from 2.38 mm to 0.84 mm. The grid-screens were located in three different elevations of $X_s = 0.14$ m, 0.22 m, and 0.33 m, as indicated by dashed and dotted lines in Figure 2.10. Bubble sizes in bubble plumes without a grid-screen decreased linearly with the vertical distance from the nozzle whereas bubble sizes in bubble plumes with a grid-screen were constant along the plume axis. As can be seen in Figure 2.10, the size of bubbles in bubble plumes with and without a grid-screen became similar far from the nozzle. This indicates that the efficiency of grid-screens in reducing the bubble size is

suitable at a certain distance above the screen and a series of grid-screens may require for further improvement of oxygen transfer. Although bubbles after a grid-screen eventually reached a relatively similar size than that bubbles without a grid-screen; however, the magnitude of PDF (as shown in Figure 2.8) indicated that the resultant bubbles are more uniform after the grid-screen. By employing the linear bubble size reduction in bubble plumes without a grid-screen, bubble size in bubble plumes with and without a grid-screen reached the same sizes at $x/d_o = 310$ and 550 for $Q_a = 4$ L/min and 8 L/min, respectively.

Relatively large bubbles were measured before the grid-screens. This indicates that the bubbles were accumulated under the grid-screen and form forced bubble coalescence. As can be seen in Figure 2.10, by increasing the screen elevation, X_s , from 0.14 m to 0.30 m, the bubbles under the screen merged due to bubble velocity reduction. The forced bubble coalescence increased the bubble size by approximately 19% of the bubble size in tests without a grid-screen. This can be confirmed by the time-history of bubble velocity as presented in Figure 2.7. In bubble plumes with a grid-screen size of $d_s = 0.841$ mm and with different distances from the nozzle, X_s , bubble diameters after the grid-screen decreased from the benchmark test by approximately 22%.

To study the effect of grid-screen on bubble velocity, the vertical variations of bubble velocity were plotted for bubble plumes with different nozzle sizes and air discharges. The grid-screen size has multiple effect on the averaged bubble velocity. The velocity of bubbles reduced by reducing the bubble size due to smaller buoyancy force and grid-screens with smaller screen size also reduce the momentum flux of the carrier fluid, which can reduce the mean and turbulence momentum transfer between air bubbles and the carrier fluid. The experimental results on vertical variations of bubble velocity with different grid-screen sizes and for the maximum grid-screen elevation of $X_s = 0.30$ m are shown in Figure 2.11. Figure 2.11 shows the variations of bubble velocity, u_b , normalized with the averaged bubble velocity along the vertical axis, u_{ave} , with the normalized vertical distance from the nozzle, x/h . The proposed model for prediction of bubble velocity in bubble plumes by Bombardelli et al. (2007) was added in Figure 2.11e for comparison and validation of the experimental data. As can be seen in Figure 2.11, the centerline velocity

scales with $x^{-1/3}$ in bubble plumes with relatively high air discharges (Fisher et al., 1979; Lai and Socolofsky, 2019; Bomabardelli et al., 2007).

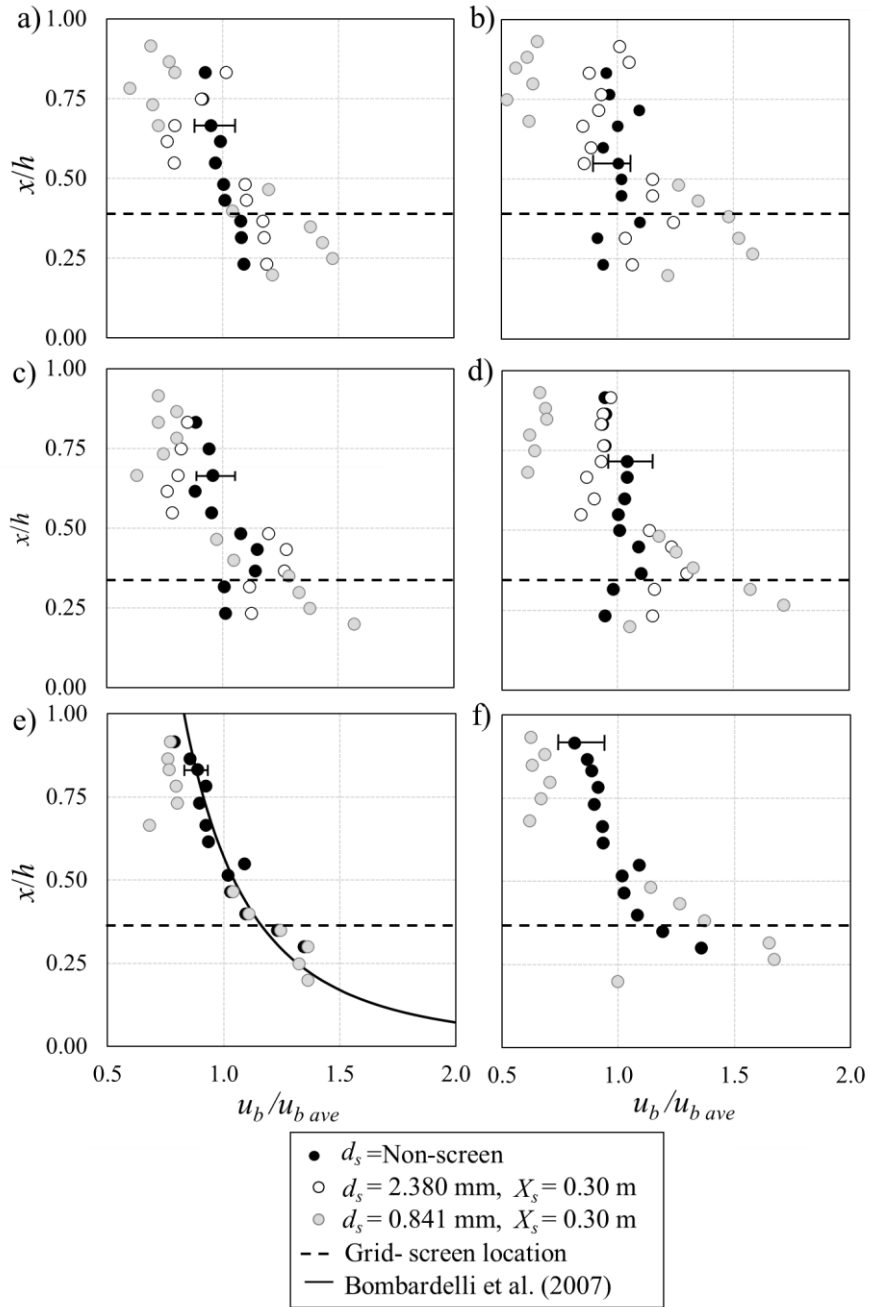


Figure 2. 11: Variations of the normalized bubble velocity with normalized vertical distance from the nozzle in bubble plumes with different air discharges, Q_a , nozzle sizes, d_o , and grid-screen sizes, d_s . The grid-screen was located at $X_s = 0.30 \text{ m}$: a) $Q_a = 4 \text{ L/min}$, $d_o = 1 \text{ mm}$; b) $Q_a = 4 \text{ L/min}$, $d_o = 3 \text{ mm}$; c) $Q_a = 6 \text{ L/min}$, $d_o = 1 \text{ mm}$; d) $Q_a = 6 \text{ L/min}$, $d_o = 3 \text{ mm}$; e) $Q_a = 8 \text{ L/min}$, $d_o = 1 \text{ mm}$; f) $Q_a = 8 \text{ L/min}$, $d_o = 3 \text{ mm}$.

Despite bubble size, the effect of grid-screen size on variations of bubble velocity was significant. As can be seen in Figures 2.11a-2.11d, by decreasing the grid-screen size from 2.38 mm to 0.841 mm normalized bubble velocity decreased by 14% and 38% for nozzle size $d_o = 1$ mm and 3 mm, respectively. Such variations showed that increasing the nozzle size caused the air to move through the water with a higher velocity and smaller bubble diameter, which can improve the oxygen transfer after the grid-screen.

The accumulation of bubbles below the grid-screen increased with increasing air discharge. The bubble size below the grid-screen raised due to bubble coalescence and increased the averaged bubble velocity in comparison with bubble velocity without a grid-screen by 52%, 43%, and 23% for air discharges of 4 L/min, 6 L/min, and 8 L/min, respectively (see Figure 2.11). Figure 2.12 shows the images of bubble coalescence before and after the grid-screen for different air discharges. A comparison of bubble sizes for bubble plumes before and after the grid-screen indicated that the accumulation of bubbles occurred below the grid-screen while significant bubble size reduction occurred after the grid-screen.

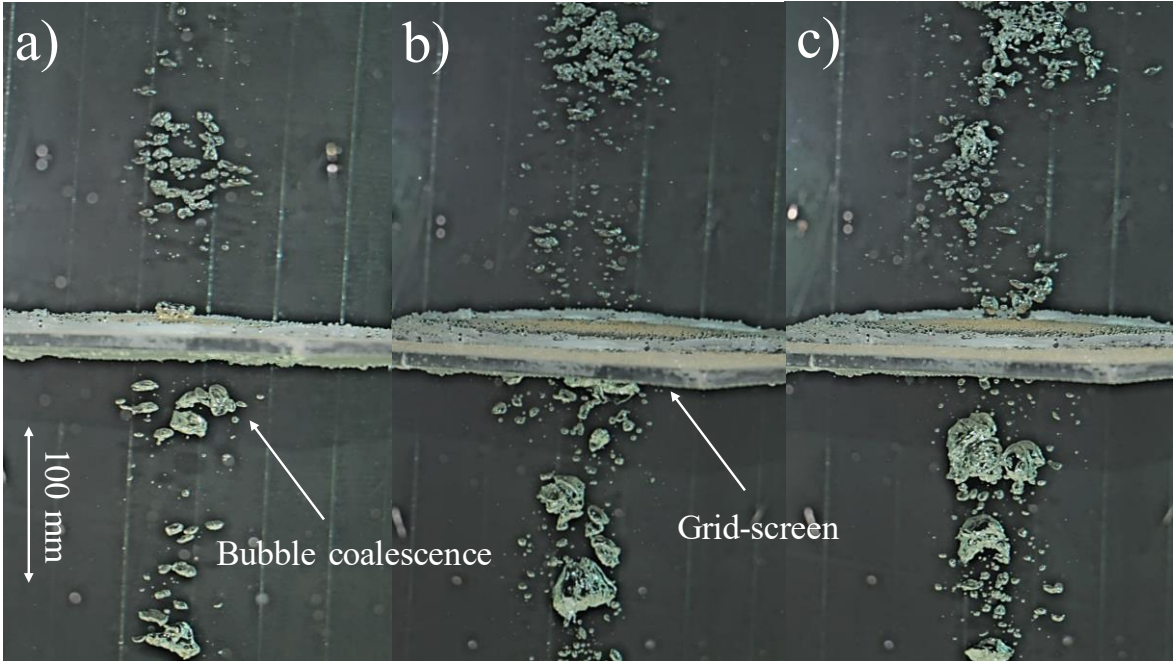


Figure 2. 12: Snapshot images of bubbles before and after a grid-screen with $d_s = 0.841$, $X_s = 0.22$ m, $d_o = 1$ mm, and different air discharges: a) $Q_a = 4$ L/min, (Test No. 20); b) $Q_a = 6$ L/min (Test No. 23); c) $Q_a = 8$ L/min, (Test No. 26).

2.3.4 Regime classification

Detailed observations on variations of bubble velocity along the vertical axis resolved four flow regimes. Figure 2.13a shows the vertical variations of normalized bubble velocity with normalized distance from the nozzle, x/h , for test BP-1-4-16 as a representative of other tests to identify the proposed flow regimes. In this figure, bubble velocities were normalized with the initial jet velocity, u_o . The first regime (Regime *I*) is formed near the nozzle and is defined when bubble velocity is comparable with the initial jet velocity (i.e., $u_b/u_o \approx 1$). As bubbles move up far from the nozzle, their velocities increase due to positive buoyancy force (Regime *II*). As bubbles passed the grid-screen, the screen openings break the boundary of the bubbles and increase the number of bubbles as well (see Figure 2.9). Consequently, due to the larger contact area in break up bubbles, the energy dissipation after the grid-screen increased significantly. As a result of force imbalance after the grid-screen, bubble velocity decreased until reached the equilibrium velocity. The region of velocity decay after the grid-screen is labeled as Regime *III*. The split bubbles merged due to bubble coalescence and reached the equilibrium velocity in Regime *IV*. Figure 2.13 shows the snapshot images of bubbles at different flow regimes for Test BP1-4-16.

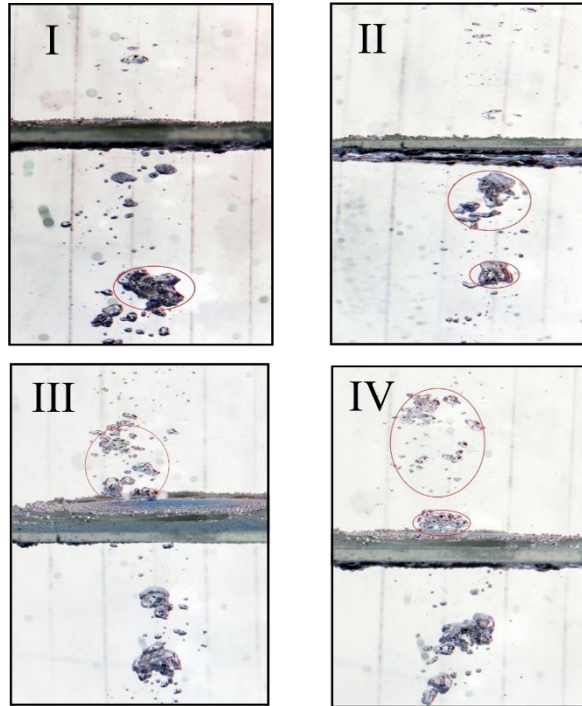
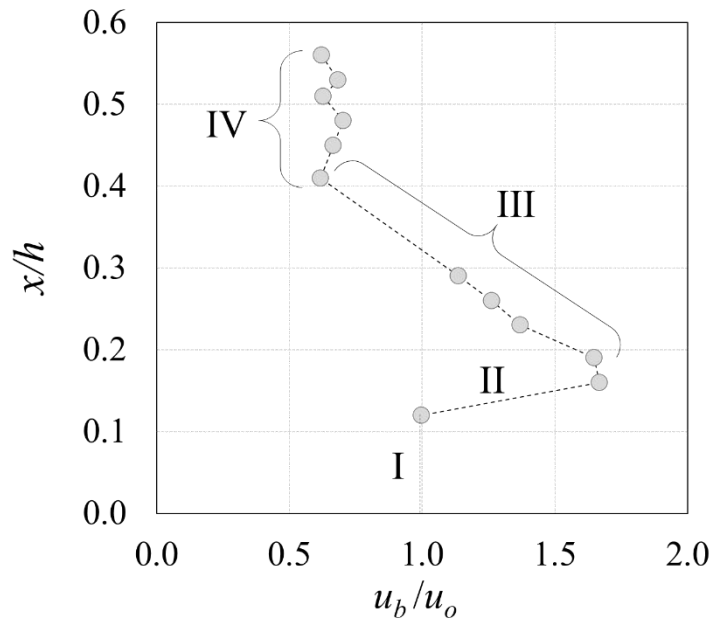


Figure 2. 13: Regime classification in bubble plumes passing through a grid-screen. The classification is defined based on bubble velocity variations and distance from the nozzle (Test No.7, BP1-4-16).

The boundary between regimes three and four, X_{3-4} , is defined as a distance from the nozzle to the point that regime (IV) begins. Experimental results indicated that at this

distance, bubble velocities became approximately 85% of the initial bubble velocity. The boundary between regimes three and four, X_{3-4} , corresponds to the time residence of bubbles. To improve oxygen transfer efficiency in bubble plumes, a new grid-screen is required at X_{3-4} . Figure 2.14 shows the effects of the distance between grid-screen and nozzle, X_s , and initial Reynolds number Re , on variations of the boundary between regime three and four, X_{3-4} . Figure 2.14 shows the capacity of grid-screens to reduce bubble velocity in which such capacity increased with increasing the initial Reynolds number.

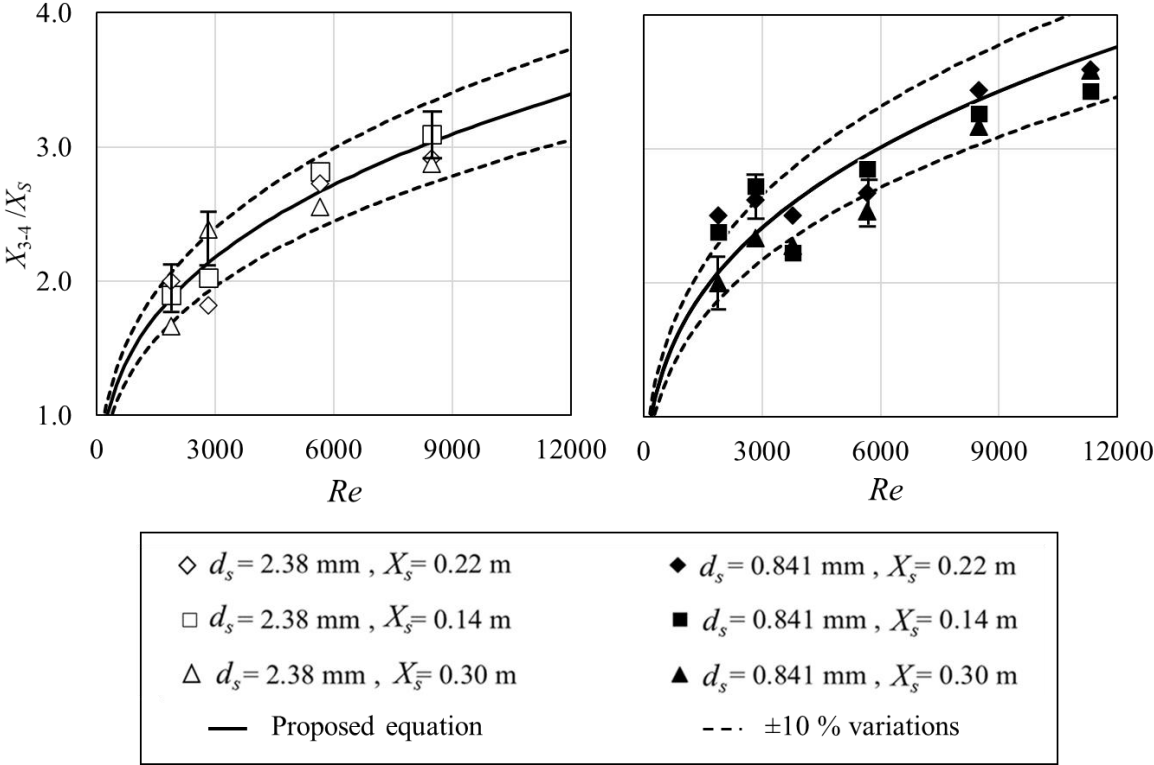


Figure 2. 14: The correlation of boundary height between regimes (III) and (IV) and Nozzle Reynolds number for bubble plumes passing through a grid screen: a) $d_s = 2.38$ mm; b) $d_s = 0.841$ mm.

The boundary between regimes three and four is affected by nozzle size and air discharge. It is deduced that increasing air discharge and decreasing nozzle diameter raise the height of the regime (III). Two equations are proposed to predict the position of the second layer of grid-screen. Eq. (2.2) is suitable for bubble plumes with a grid-screen opening of $d_s = 2.38$ mm and Eq. (2.3) is suitable for the tests with a grid-screen opening of $d_s = 0.841$ mm.

$$\left(\frac{x_{3-4}}{x_s}\right) = 0.168(\text{Re}^{0.32}) \quad (2.2)$$

$$\left(\frac{x_{3-4}}{x_s}\right) = 0.1846(\text{Re}^{0.32}) \quad (2.3)$$

The coefficients of determination, R^2 , for Eq. (2.2) and (2.3) are 0.91 and 0.93, respectively. The $\pm 10\%$ variations of the empirical correlations were also added to Figure 2.13, indicating that almost all data points are within $\pm 10\%$ variations.

Figure 2.15 shows the effect of distance between grid-screen and nozzle, X_s , and bubble Reynolds number, Re_b , on variations of the boundary between regime three and four, X_{3-4} . Bubble Reynolds number is defined as the ratio of bubble inertial force to water viscous force as $\text{Re}_b = \rho_a u_b d_b / \mu_w$, where u_b is the bubble velocity, d_b is the bubble diameter, ρ_a is the air density, and μ_w is the kinematic viscosity of water. As can be seen in Figures 2.15a and 15b, the distance between grid-screen and nozzle was increased, by increasing the bubble Reynolds number. It was observed that by decreasing the grid-screen size, the correlation slope decreased and lead to higher values of distance between grid-screen and nozzle. Two equations were proposed to predict the boundary between two specified regimes (e.g., regimes three and four). Eq. (2.4) is for grid-screen size of $d_s = 2.38$ mm and Eq. (2.5) is for grid-screen size of $d_s = 0.841$ mm.

$$\left(\frac{x_{3-4}}{x_s}\right) = 0.23(\text{Re}_b) \quad (2.4)$$

$$\left(\frac{x_{3-4}}{x_s}\right) = 0.1(\text{Re}_b) \quad (2.5)$$

The coefficients of determination for Eq. (2.4) and (2.5) are 0.92 and 0.91, respectively. The $\pm 20\%$ variations of the empirical correlations were also added to Figure 2.15, indicating that almost all data points are within $\pm 20\%$ variations. It should be noted that the material type of grid-screens might slightly change the variation of data.

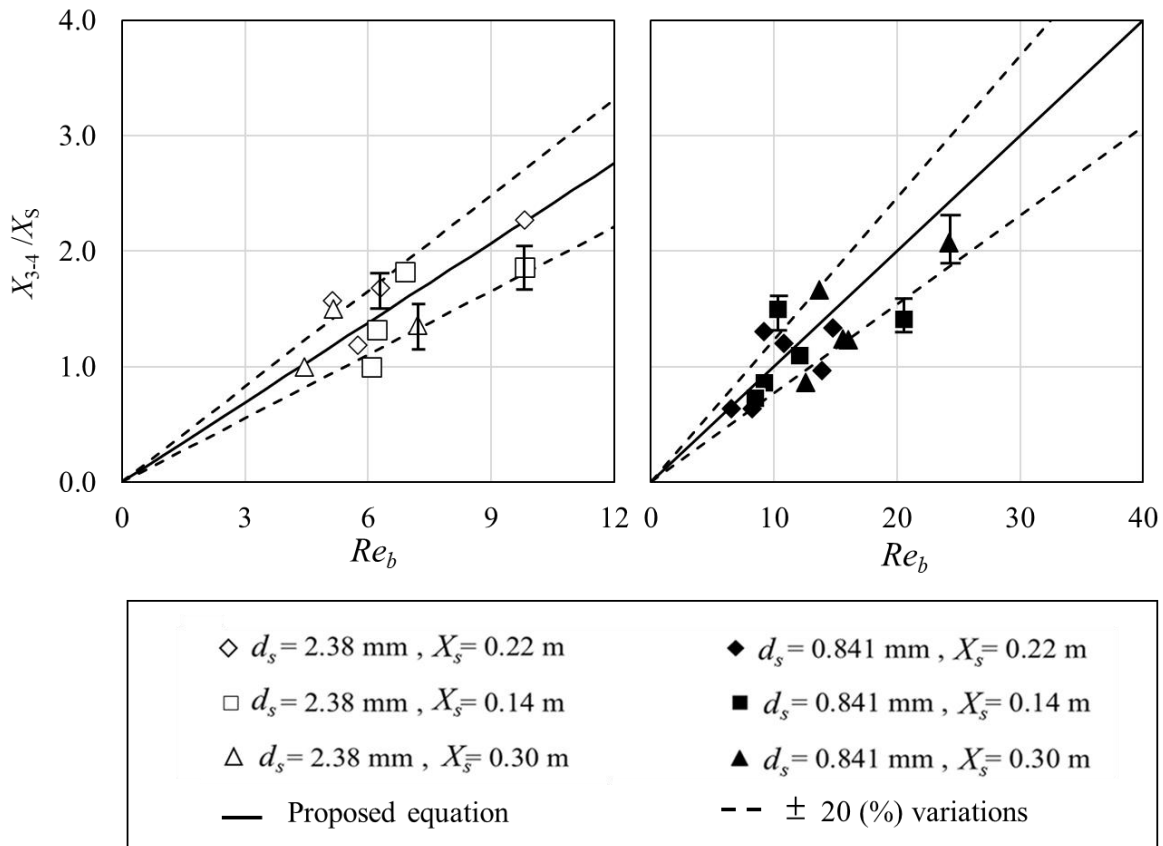


Figure 2. 15: The correlation of boundary height between regimes (III) and (IV) and Bubble Reynolds number for bubble plumes passing through a grid screen: a) $d_s = 2.38$ mm; b) $d_s = 0.841$ mm.

Figure 2.16 shows the variations of normalized bubble diameter at the beginning of Regime IV with the initial Reynolds number, Re . The results indicated that Reynolds number had negligible impact on the normalized bubble size for the grid-screen with larger openings, $d_s = 2.38$ mm. On the other hand, for $d_s = 0.841$ mm the normalized bubble size increased by the initial Reynolds number. It is deduced that small grid-screen caused the bubble plume to reach the regime (IV) at the lower elevations and therefore, a second layer of grid-screen will be beneficial for mixing improvement. A non-linear equation was proposed to correlate the normalized bubble diameter at the onset of regime (IV) with the initial Reynolds number as:

$$\left(\frac{d_b}{d_{bo}}\right) = 0.0149(\text{Re}^{0.43}) \quad (2.6)$$

The coefficient of determination of Eq. (2.6) is $R^2 = 0.92$. The $\pm 10\%$ variations of the empirical correlations were also added to Figure 2.16. The variation curves indicated that almost all data points are within $\pm 10\%$ variations. Considering measurement uncertainties, it was found that the proposed equation is suitable for prediction of the onset of Regime IV with a reasonable accuracy.

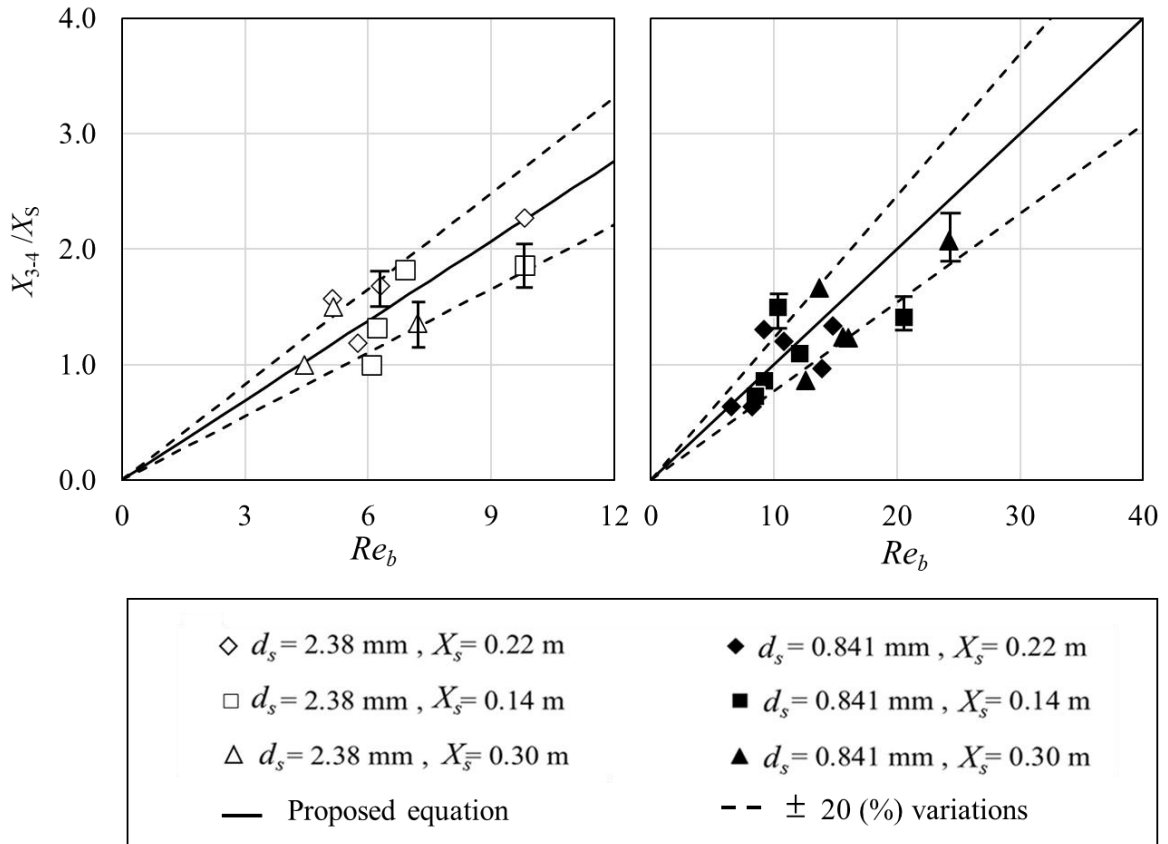


Figure 2. 16: The correlation of boundary height between regimes (III) and (IV) and Bubble Reynolds number for bubble plumes passing through a grid screen: a) $d_s = 2.38$ mm; b) $d_s = 0.841$ mm.

2.4 Conclusions

A series of laboratory experiments was conducted to investigate the effect of grid-screen and its location on the bubble properties in a circular bubble plume. The RBI bubble probe

was employed to investigate the effects of air discharge on variations of bubble velocity and bubble size after the grid-screen. By installing a grid-screen at 0.3 m above the nozzle, the time-averaged bubble concentration increased by 18% and the time-averaged bubble velocity decreased by approximately 31% in comparison with the benchmark test without a grid-screen. The experimental observations indicated that the installation of a grid-screen not only decrease the bubble sizes but also increase uniformity of bubble size distribution. It was observed that the effect of grid-screen on bubble size reduction was more significant in bubble plumes with higher air discharge. Additionally, the experimental results showed that bubble velocity after the grid-screen decreased as the screen opening decreased.

The velocity of bubbles was measured along the centerline axis of the bubble plumes. The results revealed that total bubble numbers after the grid-screen increased in tests with higher airflow rates (i.e., 6 L/min). This indicated that the bubble diameter decreased along the centerline axis of the plume and above the nozzle. Our observations indicated that the bubble size decreased right after the grid-screen. However, it gradually increased as it moved towards the water surface. A regime classification was introduced based on the variations of bubble velocity along the axis of the plume. Bubble velocity was constant in the first regime near the nozzle. The second regime was defined as the position that bubble velocity increased with distance from the nozzle, and it ended at the position of grid-screen. The third regime started from the grid-screen position to the depth where the bubble velocity became constant. Bubble velocity was constant in regime four indicating that the effect of grid-screen was insignificant beyond this depth. The distance from the nozzle to a point where bubble velocity reached the equilibrium was defined as a length scale and it was measured for all cases. It was found that the depth at which the equilibrium velocity occurred is correlated with the bubble Reynolds number. It was found that the normalized bubble size is also correlated with the bubble Reynolds number. Empirical equations were proposed to estimate bubble size and the location of regime boundary, which can be used for designing grid-screen layers and estimation of oxygen transfer after grid-screens.

Notation

The following symbols are used in this paper:

C_b = bubble concentration, vol/vol;
 h = Height of water, m;
 H = Height of tank, m;
 h_n = nozzle height, m;
 d_b = Bubble diameter, mm;
 d_{bo} = Bubble diameter at the nozzle, mm;
 d_o = Nozzle diameter, mm;
 d_s = Grid-screen diameter, mm;
 L = length of the tank, m;
 Q_a = Volumetric airflow rates, L/min;
 t = time, s;
 u_b = Bubble velocity, m/s;
 u_o = Initial bubble velocity, m/s;
 x = Elevation of measured point, m;
 X_s = Elevation of grid-screen, m;
 Re = Reynolds number;
 Re_b = Bubble Reynolds number.

Subscribes

a = air;
 avg = average;
 i = numbers;
 o = nozzle;
 s = screen;

Chapter 3

Effects of air discharge on bubble dynamics in vertically discharged bubble plumes

3.1 Introduction

Bubble plumes have been extensively used in many industrial applications, including in civil, chemical, mechanical, and environmental engineering projects (Davidson and Amick, 1956; Leibson et al., 1956; Clift et al., 1978; Oguz and Prosperetti, 1993; Socolofsky and Adams, 2002; and Besagni and Deen, 2020). Bubble plumes are generated by injecting air through a nozzle, airborne stone, or a group of orifices in water. The hydrodynamic characteristics of bubble plumes are complex, and it is classified as two-phase air-liquid turbulent flow. Bubble plumes have been utilized as an efficient method of enhancing air/oxygen transfer in lakes, rivers, and wastewater treatment plants and have shown a great mixing ability (Clift et al., 1978; Lima Neto et al., 2008a; Niida and Watanabe, 2018). They are advantageous in mixing and oxygen transfer in comparison with other mechanical systems due to simplicity of construction and relatively low operation costs (Pacheco and Lima Neto, 2017; Lima and Lima Neto, 2018). Many experimental studies have been conducted to investigate the effects of controlling parameters in enhancing oxygen transfer rate (Wüest et al., 1992; Clift et al., 2016, Behzadipour et al., 2022), to study oscillating bubble plumes and bubble jet-plumes (Simiano et al., 2006; Funaki et al., 2009; Yang et al., 2016), and to investigate the impacts of bubble shape on mixing efficiency in bubble plumes (Aoyama et al., 2016; Ibelings et al., 2016).

Bubble plumes are also utilized to enhance dissolved oxygen level in lakes and natural streams, to reduce phosphorus release from sediments, and to inhibit algal growth (Soltero et al., 1994, Moura et al., 2020). Other applications of bubble plumes are in sewage oxygenation in sewer pipes and wastewater treatment plants (Schladow, 1992, 1993), in destratification of lakes and reservoirs (Lima Neto et al., 2016, Ibelings et al., 2016) and in mixing of very hot and toxic liquids (Aoyama et al., 2016). Moreover, air injection into effluent diffusers can be an efficient alternative for artificial aeration of water in ponds and lakes (Lima Neto et al., 2007).

Some mathematical models and empirical correlations have been proposed based on experimental data to predict bubble characteristics such as bubble diameter and velocity in bubble plumes (Milgram, 1983; Socolofsky and Adams, 2003, 2002; Bombardelli et al., 2007; Lima Neto et al., 2008a, 2012; Wang et al., 2019; Bohne et al., 2020; Behzadipour et al., 2022, Behzadipour and Azimi, 2022). Wang et al. (2019) studied weak bubble plumes, at which air discharge ranging between 0.25 L/min and 1.2 L/min, in stationary and unstratified water. It was observed that the weak bubble plumes spread slower than the linear rate of classic plumes. Wang et al. (2019) investigated the mean flow characteristics of weak plumes, which included entrainment of ambient water, plume spreading, and centerline velocity. They found that the entrainment coefficient, α , in weak bubble plumes decreased with the distance from the nozzle, x , following $\alpha \sim x^{1/2}$, and entrained less ambient fluid than those of classic bubble plumes.

Experimental studies have shown that air discharge has a significant impact on bubble configuration and mixing (Fraga and Stoesser, 2016; Ziegnehein and Lucas, 2017; Lima Neto et al., 2008a and Rensen and Roig, 2001). The effects of air discharge, Q_a , on

the mean bubble diameter and bubble velocity were experimentally and numerically studied by Fraga and Stoesser (2016). Their research outcomes indicated that the magnitude of the time-averaged bubble velocity increased by approximately 40% as air discharge increased from 0.5 L/min to 1.5 L/min. Ziegnehein and Lucas (2017) also demonstrated a correlation between bubble size and air discharge due to formation of external pressure at the nozzle. Bubble size distribution was found to be narrow at relatively low air discharges varied between $Q_a = 0.61$ L/min and 1.01 L/min. On the other hand, larger bubbles with a wide bubble size distribution were generated in relatively high air discharges ranging between $Q_a = 4.51$ L/min and 4.80 L/min. Their results revealed that the most probable bubble diameters were reduced by 35% and 45% when air discharge reduced from high to low range of air discharges. Rensen and Roig (2001) studied the effect of air discharge on the mean bubble diameter, d_b , and found that by increasing air discharge from 1.26 L/min to 3.24 L/min, the mean bubble diameter increased by 17%.

Although previous studies have investigated the effects of air discharge on bubble plume centerline velocity and bubble size, less attempt has been made to investigate the effect of air discharge on other important parameters and processes such as the variation of gas fraction (i.e., bubble concentration) and bubble interfacial area with distance from the source. The mentioned parameters are critical for air entrainment and oxygen transfer rate in stagnant ambient. The recent study of Bohne et al. (2020) confirmed a strong correlation between bubble size and air discharge for $Q_a = 0.5, 2,$ and 2.6 L/min. It was found that the mean bubble diameter decreased by 33% as air discharge decreased from 2.6 L/min to 0.5 L/min. Bohne et al. (2020) also showed that bubbles size distribution are more uniform,

and bubble diameters ranged between $d_b = 8$ mm and 45 mm at a distance ranging from $x/d_o = 250$ to 2000 where d_o is the nozzle diameter.

The impact of point source air discharge on the ambient water has been studied by many researchers (Soga and Rehmann, 2004; Wain and Rehmann, 2005; Laupsien et al., 2017; Lima Neto et al., 2008a; Liu et al. 2019; and Behzadipur et al. 2022). The effects of nozzle configuration on bubble dynamics were evaluated by conducting laboratory experiments on bubble plumes discharging air from single, multiple nozzles, and porous air stone (Lima Neto et al., 2008a). It was found that the bubble size at a certain distance from the nozzle decreased by 34% as the number of orifices increased at the nozzle in comparison with a single nozzle with the same cross-sectional area. Their results revealed that more uniform bubbles were also formed from bubble plumes with a number of orifices in a nozzle. In addition, using porous air stone instead of single nozzle (i.e., $d_o = 3$ mm), decreased the bubble mean diameter by approximately 50%.

The effects of nozzle configuration on bubble size were recently studied by Liu et al. (2019). Air stone and single orifice with a diameter of $d_o = 8$ mm were used and air discharges ranged from $Q_a = 0.25$ L/min to 1.2 L/min. The results showed that for air discharges of $Q_a = 0.25$ L/min and 1.25 L/min, the mean bubble diameter increased respectively by 65% and 47% in plume discharging from air stone in comparison with single orifice. Lima and Lima Neto (2018) examined the effects of different nozzle shapes to examine the Standard Oxygen Transfer Efficiency (SOTE). It was found that with the same initial momentum and buoyancy fluxes, the oxygen transfer efficiency increased by approximately 300% when multiple-orifice nozzles were used instead of a single orifice nozzle having the same cross sectional area. Recently, a series of laboratory experiments

was carried out to understand the effect of nozzle size and air discharge on variations of mean bubble diameter, bubble concentration/gas fraction, and bubble velocity in strong bubble plumes (Behzadipour et al., 2022). Their results revealed that more uniform air bubbles were generated, and the mean bubble diameter decreased by 34% as air discharge increased from 4 L/min to 8 L/min.

Many research studies have focused on the effects of controlling parameters such as air discharge and nozzle configuration on variations of bubble size, bubble size distribution, and bubble velocity. However, less attempts have been made to study the effect of air discharge on other important parameters of bubbles such as interfacial area, size, frequency, velocity, velocity fluctuations, and turbulent intensity. The present study investigated the effects of air discharge on variations of bubble characteristics along the vertical axis of bubble plumes and provided detailed information on the mentioned bubble characteristics. The larger contact surface between air and water enhances the oxygen transfer and improves the efficiency of aerators using in natural water bodies, which can be controlled by variations of air discharge. The contact surface can be increased either by increasing air discharge or reducing the bubble size by changing the nozzle shape or inserting a grid-screen (Behzadipour et al., 2022). Increasing air discharge requires a larger pump and higher electrical energy which consequently raises the overall costs of operation. Therefore, it is critical to find a correlation between bubble characteristics and air discharge to optimize the oxygen transfer rate based on the design requirements.

In this study, the variations of bubble characteristics such as size, concentration, interfacial area, frequency, mean velocity, velocity fluctuations, and turbulent intensity along the vertical axis of bubble plumes are measured with a novel and accurate RBI

bubble probe for relatively higher air discharge range than that was tested in the literature. The effects of air discharge are examined to know how the variations of air discharge affect bubble plume characteristics. The outcomes of the proposed research study support the designers for selecting the optimum air discharge based on mixing requirements.

3.2 Experimental Setup

A series of laboratory experiments was carried out to study the effects of air discharge on bubble characteristics of vertically discharged bubble plumes. The experiments were conducted in the Multiphase Flow Research Laboratory (MFRL) at Lakehead University. Figure 3.1 shows the experimental setup and the images of optoelectronic unit and optical probe tip of the Refractive Bubble Instrument (RBI instrumentation, Meylan, France). The experimental tank is 1.60 m long, 0.85 m wide, and 0.80 m deep. The bottom of the tank is made of galvanized plate and the sidewalls are made of tempered glass. The water temperature in the tank was kept constant with a value of $20^{\circ}\text{C} \pm 1^{\circ}\text{C}$, and the water depth from the nozzle was $H = 0.70$ m. An air compressor was employed to provide the required air pressure, which stabilized the pressure at $P = 60$ psi. A pipe with an interior diameter of 3 mm was installed at the bottom of the experimental tank and it was connected to a circular nozzle with a diameter of $d_o = 3$ mm. Different air discharges of $Q_a = 3, 6, 9$ and 12 L /min were selected, and they were measured at the inlet by an accurate rotameter (LZM series Zyia OEM, Zhejiang, China) with a measurement uncertainty of $\pm 4\%$.

Four experiments were carried out to investigate the effect of the air discharge, Q_a , on bubble dynamics in vertically discharged bubble plumes. Bubble characteristics such as

bubble size, d_b , instantaneous bubble velocity, u_b , interfacial area, a , and instantaneous bubble concentration, C , were measured at different distances, x , from the nozzle. Other bubble characteristics such as bubble frequency, f_b , bubble mean velocity, $u_{b(ave)}$, and bubble velocity fluctuations, $u'_{b(ave)}$, were extracted from experimental data. The interfacial area of bubbles was calculated as $a = 4f_b/u_{b(ave)}$. The experimental parameters and the associated non-dimensional variables such as bubble Reynolds number at the nozzle, $Re_o = \rho_a u_{bo} d_{bo} / \mu_w$, initial momentum flux, $M_o = Q_a u_{bo}$ and initial buoyancy flux, $B_o = g Q_a (\rho_w - \rho_a) / \rho_w$ are listed in Table 3. 1 where u_{ao} is the air velocity at the nozzle, d_{bo} is the

Test. No.	Q_a (L/min)	d_o (mm)	u_o (m/s)	M_o (m ⁴ /s ²)	B_o (m ⁴ /s ³)	d_b (mm)	u_b (m/s)	C_b (%)	Re_o
1	3	3	7.0771	0.00035	4.99E-05	0.62	0.88	3.29	1415.4
2	6	3	14.154	0.00142	9.98E-05	12.2	1.005	4.23	2830.9
3	9	3	21.231	3.18E-03	1.50E-04	13.02	1.104	5.47	4246.3
4	12	3	28.309	0.00566	2.00E-04	13.2	1.153	6.05	5661.7

bubble size at the nozzle, g is the gravitational acceleration, μ_w is the dynamic viscosity of water, and ρ_w , and ρ_a are the densities of water and air, respectively.

Table 3. 1: Experimental parameters and bubble characteristics of vertically discharged bubble plumes.

A double-tip optical fiber probing system (RBI instrumentation, Meylan, France) was used to measure bubble characteristics such as bubble size, bubble velocity, and bubble concentration/gas fraction at different distances from the nozzle. Two sapphire crystals are installed at the end of probe's tips (see Figure 3.1) to measure bubble characteristics. The probes' tips have 15 mm length and are 2.5 mm apart from each other. The emitted light from the probe is refracted when the probe's tip is in the water and is reflected in the module when the probe's tip is in the air (i.e., inside a bubble). The

reflected light passes through a semi-transparent mirror combined with a prism towards a photosensitive diode in the module. The light transmission system enables the probe to acquire voltage signals with a sampling frequency of 1 MHz (RBI User Manual, Meylan, France).

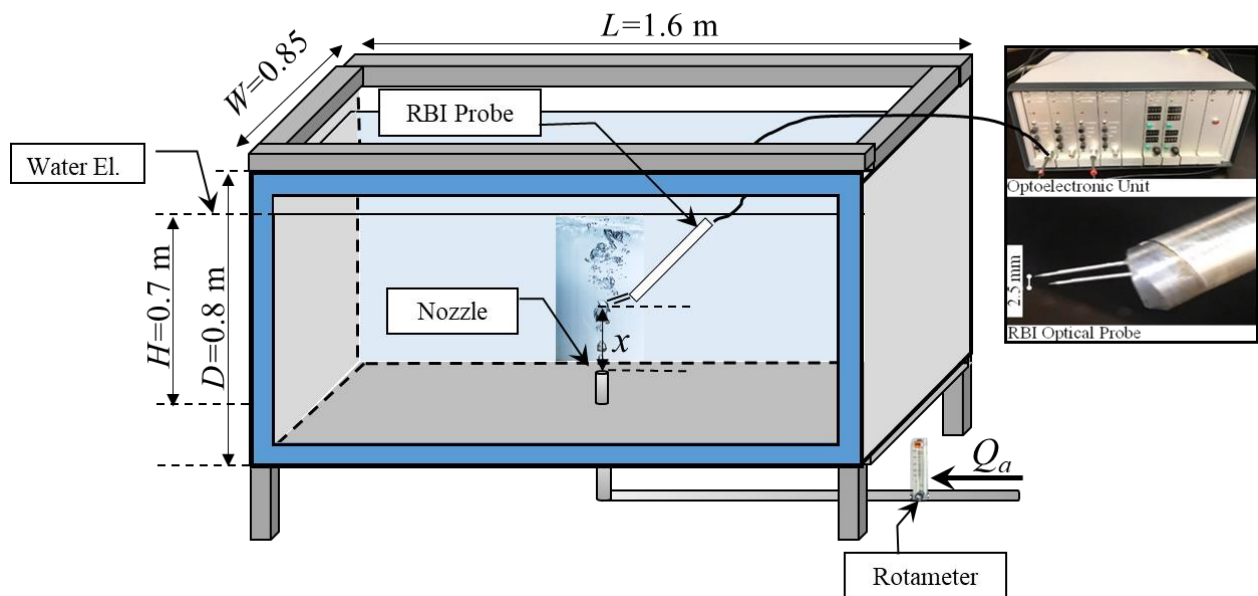


Figure 3. 1: The schematic of experimental setup, images of optoelectronic unit, and optical probe tip of the Refractive Bubble Instrument (RBI).

The double-tip optical fiber probe is capable of measuring bubble size, gas fraction (i.e., bubble concentration), and bubble frequency by analyzing the digitalized voltage signals. Furthermore, bubble velocities were measured by cross correlation of the time series of voltage signals. The RBI probe is able to measure bubble diameter and chord length by measuring the time lag between each voltage signals, Δt (see Behzadipour et al., 2022). The voltage signals indicating 6 Volts when the probe is in water and no voltage when the probe is inside the bubble (i.e., probe detecting air). The bubble mean diameter

and bubble size distribution are calculated knowing the time duration and velocity of bubbles as $d_b = u_b \times \Delta t$. Bubble concentration is estimated by the phase identification mechanism. The ratio of the time that the RBI probe detects air phase to the time detecting the water phase is used as an indicator of bubble concentration/gas fraction at the measurement point.

The RBI double-tip optical fiber probe has been successfully employed in many experimental studies (Rensen and Roig, 2001; Boes and Hager, 2003; Kiambi et al., 2003; Chaumat et al., 2005; Murzyn et al., 2005; Lima Neto et al., 2008a, b, c; Behzadipour et al., 2022, Behzadipour and Azimi, 2022). A comparison between the outcomes of the double optical probe and snapshot images has shown discrepancies of 14% and 6% in bubble concentration for tests with a mean bubble size of $d_b = 2.15$ mm and 4.5 mm, respectively (Kiambi et al., 2003). The accuracy of the RBI optical probe has been tested with the PIV measurements as well (Lima Neto et al., 2008a). A discrepancy of 10% for bubble size measurement and 29% for velocity measurements was found between the mentioned measurement techniques, which are considered acceptable due to the complex nature of bubble dynamics in bubble plumes and uncertainties in the measurement techniques.

3.3 Results and discussion

The effect of air discharge on the motion of bubbles was studied by careful visualization of bubbles using high-resolution images. The images were captured by a high-resolution camera (Prosilica GT 1910c CCD, Germany) and with a speed of 20 frames per second. The camera has a 90-mm Kowa lens with a focal length of 1.8 m

(Kowa, Japan) and it was located at a perpendicular distance of 1.4 m from the tank. The snapshot images of bubble plumes with different air discharges are shown in Figure 3.2. Figure 3.2 shows a transitory regime, intermittent close to the nozzle (i.e., low frequency, large bubble size) and dispersed bubbly flow close to the free surface. These images show the effect of air discharge on variations and magnitude of bubble sizes along the axis of the plume. As can be seen, relatively large bubbles are formed near the nozzle, and they were expanded along the direction of plume due to pressure reduction. Bubble breakup occurred when the bubble clusters moved towards the water surface, and they burst into large number of small bubbles as illustrated in Figure 3.2.

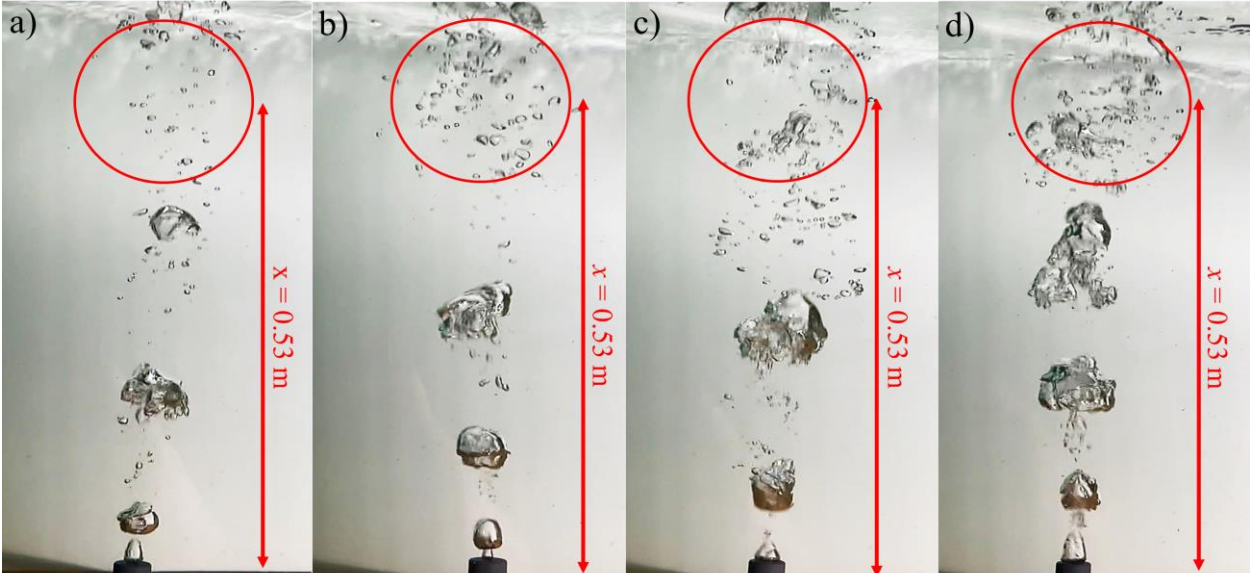


Figure 3. 2: Snapshot images of bubbles showing the effects of air discharge, Q_a , on formation of bubble plume and bubble size distribution at a certain distance from the nozzle, $x/d_o = 177$: a) $Q_a = 3$ L/min; b) $Q_a = 6$ L/min; c) $Q_a = 9$ L/min; d) $Q_a = 12$ L/min.

Figure 3.3 shows the time-history snapshot images of bubble plumes with different air discharges. The time interval between each consecutive images was $\Delta t = 0.07$ seconds. As air discharge increases, the large pocket of air breaks up into a cluster of small bubbles

and forms a cloud of bubbles. Due to bubble breakup, the surface of bubbles significantly increased, which also increased the contact area and subsequently the oxygen transfer rate along the vertical axis of the plume. Similar to Figure 3.2, Figure 3.3 shows the transitory regime of bubbly plume at which intermittent close to the nozzle, bubble frequency is low and bubble sizes are relatively large. Whereas close to the water surface it shows dispersed bubbly flow with a cluster of bubbles.



Figure 3. 3: Images of bubble plume variations with time for the plume tests with $d_o = 3$ mm. The time step between each image is 0.07 seconds: a) $Q_a = 3$ L/min; b) $Q_a = 6$ L/min; c) $Q_a = 9$ L/min; d) $Q_a = 12$ L/min.

3.3.1 Bubble velocity and concentration

Figure 3.4 illustrates the time histories of the cumulative average of bubble velocity at two different distances of $x = 0.35$ m (i.e., $x/d_o = 117$) and 0.53 m (i.e., $x/d_o = 177$) m from the nozzle. The cumulative average plots are helpful to determine the required

sampling time to achieve accurate estimation of time-averaged values. The total acquisition time of the measurements was 180 seconds and the dashed lines in Figure 3.4 indicate the $\pm 4\%$ variations of the time-averaged bubble velocity. It is deduced from bubble plume tests that the steady state time-averaged bubble velocity occurred after 100 seconds for all cases. To ensure the steady state regime and enhance the quality of data for prediction of time-averaged bubble velocity, an acquisition time of $t = 180$ seconds was selected for all experiments. Figures 3.4a and 3.4c show the effect of air discharge on variations of bubble velocity at $x/d_o = 117$. Similarly, Figures 3.4b and 4d show the variations of equilibrium bubble velocity with different air discharges at $x/d_o = 177$. As can be seen from Figures 3.4a and 3.4c, the time-averaged bubble velocity decreased from $u_b = 1.264$ m/s to 1.21 m/s as the air discharge decreased by 50%. This indicates an approximate reduction of 4.2% in time-averaged bubble velocity as air discharge reduced by 50%. Far from the nozzle at $x/d_o = 177$, the steady-state bubble velocity decreased from $u_b = 0.98$ m/s to 0.78 m/s as air discharge reduced from $Q_a = 9$ L/min to 3 L/min. The results indicate that by reducing air discharge by one-third, bubble velocity decreased by approximately 20.5%.

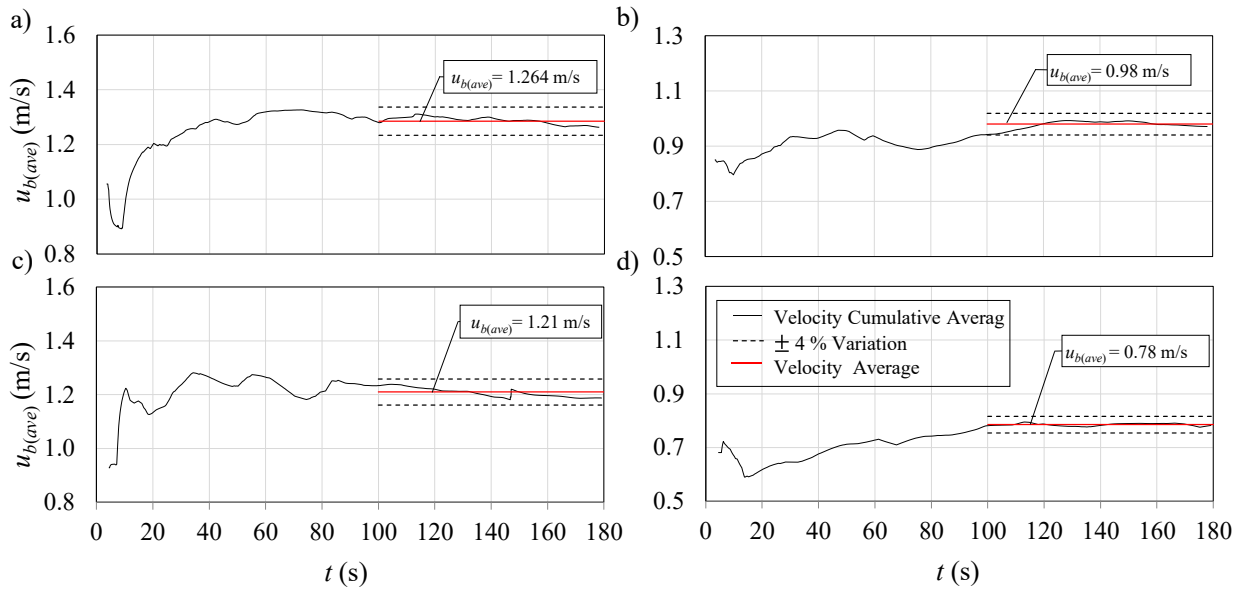


Figure 3. 4: Variations of the cumulative average of bubble velocity with distance from the nozzle: a) $x/d_o = 117$ and $Q_a = 12$ L/min; b) $x/d_o = 177$ and $Q_a = 9$ L/min; c) $x/d_o = 117$ and $Q_a = 6$ L/min; d) $x/d_o = 177$ and $Q_a = 3$ L/min. The dashed lines indicate the $\pm 4\%$ variations of the time-averaged bubble velocity.

The instantaneous variations of bubble velocity with time at $x = 0.35$ m (i.e., $x/d_o = 117$) and for different air discharges are shown in Figure 3.5. As can be seen, by decreasing the air discharge from $Q_a = 12$ to 3 L/min, the time averaged bubble velocity decreased from $u_b = 1.264$ m/s to 1.037 m/s, respectively. The time-averaged velocities were plotted as horizontal lines to indicate the magnitude of velocity fluctuations. Bubble velocity increased due to increasing air discharge which indicates that air bubbles had a smaller contact time with the ambient water. As a result, oxygen transfer reduced along the vertical axis of bubble plumes as air discharge increased.

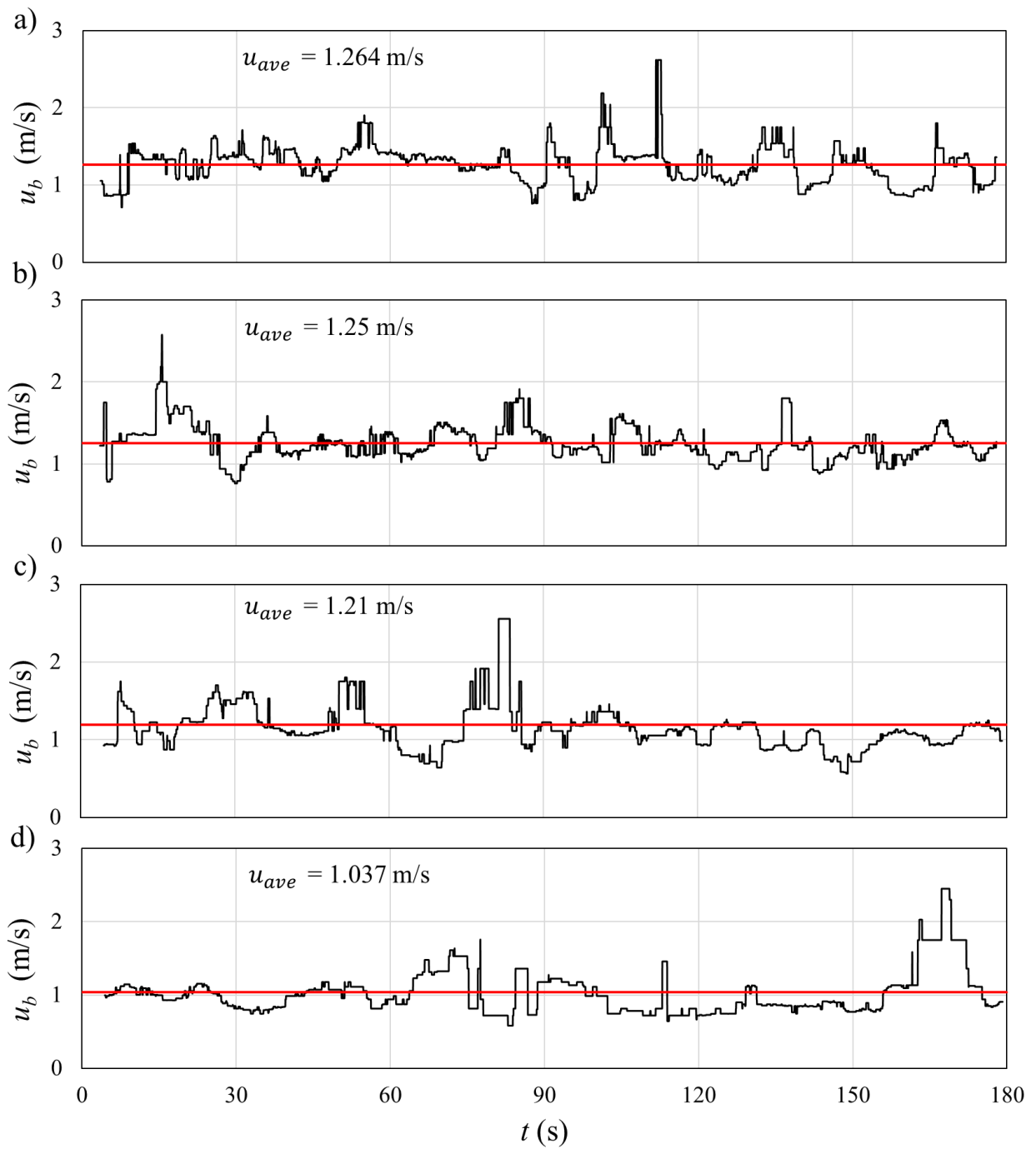


Figure 3. 5: Effect of air discharge, Q_a , on the time-histories of bubble velocity at $x/d_o = 117$: a) $Q_a = 12$ L/min; b) $Q_a = 9$ L/min; c) $Q_a = 6$ L/min; d) $Q_a = 3$ L/min.

Figure 3.6 illustrates the effect of air discharge on the time-history of bubble concentration at the centerline of bubble plumes and at $x/d_o = 117$. Bubble concentrations were collected for a duration of three minutes and the time-averaged concentrations were

shown as horizontal lines in Figure 3.6. The results revealed that increasing in air discharge increased the number of bubbles, which subsequently increased the surface area of bubbles and enhanced air-water mixing. This shows the positive effect of air discharge on mixing capacity of bubble plumes, which should be further evaluated with the negative effect of air discharge due to reduction of contact time.

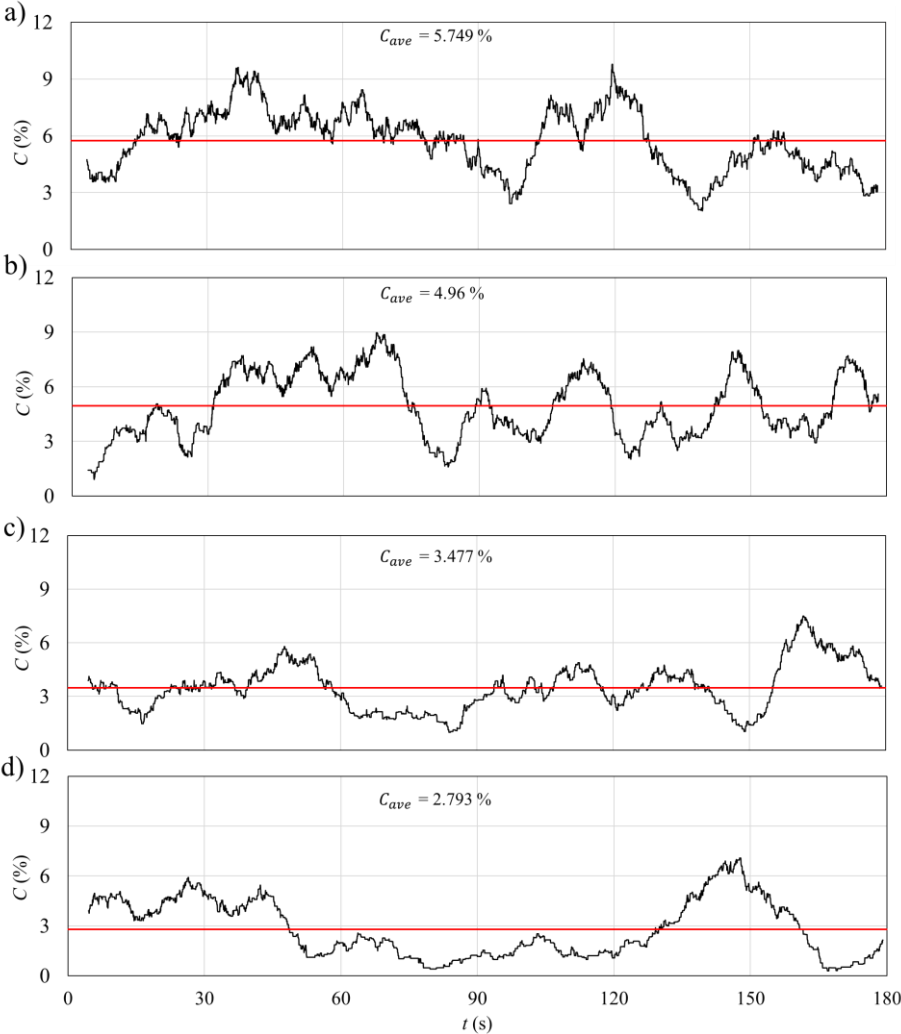


Figure 3. 6: Time-histories of bubble concentration with different air discharges at $x/d_o = 117$: a) $Q_a = 12$ L/min; b) $Q_a = 9$ L/min; c) $Q_a = 6$ L/min; d) $Q_a = 3$ L/min.

Figure 3.7 shows the effect of air discharge on variations of time-averaged bubble concentration and velocity. A comparison between the tests with different air discharges indicated that bubble concentration at the centerline of bubble plume increased linearly as air discharge decreased (see Figure 3.7a). The slope and intercept of the linear correlation between air discharge and bubble concentration are 0.345 and 1.657, respectively with a coefficient of determination of $R^2 = 0.97$. Based on the variations of time-averaged bubble velocity and air discharge, a power law equation was proposed between time averaged bubble velocity and air discharge with a base and exponent of 0.88 and 0.15, respectively (see Figure 3.7b). The coefficient of determination of the proposed equation was $R^2 = 0.97$.

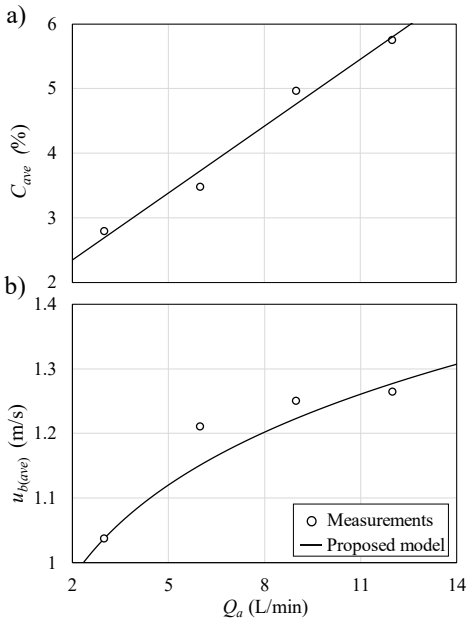


Figure 3. 7: Correlations between air discharge and bubble characteristics at $x/d_o = 117$: a) variations time average bubble concentration with Q_a , b) variations of time average bubble velocity with Q_a .

3.3.2 Bubble size distribution

Figure 3.8 shows the effect of air discharge on bubble size distribution by measuring the Probability Density Function (PDF) of bubble diameter at different distances from the nozzle (i.e., $x/d_o = 203, 177, 127$ and 107). The peak value in each PDF curves indicates the most probable bubble size at a certain location and air discharge. The bubble size distribution of bubble plumes with $Q_a = 4, 6,$ and 8 L/min from the recent study of Behzadipour et al. (2022) were also added for comparison. A comparison between the present experimental data and recent observations of Behzadipour et al. (2022) shows a good agreement with an acceptable uncertainty range in the repeated test (i.e., $Q_a = 6$ L/min). Also, Ziegnehein and Lucas (2017) conducted experimental study that revealed bubble plumes with high flow rates generated a more uniform bubble size distribution.

As can be seen in Figure 3.8, the most probable bubble diameter decreased with increasing air discharge, however; the probability in the peak bubble size distribution increased with increasing air discharge. In other words, at a certain distance from the nozzle, increasing air discharge increased the number of bubbles with a smaller size. A comparison among the results of the PDF in different distances from the nozzle indicated that the area of PDF curves decreased with increasing the distance from the nozzle. This indicates that the total number of bubbles at the centerline of the plume decreased with increasing the distance from the nozzle. The air volume either dissolved in ambient water or spread from the plume's centerline. Figures 3.8a and 3.8d show that the most probable bubble diameter decreased on average by approximately 50% from $x/d_o = 107$ to 203 .

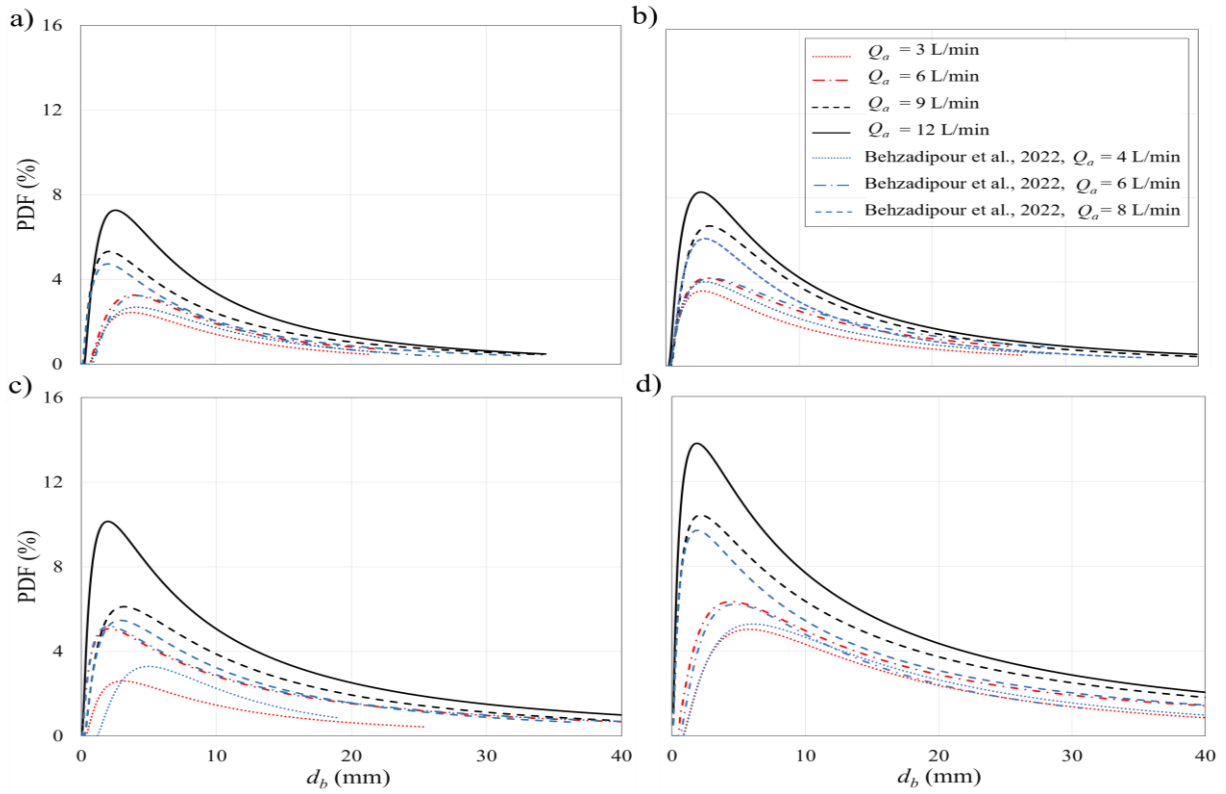


Figure 3. 8: Effects of air discharge, Q_a , on bubble size distribution: a) $x/d_o = 203$; b) $x/d_o = 177$; c) $x/d_o = 127$; d) $x/d_o = 107$.

To better analyze the experimental data on bubble size distribution and study the effect of air discharge and distance from the nozzle, the correlation between bubble size and its probability is shown in semi-log plot in Figure 3.9. Figure 3.9a shows bubble size distribution at $x/d_o = 203$. As can be seen, the most probable bubble size for $Q_a = 3$ and 12 L/min are 4.5 mm and 2.5 mm, respectively. Whereas close to the nozzle at $x/d_o = 107$, the deviation between the most probable bubble size was larger. As can be seen in Figure 3.9d, the most probable bubble size for $Q_a = 3$ and 12 L/min are 6 mm and 2 mm, respectively.

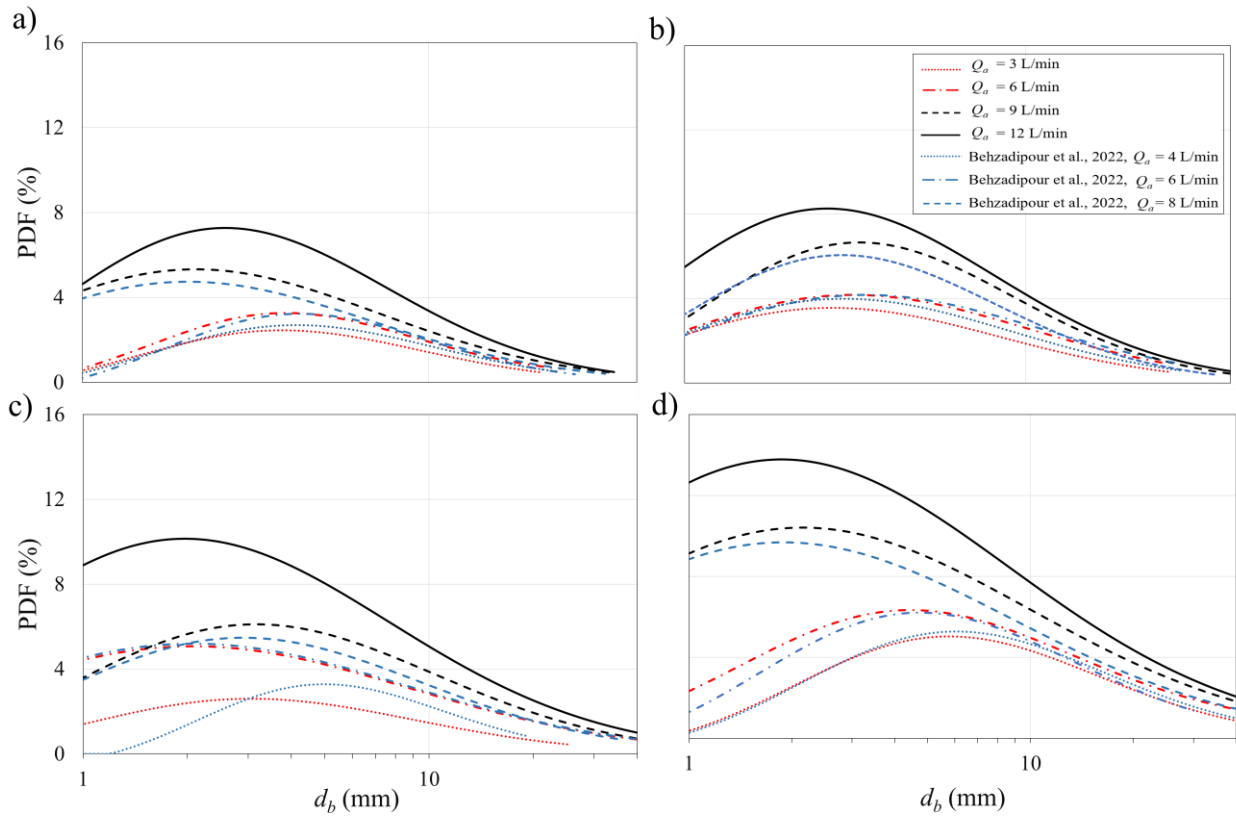


Figure 3. 9: Variations of bubble size distribution using the Probability Density Function (PDF) with air discharge, Q_a , at different distances from the nozzle, x/d_o : a) $x/d_o = 203$; b) $x/d_o = 177$; c) $x/d_o = 127$; d) $x/d_o = 107$.

3.3.3 Bubble characteristics

Figure 3.10 shows the effect of air discharge on variations of bubble characteristics along the vertical axis of bubble plumes. The over bars in this figure show the measurement uncertainty in detecting bubble characteristics with the RBI optical probe. The distance from the nozzle, x , was normalized with the total depth of water, H , to show the variations of bubble characteristics as bubbles approached the water surface. Figure 3.10a shows the effect of air discharge on the vertical variations of time-averaged bubble velocity, $u_{b(ave)}$. The proposed equations of Bombardelli et al. (2007) and Behzadipour et al. (2022) on vertical variations of bubble velocity with different air discharges were also

added in Figure 3.10a. Bombardelli et al. (2007) conducted different range of air discharges from 12 L/min to 52 L/min. A comparison between the present experimental data and proposed equations indicated a good agreement in prediction of time-averaged bubble velocity along the axis of the plume. As can be seen, the mean bubble velocity at each water depths increased with increasing air discharge; however, the correlation between air discharge and bubble velocity was non-linear. As can be seen, bubble velocity trends were close to each other in air discharges of 9 L/min and 12 L/min indicating that bubble velocity reached to its limit and further increasing air discharge does not change the trend of bubble velocity with vertical distance from the nozzle. The variations of bubble velocity over water depth indicate that bubble velocity decreases as bubbles ascend to water surface and the rate of velocity reduction increases with air discharge, which shows the same result that Wang et al. (2019) obtained. Their observations indicated that the normalized bubble velocity decreased with a distance from the nozzle in form of $u_{b(ave)}/u_s \sim x^{-1/2}$ where u_s is the bubble slip velocity.

Figure 3.10b illustrates the vertical profile of interfacial area, $a = 4f_b/u_{b(ave)}$, over normalized water depth and with different air discharges. As can be seen, the interfacial area decreased significantly from 55 m^{-1} to 30 m^{-1} in relatively short depth (i.e., $0.24 < x/H < 0.4$). For $x/H \geq 0.4$, the variations of interfacial area were almost invariant with water depth, and it only varied with the air discharge. In addition, the interfacial area was always less than 30 m^{-1} for $x/H \geq 0.4$. In this regime, the interfacial area of bubbles decreased with decreasing air discharge with values of $a = 11.2, 14.3, 18.2$ and 20.3 m^{-1} for $Q_a = 3, 6, 9,$ and 12 L/min , respectively. A linear correlation between air discharge and interfacial area was formulated with a slope of 1.04 and an intercept of 8.2. The coefficient of

determination of the proposed equation was $R^2 = 0.98$. It should be noted that, the proposed linear equation is not valid for $Q_a < 3$ L/min. However, a power law model describes the correlation between interfacial area and air discharge by including the boundary value of $a \rightarrow 0$ as $Q_a \rightarrow 0$. The base and power of the proposed power law equation are 6.81 and 0.44, respectively. The coefficient of determination of the proposed power law equation was $R^2 = 0.99$.

Figure 3.10c shows the effect of air discharge on variations of bubble diameter along the vertical axis of bubble plume from the nozzle to water surface. The variations of bubble size along the axis of bubble plume is important to estimate the mass transfer coefficient, K_L (Wüest et al., 1992). As it can be seen from Figure 3.10c, bubble diameter in bubble plumes constantly decreased from the nozzle to water surface. The prediction model of Behzadipour et al. (2022) for a narrow range of air discharges was also added for comparison. A comparison between experimental data and model prediction indicated that at constant elevation of $x/H = 0.5$, bubble diameter increased by an average of 22.3%, 21.1%, and 19.2% as air discharge increased from $Q_a = 3$ to 6 L/min, 6 to 9 L/min, and 9 to 12 L/min, respectively.

Figure 3.10d shows the vertical profile of bubble frequency for different air discharges. As it can be seen, bubble frequency increased non-linearly with air discharge and decreased with the vertical distance from the nozzle. The proposed model of Iguchi et al. (1995) for prediction of the vertical profile of bubble frequency was also added in Figure 3.10d. The bubble frequency decreased rapidly from 16 Hz to 10 Hz at relatively short distance from the nozzle (i.e., $0.25 < x/H < 0.4$) and similar trend was observed from prediction model of Iguchi et al. (1995). The effect of air discharge was more pronounced

for $x/H \geq 0.4$. As can be seen from Figure 3.10d, bubble frequency decreased almost linearly with water depth from $x/H = 0.4$ to water surface (i.e., $x/H \approx 0.9$). A correlation between bubble frequency and air discharge implies that the number of bubbles at a certain position increased with increasing air discharge. The prediction model of Iguchi et al. (1995) is applicable for $Q_a \leq 2.5$ L/min confirming the correlation between air discharge and bubble frequency.

The variations of bubble concentration along the vertical axis of bubble plumes with different air discharges are shown in Figure 3.10e. Based on the static pressure law, the values of pressure inside the bubbles and the pressure in ambient water should eventually form an equilibrium. Such equilibrium condition occurs over a distance from the nozzle and it occurred at $x/H \approx 0.375$ in this study. For $x/H \geq 0.375$, the compacted bubbles and air clouds break up and lead to higher bubble concentrations in bubble plumes with high air discharges. Therefore, bubble concentration increased due to increasing air discharge at a constant from the nozzle. A non-linear correlation was developed between air concentration and air discharge over a vertical distance from the nozzle by employing multi-regression analysis as:

$$\frac{x}{H} = 1.7C_{ave}^{-3/4} \quad (3.1)$$

The coefficient of determination of the proposed model is $R^2 = 0.92$ and the proposed equation is valid for air discharges ranging between 9 L/min and 12 L/min and for $x/H < 1$. Similar prediction model was proposed for estimation of bubble concentration in weak plumes (i.e., $Q_a \leq 2.5$ L/min) by Iguchi et al. (1995) and the model was added in Figure 3.10e. Figure 3.10f demonstrates the variations of bubble Reynolds number (i.e., $Re_b = \rho_a u_{bo} d_{bo} / \mu_w$) over the vertical profile of bubble plumes and the effects of air discharge

on variations of Re_b . Similar to variations of bubble velocity with air discharge, bubble Reynolds number increased by increasing air discharge; however, similar trend was observed for $Q_a \geq 9$ L/min and the effect of air discharge became negligible for $Q_a \geq 6$ L/min.

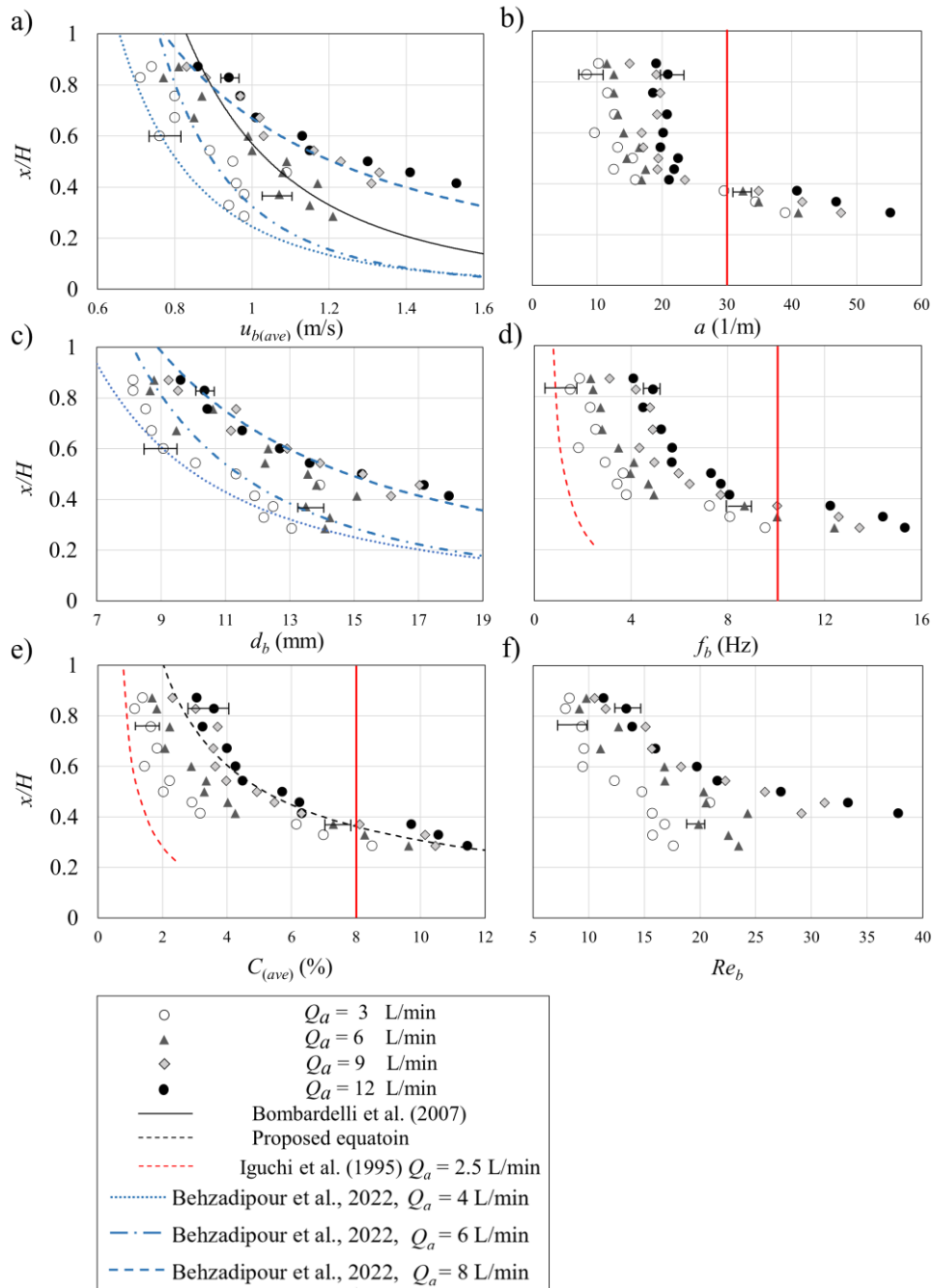


Figure 3. 10: Variations of the bubble hydrodynamics along the vertical axis of bubble plumes with different air discharges of $Q_a = 3, 6, 9$ and 12 L/min: a) bubble mean velocity;

b) interfacial area of bubbles; c) bubble mean diameter; d) bubble frequency; e) bubble concentration; f) bubble Reynolds number. The red vertical lines show the onset of bubble dispersion stage.

The total number of bubbles is estimated by the measured data from the RBI probe which represents the combination of bubble size and bubble concentration. The total number of bubbles during 100 seconds of measurements was detected by the RBI probe. Figure 3.11 shows the effect of air discharge on variations of the total number of bubbles for different distances from the nozzle. The model prediction results for estimation of bubble number from the study of Behzadipour et al. (2022) for a narrow range of air discharges was also added for comparison. The results show an acceptable agreement between model prediction and measurements indicating that the proposed model can be extended for a wider range of air discharges between $Q_a = 3$ L/min and 12 L/min. As it can be seen, the number of bubbles decreased by increasing the distance from the nozzle, which may be due to bubble coalescence, bubble interactions, and formation of bubble cloud at higher distances from the nozzle. A sudden drop on the number of bubbles was observed at $x/d_o = 120$ indicating that bubble coalescence especially occurred in bubble plumes with high air discharges (i.e., $Q_a \geq 9$ L/min).

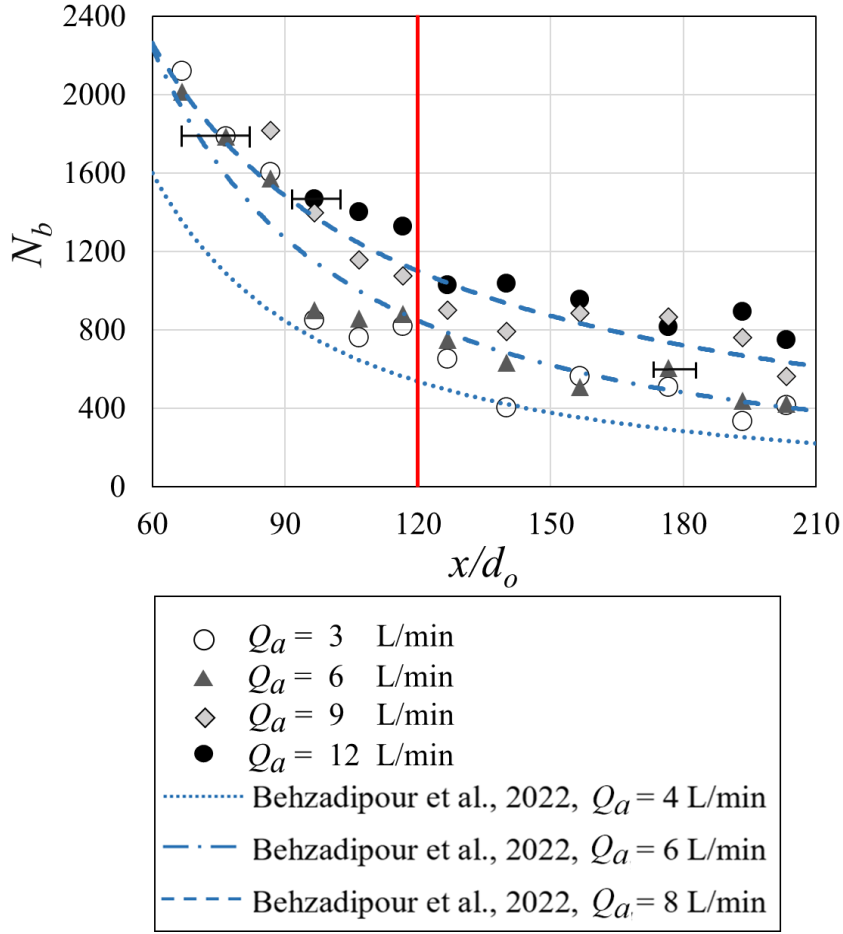


Figure 3. 11: Effect airflow discharge, Q_a , on the total number of bubbles, N_b , above the nozzle with $d_o = 0.003$ m. The number of bubbles was detected during the 100 seconds of measurements.

3.3.4 Momentum and buoyancy fluxes

The momentum and buoyancy fluxes in strong bubble plumes were calculated from measurements and the results were normalized with the initial momentum and buoyancy fluxes at the nozzle. Figure 3.12 shows the effects of air discharge on variations of normalized momentum and buoyancy fluxes along the normalized vertical distance from the nozzle, x/d_o . The variations of normalized momentum flux, M_b/M_o , with x/d_o for different air discharges are shown in Figure 3.12a where $M_b = A_b \times u_{b(ave)}^2$ where A_b is the cross sectional area of bubble plume. A comparison among the normalized momentum

fluxes indicated that the momentum flux in bubble plumes with relatively high air discharges (i.e., $Q_a \geq 9$ L/min) significantly increased with increasing air discharge for $x/d_o < 100$. The peak momentum flux occurred at $x/d_o = 110$. For $Q_a = 12$ L/min, the momentum flux reached to approximately three times of the initial momentum flux.

The values of normalized momentum flux reduced with x/d_o and reached the minimum value of $M_b/M_o \approx 0.65$ at the water surface. Close to the nozzle and for $x/d_o < 100$, air bubbles are still affected by the air pressure, which can predominantly increase the momentum forces. Figure 3. 12b illustrates the variations of normalized buoyancy fluxes along the jet axis, $B_b = g(\rho_w - \rho_a)/\rho_w \times A_b \times u_{b(ave)}$ where g is the gravitation acceleration, ρ_a and ρ_w are the densities of air and water, respectively. As can be seen, buoyancy fluxes increased sharply with distance from the nozzle and reached the maximum value of $B_b/B_o = 2.45$ at $x/d_o = 110$ for the air discharge of $Q_a = 12$ L/min. The normalized buoyancy fluxes gradually decreased from the nozzle and reached the minimum value of $B_b/B_o \approx 0.65$ at the water surface. The justification of such maximum values is due to the interior pressure fluctuations and their relationships with the local static pressure.

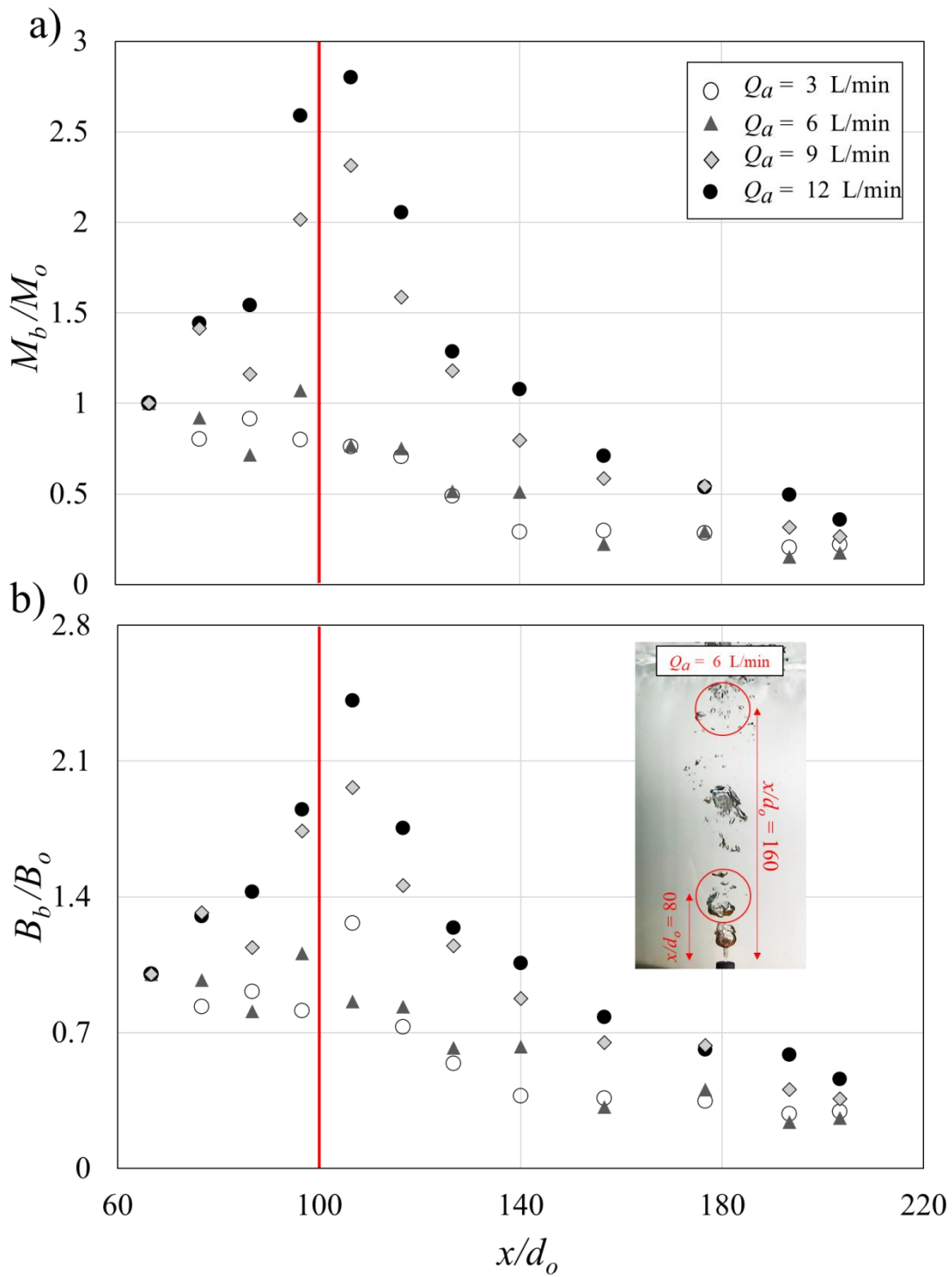


Figure 3. 12: Effect of airflow discharge on the normalized momentum and buoyancy above the nozzle, $d_o = 0.003$ m: a) normalized momentum flux; b) normalized buoyancy flux.

Figure 3. 13 shows the correlation between dimensionless bubble plume number expressing as $Q_a/[(gd_b^5)]^{1/2}$ and normalized vertical axis, x/H . Experimental data indicated a dependency on air discharge which can be formulated using the multi-regression analysis. The proposed model estimates the variations of bubble size along the vertical axis of the plume and it is described by:

$$\frac{x}{H} = [0.4355 - 0.007Q_a] \left[\frac{Q_a}{(gd_b^5)^{1/2}} \right]^{[0.85Q_a^{-0.27}]} \quad (3.2)$$

The coefficients of determination for prediction of the base and power of the proposed equation were $R^2 = 0.88$ and 0.90 , respectively. The proposed equation is applicable for a range of air discharge between $Q_a = 3$ L/min and 12 L/min.

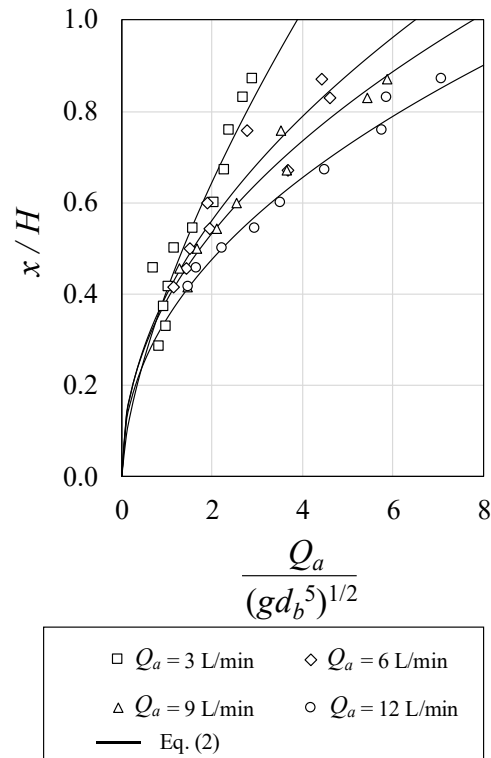


Figure 3. 13: Variations of non-dimensional discharge of vertical bubble plume along the vertical axis.

The variations of bubble size along the vertical axis of the plume is estimated knowing the air discharge. Relatively simpler correlation was achieved by plotting the normalized bubble diameter, d_b/d_o , with the bubble Reynolds number, $Re_b = \rho_a u_{bo} d_{bo} / \mu_w$ where μ_w is the dynamic viscosity of water. Figure 3. 14 shows a linear correlation between normalized bubble diameters versus bubble Reynolds number. The experimental data of Behzadipour et al. (2022) on bubble plumes with relatively smaller air discharge range were also added to Figure 3. 14 for comparison. A linear equation with a coefficient of determination of $R^2 = 0.97$ was proposed to correlate the normalized bubble diameter with bubble Reynolds number as:

$$\left(\frac{d_b}{d_o}\right) = 0.126Re_b + 1.8 \quad (3.3)$$

The $\pm 10\%$ variations of the empirical correlations were also added to Figure 3. 14 as dashed lines. Despite the simple linear correlation between bubble diameter and bubble Reynolds number, estimation of bubble Reynolds number requires knowing bubble velocity and bubble size. Variations of bubble velocity along the vertical axis of the plume was introduced in the studies of Wüest et al. (1992), Bombardelli et al. (2007) and recently by Behzadipour et al. (2022). Since bubble diameter appeared in both sides of Eq. (3.3), estimation of bubble diameter can be achieved through iterative procedure.

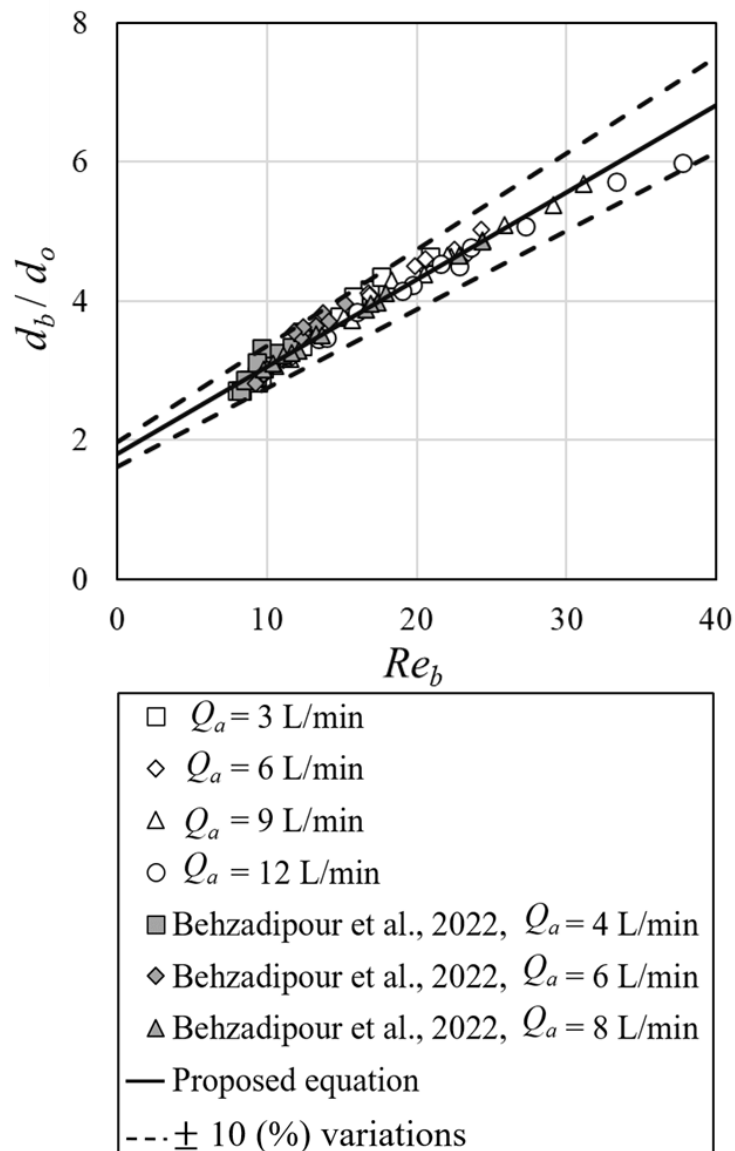


Figure 3. 14: Effect of airflow discharge on variations of normalized bubble size with bubble Reynolds number.

3.3.5 Bubble velocity fluctuations

The measured data provided detailed information on the time-averaged characteristics of bubble plumes which were compared with the proposed formulations from the literature in relatively weak plumes. It is important to understand the effects of air discharge on the turbulence characteristics of bubble plumes as turbulent dispersion also

contribute in oxygen transfer and mixing. The effect of air discharge on the vertical profile of bubble velocity fluctuations is shown in Figure 3. 15. Figure 3. 15a shows the variations of bubble velocity fluctuations with normalized distance from the nozzle, x/d_o . As it can be seen, the vertical velocity fluctuations were within 0.01 m/s to 0.1 m/s and velocity fluctuations increased non-linearly as bubbles approached the water surface. The higher value of bubble velocity fluctuations may be due to pressure reduction near the water surface. The turbulent intensity, $I = u'_{b(ave)} / u_{b(ave)}$, in bubble plumes is determined by normalizing bubble velocity fluctuations with the mean bubble velocity. Figure 3. 15b shows that bubble turbulent intensity in the vertical direction varied between 1% and 8% and it increased with increasing the distance from the source.

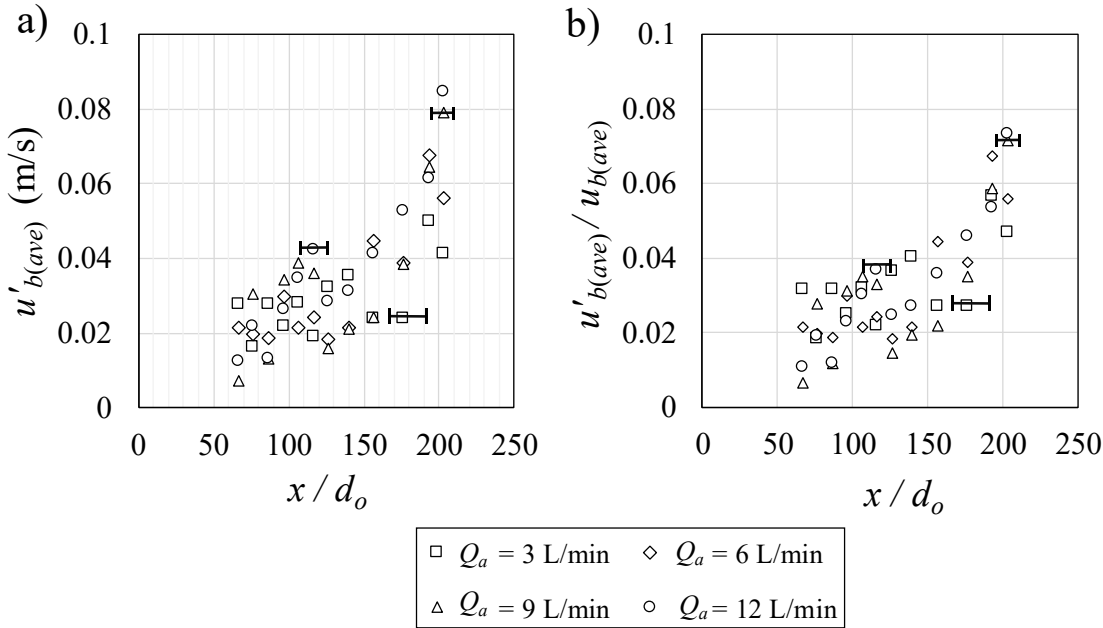


Figure 3. 15: Effect of airflow discharge on variations of bubble velocity fluctuations above the nozzle, $d_o = 0.003$ m: a) bubble velocity fluctuations with x/d_o ; b) normalized bubble velocity fluctuations with x/d_o .

In addition to the vertical profile of turbulent intensity in bubble plumes, the distribution of turbulent intensity plays an important role in turbulent momentum transfer and mixing. The turbulent intensity range was divided into nine bands and the probability of each band was extracted from the time history of turbulent intensity data. Figure 3. 16 shows the effects of air discharge on distribution of turbulent intensity range at $x/d_o = 177$. As can be seen, the low ranges of turbulent intensity (i.e., $I \leq 10\%$) contains approximately 50% of the probability and is relatively constant with variations of air discharge. Whereas the high ranges of turbulent intensity ($I \geq 25\%$) significantly decreased with air discharge. The probability of turbulent intensity of larger than 25% for $Q_a = 3, 6, 9,$ and 12 L/min were 21.8%, 17.3%, 10.5%, and 3.6%, respectively. This indicates that higher air discharge reduces the extreme fluctuations of bubbles in vertically discharges bubble plumes.

The discussed parameters in this study are very important on prediction of mixing efficiency in vertically discharged bubble plumes and can assist engineers for designing new mixing tanks and monitoring/improvement of the existing mixing systems. Based on dimensional analysis the normalized distance from the nozzle to water surface for a water depth of $H = 0.7$ m and nozzle diameter of $d_o = 0.003$ m (i.e., 3 mm) is $H/d_o = 233$. Using a prototype to model scaling ratio of 8, gives the nozzle diameter of 24 mm (i.e., close to 1 inch) and water depth of 5.6 m, which is comparable to the depth of aeration tanks in wastewater treatment plants. Using the similarity rule in the initial bubble Reynolds number and the model-to-prototype ratio of 8, the initial velocity at the nozzle ranging between 0.88 m/s and 3.54 m/s, which gives air discharge ranging between 24 L/min to 96 L/min (i.e., 0.4 L/s and 1.6 L/s), which is easily achievable by a small air compressor.

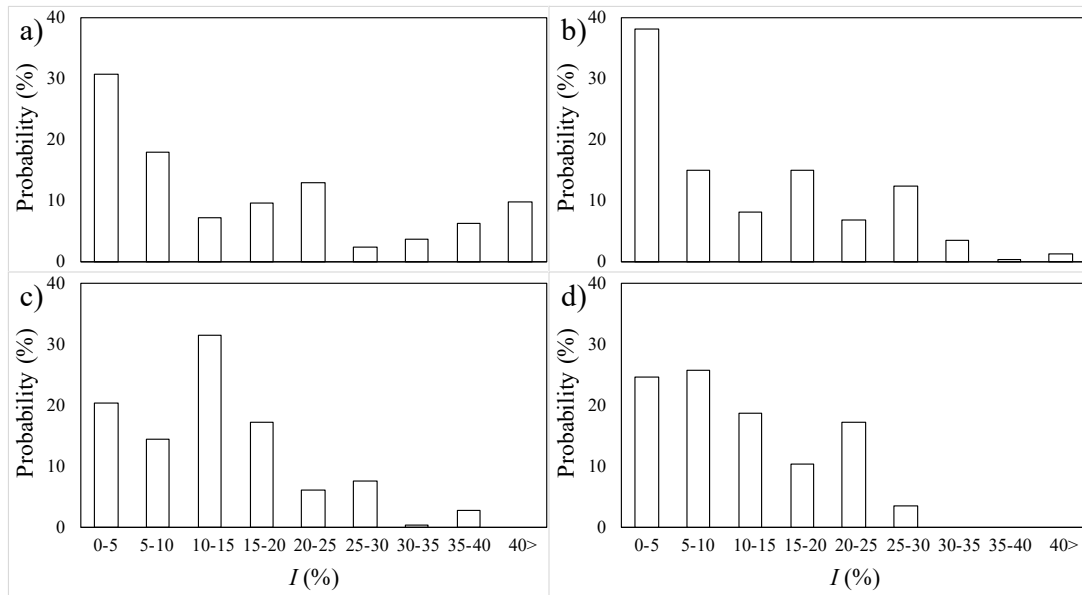


Figure 3. 16: Effect of air discharge on the distribution of bubble turbulent intensity, I at $x/d_o = 177$ a) $Q_a = 3$ L/min; b) $Q_a = 6$ L/min; c) $Q_a = 9$ L/min; d) $Q_a = 12$ L/min.

3.4 Conclusions

A series of laboratory experiments was carried out to study the effects of air discharge on the bubble characteristics of vertically discharged bubble plumes. The nozzle diameter was 3 mm and the range of air discharge was selected between 3 L/min to 12 L/min to form strong bubble plumes. The primary indicators of bubbles such as bubble size, bubble size distribution, bubble concentration/gas fraction, and velocity were measured along the vertical axis of the plume with a state-of-art RBI bubble probe. The effects of air discharge on the primary indicators were evaluated. Within the air discharge range tested in this study, the time averaged bubble velocity at the plume's centerline varied non-linearly with air discharge and a power law model was proposed to correlate the variations of bubble velocity with air discharge. However, the time averaged bubble concentration at the centerline of the plume varied linearly with air discharge. The effect of air discharge on distribution of bubble size along the vertical axis of bubble plumes was

studied and it was found that the most probable bubble size decreased with increasing air discharge which helps the air/oxygen transfer with the ambient water.

Experimental data indicated a direct correlation between air discharge and bubble velocity indicating that the bubble mean velocity increases with increasing discharge. However, such direct correlation was noticeable for relatively smaller air discharge (i.e., $Q_a < 9$ L/min) and further increasing air discharge slightly increased the mean bubble velocity. The variation of bubble concentration along the vertical axis of bubble plume indicated that bubble concentration decreased in the plume's centerline due to plume spreading and bubble concentration increased with increasing air discharge as $x \sim C^{-3/4}$.

Other important parameters on bubble dynamics and mixing such as interfacial area, frequency, velocity fluctuations and turbulent intensity of bubbles were extracted. The vertical profile of bubble interfacial area showed two distinct zones of mixing. Close to the nozzle, the effect of air discharge on variations of bubble interfacial area was marginal and the interfacial area significantly decreased for $0.24 < x/H < 0.4$. The effect of air discharge became significant for $x/H \geq 0.4$ and the interfacial bubble area increased with increasing air discharge indicating a more efficient and better mixing with increasing air discharge. The results showed that bubble frequency increased non-linearly with air discharge and decreased along the vertical axis of the plume. It rapidly decreased at relatively short distance from the nozzle (i.e., $0.25 < x/H < 0.4$) and air discharge came to effect for $x/H \geq 0.4$. Laboratory measurements showed that bubble velocity fluctuations at the centerline of the plume increased non-linearly with distance from the nozzle and no correlation was found between air discharge and bubble velocity fluctuations and the high ranges of turbulent intensity ($I \geq 25\%$) significantly decreased with air discharge.

Some integral quantities such as momentum and buoyancy fluxes were calculated and the results were compared with the initial momentum and buoyancy fluxes at the nozzle. The results indicated that the momentum fluxes significantly increased from the nozzle to $x/d_o = 110$, reached the maximum value of three times of the initial momentum flux for $Q_a = 12$ L/min and then decreased to 65% of the initial momentum flux. The maximum buoyancy flux in the highest air discharge was approximately 2.5 times of the initial buoyancy flux and it decreased close to water surface to 65% of the initial buoyancy flux.

Notations

The following symbols are used in this paper:

- a = interfacial area of bubble, m^{-1} ;
 A_b = cross sectional area of bubble plume, m^2 ;
 C = instantaneous bubble concentration, vol/vol;
 C_{ave} = time-averaged bubble concentration, vol/vol;
 d_b = bubble diameter, m;
 d_{bo} = bubble diameter at the nozzle, m;
 d_o = nozzle diameter, m;
 D = depth of the tank, m;
 g = gravitational acceleration, m/s^2 ;
 h_n = nozzle height above the bed, m;
 H = height of water above the nozzle, m;
 K_L = mass transfer coefficient;
 L = length of the tank, m;
 Q_a = air discharge, m^3/s ;
 Re_b = bubble Reynolds number;
 t = time, s;
 u_b = instantaneous bubble velocity, m/s;
 $u_{b(ave)}$ = time-averaged bubble velocity, m/s;
 u_{bo} = bubble velocity at the nozzle, m/s;
 u_s = bubble slip velocity, m/s;
 x = distance from the nozzle;
 ρ_a = air density, kg/m^3 ;
 ρ_w = water density, kg/m^3 ;
 μ_w = dynamic viscosity of water, kg/m.s .

Chapter 4

Hydrodynamic modifications in vertical bubble plumes by a grid-screen

4.1 Introduction

Discharge of air through a nozzle and into a stagnant ambient forms bubbly jets or plume. Bubbly jets and plumes have many applications in the civil, mechanical, chemical, and environmental engineering projects and have been utilized in oxygen transfer enhancement, increasing dissolved oxygen level, and water quality improvement in manmade ponds, natural lakes, and streams. They have been employed in many engineering designs such as in chemical reactors, lake aeration, Dissolved Air Flootation (DAF) systems in water treatment plants, and in subsea gas leakage (Paerl and Otten, 2013; Ibelings et al., 2016; Pan et al., 2021; Behzadipour et al., 2022, 2023). Bubbly jets are formed as a mixture of air and water and are discharged with an initial momentum. While bubbly plumes are formed as air is discharged with a dominant buoyancy due to the density difference between air bubbles and the ambient water (Lima Neto et al., 2008, 2016). Knowing the properties of bubble plumes such as the vertical variations of bubble size, concentration, and velocity is necessary to optimize the aerator by enhancing air-water mixing and reducing the cost of operation.

The magnitude of acting forces on bubbles depends on the hydrodynamic characteristics of bubbles and the initial discharge conditions. The motion and expansion of bubbles in bubble plumes are primarily controlled by the interactions of buoyancy, drag, and added mass forces acting on the bubbles. Many research studies have evaluated the effects of acting forces on bubble plumes such as buoyancy, added mass, and drag forces (Crouse et al., 2007; Fraga, and Stoesser, 2016; Duan et al., 2018; Fleck and Rzehak,

2019). As bubbles rising towards the water surface, the buoyancy force between air bubbles and the ambient water is eventually balanced with the drag and added mass forces, which results in developing an approximately constant bubble velocity relative to the ambient water (Crouse et al., 2007).

Many experimental studies have been performed to investigate the effects of initial parameters on bubble dynamics and to model the contributed forces on bubbles as raising towards the water surface. Felton and Loth (2001) conducted a series of laboratory experiments and employed the Particle Image Velocimetry (PIV) technique to measure bubble characteristics and to calculate the relevant hydrodynamic forces. The initial velocity of bubbles ranged from 0.4 m/s to 0.9 m/s and the mean bubble diameter ranged between 0.37 mm and 1.2 mm. Felton and Loth (2001) found that for a fixed bubble diameter, the drag coefficient in bubbles decreased with increasing bubble Reynolds number, $Re_b = \rho_w u_b d_b / \mu_w$, where u_b is the bubble velocity, d_b is the bubble diameter, ρ_w is the density of water, and μ_w is the kinematic viscosity of water. It was found that, the effect of bubble deformation on the coefficient of lift force is significant as bubble diameter increased. For a constant bubble Reynolds number, the instantaneous drag coefficient decreased due to increasing the turbulence intensity in bubbles. Their result revealed that for a bubble diameter of $d_b = 0.82$ mm, the buoyancy and drag forces had the most impact amongst other forces and they were approximately 2.5 times of the lift force.

The variations of drag and lift forces on ellipsoidal air bubbles moving through a turbulent ambient water were analyzed from the PIV data (Ford and Loth, 1998). Air bubbles with mean diameters ranging from 1.5 mm to 4.5 mm were injected directly into a shear layer flow that was generated in a single slender tube. Their results revealed that for a fixed bubble diameter, drag coefficient decreased from 0.75 to 0.30 as bubble Reynolds

number increased from 300 to 500. In addition, a non-linear correlation was proposed between drag coefficient and bubble Reynolds number. Hibiki and Ishii (2007) modeled the motion of a single bubble and studied the effect of bubble deformation on the variations of the lift force. The proposed model estimated the variations of the lift force as a function of bubble Reynolds number and the results were applicable for bubble Reynolds number ranging from 3.68 to 78.8.

The presence of air bubbles in bubble plumes has a considerable impact on the motion of the surrounding water. The experimental study of Besbes et al. (2020) indicated that nozzle diameter controls the bubble size in relatively small gas flow rates, Q_g , ranged between 0.00085 L/min and 0.00255 L/min. Their results have shown that the terminal velocity of bubbles increases with the gas discharge and the buoyancy force in bubbles. Bubble shape deformation was observed due to the balance between the surface tension and buoyancy forces, which was correlated with the Morton number ($Mo = [g\mu_w^4\Delta\rho]/[\rho_w^2\sigma^3]$) where ρ_w and μ_w are the density and viscosity of water, respectively, $\Delta\rho$ is the density difference between air and water, and σ is the surface tension coefficient. It was found that the drag force performed the primary role in variations of bubble terminal velocity and the hydrodynamic configuration of bubble plumes.

Lai and Socolofsky (2019) conducted a series of experimental studies to evaluate the kinetic energy budget in bubble plumes. Bubble diameters ranged between 1 mm and 4 mm and bubble concentration varied between 0.7% and 1.8%. A non-linear correlation was proposed between the momentum flux of bubbles, $M = (\pi d_b^2/4)u_b^2$, and the distance from the nozzle, x , in form of $M \sim x^{4/3}$. Behzadipour et al. (2023) conducted a comprehensive experimental study on the effects of nozzle size and air discharge (i.e., $Q_a = 3, 6, 9$ and 12 L /min) on bubble plume characteristics. They showed that bubble size distribution are

relatively uniform when air discharge increases from 4 L/min to 8 L/min, and air discharge reduces the mean bubble diameter by approximately 34%. Their results revealed that by reducing air discharge by one-third, bubble velocity decreases by approximately 20.5%.

Both numerical and experimental studies were performed to study bubble plume dynamics in a 1 m × 1 m × 1 m tank by Fraga et al. (2016). They used air discharge ranged between 0.5 L/min and 1.5 L/min with mean bubble diameter ranged from 1 mm to 4 mm. The buoyancy force in bubbles increased by increasing bubble diameter, which caused a higher range of bubble velocity. Their results indicated that the average slip velocity for a given bubble size is mainly determined by the equilibrium between the buoyancy and drag forces. The added mass force appears to play an important role in balancing the oscillations of the drag component.

Many experimental and numerical studies have been carried out to investigate the effects of forces acting on single bubble and bubble clusters in vertically discharged bubble plumes (Duan et al., 2018). However, the present experimental study aims at investigating the performance of a vertically discharged bubble plume passing through a grid-screen at different distances from the nozzle. Our recent studies on the effect of grid-screen and air discharge on bubble characteristics along the vertical axis of bubble plumes showed a significant change in bubble parameters such as bubble size, and velocity (Behzadipour and Azimi, 2022; Behzadipour et al., 2022; 2023). Despite the extensive study on the effect of grid-screen on bubble dynamics, detailed information about the forces acting on bubbles and the grid-screen are required to achieve the optimum design parameters and plan for a proper maintenance. The variations of bubble concentration and the resultant forces acting on bubbles and grid-screen have not been yet studied and require more attention.

The main objective of the present study is to understand the effect of grid-screens with different openings and distances from the nozzle on variations of bubble concentration and force balance between bubble clusters and screen structure. For proper design and efficient operation, the maximum air discharges for efficient bubble size reduction are measured for different grid-screen openings and distances from the nozzle. The present study provides a detailed analysis on variations of all acting forces on bubble plumes passing through a grid-screen and the outcomes of the present study will be suitable for design optimization and validation of numerical models.

4.2 Experimental Setup

A series of laboratory experiments was carried out in the Multiphase Flow Research Laboratory (MFRL) at Lakehead University, Canada. Experiments were conducted in a glass-walled tank of 1.60 m long, 0.85 m wide, and 0.80 m deep. The tank was filled with water having a temperature of $20\text{ }^{\circ}\text{C} \pm 1^{\circ}\text{C}$ and a depth of $h = 0.70\text{ m}$. The air pressure was provided by an air compressor providing a maximum air pressure of $P = 4\text{ psi}$. Different air discharges of $Q_a = 4\text{ L/min}$, 6 L/min , and 8 L/min were tested in this study and air discharges were measured with an accurate rotameter (LZM series Zyia OEM, Zhejiang, China) with an accuracy of $\pm 0.2\text{ L/min}$. Two circular nozzles with diameters of $d_o = 1\text{ mm}$ and 3 mm were used to study the effect of nozzle size and to study the effects of bubble Reynolds number, Re_b , on variations of hydrodynamics forces. Standard grid-screens with two different sieve openings of $d_s = 0.841\text{ mm}$ (i.e., sieve number #20) and $d_s = 2.380\text{ mm}$ (i.e., sieve number #16) (ASTM, 2007) was employed to study the effect of grid-screen size on bubble breakup and coalescence. Grid-screens were placed at three different distances from the nozzle at $X_s = 0.14\text{ m}$, 0.22 m , and 0.30 m to

investigate the effect of screen's elevation on the input forces. Figure 4. 1 shows the schematic of experimental setup, coordinate system, and the related parameters.

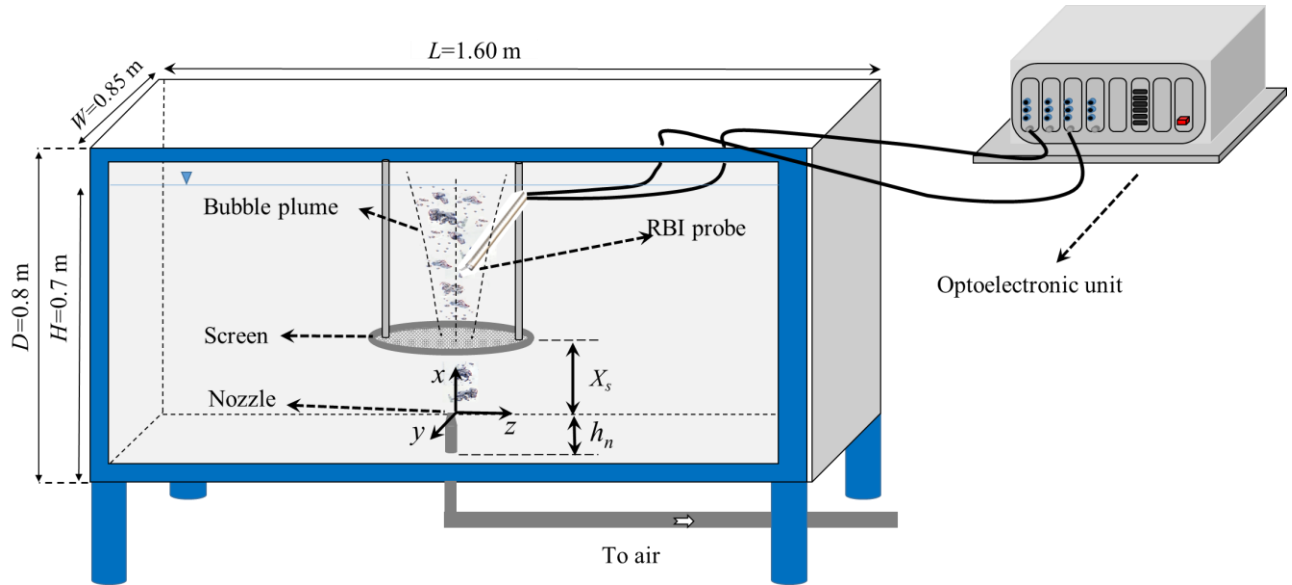


Figure 4. 1: The schematic of experimental setup, optoelectronic unit, and coordinate system of a vertical bubble plume passing through a grid-screen.

A high-resolution camera (Prosilica GT 1910c CCD, Germany) with a speed of 20 frames per second was employed and placed at a 1.4 m distance from the tank to take images and compare bubble characteristics before and after the grid-screen. The camera was fitted with either a 90-mm Kowa F 1.8 (Kowa, Japan) or an 18–55 mm AF-Sinckor, 13.5–5.6 GII (Nikon, Japan) lens. An optoelectronic unit with an accurate fiber optic probe were utilized to measure bubble properties. A **Refractive Bubble Instrument** (RBI instrumentation, Meylan, France) was used to measure bubble size, concentration, and velocity as bubbles passed through the two needles at the tip of the RBI probe. The probes' tips are 15 mm long, 2.5 mm apart, and have two sapphire crystals at the end of probe's tips (see Figure 4. 2). A module emits infrared light via two fiber-optic cables to the tips of the probe. The emitted light is refracted when the probe's tip is in water and is reflected in

the module when the probe's tip is in the air (i.e., inside a bubble). The reflected light passes through a semi-transparent mirror combined with a prism towards a photosensitive diode in the module. The light transmission system enables the probe to acquire voltage signals with a sampling rate of 1 MHz (RBI User Manual, Meylan, France). The RBI probe recorded the data for 180 seconds to achieve the statistically steady-state bubble characteristics by employing the cumulative averaging method (Behzadipour et al., 2022, 2023).

Figure 4. 2 illustrates the details of the experimental setup such as the nozzle and the grid screen, the optoelectronic unit (ISO Lite Software, RBI Optical probe, France), and the tips of the RBI probe. The optoelectronic unit converts the analog signals from the probe's tips to digital voltage signals. By analyzing digital voltage signals, the double-tip optical fiber probe (see Figure 4. 2b) is capable of measuring the variations of bubble size, void fraction (i.e., bubble concentration), bubble frequency, and bubble velocity with time. The time series of bubble velocity is calculated by cross-correlation of voltage signals from the probe's tips. The RBI double-tip optical fiber probe has been successfully employed in many experimental studies, and the accuracy and robustness of the system have been verified in measuring bubble characteristics in two-phase gas-liquid turbulent flows (Rensen and Roig, 2001; Boes and Hager, 2003; Kiambi et al., 2003; Chaumat et al., 2005; and Murzyn et al., 2005; Behzadipour et al., 2022a, b, 2023).

In total, 42 experiments were conducted to test the effects of nozzle size, d_o , air discharge, Q_a , grid-screen size, d_s , and grid-screen distance from the nozzle, X_s . In addition, six benchmark tests were carried out to measure bubble characteristics in bubble plumes without a grid-screen. The benchmark tests enable us to evaluate the performance

of grid-screens on variation of bubble characteristics and the resultant forces within the bubble plume. All measurements were repeated three times to ensure the repeatability of the tests and the averaged values were used for the analysis of the results. The overbars indicating the measurement uncertainties were also determined and were presented in the results section. The experimental parameters, bubble characteristics, and the associated non-dimensional parameters are listed in Table 1. In Table 1, u_b is the bubble velocity, d_b is the bubble diameter, and C_b is the bubble concentration. The variations of momentum and buoyancy fluxes along the vertical axis of the plume and hydrodynamic forces such as drag, added mass, and surface tension forces were calculated in a selected control volume and along with the vertical axes of bubble plumes.



Figure 4. 2: Images of the RBI instrumentation and bubbly plume: a) RBI optoelectronic unit; b) double-tip optical fiber probe; c) vertical bubble plume passing through a grid-

screen with $X_s = 0.14$ m from the nozzle. The air discharge in this image is $Q_a = 4$ L/min and screen opening is $d_s = 0.841$ mm.

Table 4. 1: Experimental parameters and bubble characteristics of vertically discharged bubble plumes passing through a grid-screen.

No.	Test Label	X_s (mm)	d_o (mm)	Q_a (L/min)	Sieve No/size		u_b (m/s)	d_a (mm)	C_b (%)	Re_o (x_{3-4}) $\times 10^4$
					No.	d_s (mm)				
1	BP1	0	1	4	-	-	0.855	8.94	3.98	-
2	BP2	0	1	6	-	-	0.96	10.57	4.74	-
3	BP3	0	1	8	-	-	1.085	10.4	9.05	-
4	BP4	0	3	4	-	-	0.76	9.22	3.67	-
5	BP-5	0	3	6	-	-	0.846	10.32	4.59	-
6	BP-6	0	3	8	-	-	1.12	13.64	5.85	-
7	BP1-14-16	14	1	4	16	2.38	0.734	7.63	4.02	34.0
8	BP1-22-16	22	1	4	16	2.38	0.68	7.56	3.27	34.0
9	BP1-30-16	30	1	4	16	2.38	0.66	7.43	2.89	34.0
10	BP2-14-16	14	1	6	16	2.38	0.797	7.68	5.46	76.4
11	BP2-22-16	22	1	6	16	2.38	0.73	7.24	4.37	76.4
12	BP2-30-16	30	1	6	16	2.38	0.698	7.26	4.19	76.4
13	BP3-14-16	14	1	8	16	2.38	0.812	7.9	6.1	135.9
14	BP3-22-16	22	1	8	16	2.38	0.76	7.65	5.4	135.9
15	BP3-30-16	30	1	8	16	2.38	0.725	7.55	5.1	135.9
16	BP4-14-16	14	3	4	16	2.38	0.688	6.82	3.94	3.8
17	BP4-22-16	22	3	4	16	2.38	0.65	6.9	3.38	3.8
18	BP4-30-16	30	3	4	16	2.38	0.62	6.8	3.36	3.8
19	BP5-14-16	14	3	6	16	2.38	0.769	7.36	5.24	8.5
20	BP5-22-16	22	3	6	16	2.38	0.727	7.12	4.63	8.5
21	BP5-30-16	30	3	6	16	2.38	0.67	6.86	4.1	8.5
22	BP5-30-16	14	3	8	16	2.38	0.79	0.766	5.9	15.1
23	BP6-14-16	22	3	8	16	2.38	0.756	7.54	5.33	15.1
24	BP6-22-16	30	3	8	16	2.38	0.714	0.72	5.12	15.1
25	BP1-14-20	14	1	4	20	0.841	0.676	7.42	2.64	34.0
26	BP1-22-20	22	1	4	20	0.841	0.61	7.22	1.96	34.0
27	BP1-30-20	30	1	4	20	0.841	0.54	6.45	1.64	34.0
28	BP2-14-20	14	1	6	20	0.841	0.78	7.57	4.49	76.4

29	BP2-22-20	22	1	6	20	0.841	0.73	7.56	3.99	76.4
30	BP2-30-20	30	1	6	20	0.841	0.65	7.03	3.24	76.4
31	BP3-14-20	14	1	8	20	0.841	0.89	7.63	7.01	135.9
32	BP3-22-20	22	1	8	20	0.841	0.86	7.86	7.24	135.9
33	BP3-30-20	30	1	8	20	0.841	0.78	7.34	6.34	135.9
34	BP4-14-20	14	3	4	20	0.841	0.73	7.22	3.7	3.8
35	BP4-22-20	22	3	4	20	0.841	0.58	6.65	1.86	3.8
36	BP4-30-20	30	3	4	20	0.841	0.5	5.96	1.54	3.8
37	BP5-14-20	14	3	6	20	0.841	0.81	7.67	5.03	8.5
38	BP5-22-20	22	3	6	20	0.841	0.67	6.99	3.42	8.5
39	BP5-30-20	30	3	6	20	0.841	0.62	6.84	3.22	8.5
40	BP6-14-20	14	3	8	20	0.841	0.89	8.16	6.48	15.1
41	BP6-22-20	22	3	8	20	0.841	0.77	7.65	5.38	15.1
42	BP6-30-20	30	3	8	20	0.841	0.67	7.96	5.34	15.1

4.3 Results and Discussion

4.3.1 Bubble characteristics

Snapshot images of bubbles before and after a grid-screen and at different distances from the nozzle are shown in Figure 4. 3. Figure 4. 3 shows the effect of grid-screen on the shape of bubble clusters, bubble size distribution, and spreading of bubbles along the vertical axes of the bubble plume. The left image in Figure 4. 3a shows a bubble plume without a grid-screen with an air discharge of 4 L/min (i.e., Test No.1) and the right image shows a bubble plume with a grid-screen (Test No.7). Figure 4. 3b shows the snapshot images along the vertical axes and at the centerline of the bubble plumes. A visual comparison between the images indicates that a grid-screen is able to reduce bubble size; however, it does not provide enough information on the effect of grid-screen on bubble velocity, which requires supporting data from the RBI probe measurements.

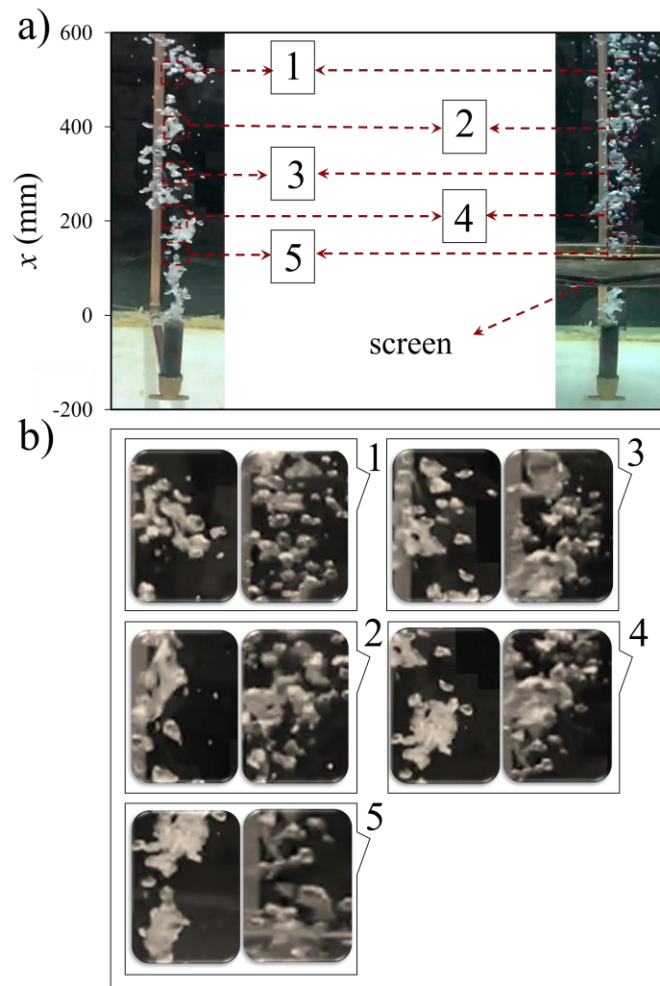


Figure 4. 3: Effect of grid-screen on the size and shape of bubbles after the screen: a) bubble plume without a grid-screen (Benchmark test, Test No.1, BP1); b) bubble plume with a grid-screen (Test No.7, BP1-14-16).

The variations of bubble velocity along the vertical axis in Test No.1 was compared with other experimental studies in the literature to test the performance of the bubble probe (see Figure 4. 4). The vertical variations of bubble velocity indicated that bubble velocity slightly decreases along the vertical distance from the nozzle. The reduction trend of bubble velocity along the vertical axes follows the trends of velocity from other studies in the literature and the main difference on the magnitude is due to the initial air discharge.

For instant, the air discharge in the study of Lima Neto et al., (2012), with a value of $Q_a = 1.5$ L/min, is much smaller than the minimum air discharge in the present study.

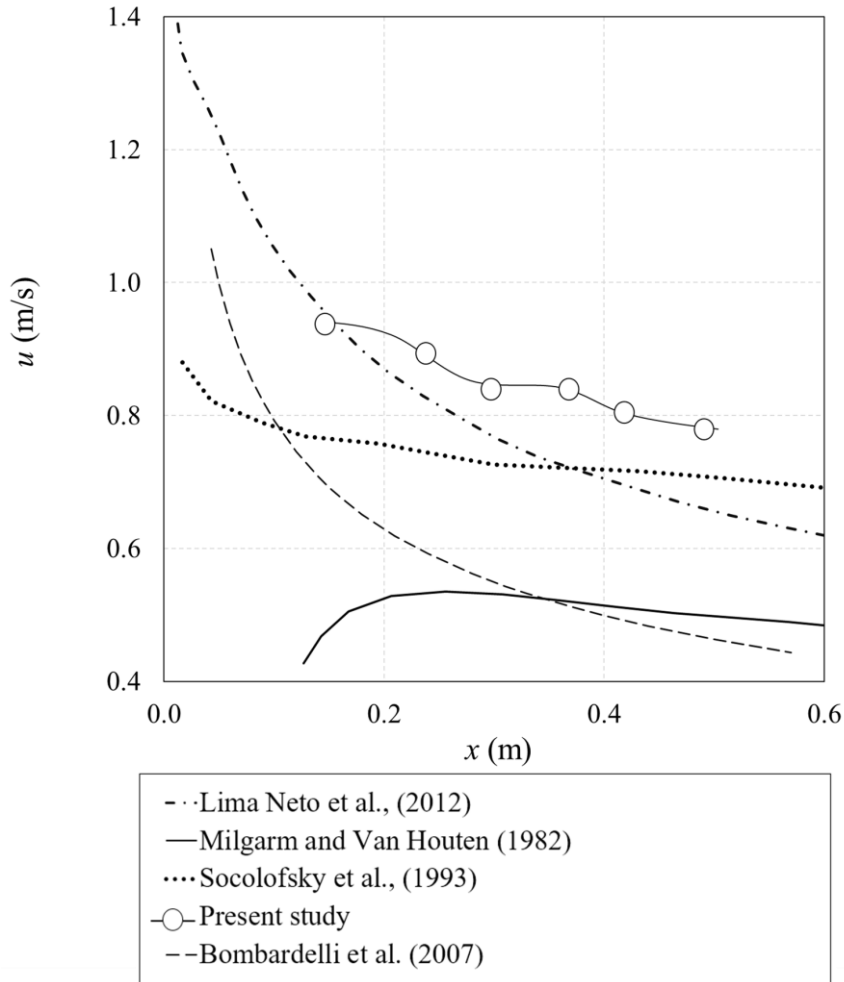


Figure 4. 4: Vertical variations of the centerline velocity of bubbles above the nozzle for $Q_a = 6$ L/min, $d_o = 1$ mm (Test No. 2, BP2) and other similar tests in the literature.

Bubble concentrations along the vertical axis of bubble plumes were measured with the RBI probe. Figure 4. 5 demonstrates the variations of bubble concentration along the vertical axis and at the centerline of the plumes with different nozzle size and air discharges. The left subplots in Figure 4. 5 show bubble concentration variations for $d_o = 1$ mm and the right subplots belong to bubble plumes issued from a nozzle with $d_o = 3$ mm.

Air discharges increase from the top row to the bottom row with the values of $Q_a = 4, 6$ and 8 L/min, respectively. As can be seen from Figure 4. 5, bubble concentration at the centerline of the plume decreases almost linearly with increasing the distance from the nozzle.

The proposed models by Kubasch (2001) and Lima Neto (2015) with air discharges of 4 L/min were also added in Figure 4.5b and 4.5d for comparison. As can be seen, in both proposed power law models, the power of correlation is close to unity (i.e., $C_b \sim x^{-1.15}$ and $x^{-1.25}$) indicating a nearly linear correlation between bubble concentration and distance from the nozzle. In all subplots, the values of bubble concentration passing through a grid-screen with a larger opening (i.e., $d_s = 0.831$ mm) become less than the tests with smaller openings. It can be deduced that bubble interactions with a fine grid-screen, decreases the centerline bubble concentration and the resulted small bubbles passing through fine grid-screen have less time to collide with the RBI probe; whereas large bubbles have more time to pass through the tips of the probe and this increases the exposed time of air bubbles and consequently higher air concentration. It was found that bubble concentration increases with increasing air discharge; however, air discharge does not significantly affect bubble concentration at the water surface due to bubble coalescence far from the nozzle. Furthermore, a comparison among the tests with different nozzle diameters indicates that the effect of nozzle diameter on the centerline bubble concentration is negligible.

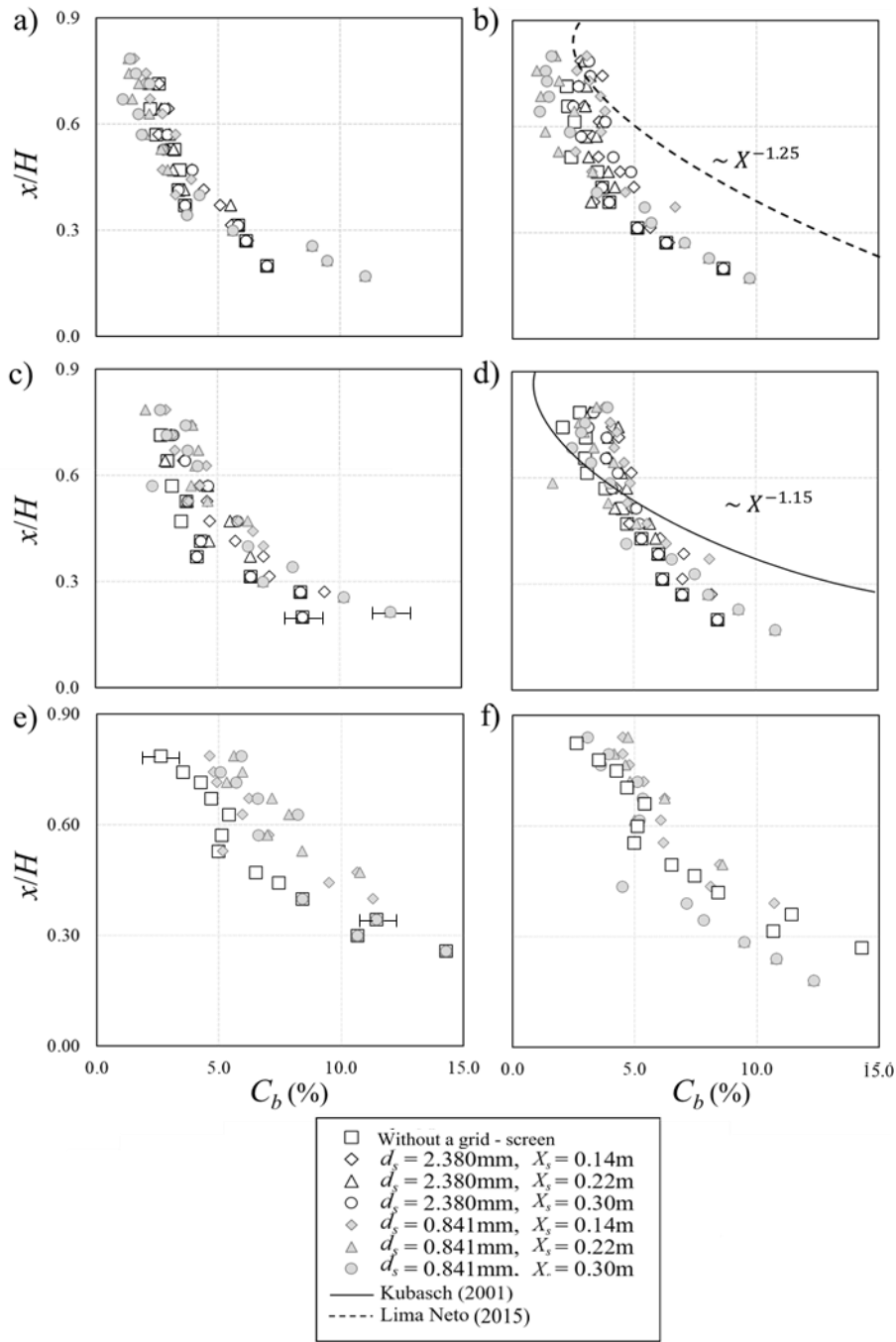


Figure 4. 5: Effect of air discharge on the vertical profile of bubble concentration in bubble plumes with different nozzle sizes, d_o , and grid-screen openings, d_s . The grid-screen was located at $X_s = 0.30$ m from the nozzle: a) $Q_a = 4$ L/min, $d_o = 1$ mm; b) $Q_a = 4$ L/min, $d_o = 3$ mm; c) $Q_a = 6$ L/min, $d_o = 1$ mm; d) $Q_a = 6$ L/min, $d_o = 3$ mm; e) $Q_a = 8$ L/min, $d_o = 1$ mm; f) $Q_a = 8$ L/min, $d_o = 3$ mm.

The times at which the probe's tip is in either air or water are detected by the optical probe and are called the gas and liquid times, respectively. Both gas and liquid times are the signature of bubble concentration and can be used to measure bubble velocity by employing the cross correlation between the two adjacent probes (see Figure 4. 2b). The effect of grid-screen on variations of gas and liquid times can be used to interpret the effectiveness of a grid-screen on oxygen transfer and mixing. Figure 4. 6 shows the time history of bubble velocity, gas and liquid times for both grid-screen with a screen size of $d_s = 2.38$ mm (i.e., Test No.7) and the benchmark test (i.e., Test No.1) with an air discharge of 4 L/min. The grid-screen was located at $X_s = 0.14$ m above the nozzle and the measurements were taken at $x = 0.40$ m (i.e., $x/d_o = 400$). The time-averaged velocities for tests with and without a grid-screen are 0.70 m/s and 0.79 m/s, respectively. A comparison between the two tests indicates that by installing a grid-screen above the nozzle, bubble velocity reduces by 13%. The Root-Mean-Square (RMS) values of bubble velocity for bubble plumes without a grid-screen and with a grid-screen at $X_s = 0.14$ m reduced from 0.113 m/s to 0.078 m/s, respectively. This indicates a reduction of 30% in the RMS of bubble velocity as a result of grid-screen installation. The average values of gas and liquid times were recorded for 180 seconds. The gas time for tests without and with a grid-screen are 7.25 s and 6.9 s, respectively. Accordingly, the averaged liquid times are 172.75 s and 173.1 s for tests with and without a grid screen, respectively.

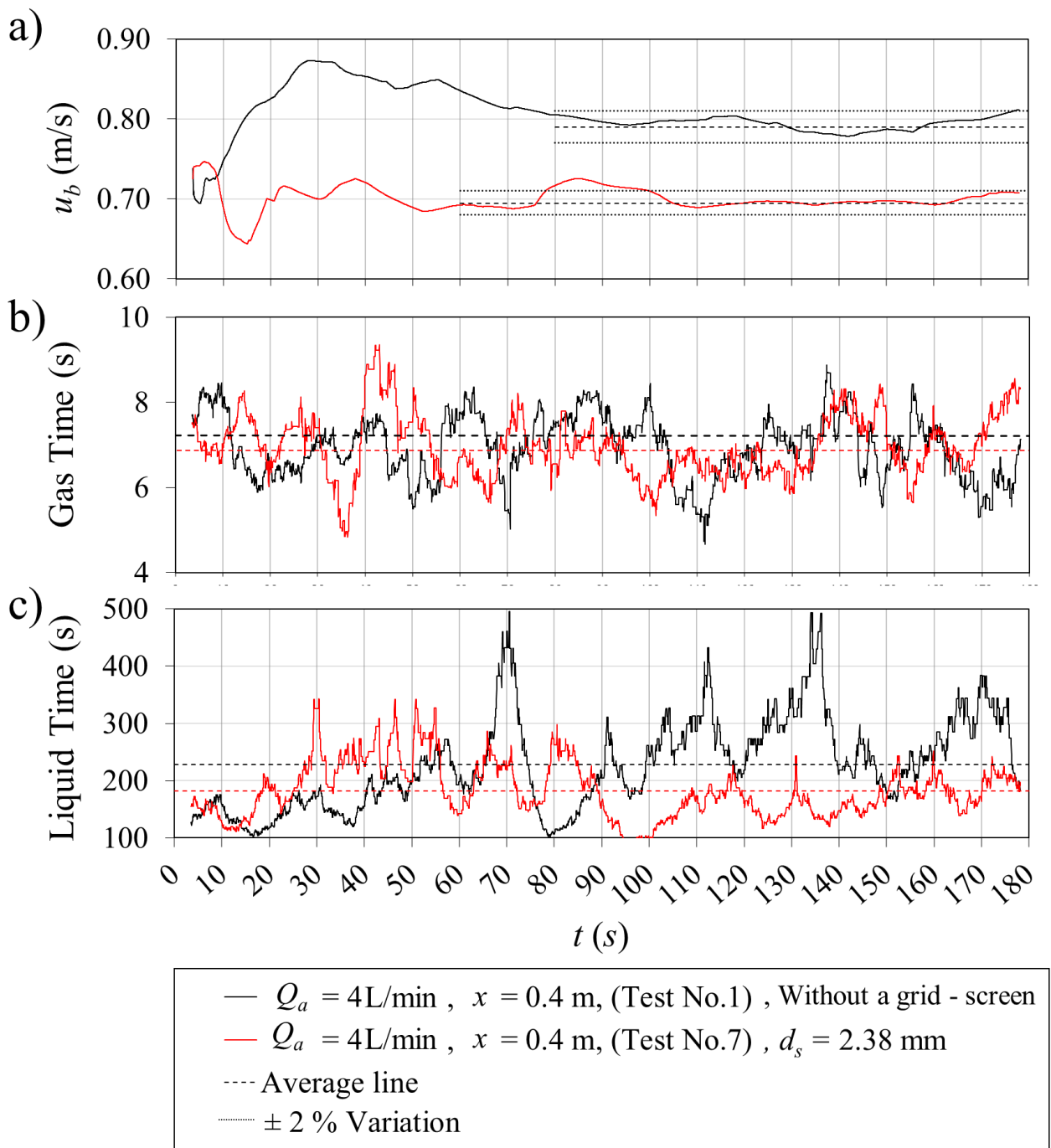


Figure 4. 6: Time history plots of bubble plume characteristics: a) bubble velocity; b) gas time; c) liquid time.

Figure 4. 7 shows the effects of grid-screen and its location from the nozzle on the vertical profile of the time averaged gas time, t_g . The data identified by solid circles

represent the vertical profile of gas time for the benchmark test (i.e., without a grid screen) and the open symbols show the gas time in bubble plumes with a grid-screen. The left sub-plots in Figure 4. 7 shows the experiments with $d_o = 1$ mm and the right plots are related to the experiments with $d_o = 3$ mm. Figure 4.7a and 4.7b show the gas time data for an air discharge 4 L/min and the air discharge is 8L/min in Figure 4.7c and 4.7d. Overall, the gas time at the centerline of the plume reduces by placing a grid-screen and the reduction is significant in high values of bubble Reynolds number, Re_b . This can be shown by comparing the results between Figure 4. 7a and 7d at which both nozzle diameter and air discharge is larger in Figure 4. 7d. Regardless of the bubble Reynolds number, the gas time significantly reduces as the grid-screen becomes close to the nozzle. This indicates that the bubbles spread throughout the screen and fewer bubbles pass through the RBI probe at the centerline of the plume. The effect of grid-screen on reducing the gas time decreases by increasing the nozzle diameter and this can be evaluated by comparing the left and right sub-plots.

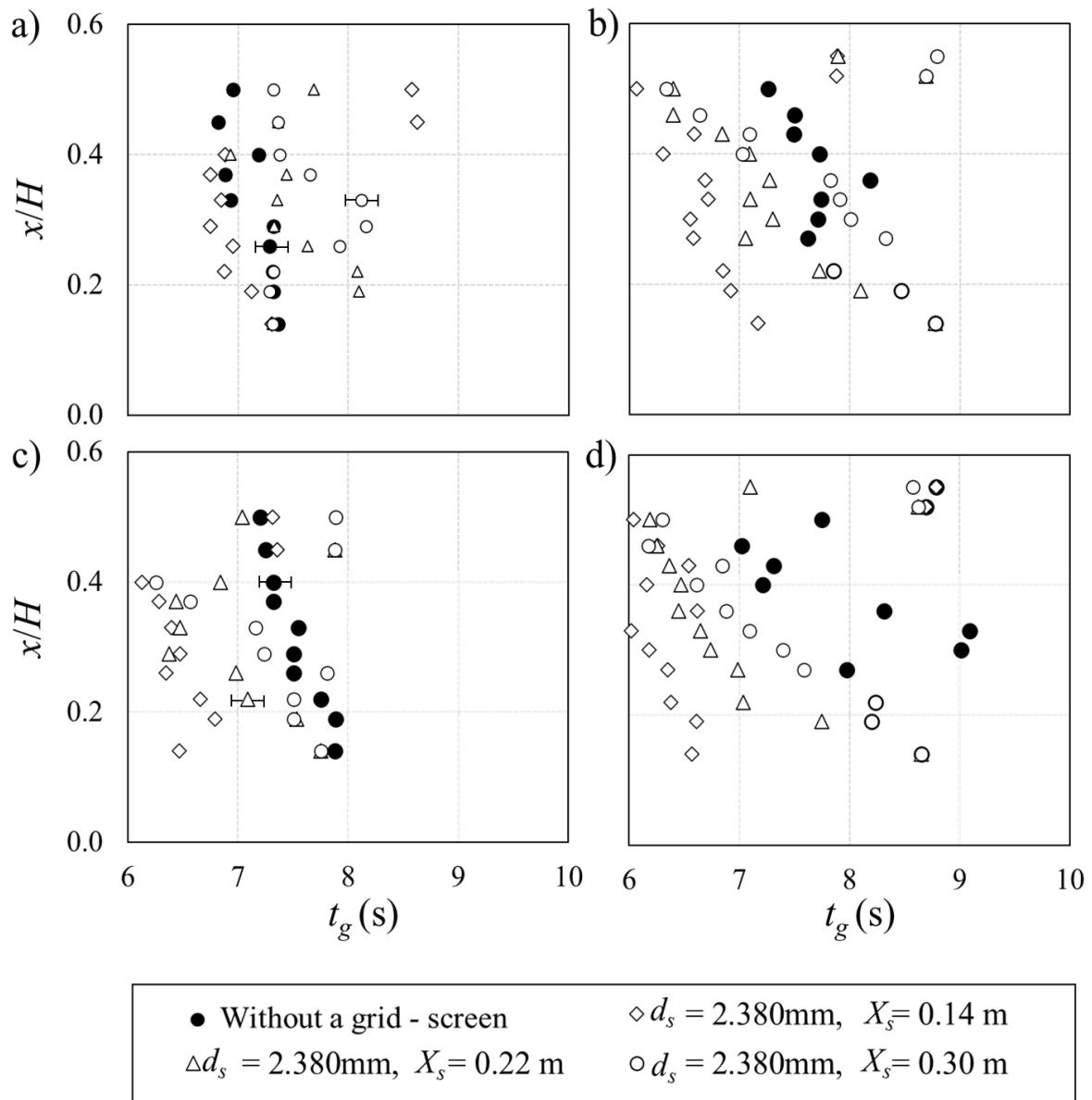
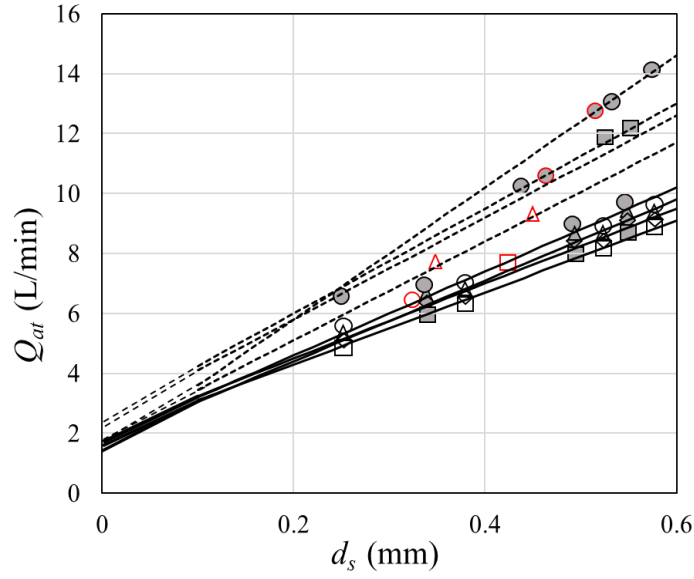


Figure 4. 7: Vertical profile of average gas time at different distances from the nozzle: a) $Q_a = 4\text{ L/min}$, $d_o = 1\text{ mm}$; b) $Q_a = 4\text{ L/min}$, $d_o = 3\text{ mm}$, $d_s = 2.38\text{ mm}$; c) $Q_a = 8\text{ L/min}$, $d_o = 1\text{ mm}$; d) $Q_a = 8\text{ L/min}$, $d_o = 3\text{ mm}$.

It is important to study the maximum capacity of grid-screens in passing air bubbles when the system is working with the full capacity. The over discharging air bubbles should be avoided as it may result in trapping air behind the grid-screen and

occurring bubble bypass. In order to determine the threshold air discharge, Q_{at} , and to define the full capacity of grid-screens, Q_a systematically increased in bubble plumes with a wide ranges of grid-screens and the effects of screen size, d_s , and the distance from the nozzle, X_s , on the threshold air discharge was examined for each test. It was observed that in the over discharge incidents, air is accumulated under the grid-screen until it by passes from the side of the adjusted screens. Figure 4. 8 shows the correlation between grid-screen size and the threshold air discharge, Q_{at} , for different nozzle diameter and distances from the nozzle. As can be seen, the theshold air discharge increases linearly with the screen size as $Q_{at} = a(d_s) + b$. The slope, a , and the intercept of correlations, b are listed in Table 2.



□ $X_s = 0.14 \text{ m}, d_o = 1 \text{ mm}$	-□- $X_s = 0.14 \text{ m}, d_o = 1 \text{ mm}$
◇ $X_s = 0.22 \text{ m}, d_o = 1 \text{ mm}$	-◇- $X_s = 0.22 \text{ m}, d_o = 1 \text{ mm}$
△ $X_s = 0.30 \text{ m}, d_o = 1 \text{ mm}$	-△- $X_s = 0.30 \text{ m}, d_o = 1 \text{ mm}$
○ $X_s = 0.38 \text{ m}, d_o = 1 \text{ mm}$	-○- $X_s = 0.38 \text{ m}, d_o = 1 \text{ mm}$
■ $X_s = 0.14 \text{ m}, d_o = 3 \text{ mm}$	-■- $X_s = 0.14 \text{ m}, d_o = 3 \text{ mm}$
◇ $X_s = 0.22 \text{ m}, d_o = 3 \text{ mm}$	-◇- $X_s = 0.22 \text{ m}, d_o = 3 \text{ mm}$
△ $X_s = 0.30 \text{ m}, d_o = 3 \text{ mm}$	-△- $X_s = 0.30 \text{ m}, d_o = 3 \text{ mm}$
○ $X_s = 0.38 \text{ m}, d_o = 3 \text{ mm}$	-○- $X_s = 0.38 \text{ m}, d_o = 3 \text{ mm}$

Figure 4. 8: variations of the threshold air discharge, Q_{at} , in bubble plumes with different grid-screen openings, d_s , and distances from the nozzle, X_s .

Table 4. 2: The values slope and intercept of the proposed equations for prediction of the threshold air discharge, Q_{at} .

Test No.	d_o (mm)	X_s (mm)	a	b
1	3	38	22	19
2	3	30	17.5	16.5
3	3	22	17	16
4	3	14	16.5	15
5	1	38	14	13
6	1	30	13.5	12.5

7	1	22	12.5	12
8	1	14	12	11.5

4.3.2 Momentum equation and force balance

The motion of air bubbles in bubble plumes is described by the momentum equations for both gas (i.e., air) and liquid (i.e., water) phases. The rate of change of momentum of bubbles in a control volume is determined by the balance between the resultant forces. Figure 4.9 shows a schematic sketch of a control volume with the contributed forces at the vicinity of a grid screen. The hydrodynamic forces such as buoyancy, drag, added mass, and surface tension are acting on bubble clusters and the net force acting on the grid-screen is determined from the balance between the forces. The net acting force per unit area of a grid-screen is needed to design the support structure for installation of a grid-screen. The force balance can be formulated by assuming the acting forces are positive and the resistive forces are negative. The force balance has been developed for spherical bubbles in the past (Sridhar and Katz, 1995; Ford and Loth, 1998; Pan et al. 2021) and for a control volume at the vicinity of a grid screen is expressed as:

$$\sum F = 0 \rightarrow F_s = F_B - F_D - F_\delta - F_{Am} - F_M \quad (4.1)$$

where the F_s is the net force on the grid-screen, F_B is the buoyancy force, F_D is the drag force, F_δ is the surface tension force, F_{Am} is the added mass force, and F_M is the equivalent force due to the momentum imbalance before and after the grid-screen and it is expressed as:

$$F_M = \rho_a V_{x(i+1)}^2 A_{(i+1)} - \rho_a V_{x(i)}^2 A_{(i)} \quad (4.2)$$

where the A is the cross sectional area of the bubbles at the boundaries of the control volume (i.e., control surfaces) before (i) and after ($i+1$) the grid-screen, V_x is the time-averaged velocity of bubbles at a certain distance from the nozzle, and ρ_a is the density of air. The buoyancy force in a control volume, F_B , is expressed as:

$$F_B = \frac{4}{3}(\rho_w - \rho_a)g\pi\left(\frac{d_b}{2}\right)^3 \quad (4.3)$$

where g is the gravitational acceleration and ρ_w is the density of water. The drag force, F_D , in a control volume is expressed as:

$$F_D = \frac{1}{2}C_D\rho_w V_x^2 A \quad (4.4)$$

where C_D is the drag coefficient and it is correlated with the shape of bubble and bubble velocity. Many semi-theoretical and empirical models have been introduced to formulate the variations of drag coefficient with the Reynolds number (Clift et al., 1978; Ford and Loth, 1998; Moghadaripour et al., 2017). The classic expression for variations of drag coefficient is introduced by Clift et al. (1978) as:

$$C_D = \left[\frac{24}{Re_b}\right] [1 + 0.1Re_b^{3/4}] \quad (4.5)$$

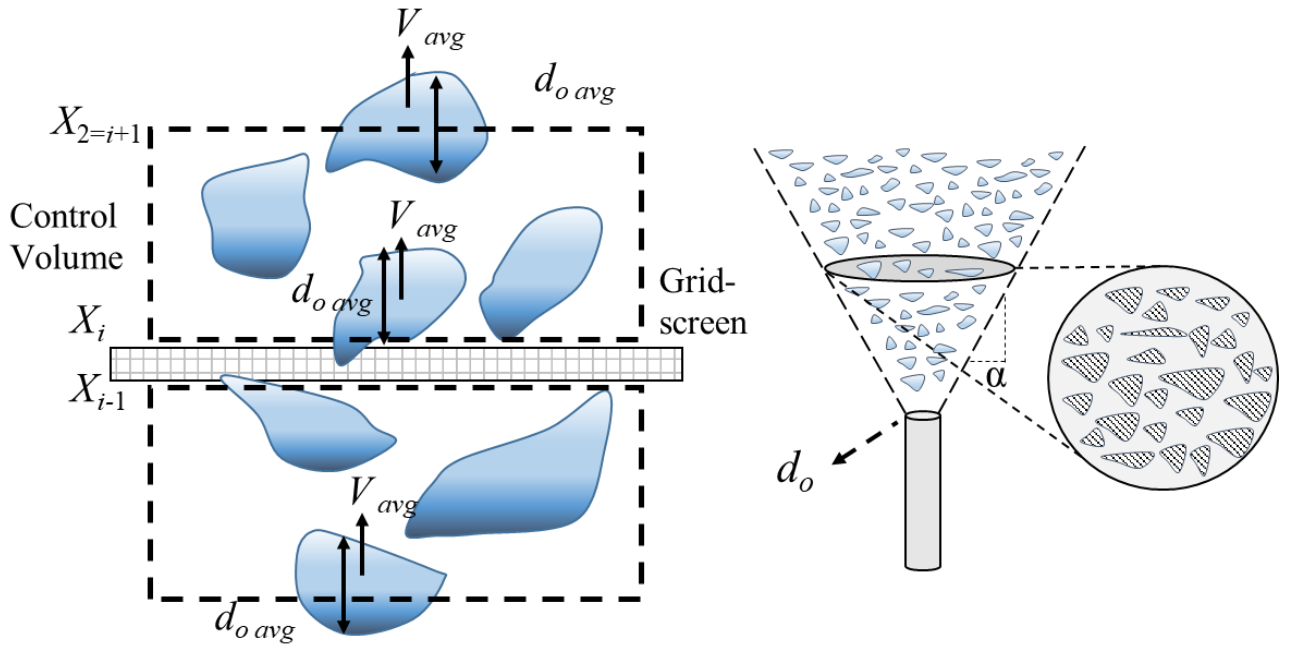


Figure 4. 9: Schematic sketch of control volume in a bubble plume passing through a grid-screen to determine forces acting on the grid-screen.

Figure 4. 10 shows the variations of drag coefficient, C_D , with the bubble Reynolds number, Re_b , and a comparison between the other proposed models in the literature. As can be seen, for the range of bubble Reynolds numbers between 1 and 49, the drag coefficient decreases by 84 %. The slope of correlation also increases as the bubble Reynolds number increases and the same slope is observed in the proposed models of Ford and Loth (1998) for bubbly flows and Moghadaripour et al. (2017) for solid-liquid particle clouds indicating that the variations of drag coefficient is similar in gas-liquid and solid-liquid phases.

The surface tension force, F_σ , is determined based on the surface tension of air bubbles in breaking to smaller bubbles as they pass through a grid screen and is considered as a resistive force. The surface tension force is expressed as:

$$F_\delta = \delta L \tag{4.6}$$

where L is the length of wires in a grid-screen per unit area $L = \pi d_b^2/16d_s^2$ and σ is the surface tension coefficient of air-water interface with a value of $72 \times 10^{-3} \text{ Nm}^{-1}$. A portion of momentum in the gas phase is transferred to the ambient water by moving the water around each individual bubble. The amount of water moving along with the bubbles is quantified by the added mass force, F_{Am} , and is expressed as:

$$F_{Am} = \frac{1}{2} C_{Am} \rho_w V_x^2 A \quad (4.7)$$

where the C_{Am} is the added mass coefficient with a recommended value of 0.5 for air bubbles in water (Duan et al., 2018).

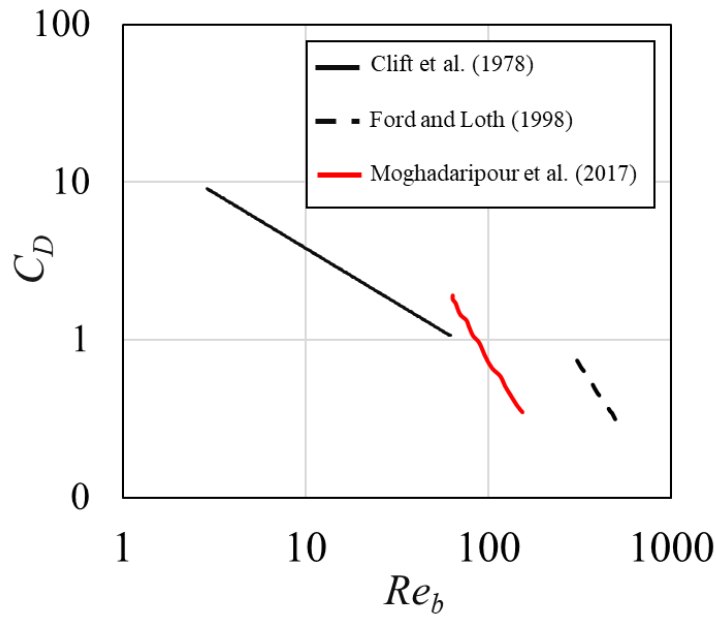


Figure 4. 10: A comparison on variations of drag coefficient used for bubble plumes, C_D , with bubble Reynolds number, Re_b , with other models.

The vertical profiles of the acting and resisting forces on a control volume before and after the grid-screen was calculated using the values of bubble size, concentration, and

velocity along the axis of bubble plume. The effects of screen size, d_s , and the distance between grid-screen and nozzle, X_s , on the contributing forces were examined. Figure 4. 11 shows the vertical variation of buoyancy force, F_B , along the vertical axis of bubble plume with and without a grid-screen. The horizontal lines in Figure 4. 11 show the location of the grid-screens in different experiments. The results of bubble plumes without a grid-screen are also shown by solid circular symbols and those data are used as benchmark to examine the effect of grid-screen on the vertical variations of buoyancy force. As can be seen in Figure 4. 11, the installation of grid-screen decreases the buoyancy force after the grid-screen and the effect of grid-screen on reduction of buoyancy force increases with increasing the air discharge. Figure 4. 11 clearly shows that the grid-screen reduces the magnitude of buoyancy force, especially right after the grid-screen, which is due to the sudden reduction of bubble size after the grid-screen. In benchmark experiments, the buoyancy force decreases almost linearly with the non-dimensional distance from the nozzle, x/H , whereas such variations are almost unchanged in bubble plumes with a grid-screen. The presented results in Figure 4. 11 indicates a marginal change of the buoyancy force due to the variations of grid-screen size so the vertical variation of the buoyancy force is independent of the grid-screen size in the range of $0.841 \text{ mm} \leq d_s \leq 2.38 \text{ mm}$.

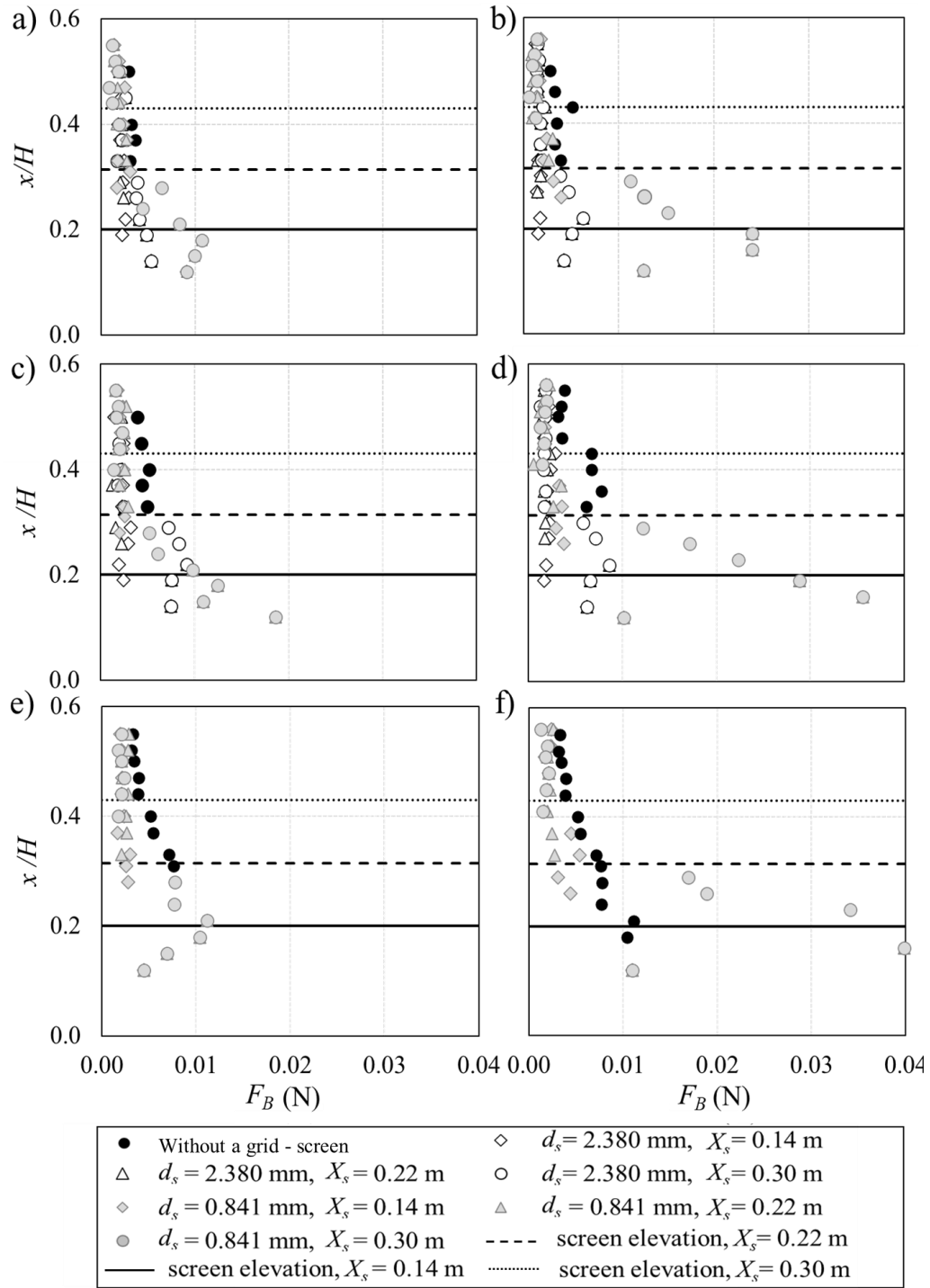


Figure 4. 11: Effect of grid-screen on the vertical profile of buoyancy force, F_B , at different distances from the nozzle: a) $Q_a = 4$ L/min, $d_o = 1$ mm; b) $Q_a = 4$ L/min, $d_o = 3$ mm; c) $Q_a = 6$ L/min, $d_o = 1$ mm; d) $Q_a = 6$ L/min, $d_o = 3$ mm; e) $Q_a = 8$ L/min, $d_o = 1$ mm; f) $Q_a = 8$ L/min, $d_o = 3$ mm.

Figure 4. 12 shows the effect of grid-screen size and its location on the vertical variations of drag force, F_D , in bubble plumes with different nozzle sizes and air discharges. The variations of drag force is due to the combination effects of the bubble size (i.e., bubble cross-sectional area) and bubble velocity (see Eq. (4.4)) variations. Similar to the vertical variations of the buoyancy force, a grid-screen significantly reduces the drag force by reducing the bubble size and velocity. The vertical variations of bubble size and velocity in bubble plumes without a grid-screen confirm the results (Behzadipour et al., 2023). In general, the addition of a grid-screen reduces the drag force by 18%, 31%, and 53% for $Q_a = 4, 6, \text{ and } 8 \text{ L/min}$, respectively. The vertical variations of drag force in bubble plumes without a grid-screen show a linear relationship with x/H ; however, the values of drag force after the grid-screen are almost constant with x/H . Similar to the effect of grid-screen on buoyancy force, the deviation between drag force with and without a grid-screen increases with the air discharge.

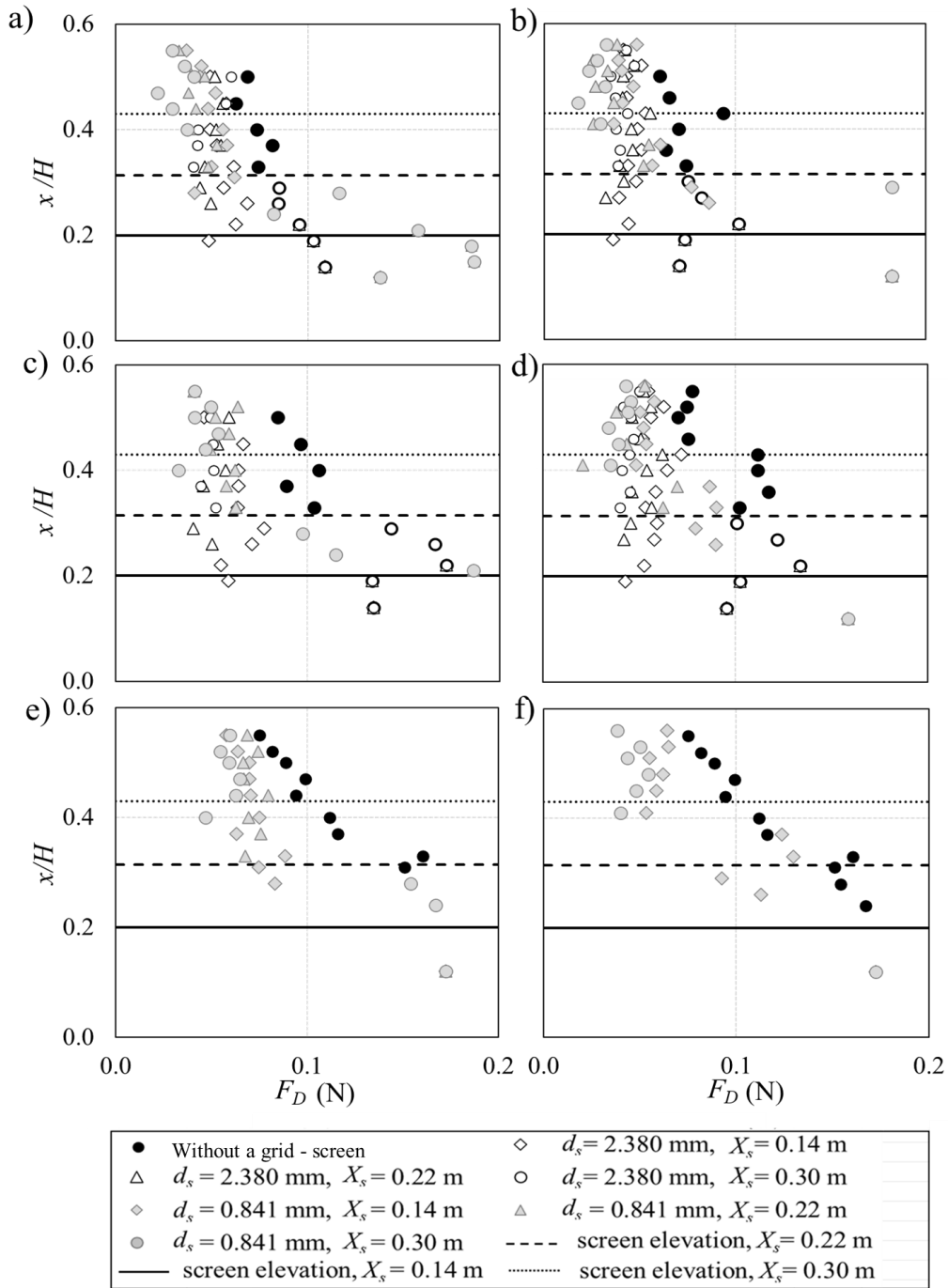


Figure 4.12: Effect of grid-screen on the vertical profile of drag force, F_D , at different distances from the nozzle: a) $Q_a = 4$ L/min, $d_o = 1$ mm; b) $Q_a = 4$ L/min, $d_o = 3$ mm; c) $Q_a = 6$ L/min, $d_o = 1$ mm; d) $Q_a = 6$ L/min, $d_o = 3$ mm; e) $Q_a = 8$ L/min, $d_o = 1$ mm; f) $Q_a = 8$ L/min, $d_o = 3$ mm.

The added mass, buoyancy, and drag forces were calculated for all experimental tests and the variations of the contributing forces with bubble Reynolds number are shown in Figure 4. 13. Figure 4. 13a shows the variation of added mass force with Re_b indicating that the experimental parameters have no significant effect on variations of added mass force with Re_b . Whereas the data scatter in variations of buoyancy force indicates that the effects of controlling parameters in variations of F_B with Re_b are not negligible (see Figure 4. 13b). Similar to the added mass force, the variations of drag force with bubble Reynolds number is independent of other controlling parameters. Empirical formulas are proposed to model the correlations of the contributing forces with Re_b as:

$$F_{Am} = 0.0001Re_b^2 \quad (4.8a)$$

$$F_B = 0.0001Re_b^{1.53} \quad (4.8b)$$

$$F_D = 0.004Re_b^{1.22} \quad (4.8c)$$

The coefficients of determination of the above equations are 0.95, 0.89, and 0.90, respectively.

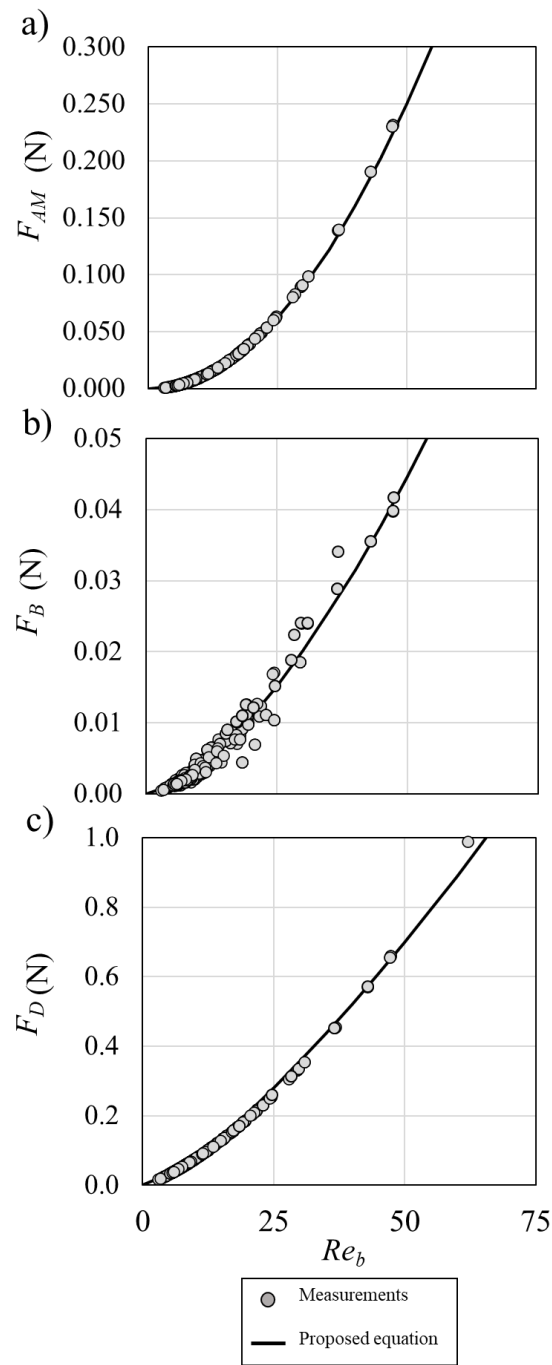


Figure 4. 13: Variations of forces after the grid-screen versus Reynolds number: a) added mass force, F_{AM} ; b) buoyancy force, F_B ; c) drag force, F_D .

Bubble Reynolds number has a direct relationship with bubble velocity and inversely related to bubble diameter. On the other hand, increasing airflow discharge increases bubble velocity and grid-screen decreases the mean bubble diameter. By increasing air discharge, more bubbles interact with the grid-screen, which increases the contact length between bubbles and grid-screen and as a result the surface tension force increases. The surface tension force was calculated (see Eq. (4.6)) and the variations of the surface tension force as a result of measurement uncertainties are shown as overbars in Figure 4. 14. As can be seen, the surface tension forces acting on a grid-screen vary linearly with bubble Reynolds number, Re_b , and the slope of variations is also controlled by Re_b . In relatively small range of bubble Reynolds number, $10 < Re_b < 20$, the slope of correlation is 6% and in relatively large range of bubble Reynolds number, $20 \leq Re_b < 50$, the slope of correlation increases by four times and reached to 24%. Some discrepancies in variations of F_σ with Re_b in the transient region indicating the effect of measurement uncertainties and other parameters may also affect the correlation between F_σ and Re_b which requires more attention.

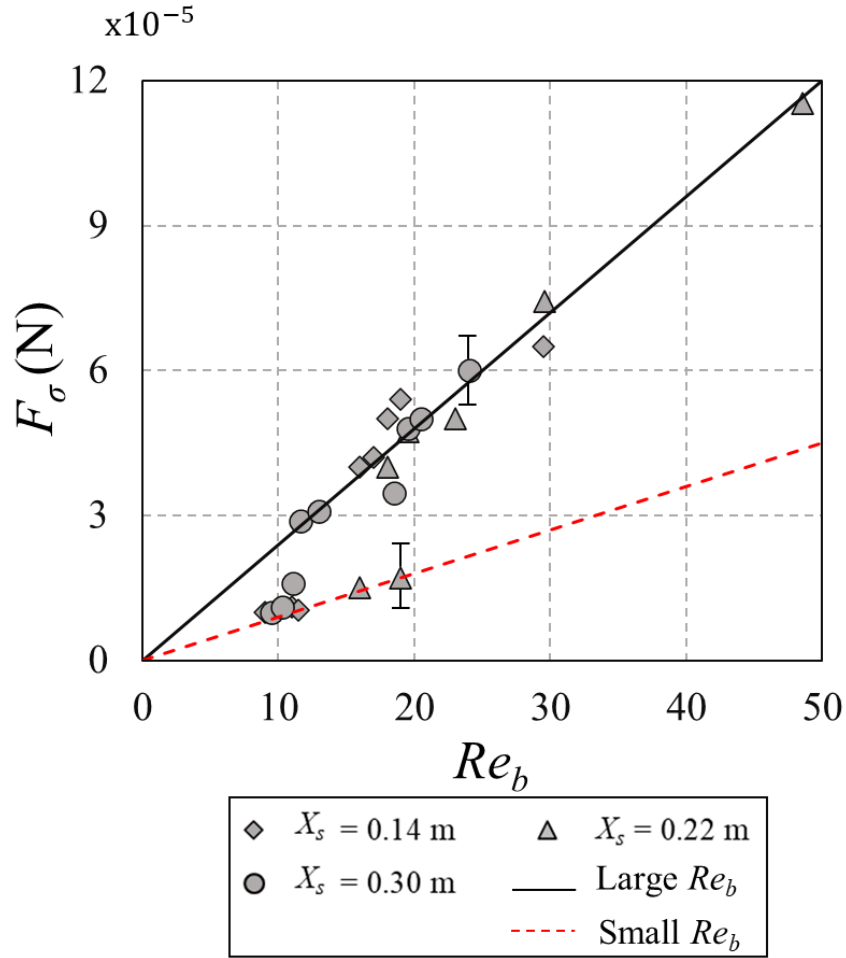


Figure 4. 14: Variation of surface tension force, F_σ , versus bubble Reynolds number in bubble plumes with a grid-screen at different distances from the nozzle.

To design the supports of the grid-screen, the resultant hydrodynamic forces acting on the grid-screen should be calculated by implementing the force balance (see Eq. (4.1)). Figure 4. 15 shows the variation of the net acting force with the bubble Reynolds number and a non-linear correlation was found between the resultant force and bubble Reynolds number as:

$$F_s = 0.002 Re_b^2 + 0.0069 Re_b - 0.0093 \quad (4.9)$$

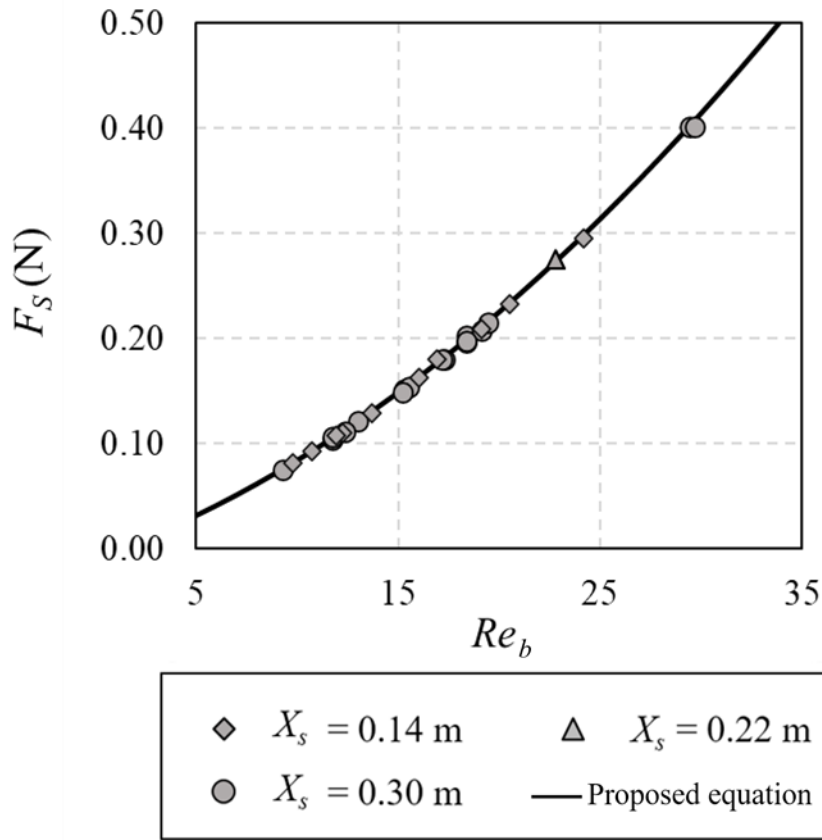


Figure 4. 15: Variation of the net acting force on the grid-screen, F_s , with Reynolds number in bubble plumes with a grid-screen and at different distances from the nozzle.

4.4 Conclusions

A series of laboratory experiments were conducted to study the effects of grid-screen and initial plume characteristics on the hydrodynamic forces acting on bubble plume and grid-screen. Three air discharges of 4, 6, and 8 L/min with two nozzle diameters of $d_o = 1$ mm and 3 mm were tested to form a wide range of bubble Reynolds numbers ranged between 10 and 50.

The effects of grid-screen size and its position respect to the nozzle on the primary parameters of bubble plume such as bubble concentration and velocity were evaluated. An

inverse correlation was found between grid-screen size and centerline bubble concentration while the centerline bubble concentration increased with increasing air discharge. The direct correlation between bubble concentration and air discharge diminished at the water surface due to bubble coalescence far from the grid-screen. It was found that the effect of nozzle size on bubble concentration is negligible. The measurements on the time averaged bubble velocity and velocity fluctuations at $x/d_o = 400$ indicated that the grid-screen a bubble plume with $Q_a = 4$ L/min and $d_s = 2.38$ mm reduced bubble velocity and the RMS of bubble velocity by 13% and 30%, respectively.

The threshold air discharge was measured for a wide range of grid-screen sizes and a series of linear correlations were proposed to estimate the threshold air discharge for different screen sizes and their locations from the nozzle. Such information are useful for proper design of bubble plums with a grid-screen and to avoid over discharging air into the system.

The acting and resisting forces on the motion of air bubbles were calculated and the net acting force on the grid-screen was calculated using the force imbalance. The effects of controlling parameters such as air discharge, nozzle diameter, grid-screen size and its location on the vertical profile of buoyancy and drag forces were examined. The buoyancy force significantly reduced due to installation of a grid-screen and such reduction increased with increasing air discharge. Although the buoyancy force reduced almost linearly in bubble plumes, the suddenly reduced buoyancy force in bubble plumes after a grid-screen remained constant over a larger distance from the nozzle. Experimental observations have shown the sudden drop in bubble size and velocity after the grid-screen. Similar to the buoyancy force, a grid-screen significantly reduced the drag force along the

vertical axis of the plume. The drag force reduction was found to be correlated with the air discharge and it reduced by 18%, 31%, and 53% for $Q_a = 4, 6,$ and 8 L/min , respectively.

The variations of drag and added mass forces with bubble Reynolds number were independent of other controlling parameters and varied non-linearly with Re_b . The surface tension forces acting on a grid-screen varied linearly with bubble Reynolds number, Re_b , and the slope of variations is also controlled by Re_b . The correlation between surface tension force and Re_b increased by four times in the range of $20 \leq Re_b < 50$. The correlation between bubble Reynolds number and the net acting force was defined and an empirical correlation was proposed for proper design of grid-screens.

Notations

The following symbols are used in this paper:

A = cross sectional area; m^2

C_b = bubble concentration, vol/vol;

d_b = Bubble diameter size; mm

d_o = Nozzle diameter size; mm

d_s = Grid screen diameter size; mm

H = Height of water, m;

h_n = nozzle height; m

L = length of the tank; m

Q_a = Volumetric air flow rates; m^3/s

Re_b = bubble Reynolds number;

t = time; s

u_b = Bubble velocity; m/s

u_o = Initial bubble velocity; m/s

x = Elevation of measured point; m

X_s = Elevation of grid-screen; m

Δ = Variation;

Subscribes

a = air;

ave = average;

b = bubble;

i = index;

o = nozzle;

s = grid-screen;

Chapter 5

Effect of bed sand on bubble plume configuration

5.1 Introduction

Aeration through vertically discharged bubble plumes is an essential component of mixing and water quality improvement in reservoir destratification, water and wastewater treatment plants, and mineral operations in mining industries. Bubble dynamics in bubble plumes plays a crucial role in enhancing oxygen transfer and air mixing in tailing ponds, lakes, rivers, and natural streams (Wüest et al., 1992; Simiano et al., 2006; Funaki et al., 2009; Paerl and Otten, 2013). The key factors that motivate industries to choose air injection mechanism over mechanical air mixing are the affordability of construction, simplicity of design, and reasonable operation costs (Pacheco and Lima Neto, 2017; Lima and Lima Neto, 2018). Over the past twenty years, researchers have shown more interest in understanding bubble formation by air injection in water in order to improve oxygen transfer efficiency, enhancing Dissolved Oxygen (DO) level and water quality (McGinnis et al., 2006; Weber et al., 2014; Wang et al., 2016a). Schladow (1992) studied the applications of bubble plumes on oxygenation of sewage in wastewater treatment plants. In a relatively deep water column of $H = 300$ m, the centerline bubble velocity was measured and it decreased from the nozzle to 18 m from the nozzle (i.e., $x/H = 0.06$) and it became constant afterwards. A linear relationship was reported between plume width and height from the nozzle to $x/H = 0.06$.

The efficacy of oxygen transfer has been a critical design factor in examining bubble plume characteristics. Oxygen transfer from bubbles to the ambient water depends on the motion of local bubbles, bubble velocity fluctuations, and residence time (Niida and

Watanabe, 2018). Niida and Watanabe (2018), examined the explicit effects of bubble size on bubble plume features and concentration of Dissolved Oxygen (DO), and proposed an empirical gas transfer model based on image analysis. The employed image analysis technique was only applicable to relatively large deformable bubbles (i.e., $d_b > 4$ mm).

Stratified flow is formed in relatively large lakes due to water temperature differences between the deep and surface water layers. Stratification occurs normally in deep lakes and the presence of freshwater river flow on the top of saline lake in estuaries (Schladow and Fisher, 1995). In the summer months, water is stratified by forming layers of water with different temperatures. The surface water has the highest temperature and the temperature linearly decreases with the water depth. Artificial destratification is achieved by mixing stratified layers to form uniform temperature over the depth of lakes and reservoirs. In addition, destratification reduces evaporation by bringing cold water from the lower layers to the surface of the lakes. Air injection in form of bubble plume can destratifies the cold hypolimnion layer as bubbles rise to the water surface and passing through different thermal layers. The air injection in bubble plumes has been used for water quality applications and has been observed to be one of the most cost effective, appropriate, and viable solutions for artificial destratification. The application of vertically discharged bubble plumes on destratification of lakes and reservoirs have been investigated by many researchers (Lima Neto et al., 2016; Mobley et al., 2019; Waterhouse et al., 2021).

Mobley et al. (2019) studied the effects of a hypolimnetic oxygenation system by employing a bubble plume line diffuser in a water column, which is used in the operation of water treatment plants. If the oxygenation system is designed, monitored, and operated

properly, diffusers successfully spread bubbles and improve the dissolved oxygen level below the hypolimnion and over the sediment bed, while preserving thermal stratification. It was reported that diffuser technology is able to (1) increase the DO level and spread bubbles laterally and longitudinally throughout the hypolimnion layer and, (2) maintain the elevated DO level throughout the hypolimnion layer during successive years of operation.

Bubble plumes are produced when gas (i.e., air/oxygen) is injected in a liquid domain (i.e., water) from either a single circular nozzle or porous diffusers, which can affect the shape, size, and initial velocity of bubbles in bubble plumes. Many parameters control the motion and properties of bubbles in bubble plumes, such as nozzle shape, diameter, initial discharge condition, and the relative densities of gas and liquid phases. Many experimental studies have been carried out to investigate the effects of nozzle configuration on the bubble properties in vertically discharged bubble plumes (Rosso and Stenstrom, 2006; Lima Neto et al., 2008a; Lima Neto, 2012; Laupsien et al., 2017; Lai and Socolofsky, 2019; Liu et al., 2019; Chen, 2019).

Effects of different nozzle types on the centerline bubble velocity and mean bubble diameter were experimentally studied by Lima Neto et al. (2008a). A single and multiple circular nozzles were tested and the results were compared with a porous airstone. It was found that the initial nozzle configuration has negligible effect on variations of the centerline bubble velocity. However, the bubble mean diameter decreased by approximately 50% using the porous airstone instead of a single circular nozzle. The impact of different diffusers, including single- and multiple-nozzles on jet aeration systems was experimentally studied by Lima and Lima Neto (2018). They used four different setups for initial geometry condition: Nozzle A, with one opening and nozzle diameter of

$d_o = 30$ mm; Nozzle B, with one opening and $d_o = 10$ mm; Nozzle C, with four openings and $d_o = 5$ mm; and Nozzle D, with eight openings and $d_o = 3.5$ mm. Their results revealed that reducing nozzle diameter or increasing the number of nozzles, reduced bubble diameter by approximately 26%. With the same initial momentum and buoyancy fluxes, the oxygen transfer efficiency increased by approximately three times when multiple nozzles were replaced by a single nozzle of having the same total cross-sectional area.

Recent experimental studies have shown the effects of Physical Bubble Reducers (PBRs) such as mesh wire and grid-screen on bubble plume characteristics (Jain et al., 2013, 2014; Sujatha, 2015; Behzadipour et al., 2022a, 2022b, 2023). The performance of Micro Structured Bubble Column (MSBC) on bubble dynamics was investigated numerically by Jain et al. (2013). The results of the validated numerical model to simulate MSBC system indicated that wire meshing could cut the bubbles, increases the interfacial area of bubbles, and enhances the interface dynamics. A comparison between one and two layers of mesh with the benchmark tests (i.e., bubbles in a tank without a mesh) indicated that bubble size decreased by 22.7% and 29.7%, gas hold up increased by 5.7% and 9.7%, and interfacial area increased by 34.8% and 43.5%, respectively.

Different configurations in bubbly flow were achieved by injecting bubbles through the wire mesh and visual observations were made for different types of bubbly jets (Sujatha, 2015). Three different regimes were observed in bubbly flows and were named as: (1) bubble cutting, (2) bubble cutting followed by re-coalescence, and (3) gas pocket formation regimes. Laboratory experiments were employed to investigate the effects of nozzle size and air discharge on variations of mean bubble diameter, bubble concentration,

and bubble velocity in vertically discharged bubble plumes with and without a grid-screen (Behzadipour et al., 2022a; 2022b). Their results have shown more uniform air bubbles and found that the mean bubble diameter decreased by 34% as air discharge increased from 4 L/min to 8 L/min. It was shown that the average bubble size after the grid-screen with $d_s = 2.38$ mm was 7.5 mm and it decreased to 5 mm as the screen's openings decreased from 2.38 mm to 0.84 mm. Also, at $x/d_o = 550$, the average bubble size decreased by 32% as grid-screen size, d_s , reduced from 2.38 mm to 0.84 mm.

The present study is motivated by the effect of Physical Bubble Reducers (PBRs) such as porous air-stone nozzles, wire meshing, and grid-screens in reducing bubble size and increasing the contact area between air and water in vertically discharged buoyancy-driven bubble plumes. The larger surface contact between air bubbles and water enhances the oxygen transfer between air and water. Recent investigations have shown that the physical bubble cutters (i.e., PBRs) are efficient in enhancing the oxygen transfer rate (Jain et al., 2013; Sujatha, 2015; Behzadipour et al., 2022a). Most of the physical intervention designs such as mesh wiring and grid-screen are not sustainable and require frequent monitoring and maintenance. A sustainable approach to improve oxygen transfer rate while reducing the operation and maintenance costs is the use of natural sand beds as a natural layer that works similar to a Physical Bubble Reducers (PBRs). In this chapter, sand beds with different grain sizes are introduced to reduce bubble diameter and improve oxygen transfer as an example of sustainable and cost effective approach. The proposed PBR design including the bed grain size and the thickness of the bed layer are design in a way to minimize the head losses and clogging of sediment layer over time to optimize the frequency and cost of operation and maintenance.

5.2 Experimental setup

A series of laboratory experiments was conducted in the Multiphase Flow Research Laboratory (MFRL) at Lakehead University, Canada, to investigate the efficiency of the new sustainable design of the Physical Bubble Reducers (PBRs) in improving oxygen transfer rate and dissolved oxygen level in lakes, manmade industrial reservoir, and natural water ponds. Figure 5.1 shows the schematic sketch of a glass-walled experimental tank of 1.60 m long, 0.85 m wide, and 0.80 m high. In order to inject air through the ambient water, a pipe with 3 mm interior diameter was installed at the bottom of experimental tank. The bottom of the tank is made of galvanize plate which is strong enough to hold the weight of the water and sand bed layer. The water temperature within the tank was kept constant at $20^{\circ}\text{C} \pm 1^{\circ}\text{C}$ and the water depth was kept constant at $H = 0.70$ m. An air compressor was employed to control the required air pressure at the vicinity of $P = 60$ psi. Different air discharges of $Q_a = 3$ L/min, 6 L/min, 9 L/min, and 12 L/min were selected to test the effect of air discharge on the dynamics of bubbles in vertically discharged bubble plume. Air discharges were regulated and measured by an accurate rotameter (LZM series Zyia OEM, Zhejiang, China), which had an accuracy of $\pm 4\%$ of the maximum discharge. A circular nozzle with a diameter of $d_o = 3$ mm was selected to form bubble plume.

An optoelectronic unit (ISO Lite Software, RBI Optical probe, France) was utilized to accurately measure bubble properties at different distances from the nozzle. The RBI probe has been employed in number of studies to measure different bubble properties (Rensen and Roig, 2001; Boes and Hager, 2003; Kiambi et al., 2003; Chaumat et al., 2005; and Murzyn et al., 2005). Figure 5.1 shows the details of experimental set up such as:

nozzle configuration, optoelectronic unit, and the rotameter for measuring air discharge. The optoelectronic unit with the probe's tip is able to accurately measure bubble diameter, bubble size distribution, bubble concentration, and bubble velocity. The probe consists of two sapphire crystals, each 15 mm long and are placed 2.5 mm apart (see Figure 5.1). The probe is precisely submerged in water and bubble properties were measured based on light refraction detected by the probe's diodes. The emitted light is refracted when the probe's tip is in the water and is reflected in the module when the probe's tip is in the air (i.e., inside a bubble). The reflected light passes through a semi-transparent mirror that is combined with a prism towards a photosensitive diode in the module. The light transmission system enables the probe to acquire voltage signals with a sampling rate of 1 MHz (RBI User Manual, Meylan, France). By analyzing the digitalized voltage signals from the probe's outputs, the double-tip optical fiber probe is capable of measuring bubble size, bubble size distribution, void fraction (i.e., bubble concentration), and bubble frequency. Furthermore, bubble velocities are calculated by cross-correlation of voltage signals and dividing the calculated time lags between the two timeseries of raw data by the distance between the two probe's tips (i.e., ~2.5 mm).

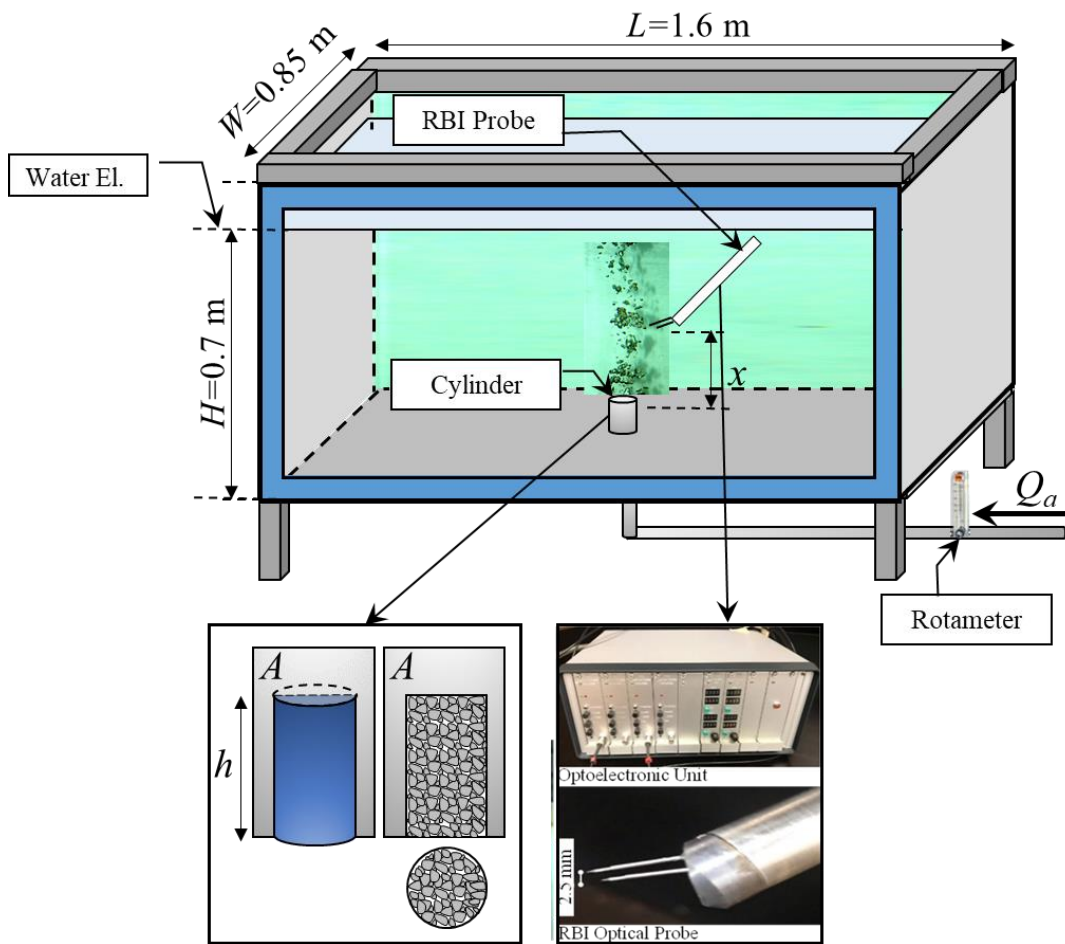


Figure 5. 1: The schematic of experimental setup, image of bubbly plume passing through bed sand, the components of an optoelectronic unit, and the Refractive Bubble Instrument (RBI) optical probe tip.

Bed sands with different thicknesses and grain sizes were installed above the nozzle and the effects of sand grain size and sand layer thickness on bubble characteristics are investigated in this chapter. Three sand aggregates with the mean diameters of $d_s = 2.38\text{ mm}$, 4.76 mm , and 12.5 mm were selected. Two sand bed thicknesses of $h = 0.10\text{ m}$ and 0.20 m were tested as well.

Table 5. 1: Experimental parameters and bubble characteristics of vertically discharged bubble plumes passing through a layer of sand bed. The nozzle diameter in this study is $d_o = 3$ mm.

No.	Test. symbol	Q_a (L/min)	d_s (mm)	h (m)	u_o (m/s)	d_b (mm)	u_b (m/s)	C_b (%)	Re_o
1	B-3	3	-	-	7.0771	10.62	0.88	3.28	1415.4
2	B-6	6	-	-	14.154	12.195	1.005	4.23	2830.9
3	B-9	9	-	-	21.231	13.19	1.104	5.47	4246.3
4	B-12	12	-	-	28.309	13.23	1.153	6.054	5661.7
5	B-12-0.1-2.76	12	2.76	0.1	28.309	8.85	1.018	5.87	5661.7
6	B-3-0.1-4.76	3	4.76	0.1	7.0771	7.71	0.77	5.18	1415.4
7	B-6-0.1-4.76	6	4.76	0.1	14.154	8.22	0.86	6.57	2830.9
8	B-9-0.1-4.76	9	4.76	0.1	21.231	9.33	0.96	7.25	4246.3
9	B-12-0.1-4.76	12	4.76	0.1	28.309	10.126	1.045	9.187	5661.7
10	B-3-0.1-12.5	3	12.5	0.1	7.0771	7.15	0.73	3.96	1415.4
11	B-6-0.1-12.5	6	12.5	0.1	14.154	7.72	0.797	4.74	2830.9
12	B-9-0.1-12.5	9	12.5	0.1	21.231	8.87	0.87	5.36	4246.3
13	B-12-0.1-12.5	12	12.5	0.1	28.309	9.32	0.93	6.92	5661.7
14	B-3-0.2-2.76	3	2.76	0.2	7.0771	6.48	0.79	4.74	1415.4
15	B-6-0.2-2.76	6	2.76	0.2	14.154	6.89	0.89	6.57	2830.9
16	B-9-0.2-2.76	9	2.76	0.2	21.231	7.04	0.97	8.55	4246.3
17	B-12-0.2-2.76	12	2.76	0.2	28.309	7.45	1.05	10.13	5661.7
18	B-3-0.2-4.76	3	4.76	0.2	7.0771	7.22	0.75	3.24	1415.4
19	B-6-0.1-4.76	6	4.76	0.2	14.154	7.46	0.818	6.31	2830.9
20	B-9-0.2-4.76	9	4.76	0.2	21.231	8.02	0.855	7.24	4246.3
21	B-12-0.2-4.76	12	4.76	0.2	28.309	8.38	0.938	8.33	5661.7
22	B-3-0.2-12.5	3	12.5	0.2	7.0771	6.72	0.71	3.24	4923.1
23	B-6-0.2-12.5	6	12.5	0.2	14.154	7.87	0.82	4.89	2830.9
24	B-9-0.2-12.5	9	12.5	0.2	21.231	8.66	0.87	6.02	4246.3
25	B-12-0.2-12.5	12	12.5	0.2	28.309	9.14	0.95	7.5	5661.7

Twenty eight experiments were carried out to investigate the effect of sand bed, on bubble dynamics in vertically discharged bubble plumes. Bubble characteristics such as bubble size, d_b , bubble velocity, u_b , and bubble concentration, C_b , were measured at different distances, x , from the nozzle. The experimental parameters and the associated non-dimensional variables such as initial bubble Reynolds number, $Re_o = \rho_a u_o d_{bo} / \mu_w$ are

listed in Table 5.1. To ensure the repeatability of the results, the Test B-12-0.1-2.76, and B-6-0.2-12.5 were selected and each were repeated three times.

The flow visualization of bubble plumes passing through sand beds with different grain sizes and thicknesses was performed using high-resolution imaging. Images were captured by a high-resolution camera (Prosilica GT 1910c CCD, Germany) with an exposure time of 0.05 s. The camera was located at a perpendicular distance of 1.4 m from the tank and the lenses of the camera were either a 90-mm Kowa F 1.8 (Kowa, Japan) or an 18–55 mm AF-Sinkkor, 13.5–5.6 GII (Nikon, Japan). The images were also compared with the tests without a sand bed layer (i.e., benchmark test) to study the effect of sand bed layer on bubble formation and its movement.

5.3 Results and Discussions

5.3.1 Flow visualization

The snapshot images of bubble plumes for experiments with an air discharge of $Q_a = 6$ L/min, sand layer thickness of $h = 0.10$ m, and different sand sizes are shown in Figure 5.2. Figure 5.2a shows the image of bubble plume without a sand bed layer (i.e., benchmark test) and Figures 5.2b and 5.2d show the images of bubble plumes passing through sand bed layers with the mean sand diameters of $d_s = 2.38$ mm, 4.76 mm, and 12.5 mm, respectively. As it can be seen in the subplots of Figure 5.2, for the air discharge of 6 L/min and a constant thickness of sand bed layer, the averaged diameter of bubbles in experiments with sand bed layer are smaller. Based on visual observations of the images, the mean bubble size decreased by decreasing the mean diameter of sand particles. A direct relationship between the porosity of sand beds and bubble diameter was observed, which

such relationship will be quantified by measuring the mean bubble diameter and bubble size distribution from the outputs of the RBI probe.

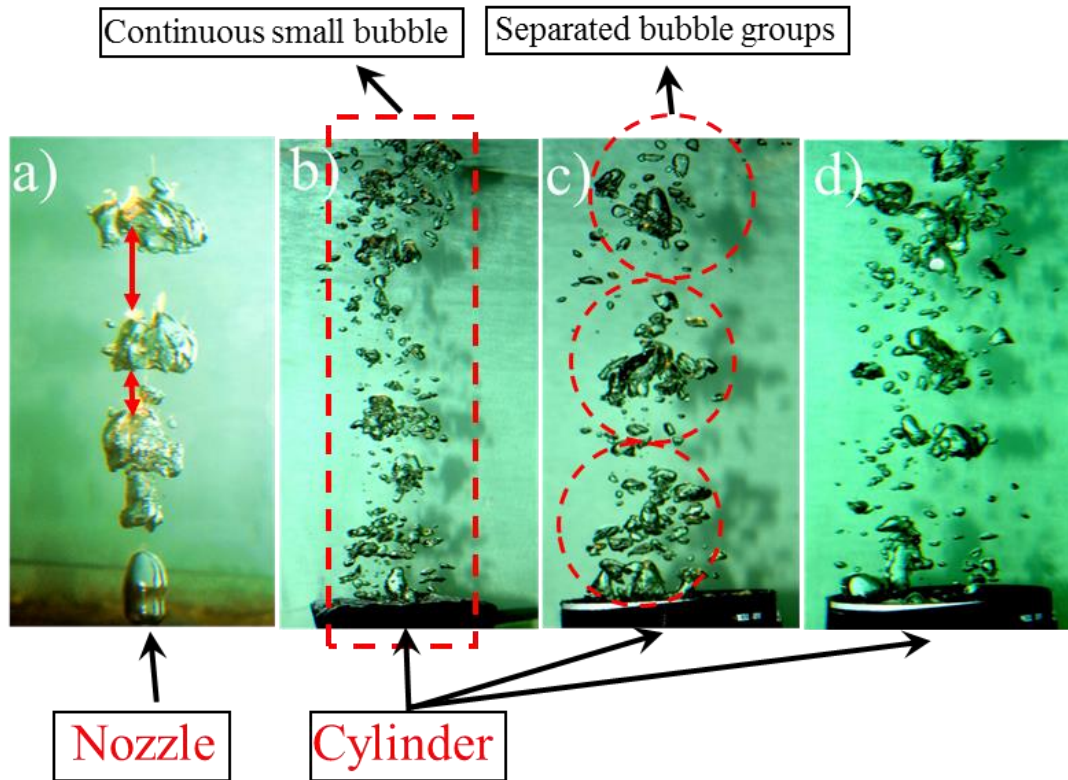


Figure 5. 2: Effects of bed sand with different grain sizes on variations of bubble mean diameter in vertically discharged bubble plumes for $Q_a = 6$ L/min, $h = 0.10$ m, and $d_o = 3$ mm: a) bubble plume without bed sand (i.e., benchmark test); b) $d_s = 2.38$ mm; c) $d_s = 4.76$ mm; d) $d_s = 12.5$ mm.

To investigate the effect of sand bed size on the anatomy of bubble plumes, the consecutive snapshot images of bubble plumes with different experimental conditions are shown in Figure 5.3. The time step between each snapshot image in Figure 5.3 is 2 seconds. As it can be seen from Figure 5.3a (i.e., Benchmark test), the developed bubble plume without a sand bed is mainly formed bubble clouds with relatively large bubble clusters. By tracking the developed bubble clusters in the benchmark test, it can be deduced that the interaction of the adjacent bubble clusters are negligible due to relatively

large distances between bubble clusters (see Figure 5.3a). A continuous cluster of small bubbles is formed in bubble plumes issued from sand beds with the smallest sand bed size of $d_s = 2.38$ mm (see Figure 5.3b); however, as sand diameter in the bed increases, the continuous flow of small bubbles spread into a group of bubbles with a wide range of bubble size that distributes in the vertical axis. It is assumed that such variations in the anatomy of bubble plumes induced by bubble interactions and coalescence between adjacent bubbles. Such bubble coalescence causes bubble size enlargement near the water surface (see Figure 5.3c). Figure 5.3d shows that bubble interactions and coalescence are enhanced by increasing sand bed size, which causes bubble cluster separation.

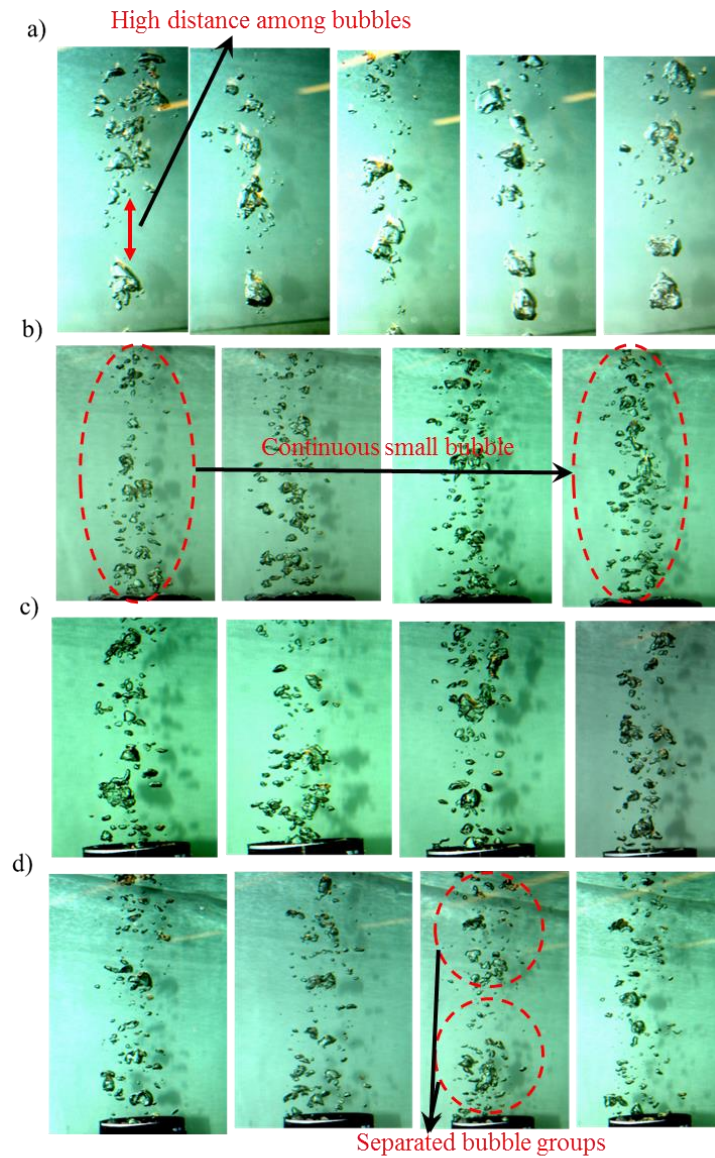


Figure 5. 3: Images on the time-series of bubble plumes passing through sand beds with different sand bed sizes for $d_o = 3$ mm, $h = 0.10$ m, and $Q_a = 6$ L/min: a) without a sand bed (i.e., benchmark test); b) $d_s = 2.38$ mm; c) $d_s = 4.76$ mm; d) $d_s = 12.5$ mm. The time step between each image is two seconds.

5.3.2 Effect of sand bed on bubble plume characteristics

To investigate the effect of sand bed thickness on bubble size and bubble size distribution and to optimize the thickness of sand bed, the Probability Density Function

(PDF) of bubble size distribution for a sand bed size of $d_s = 4.76$ mm and for the maximum air discharge of $Q_a = 12$ L/min were extracted from the time-series data and the results are shown for $x/d_o = 190$ (see Figure 5.4). Two sand bed heights of $h = 0.10$ m and 0.20 m were considered. Furthermore, the PDF of bubble size distributions from the benchmark test (i.e., without a sand bed layer) was also included in Figure 5.4. As it can be seen, the most probable bubble size, is located at the peak of bubble size distribution curve and it decreases from 2.6 mm to 1.1 mm. This is approximately equal to 58% reduction in the mean bubble size as the thickness of sand bed increases by 100% (i.e., from $h = 0.10$ m to 0.20 m). Increasing sand bed thickness also diminishes the probability density function of the maximum bubble size by approximately 22.5% as the PDF values decreases from 26.6% to 20.6%. Such reduction indicates that the thickness in bed sands has an inverse relationship with the probability of the maximum bubble size. As a result, it can be deduced that increasing the thickness of bed sand increases the probability of continuous bubbly flow with smaller bubble size. Also, the PDF results of the benchmark tests show that the bed sand thickness has a marginal effect on the reduction of the maximum bubble size and only affects the probability of bubble size distribution.

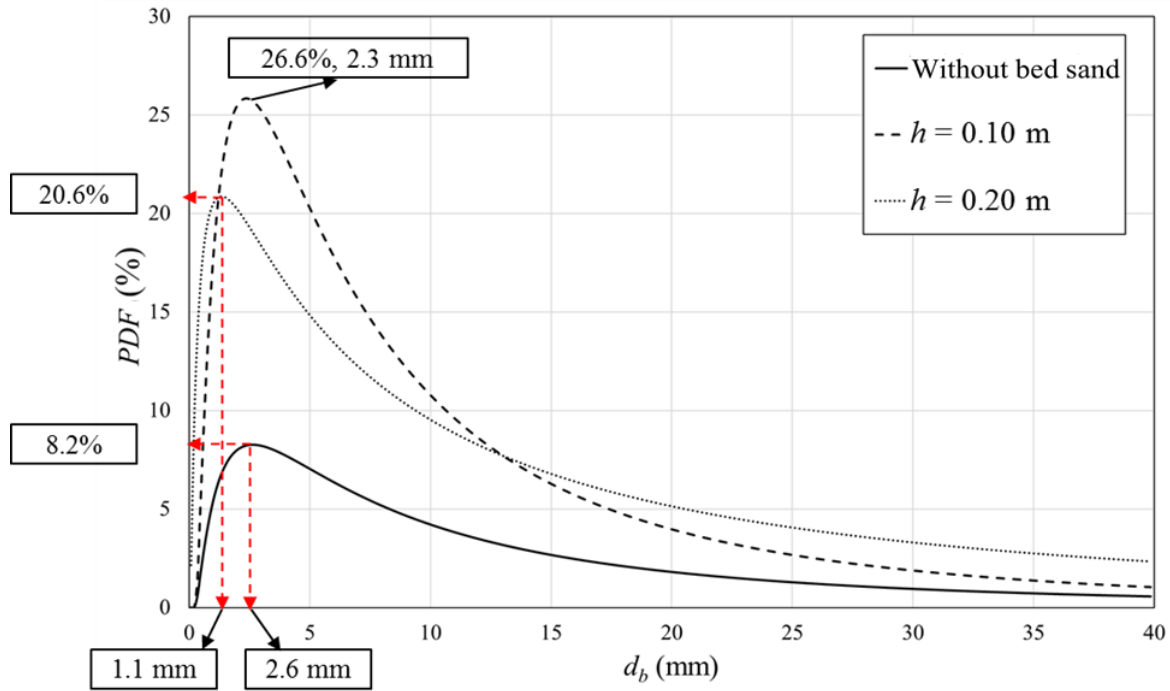


Figure 5. 4: Effects of sand bed thickness on the bubble size distribution in bubble plumes with a sand bed size of $d_s = 4.76$ mm and a maximum air discharge of $Q_a = 12$ L/min measured at $x/d_o = 190$.

Figure 5.5 shows the effects of sand bed size on bubble size distribution measured at $x/d_o = 143$ from the surface of sand bed. As it can be seen, increasing the size of aggregates in sand bed decreases the maximum bubble size in bubble plume from 4.5 mm to 3 mm. In addition, as the size of aggregates increases, the reduction in the ratio of the maximum bubble size and the increment ratio in probability density function of maximum bubble size are changed by approximately -9.3% and 3.05% , respectively. Furthermore, a comparison between the tests with different sand size and the benchmark test showed that a sand bed increases the probability of maximum bubble size by approximately 213%. This indicates that more uniform bubbles are formed in presence of a sand bed.

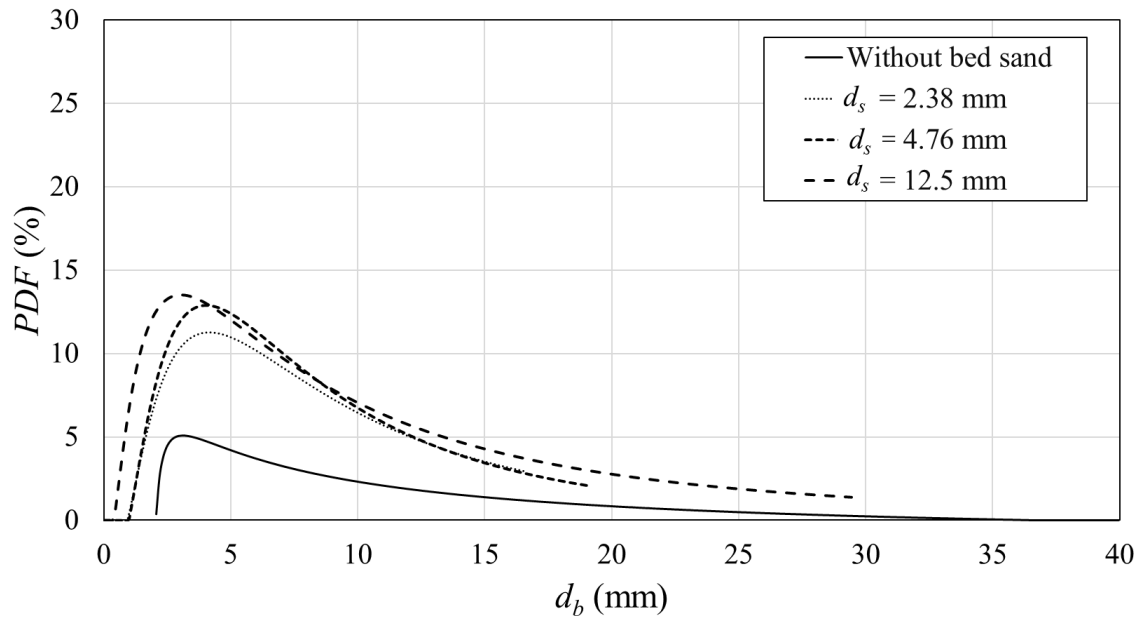


Figure 5. 5: Effects of aggregate size on bubble size distribution of a bubble plume with an air discharge of $Q_a = 6$ L/min and $h = 0.20$ m measured at $x/d_o = 143$.

In order to investigate the effect of sand bed on the anatomy of bubble plumes, the time-histories of the centerline bubble velocity at $x/d_o = 190$ were recorded from the RBI probe's measurement and the results are shown in Figure 5.6. All the measurements are for the bubble plumes with an air discharge of $Q_a = 6$ L/min and sand bed thickness of $h = 0.20$ m. The vertical velocities of bubbles were recorded for 150 seconds, and the time averaged values were calculated for the recorded period. As can be seen, the averaged bubble velocity increases between 1.4% and 14% by the presence of a sand bed.

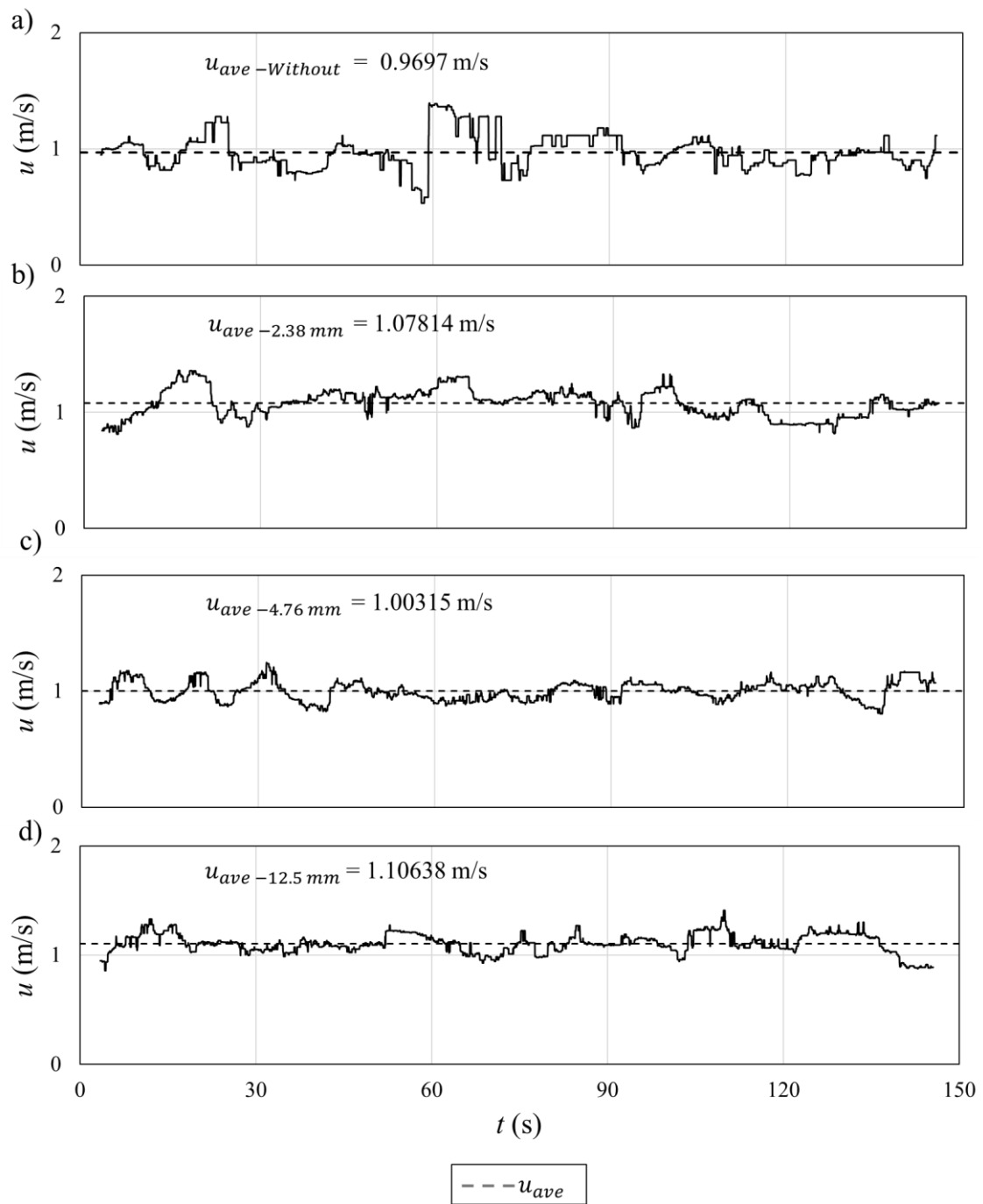


Figure 5. 6: Time-histories of bubble centerline velocity with different sand bed sizes at $x/d_o = 190$, $Q_a = 6$ L/min, and $h = 0.20$ m: a) without a sand bed (i.e., Benchmark test); b) $d_s = 2.76$ mm; c) $d_s = 4.76$ mm; d) $d_s = 12.5$ mm.

The effect of sand bed size on variations of the time averaged bubble concentration was studied by measuring the timeseries of bubble concentration for tests with an air discharge of $Q_a = 6$ L/min and sand bed thickness of $h = 0.20$ m. All measurements were taken at $x/d_o = 190$. As can be seen in Figure 5.7, a comparison between the experimental tests with sand bed and the benchmark test indicates that sand bed increases the averaged bubble concentration by approximately 200%, 262%, and 246% for sand beds with sand diameters of $d_s = 2.38$ mm, 4.76 mm, and 12.5 mm, respectively.

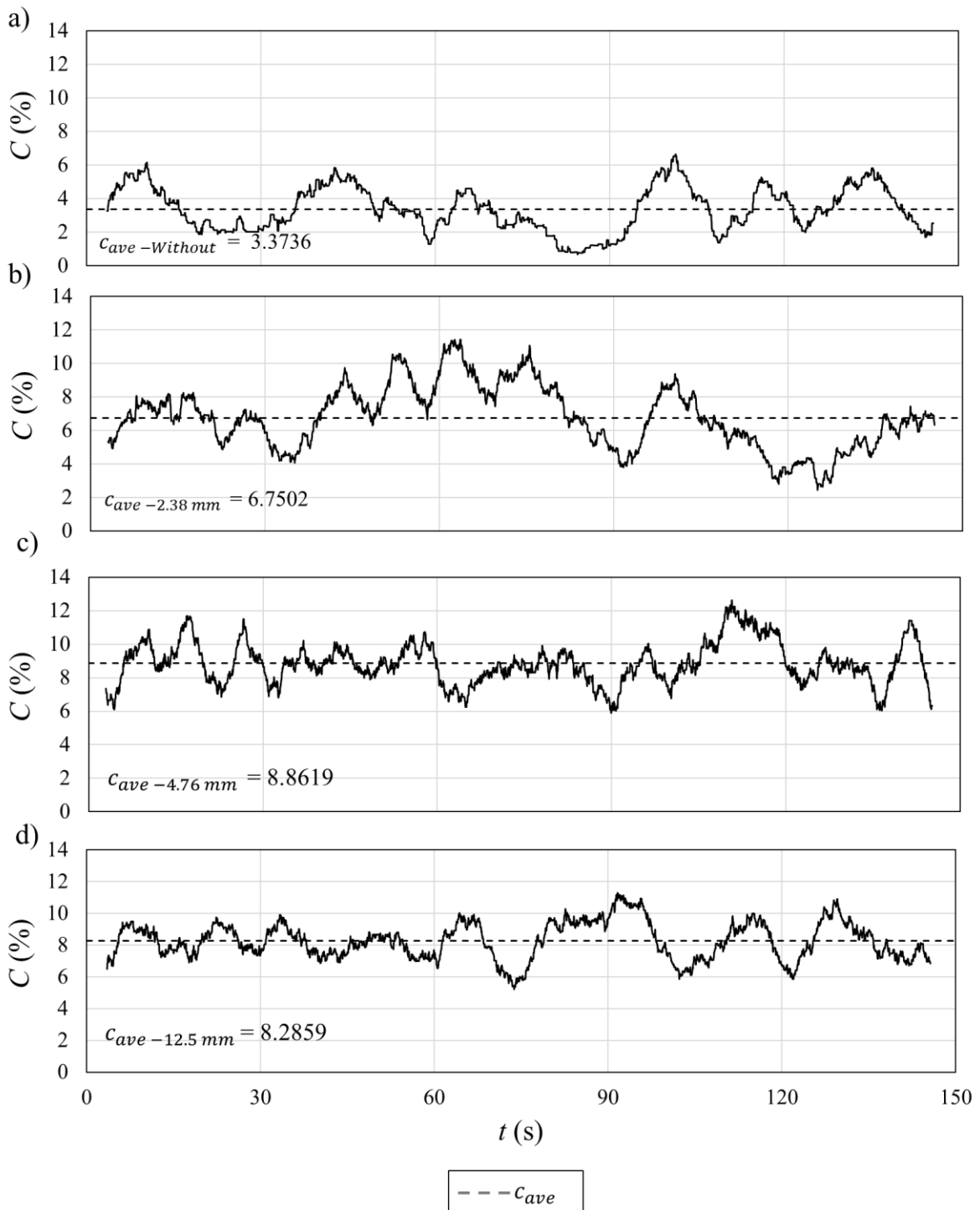


Figure 5. 7: Time-histories of bubble concentration for tests with an air discharge of $Q_a = 6$ L/min, sand bed thickness of $h = 0.20$ m, and with different sand bed sizes measured at $x/d_o = 190$: a) without sand bed (Benchmark test); b) $d_s = 2.76$ mm; c) $d_s = 4.76$ mm; d) $d_s = 12.5$ mm.

Figure 5.8 shows the variation of bubble velocity along the vertical axis of bubble plume for different air discharges and bed sand with different aggregate sizes. Different rows in Figure 5.8 show the results for different air discharges in which the first, second, and third subplots have the air discharges of $Q_a = 3$ L/min, 6 L/min, and 12 L/min, respectively. Also, the left and right columns in Figure 5.8 show the effect of sand bed thickness for $h = 0.10$ m and 0.20 m, respectively. The results of the experiments without bed sands (i.e., Benchmark test) are shown with solid circular symbols and the tests with sand bed and with different sand size are shown with open symbols. A comparison among different air discharges with the same sand thickness indicates that sand bed thickness reduces the vertical velocity of bubbles from the nozzle up to $x/d_o = 133$. Also, an inverse correlation was found between air discharge and the centerline velocity of bubbles. For example, at $x/d_o = 67$, the reduction in bubble velocity due to the change in air discharge from $Q_a = 3$ L/min to $Q_a = 12$ L/min is 28%. Furthermore, increasing the thickness of sand bed decreases the mean bubble velocity. For example, at $x/d_o = 67$ and $Q_a = 12$ L/min, the mean bubble velocity decreases by 26 % as the bed sand thickness increased.

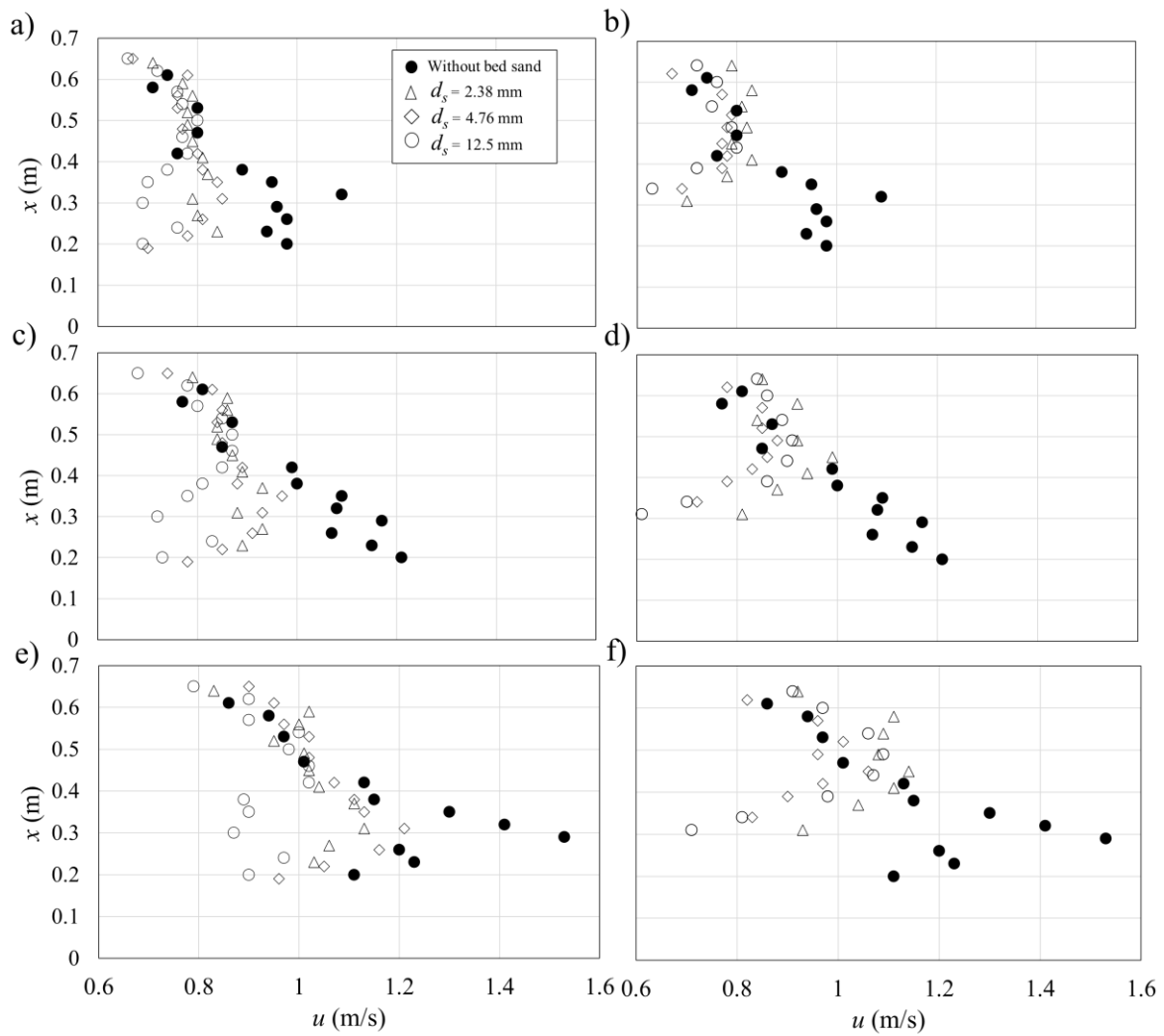


Figure 5. 8: Effect of sand bed thicknes and aggregate size on variations of the centreline bubble velocity with the vertical distance from the nozzle: a) $Q_a = 3$ L/min, $h = 0.10$ m; b) $Q_a = 3$ L/min, $h = 0.20$ m; c) $Q_a = 6$ L/min, $h = 0.10$ m; d) $Q_a = 6$ L/min, $h = 0.20$ m; e) $Q_a = 12$ L/min, $h = 0.10$ m; f) $Q_a = 12$ L/min, $h = 0.20$ m.

Figure 5.9 shows the effects of sand bed thickness and grain size on variations of normalized bubble velocity with normalized distance from the sand bed surface. Bubble velocity was normalized by the depth averaged bubble velocity and the vertical distance from the nozzle was normalized with the nozzle diameter. Figure 5.9 shows that bed sands with relatively small air discharge has less effect on the normalized bubble velocity. By

increasing air discharge from $Q_a = 3$ L/min to 12 L/min, the mean bubble velocity becomes smaller than the average velocity over the water depth and such reduction is approximately 38 % at $x/d_o = 100$.

For $x/d_o \geq 125$, the tests with bed sands attained higher values of normalized bubble velocity, u/u_{ave} , than the benchmark test (e.g., without a sand bed). However, for $x/d_o < 125$, the tests with bed sands attained lower values of u/u_{ave} than the corresponding benchmark tests. For example, at the specific normalized distance of $x/d_o = 150$, in Test B-12-0.1-12.5, the mean bubble velocity becomes 32% less than the average bubble velocity in the benchmark test. The results indicate the possibility of designing an optimum height of the bed sand to be able to control the vertical variations of bubble velocity in bubble plumes. As it was mentioned in Figures 5.2 and 5.3, by adjusting the thickness of bed sand and aggregate sizes, it is possible to reduce the mean diameter of air bubbles and consequently improve the contact time and enhance the contact surface between air and water.

The interfacial area of bubbles is an important parameter to indicate the degree of mixing and oxygen transfer rate as it is expressed by the first order decay rate (Mueller et al. 2002) as:

$$\frac{dC}{dt} = K_L a (C_s - C) \quad (5.1)$$

where C is the Dissolved Oxygen (DO) concentration in the ambient water, C_s is the saturation concentration of dissolved oxygen, and K_L is the mass transfer coefficient or liquid film coefficient.

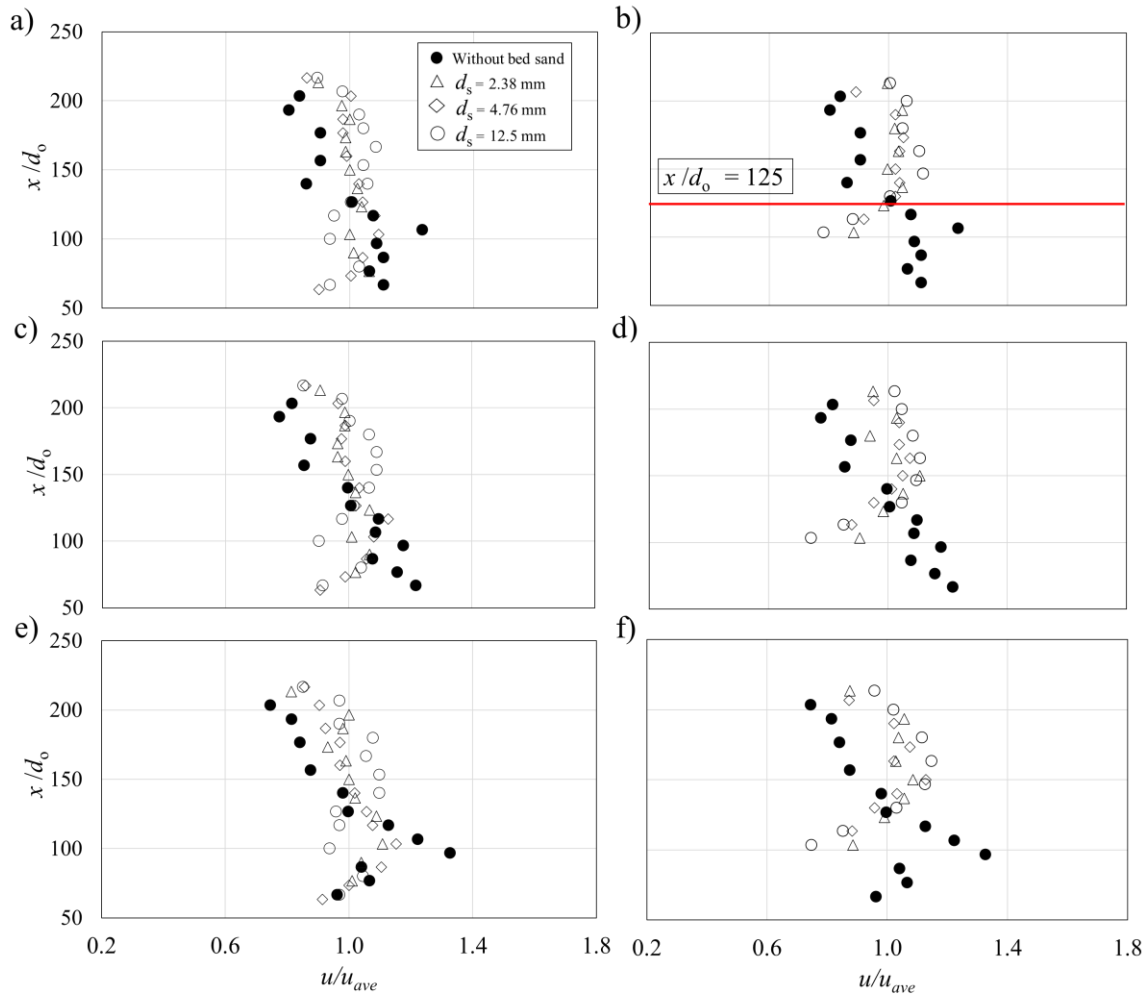


Figure 5. 9: Variations of the normalized bubble velocity with normalized vertical distance from the nozzle in bubble plumes with different air discharges, Q_a , and sand bed thicknesses, h : a) $Q_a = 3$ L/min, $h = 0.10$ m; b) $Q_a = 3$ L/min, $h = 0.20$ m; c) $Q_a = 6$ L/min, $h = 0.10$ m; d) $Q_a = 6$ L/min, $h = 0.20$ m; e) $Q_a = 12$ L/min, $h = 0.10$ m; f) $Q_a = 12$ L/min, $h = 0.20$ m.

Figure 5.10 illustrates the variations of bubble interfacial area, a , along the vertical axis of the bubble plume with air discharge, Q_a , bed sand height, h , and sand size, d_s . As it can be seen, the installation of sand bed significantly increases the interfacial area in comparison with the benchmark tests. The interfacial area of bubbles linearly decreases

with the distance from the nozzle in bubble plumes passing through a sand bed layer whereas interfacial area of bubbles are nearly constant for $x > 0.25$ m (i.e., $x/d_o > 84$) in benchmark test. Increasing the size of aggregates in sand bed layer decreases the interfacial area and such reduction continues even more near the nozzle position. As can be seen in Figure 5.10f, bed sands with aggregate sizes of 2.38 mm, 4.76 mm, and 12.5 mm result in smaller depth-averaged interfacial area by 23%, 31%, and 38%, respectively.

As can be seen in Figure 5.10d and Figure 5.10f, at $x = 0.35$ m above the nozzle (i.e., $x/d_o = 117$), the interfacial area increases by 35% above the bed sands as air discharge increases from 6 L/min to 12 L/min. Further away from the nozzle at $x = 0.42$ m above the nozzle (i.e., $x/d_o = 140$), the results indicate that the interfacial area increases by approximately 32% when air discharge increases from 6 L/min to 12 L/min. A comparison amongst the available data from the literature (i.e., Lima Neto et al., 2008a) on variations of air discharge with interfacial area indicates that our observations are consistent. In their study, increasing air discharge from 2 L/min to 3 L/min increased the interfacial area by 18%.

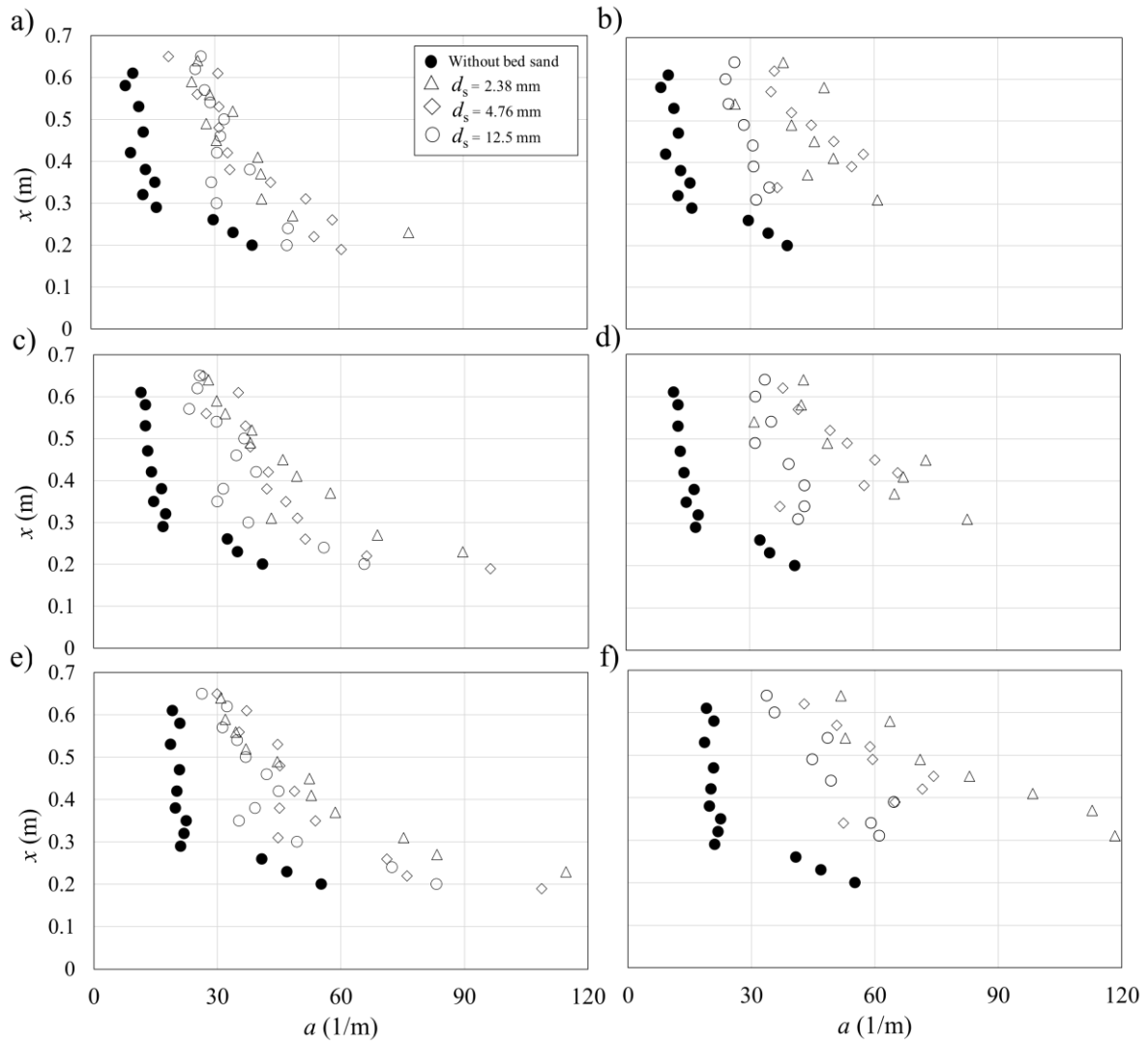


Figure 5. 10: Effect of grain size in bed sand, d_s , on variations of bubble interfacial area with vertical distance from the nozzle in bubble plumes with different air discharges, Q_a and sand bed thicknesses, h : a) $Q_a = 3$ L/min, $h = 0.10$ m; b) $Q_a = 3$ L/min, $h = 0.20$ m; c) $Q_a = 6$ L/min, $h = 0.10$ m; d) $Q_a = 6$ L/min, $h = 0.20$ m; e) $Q_a = 12$ L/min, $h = 0.10$ m; f) $Q_a = 12$ L/min, $h = 0.20$ m.

Figure 5.11 shows the vertical profile of bubble diameter for different air discharges and thicknesses of sand bed. A comparison between two columns in Figure 5.11 indicates that the effect of bed sand thickness is less significant on variations of bubble diameter in relatively low air discharges. As bed sands thickness increases from 0.10 m to 0.20 m, the mean bubble size decreases by an average of 14 %. On the other hand, the reduction on the mean bubble size due to doubling the thickness of sand bed at high air discharge of 12 L/min is 23%. In addition, as the bed size decreases from 10 mm to 6 mm, the mean bubble diameter reduces by an average of 14 % in tests with $h = 0.1$ m. Reducing the size of sand aggregates reduces the porosity of sand beds which results in generation of smaller bubbles.

A comparison between bubble plumes with air discharges of $Q_a = 6, 9,$ and 12 L/min shows that increasing the air discharge increases the mean bubble diameter. At $x = 0.6$ m above nozzle, the mean bubble diameter increases by 50% as air discharge increases from $Q_a = 3$ L/min to $Q_a = 12$ L/min. Similar comparison for bubble plumes passing through a sand bed with a grain size of $d_s = 12.5$ mm, thickness of $h = 0.10$ m, and at $x = 0.6$ m indicates an increase in the mean bubble diameter by 43% as the air discharge increases from $Q_a = 3$ L/min to $Q_a = 12$ L/min.

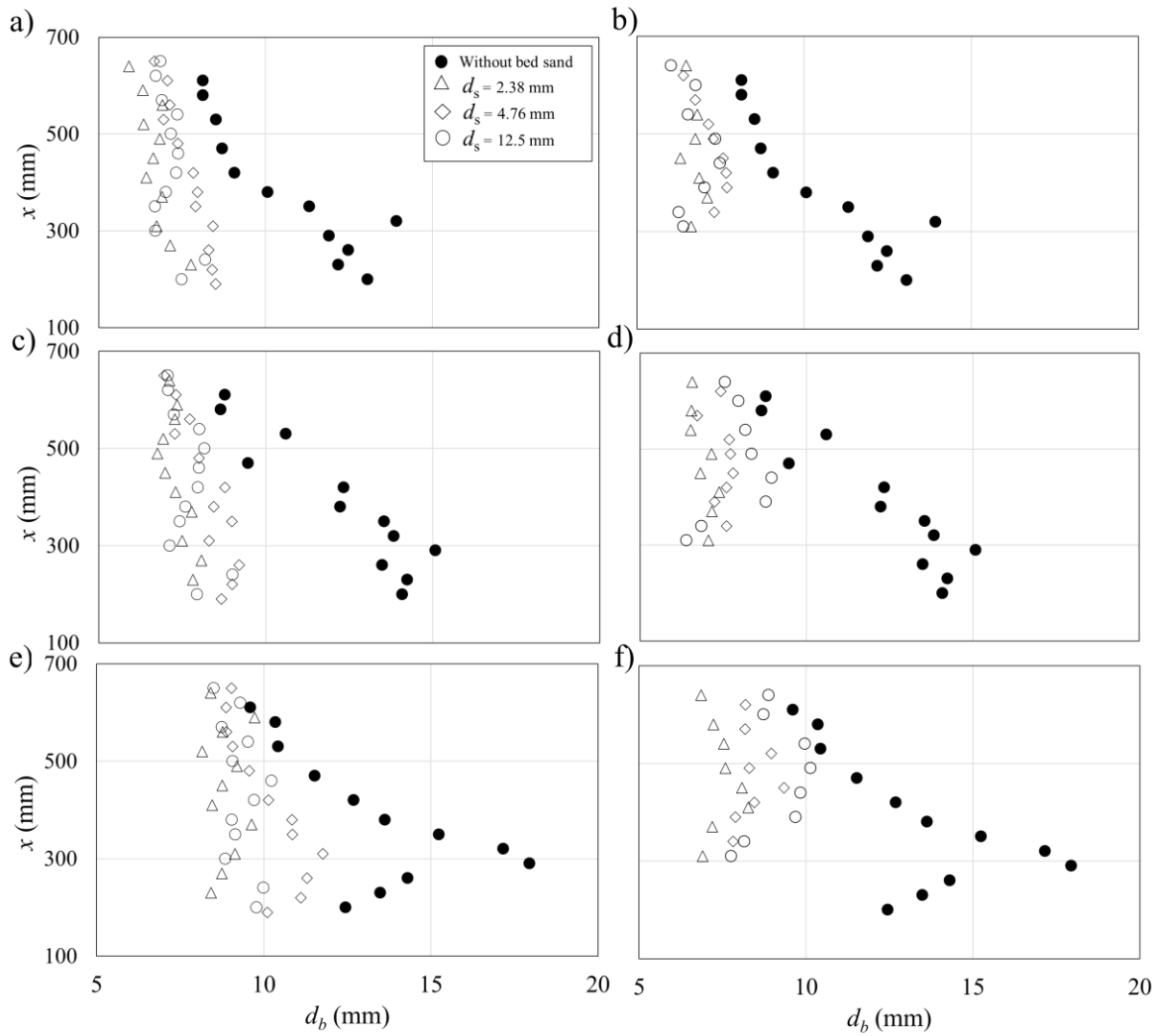


Figure 5. 11: Effect of sand bed size, d_s , on variations of the mean bubble diameter with vertical distance from the nozzle in bubble plumes with different air discharges, Q_a , and sand bed thicknesses, h : a) $Q_a = 3$ L/min, $h = 0.10$ m; b) $Q_a = 3$ L/min, $h = 0.20$ m; c) $Q_a = 6$ L/min, $h = 0.10$ m; d) $Q_a = 6$ L/min, $h = 0.20$ m; e) $Q_a = 12$ L/min, $h = 0.10$ m; f) $Q_a = 12$ L/min, $h = 0.20$ m.

Figure 5.12 shows the effects of the sand size and air discharge on the variations of bubble concentration along the vertical axis of bubble plumes. As it can be seen from Figure 5.12, bubble concentration decreases from the nozzle to the water surface by 46% in the case without bed sand when $Q_a = 3$ L/min and $h = 0.10$ m. The installation of sand bed

increases bubble concentration at the centerline of bubble plume and inverse correlation was found between sand aggregate size and bubble concentration. In addition, bed sands with a thickness of $h = 0.20$ m has a greater effect on increasing bubble concentration than bed sands with a thickness of $h = 0.10$ m. In such condition, bubble concentration increases by 16% as sand thickness increases from 0.10 m to 0.20 m. The results indicate that bed sands with the largest size (i.e., $d_s = 12.5$ mm) has less effect on bubble concentration in comparison with the bed sand having an aggregate size of $d_s = 2.38$ mm. Overall, by reducing the grain size from 12.5 mm to 2.38 mm, the time-averaged bubble concentration increases by 18 %.

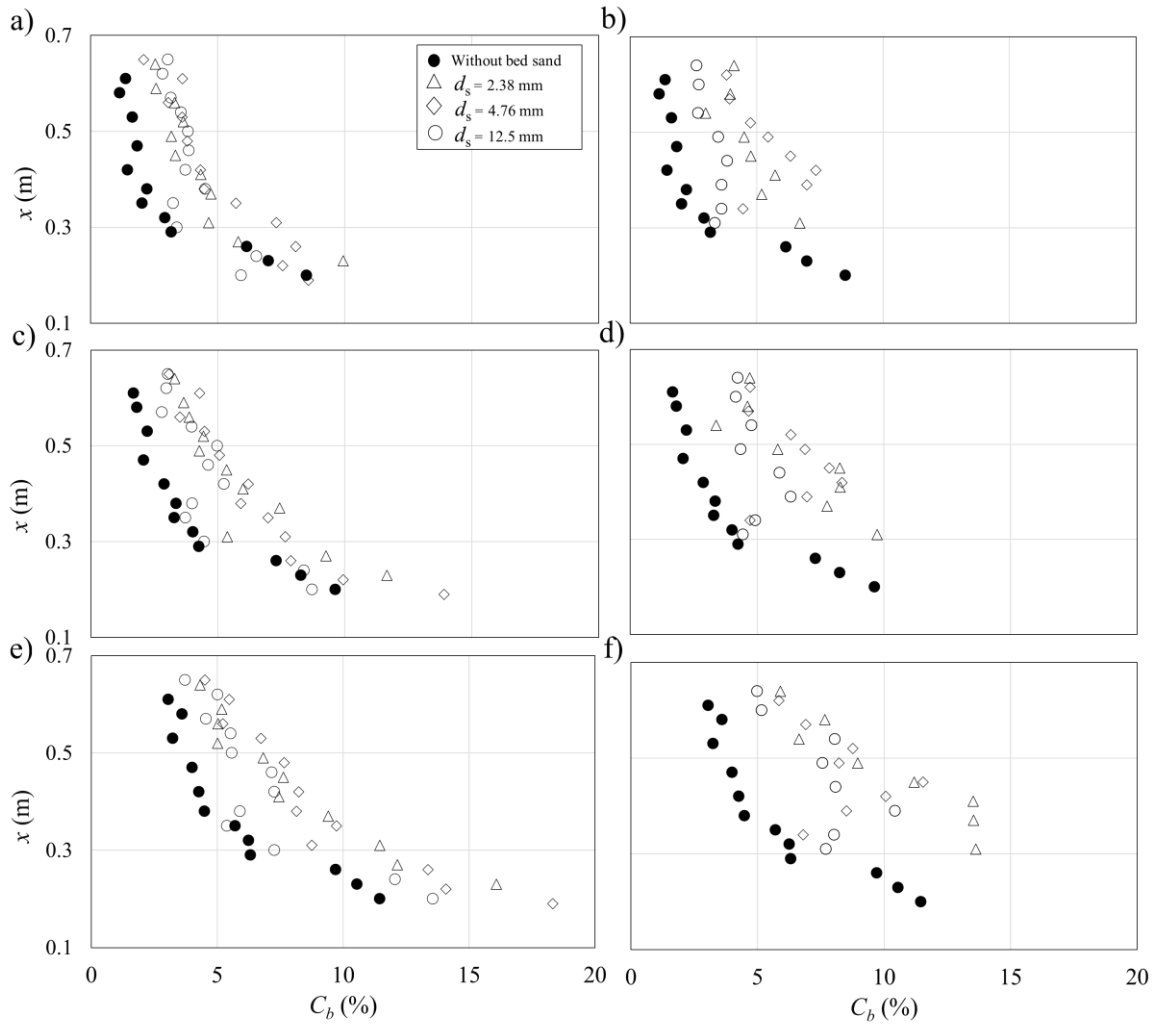


Figure 5. 12: Effects of sand bed size, d_s , on variations of bubble concentration with the vertical distance from the nozzle in bubble plumes with different air discharges, Q_a , and sand bed thicknesses, h : a) $Q_a = 3$ L/min, $h = 0.10$ m; b) $Q_a = 3$ L/min, $h = 0.20$ m; c) $Q_a = 6$ L/min, $h = 0.10$ m; d) $Q_a = 6$ L/min, $h = 0.20$ m; e) $Q_a = 12$ L/min, $h = 0.10$ m; f) $Q_a = 12$ L/min, $h = 0.20$ m.

Figure 5.13 illustrates the effect of sand size and air discharge on variations of bubble frequency along the vertical axis of bubble plumes. Bubble frequency is the product of bubble interfacial area and mean bubble velocity and is expressed as:

$$f_b = u_b a/4 \quad (5.2)$$

A comparison among the variations bubble frequency along the centerline of bubble plumes indicates that the installation of bed sand increases bubble frequency by approximately 48%. Experimental results show that the installation of bed sand reduces the size of bubbles and hence increasing the number of bubbles in the ambient water. The results indicate that bubble frequency decreases with increasing the distance from the nozzle. The rate of bubble frequency reduction is relatively high from the nozzle until $x/d_o = 100$ and it decreases afterwards. As can be seen in Figures 5.13a and 5.13b, the slopes of correlation in bubble frequency for relatively low air discharge (i.e., $Q_a = 3$ L/min) are similar in bubble plumes with and without sand bed. Whereas, in relatively large air discharge (i.e., $Q_a = 12$ L/min), the slope of correlation in bubble plumes with sand beds follows the same trend as bubble plume without sand bed for $x/d_o \leq 100$. In general, air discharge increases the bubble frequency by 21.1% and 31.6% as air discharge increases by 50% and 100%, respectively.

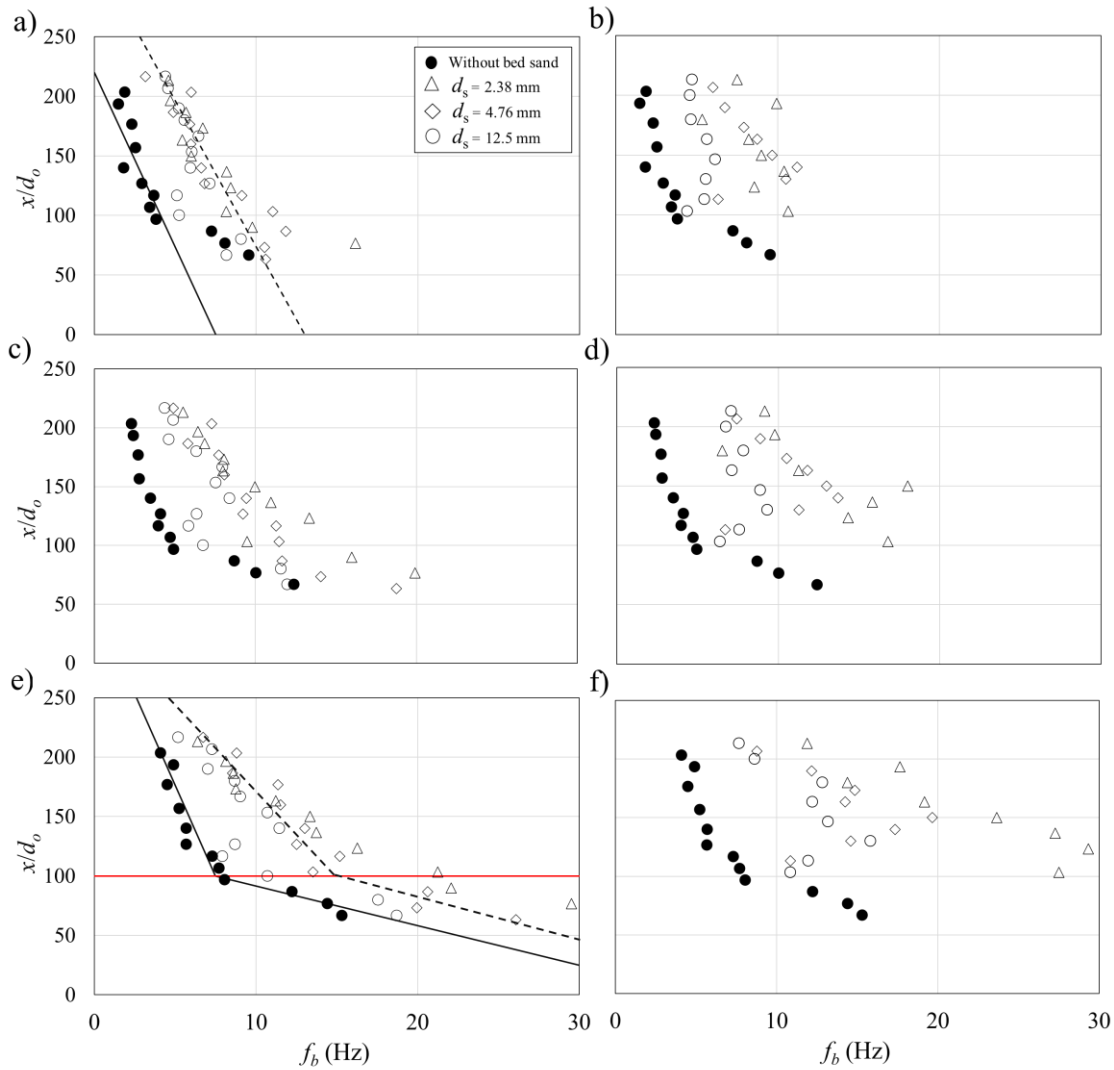


Figure 5. 13: Effect of sand bed size, d_s , on variations of bubble frequency with the vertical distance from the nozzle in bubble plumes with different air discharges, Q_a , and sand bed thicknesses, h : a) $Q_a = 3$ L/min, $h = 0.10$ m; b) $Q_a = 3$ L/min, $h = 0.20$ m; c) $Q_a = 6$ L/min, $h = 0.10$ m; d) $Q_a = 6$ L/min, $h = 0.20$ m; e) $Q_a = 12$ L/min, $h = 0.10$ m; f) $Q_a = 12$ L/min, $h = 0.20$ m. Continuous lines show the correlations for the benchmark test and dashed lines show the variations for the sand bed tests.

The combination of mean bubble diameter and time averaged bubble velocity can be expressed by the bubble Reynolds number, Re_b , as:

$$Re_b = \rho_a u_b d_b / \mu_w \quad (5.3)$$

where u_b is the bubble velocity, d_b is the bubble diameter, ρ_a is the air density, and μ_w is the kinematic viscosity of water.

Figure 5.14 shows the effects of air discharge and sand bed characteristics on variations of bubble Reynolds number. As it can be seen, bubble Reynolds number decreases almost linearly with the distance from the nozzle in bubble plumes without sand bed. The slope of reduction in bubble Reynolds number is correlated as $Re_b \sim x/d_o^{-2/3}$. A sudden drop in values of bubble Reynolds number is observed at $x/d_o = 100$, which such drop is more pronounced in tests with high air discharges, and it is due to bubble breakup in relatively large bubbles. As it was mentioned in the discussion of bubble velocity and mean bubble diameter in Figures 5.8 and 5.11, the installation of bed sand decreases the size of bubbles, but it does not significantly change the time averaged bubble velocity.

Since bubble Reynolds number is a product of bubble mean diameter and time averaged bubble velocity, it is expected that bubble Reynolds number decreases with the distance from the nozzle. Such variations are evident in bubble plumes without bed sand; however, the existence of a bed sand alters the variation of bubble Reynolds number along the vertical axis of the bubble plume. The variations of bubble Reynolds number in the vertical axis of bubble plumes issuing from a bed sand are relatively constant with a peak value at $x/d_o \approx 150$. Furthermore, it was found that the diameter of aggregates has negligible impact on variations of bubble Reynolds numbers. The values of bubble Reynolds numbers slightly increases with air discharge by 8.2% and 9.8% as air discharge increases from 6 L/min to 9 L/min and 9 L/min to 12 L/min, respectively.

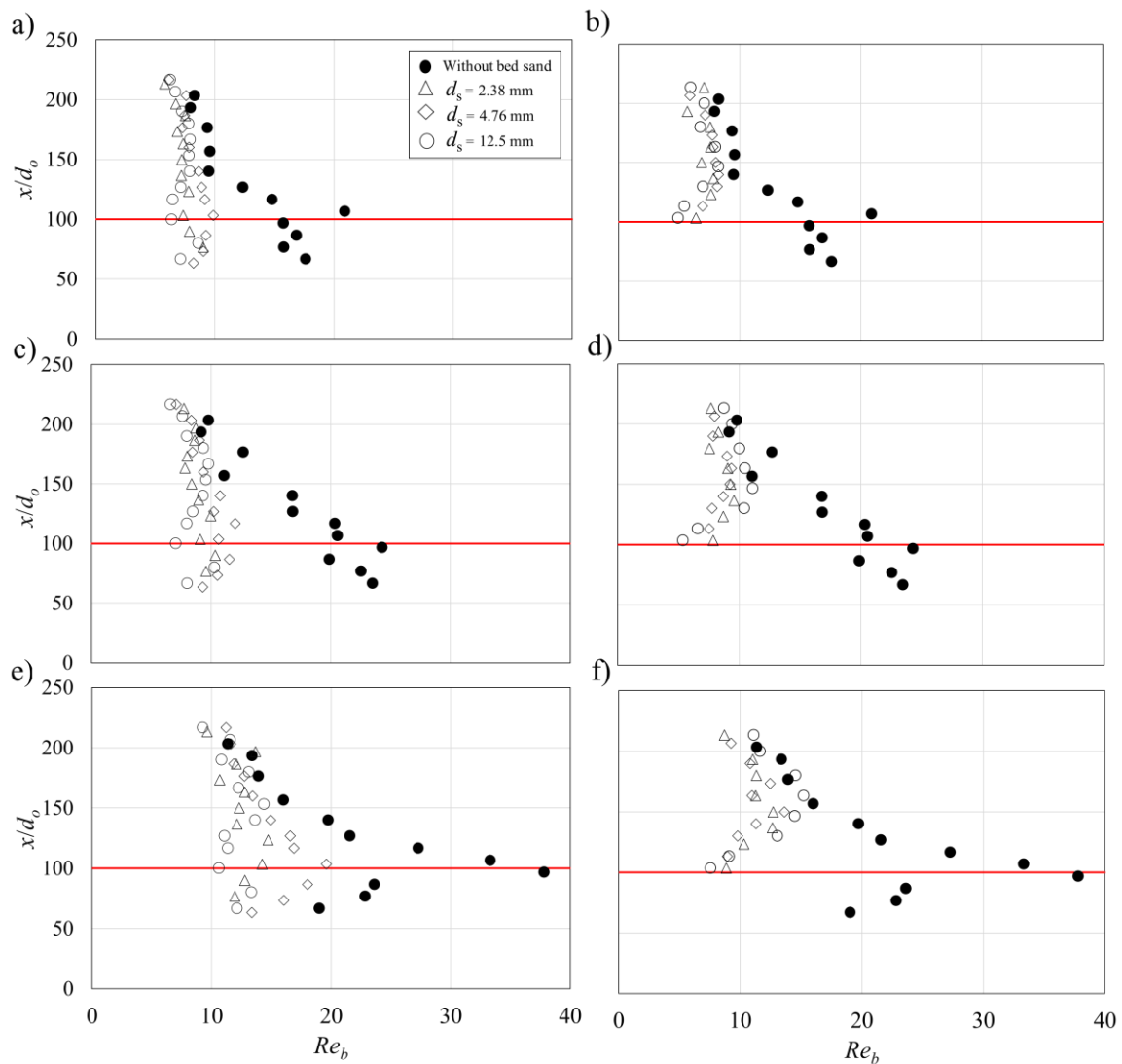


Figure 5. 14: Effect of sand bed size, d_s , on variations of bubble Reynolds number with the vertical distance from the nozzle in bubble plumes with different air discharges, Q_a , and sand bed thicknesses, h : a) $Q_a = 3$ L/min, $h = 0.10$ m; b) $Q_a = 3$ L/min, $h = 0.20$ m; c) $Q_a = 6$ L/min, $h = 0.10$ m; d) $Q_a = 6$ L/min, $h = 0.20$ m; e) $Q_a = 12$ L/min, $h = 0.10$ m; f) $Q_a = 12$ L/min, $h = 0.20$ m.

5.4 Conclusions

For better understanding of bubble plume dynamics and oxygen transfer enhancement, a series of laboratory experiments was carried to investigate the effects of sand bed layer in reducing bubble size and increasing the time residence of bubbles in

bubble plumes. The larger contact surface between air and water enhances the oxygen transfer between air and water. Different airflow discharges were tested as $Q_a = 3$ L/min, 6 L/min, 9 L/min, 12 L/min. To decrease bubble diameter, three sand aggregate sizes were selected ($d_s = 2.76$ mm, 4.76 mm, and 12.5 mm) which were placed to form sand layer thicknesses of 0.10 m and 0.20 m.

The experimental observations indicated that the most probable bubble size, is located at the peak of bubble size distribution plot and it decreased from 2.6 mm to 1.1 mm due to placement of bed sand. This is approximately equal to 58% reduction in the mean bubble size as the thickness of sand bed increases by 100% (i.e., from $h = 0.10$ m to 0.20 m). Increasing sand bed thickness also decreased the probability density function of the maximum bubble size by approximately 22.5% as the PDF values decrease from 26.6% to 20.6%. As a result, it can be deduced that increasing the thickness of sand bed increases the probability of continuous bubbly flow with smaller bubble size. Additionally, the experimental results showed that a sand bed increases the probability of maximum bubble size by approximately 213%. This indicated the generation of more uniform bubbles in presence of a sand bed. Increasing the thickness of bed sands from $h = 0.1$ m to $h = 0.2$ m, decreased the mean bubble velocity. For example at $x/d_o = 67$ and $Q_a = 12$ L/min, the mean bubble velocity decreased by 26% by increasing the bed sand thickness from 0.10 m to 0.20 m. Decreasing the mean bubble velocity, increased the residence time of bubbles which improves the oxygen transfer rate on the system.

It was found that the effect of bed sand thickness is less significant on variations of bubble diameter in relatively low air discharges ($Q_a = 3$ L/min, 6 L/min) as increasing the bed sands thickness from 0.10 m to 0.20 m reduced the bubble size by an average of 14%.

On the other hand, the reduction on the mean bubble size due to doubling the thickness of sand bed at high air discharge of 12 L/min is 23%. The results revealed that sand bed increases the averaged bubble concentration by approximately 200%, 262%, and 246% for sand beds with sand diameters of $d_s = 2.38$ mm, 4.76 mm, and 12.5 mm, respectively. Such increase in bubble concentration means to have a better oxygen transfer rate, and a bed sand with larger aggregate size should be considered. Our observations indicated an inverse correlation between air discharge and the centerline velocity of bubbles. For example at $x/d_o = 67$, the reduction in bubble velocity due to the change in air discharge from $Q_a = 3$ L/min to $Q_a = 12$ L/min was 28%.

The experimental results indicated that the interfacial area increases by approximately 32% when air discharge increases from 6 L/min to 12 L/min, which can enhance the oxygen transfer rate in bubble plume. It was found that bubble concentration decreases from the nozzle to the water surface by 46% in the case without bed sand when $Q_a = 3$ L/min and $h = 0.10$ m. Our results revealed that bubble Reynolds number decreases almost linearly with the distance from the nozzle in bubble plumes without sand bed. The slope of reduction in bubble Reynolds number was found to be $Re_b \sim x/d_o^{-2/3}$.

Notations

The following symbols are used in this paper:

a = bubble interfacial area

C = dissolved Oxygen (DO) concentration in the ambient water, mg/L;

C_s = the saturation concentration of dissolved oxygen, mg/L;

C_b = bubble concentration, vol/vol;

h = height of bed sands, m;

H = depth of water, m;

d_b = bubble diameter, mm;

d_o = nozzle diameter, mm;

d_s = sand diameter, mm;

K_L = mass transfer coefficient or liquid film coefficient,

L = length of the tank, m;

Q_a = volumetric airflow rates, L/min;

t = time, s;

u_{ave} = average bubble velocity

u_b = bubble velocity, m/s;

u_o = initial bubble velocity, m/s;

x = elevation of measured point, m;

f_b = bubble frequency, Hz;

Re_b = bubble Reynolds number.

Chapter 6

Bubble dynamics and coalescence in twin oblique bubble plumes

6.1 Introduction

Multiphase flows are predominant in natural environment and manmade infrastructures and have been the focus of notable research studies in the field of multiphase fluid dynamics. In the recent years, researchers and engineers have explored novel and efficient designs to improve mixing and oxygenation in lakes and man-made reservoirs to mitigate the harmful effects of global warming and the associated environmental impacts. Such novel designs are implemented in Dissolved Air Floatation (DAF) systems and are utilized in water quality control, mitigation, management, and risk assessment of lakes and man-made reservoirs (Socolofsky and Adams, 2002; and Besagni and Deen, 2020). Bubbly jets and plumes have been extensively employed to enhance oxygenation and aeration in lakes and natural reservoirs (Lima Neto et al. 2007; Pacheco and Lima Neto, 2017; and Behzadipour et al., 2023). Water quality in many lakes and reservoirs around the world can be improved by utilizing bubble plumes to enhance dissolved oxygen enhancement, and air entrainment (Wüest et al., 1992; Mueller et al., 2002; and Schierholz et al., 2006).

In addition to wastewater effluent discharge, the excessive loadings of phosphorous in agricultural effluent enhances the growth organic matter in natural and man-made reservoirs. Such significant mass growth elevates Biochemical Oxygen Demand (BOD) in lakes and natural detention ponds since organic matters need oxygen to decompose to carbon dioxide, water, and residuals. Stable stratification in lakes and water ponds, particularly in the summer months, causes oxygen depletion at the bottom of the water column, which necessitate water quality improvement throughout the water column. Because of summer stratification, the lower layer of lakes and ponds exhibit low water quality due to low dosage of oxygen concentration. Therefore, air/oxygen entrainment is needed to sustain a healthy lake ecosystem and to reduce the costs associated with wastewater treatment and water management (Little and McGinnis, 2001).

Considerable research studies have been performed to investigate the effects of oxygen depletion in lakes and reservoirs (Cooke and Carlson, 1989; Gantzer et al., 2009;

and Zic et al., 1992). In stratified flow condition, the warmer surface water layer is called the Epilimnion layer and the colder water layer beneath the Epilimnion is called the Hypolimnion layer. A sharp temperature gradient, known as the Thermocline layer, forms in the contact zone between both layers of Epilimnion and Hypolimnion. The Epilimnion layer exchanges heat and oxygen with the atmosphere. In addition, the Epilimnion layer frequently recirculates by wind or periods of lower temperatures during the stratification whereas the Hypolimnion is insulated from oxygen exchange during the stratification period. Depletion of oxygen in the Hypolimnion layer is a vital global problem, which negatively affects water treatment processes, cold-water fisheries, and hydropower discharge in the reservoirs (Boyce et al., 1989). Mitigation of water with low oxygen level is accomplished by implementing aerators such as bubbly jets and plumes. A properly designed bubbly jets/plumes can introduce more oxygen in water and enhances the residence time of oxygen in water to maximize oxygen-water transfer. Recent studies have shown that the oxygen transfer rate and the residence time of oxygen in water are correlated with the design parameters such as diffuser geometry and the initial discharge conditions (Lima Neto et al., 2008b; Sun and Faeth, 1986a)

Bubbly jets are formed by simultaneous injection of air and water into the ambient water. Air entrainment in bubbly jets mainly occurs due to the momentum transfer between air and water. While bubbly plumes are formed by injection of air and entrainment occurs predominantly by the buoyancy between air bubbles and the ambient water. In bubbly jets, the air pressure and the initial velocity of water at the nozzle control the motion of air bubbles. In general, the aeration by jets occurs when a gas-liquid mixture is injected with a relatively high momentum into a stagnant liquid domain (i.e., water). The density difference between air and water has smaller impacts on the bubble motion and air entrainment whereas in bubbly plumes, the initial velocity of air is near zero and bubble motion is induced by the density difference between air bubbles and the surrounding water.

Earlier studies in the field of bubbly flow have mostly focused on the dynamics of jets and plumes, air entrainment by bubbles, and mixing. The effects of initial parameters such as nozzle configuration and discharge variations in air and water on bubble dynamics and mixing were investigated in the past (Iamandi and Rouse, 1969; Jirka and Harleman,

1979; Fanneløp et al., 1991; Riess and Fanneløp, 1998; and Behzadipour et al., 2022a). These types of multiphase flows are encountered in many engineering applications such as artificial aeration and mixing in reactors, tanks, and water bodies (Sun and Faeth, 1986a, b; Kumar et al., 1989; Iguchi et al., 1998; Zhang and Zhu, 2014; and Lima Neto, 2012b, 2015). In comparison to bubble-plume aeration, the injection of air-water mixtures in water has advantages such as production of small bubbles without the need for porous diffusers, which is beneficial for gas-liquid mass transfer (Mueller et al. 2002; Lima Neto et al., 2008a-c). The two-phase flow structure induced by bubbly jets was assessed for different flow conditions, tank geometries, and nozzle diameters. However, research studies in the literature are mostly limited to bubbly jets and plumes issued from a single nozzle with relatively small nozzle diameters (i.e., $d_o < 13.5$ mm). The first comprehensive investigation on the dynamics of bubbles in bubble jet-plumes was reported by Sun and Faeth (1986a, b). Their experiments were conducted in a 0.9 m x 0.4 m tank with air discharge, Q_a , ranging from 0.1 L/min to 2.4 L/min and water discharge, Q_w , varied between 2 L/min and 2.5 L/min. The vertical bubbly jets had an initial bubble concentration of approximately 9% at the nozzle. It was found that the mean and turbulent properties of bubbly flow were not significantly affected by the inter-phase transport.

A series of laboratory experiments was carried to study the motion of bubbles in vertical bubbly jets with gas volume fractions ranging between 19% and 49% (Lima Neto et al., 2008b). A wide range of air discharges, Q_a , ranging from 1 L/min to 5 L/min and water discharges, Q_w , varied from 2 L/min to 7 L/min was tested by Lima Neto et al. (2008b). The tests included bubbly jets with gas volume fractions, C_o , ranged from 5% to 83% and initial nozzle Reynolds numbers, $Re_o = u_{wo}d_o/\nu_w$, ranged from 3,500 to 17,700 where u_{wo} is the initial water velocity, d_o is the nozzle diameter, and ν_w is the kinematic viscosity of water. Bubble diameter, d_b , was measured at $x/d_o = 167$ and ranged from 1 mm to 10 mm. Bubble dynamics in vertical bubbly jets with an initial bubble concentration of up to about $C_o = 80\%$ were studied. It was found that increasing air-water discharge increased the mean velocity of water by 21%. In addition, the mean water velocity increased significantly as the initial bubble concentration increased by 32%. A minimum initial Reynolds number, Re_o , larger than 8,000 was recommended to produce relatively small bubbles with approximately uniform bubble size distribution.

Lima and Lima Neto (2018) experimentally investigated the effects of nozzle type and shape, including the effect of diffusers with single- and multiple-orifices and with different diameters, on the hydrodynamics and mass transfer characteristics of air-water bubbly jets. The results indicated that reducing the equivalent diameter of nozzles or increasing the number of orifices, reduced the gas-liquid flow ratio incorporated by the Venturi injector. Their results also revealed that the oxygen transfer efficiency increased by up to about 300% when a single orifice nozzle was replaced by multiple-orifice nozzles with the same total cross-sectional area. Other experimental studies on the nozzle configuration in bubbly jets including jet angle, crossflow discharge, bubble collision, and periodical excitation of two-phase bubbly flows have been performed by many researchers as well (Varley, 1995; Milenkovic et al., 2007; Lima Neto et al., 2008d; Suñol and González-Cinca, 2010; and Zhang and Zhu, 2014). It was found that bubble concentration in bubbly jets in crossflow follows the Gaussian profiles similar to concentration distribution in bubbly jets in stagnant ambient (Zhang and Zhu, 2014). Additionally, it was found that a nozzle Reynolds number larger than 8,000 is indeed necessary to produce nearly uniform bubble size distributions and confirmed the recommendation of Lima Neto et al. (2008b) for the minimum Reynolds number.

This chapter presents the experimental results on the effects of nozzle configuration by obliquely discharging two adjacent bubbly jets in a stagnant ambient. The experimental observations and extracted data for Twin Inclined bubbly jets (TI-Series) were compared with the benchmark tests of Single-Vertical (SV-Series) bubbly jets having the same cross-sectional area as of the twin inclined bubbly jets. The comparisons are necessary to study the effects of bubble interaction and coalescence due to collision of bubbles in twin inclined jets. The focus of this study is on bubble dynamics, and mass transfer characteristics of twin inclined bubbly jets and the aeration induced by air-water bubbly jets injected vertically and with two inclined nozzles in stagnant water. The second objective of the present study is to evaluate the effects air-water discharge ratio and bubble Reynolds number on bubble properties as well as obtaining detailed information on bubble characteristics such as bubble velocity, bubble concentration, bubble interfacial area, and drag coefficient in twin inclined bubbly jets. The presented results are suitable for the optimum design of bubbly jets and plumes and can be used for validation of numerical

modeling for better understanding of bubble dynamics due to interaction and bubble breakup.

6.2 Experimental Setup

A series of laboratory experiments was carried out in the Multiphase Flow Research Laboratory (MFRL) at Lakehead University to investigate the effects of air-water discharge ratio and nozzle configuration on bubble coalescence and breakup in Single Vertical and Twin Inclined bubbly jets. The variations of bubble characteristics, such as bubble size, bubble velocity and concentration are studied in this Chapter and the results of Twin Inclined bubbly jets are compared with Single Vertical bubbly jets of the same nozzle diameter and air-water discharge ratio. Experiments were conducted in a glass-walled tank of 1.60 m long, 0.85 m wide, and 0.80 m deep as shown in Figure 6.1. The temperature of water in the tank was stabilized at a constant temperature of $20^{\circ}\text{C} \pm 1^{\circ}\text{C}$ and water temperature was kept uniform throughout the water depth of $H = 0.70$ m. An air pipeline provided compressed air with a pressure of $P = 4$ atm and different mixture of air and water discharges were tested. Air and water flowrates were measured with an accurate rotameter (LZM series Zyia OEM, Zhejiang, China) with an accuracy of $\pm 4\%$ at the maximum discharge. Two different circular nozzles with the inner diameters of $d_o = 3$ mm and 4.2 mm were selected for single vertical bubbly jets and two different nozzle diameters of $d_o = 2.1$ mm and 3 mm were chosen for the twin nozzle having a nozzle inclination of $\alpha = 45^{\circ}$ (see Figure 6.1). To assure having the same initial momentum in both single and twin bubbly jets, the cross-sectional area of the two nozzles in twin bubbly jets were set the same as the nozzle area of a single vertical bubbly jet.

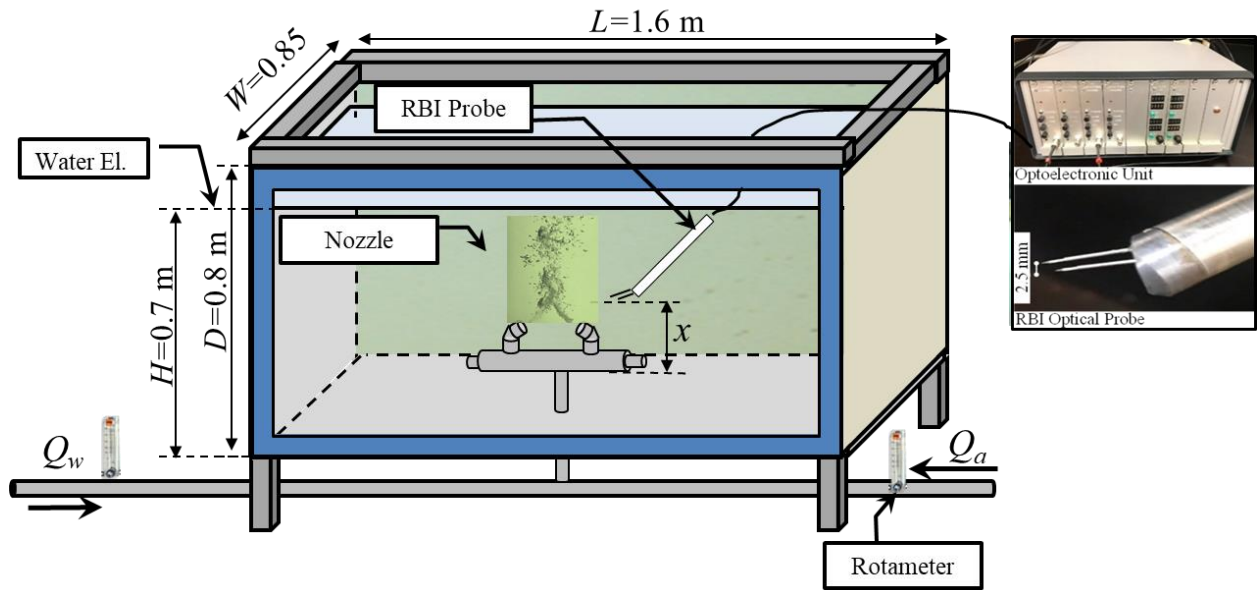


Figure 6. 1: The schematic of experimental setup, image of twin inclined bubbly jets, components of an optoelectronic unit, and Refractive Bubble Instrument (RBI) optical probe tip.

Overall, 16 experiments were conducted to investigate the effects air-water discharge ratio, nozzle configuration, and bubble coalescence in twin inclined and single vertical bubbly jets. The effects of different air-water discharge ratios on variations of bubble characteristics were tested by setting the air to water discharge ratios of $Q_a/Q_w = 0.67, 1.11, 2.00, \text{ and } 3.33$. The experimental parameters such as nozzle diameter, d_o , initial bubble concentration, C_b , air-water discharge ratio, Q_a/Q_w , and the associated non-dimensional parameters such as the initial Reynolds number, $Re_o = u_{wo}d_o/\nu_{water}$, and bubble Reynolds number, $Re_b = \rho_a u_b d_b/\mu_w$, are listed in Table 6.1. The symbols for Single Vertical bubbly jets are assigned as (SV) and for twin inclined bubbly jets is (TI) in Table 6.1. The number after either SV or TI is the air-water discharge ratio followed by the nozzle diameter in millimeter. For example, the Test TI1.11D2.1 represents a twin inclined bubbly jet with a discharge ratio of 1.11 and nozzle diameter of $d_o = 2.1\text{ mm}$.

Table 6. 1: Details of experimental tests for Single Vertical (SV-series) and Twin Inclined (TI-series) with different air and water discharge configurations and nozzle sizes for the inclined angle of $\alpha = 45^\circ$.

Test No.	Symbol	d_o (mm)	Q_a (L/min)	Q_w (L/min)	Q_a/Q_w	C_b (%)	M_{ow} $\times 10^{-5}$ (m^4/s^2)	Re_o	Re_b
1	SV0.67D3	3	2	3	0.67	1.70	3.5	11881	3167
2	SV1.11D3	3	2	1.8	1.11	1.99	2.1	7128	3492
3	SV2D3	3	6	3	2	2.76	3.5	11881	3569
4	SV3.33D3	3	6	1.8	3.33	3.16	2.1	7128	3779
5	SV0.67D4.2	4.2	2	3	0.67	1.64	6.9	8486	3339
6	SV1.11D4.2	4.2	2	1.8	1.11	1.84	4.1	5092	3829
7	SV2D4.2	4.2	6	3	2	2.50	6.9	8486	3764
8	SV3.33D4.2	4.2	6	1.8	3.33	3.09	4.1	5092	3964
9	TI0.67D2.1	2.1	2	3	0.67	1.35	1.7	16973	1608
10	TI1.11D2.1	2.1	2	1.8	1.11	1.85	1	10183	2108
11	TI2D2.1	2.1	6	3	2	2.79	1.7	16973	2492
12	TI3.33D2.1	2.1	6	1.8	3.33	3.66	1	10183	2942
13	TI0.67D3	3	2	3	0.67	1.24	3.5	11881	1430
14	TI1.11D3	3	2	1.8	1.11	1.63	2.1	7128	2598
15	TI2D3	3	6	3	2	1.65	3.5	11881	2073
16	TI3.33D3	3	6	1.8	3.33	1.85	2.1	7128	2612

A high-resolution camera (Prosilica GT 1910c CCD, Germany) with an image grabbing speed of 20 frames per second was placed perpendicular to the tank with 1.4 m from the tank to capture the experimental images of bubble plumes and segregation of bubbles along the bubble plume. The camera was fitted with either a 90-mm Kowa F 1.8

(Kowa, Japan) or an 18–55 mm AF-Sinkkor, 13.5–5.6 GII (Nikon, Japan) lens. The high-resolution images were utilized to visually examine the effect of bubble impact by twin inclined bubbly jets with different experimental configurations. The time history and snapshot images of bubbly jet-plumes are shown in Figures 6.2, 6.3, and 6.4.

Furthermore, a double-tip optical fiber probe with an optoelectronic unit (RBI instrumentation, Meylan, France) was employed to measure bubble characteristics such as bubble size, bubble velocity, and bubble concentration along the vertical axis of the jet. Measurements were performed after the two bubbly jet streams collided to characterize bubble properties in the developed region of bubbly jet-plumes. The module of the RBI probe emits infrared light via two fiber-optic cables to the light sensors of the probe in order to measure bubble characteristics. The probes' tips are 15 mm long, 2.5 mm apart, and two sapphire crystals were installed at the end of the probe's tips (see Figure 6.1). The emitted light is refracted when the probe's sensor is in water and is reflected in the module when the probe's sensor is in the air (i.e., inside a bubble). The reflected light passes through a semi-transparent mirror combined with a prism towards a photosensitive diode in the module. The light transmission system enables the probe to acquire voltage signals with a sampling rate of 1 MHz (RBI User Manual, Meylan, France).

The raw signals are directly amplified and detected through a threshold technique from the manufacturer's software (ISO Lite Software, RBI Optical probe, France). The analog signals are converted to a two-state signal corresponding to the phases of air and water. The raw voltage signals were utilized to extract more information from the outputs of the RBI measurement system (Behzadipour et al., 2022a). The double-tip optical fiber probe is capable of measuring bubble size, void fraction (i.e., bubble concentration), and bubble frequency by analyzing the digitalized voltage signals. In addition, bubble velocities are calculated by cross-correlation of voltage signals from the two sensors of the probe. The RBI double-tip optical fiber probe has been successfully employed in many research studies. The accuracy and robustness of the system have been verified in measuring bubble characteristics of many different two-phase gas-liquid flows (Rensen and Roig, 2001; Boes and Hager, 2003; Kiambi et al., 2003; Chaumat et al., 2005; and Murzyn et al., 2005; Behzadipour et al., 2022a; and Behzadipour and Azimi, 2022).

6.3 Experimental Results

6.3.1 Flow Visualization

The effect of air-water discharge ratio on the motion of bubbles in single vertical bubbly jets was studied by careful visualization of bubbles using high-resolution images. The snapshot images of bubbly jets with air-water discharges of $Q_a = 2$ L/min and $Q_w = 3$ L/min are shown in Figure 6.2. These images show the effect of air-water discharge on variations and magnitude of bubble sizes along the axis of the plume. As can be seen, by increasing the nozzle diameter from 3 mm to 4.2 mm, smaller and uniform bubbles are formed.

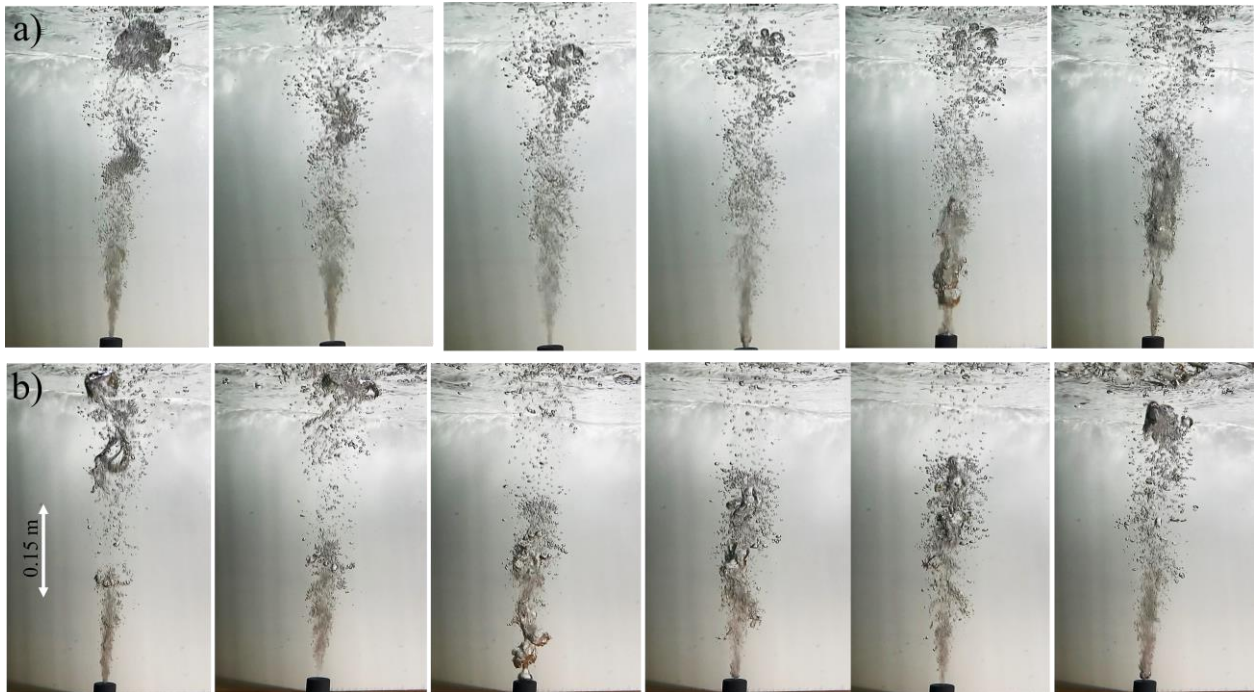


Figure 6. 2: Images of time variations of single vertical bubble jet with $Q_a = 2$ L/min and $Q_w = 3$ L/min ($Q_a/Q_w = 0.67$). The time step between each image is 0.05 second: a) $d_o = 3$ mm; b) $d_o = 4.2$ mm.

In order to investigate the effect of the air-water discharge ratio on variations of bubble dynamic in twin inclined bubbly jets, the time-series images of twin inclined bubble jet are shown for Tests No.14 ($Q_a/Q_w = 1.11$) and No.16 ($Q_a/Q_w = 3.33$). The time step between each image is 0.05 seconds. As it can be seen in Figure 6.3, the cloud of bubbles increased significantly as the air-water discharge ratio increased from 1.11 to 3.33. The

average values of bubble concentration, obtained from image analysis, increased with an average value of 45.9% as discharge ratio increased from 1.11 to 3.33.



Figure 6. 3: Time-series images of Twin-Inclined (TI-Series) bubble jets. The time step between each image is 0.05 seconds: a) Test No.14 (TI1.11D3); b) Test No.16 (TI3.33D3).

Figure 6.4 shows the snapshot images of bubbles to study the effects of inclined nozzle configuration on formation of bubble jet and bubble size distribution at a certain distance from the nozzle. A comparison between the images in Figures 6.4a and 6.4b indicates that the bubble concentration generated by a twin inclined nozzle configuration is higher than that of single vertical nozzle. Image analysis of the raw images indicated that bubble concentration increased with an average of 23.1% as nozzle configuration changed from single vertical to twin inclined. Similar comparison in higher discharge ratio (see Figures 6.4c and 6.4d) illustrates that due to increasing the discharge ratio, Q_d/Q_w , from 0.66 to 3.33, the average bubble concentration increased by 6.5%.

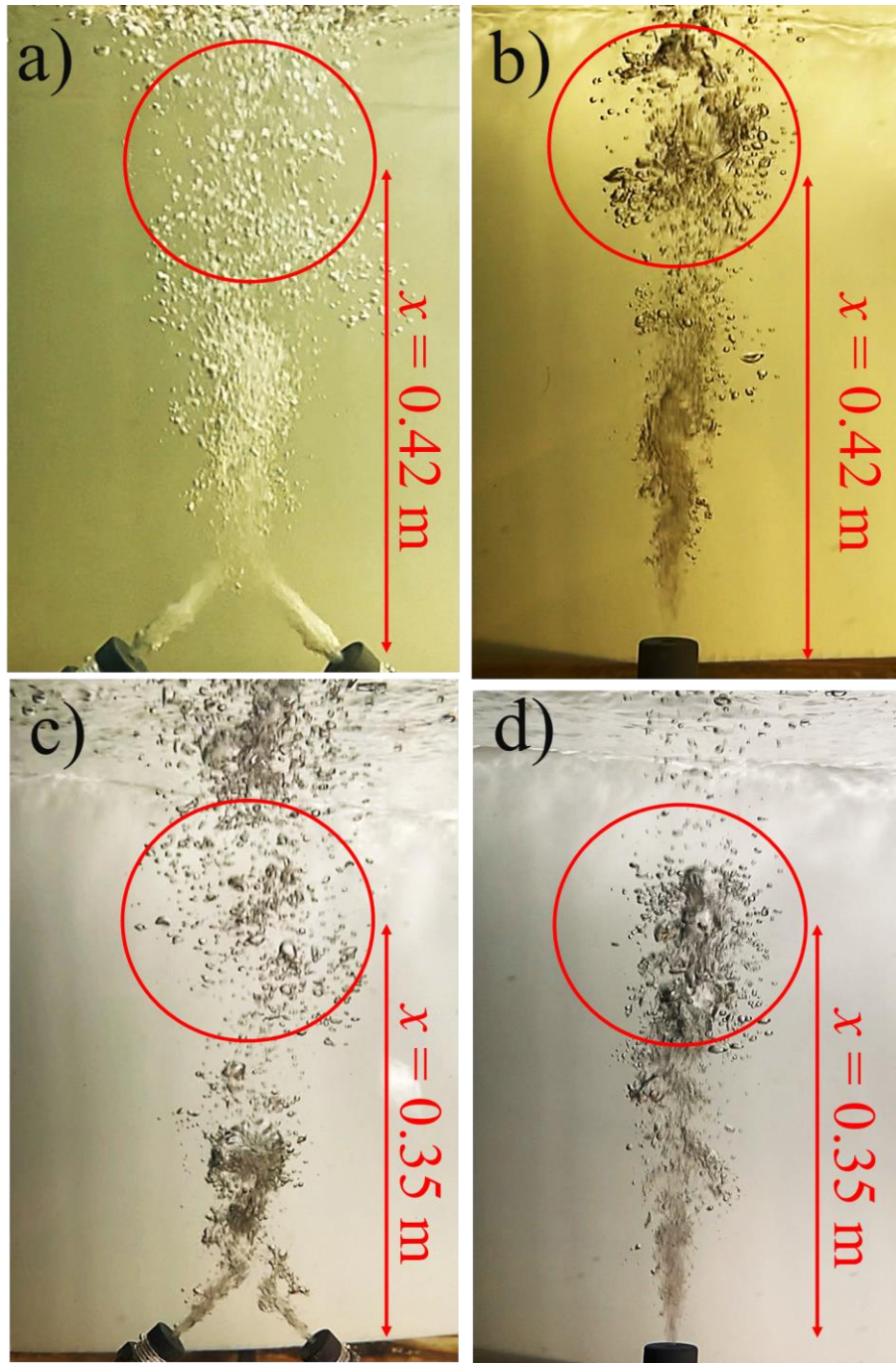


Figure 6. 4: Snapshot images of bubbles showing the effects of inclined nozzles on formation of bubble jet and bubble size distribution at a certain distance from the nozzle: a) Test No.14, TI1.11D3, $x/d_o = 140$; b) Test No.2, SV1.11D3, $x/d_o = 140$; c) Test No.16, TI3.33D3, $x/d_o = 117$; d) Test No.4, SV3.33D3, $x/d_o = 117$.

6.3.2 Bubble diameter, concentration, and velocity

The effect of nozzle configuration on the time history of instantaneous bubble velocity for $Q_a/Q_w = 0.67$ are shown in Figure 6.5. Measurements were taken at $x/d_o = 103$. Figure 6.5a and 6-5b show the time history of bubble velocity in Single Vertical and Twin Inclined bubbly jets, respectively. The time-averaged velocities were plotted as horizontal lines to indicate the magnitude of velocity fluctuations. As can be seen, a change in nozzle configuration from single vertical to twin inclined reduced the time averaged bubble velocity by 21%. For this case, oxygen transfer is expected to increase along the vertical axis of bubble jets as nozzle configuration changes from single vertical to twin inclined.

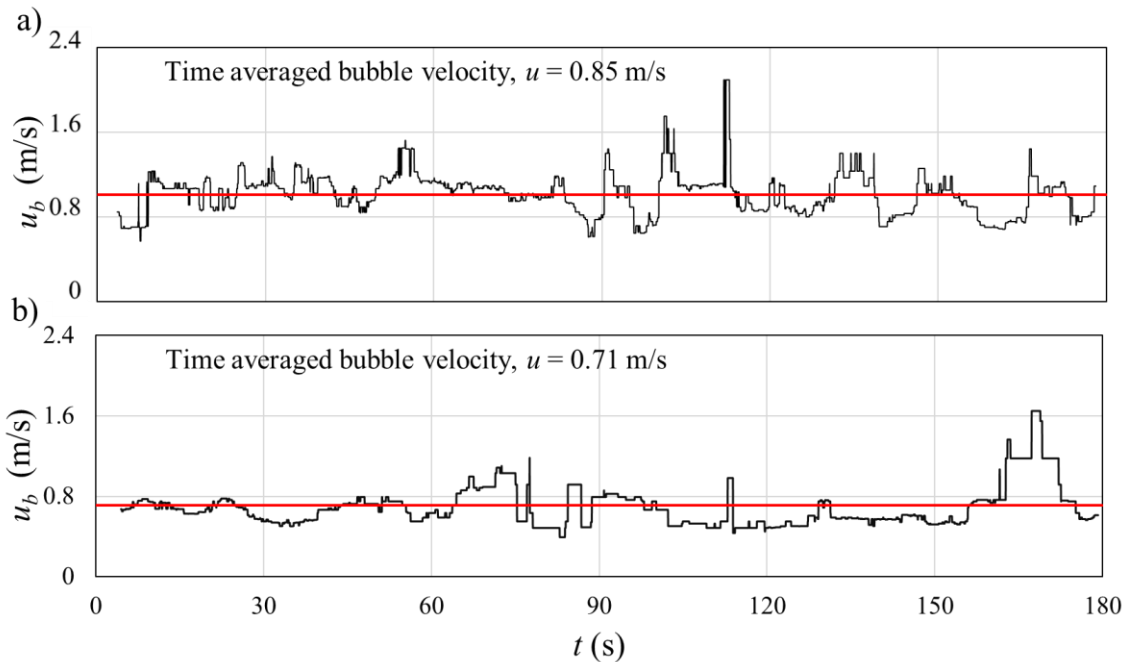


Figure 6. 5: Effect of air injection configuration on the time-histories of bubble velocity at $x/d_o = 103$ for $Q_a/Q_w = 0.67$: a) Test No.1 (SV0.67D3); b) Test No.9 (TI0.67D2.1).

Figure 6.6 shows the effects of air-water discharge ratio on variations of bubble velocity and bubble size along the vertical axis of single vertical and twin inclined bubbly jets. Figure 6.6a shows the vertical variations of bubble velocity in single vertical bubbly jets. The proposed equation for prediction of bubble velocity in bubble plumes (i.e., $Q_w = 0$ L/min and $Q_a = 6$ L/min) from the study of Behzadipour et al. (2023) was also added in Figure 6.6a for comparison. As can be seen, bubble velocity in single vertical bubbly jets increases with increasing the distance from the nozzle and reaches its maximum value at

$x/H = 0.3$ ($x/d_o = 100$). For $0.3 < x/H < 0.45$ (i.e., $100 < x/d_o < 150$), bubble velocity is constant with x and decreases as bubbles reach the water surface. Bubble velocity increases in bubbly jets due to momentum transfer from the water phase of the jet and reaches to a distance from the nozzle at which the excess momentum due to the water discharge is dissipated due to entrainment. At this stage, bubble velocity follows the same trend as bubble plumes. The effect of discharge ratio on bubble velocity indicates that the minimum bubble velocity occurs for $Q_w \approx Q_a$ and the maximum bubble velocity occurs for $Q_a/Q_w = 2$.

Figure 6.6b shows the vertical variations of bubble velocity in twin inclined bubbly jets. A comparison between Figure 6.6a and 6-6b for $Q_a/Q_w = 2$ (i.e., solid squares) indicates a relatively higher values of bubble velocities in twin inclined bubbly jets. It is observed that as the water discharge decreases (i.e., $Q_a/Q_w = 3.33$), bubble velocities for both single vertical and twin inclined bubbly jets decrease with average values of 23.1% and 19.5%, respectively. A comparison between the present experimental data and the proposed equation from the literature indicated a good agreement in prediction of time-averaged bubble velocity along the axis of the plume for $0.3 < x/H < 0.45$. Experimental results indicate that the average bubble velocity along the x -axis for the four tested discharge ratios reduced by 32%, 19%, 25%, and 11%, as the single vertical bubble jet changed to the twin inclined configuration.

Figures 6.6c and 6.6d show the vertical variations of bubble size in single vertical and twin inclined bubbly jets, respectively. A comparison between single vertical and twin inclined bubbly jets in Figures 6.6c and 6.6d show that as the discharge ratio increases from 0.67 to 1.11, bubble mean diameter increases with average value of 42.3%. An increase in discharge ratio from $Q_a/Q_w = 1.11$ to 2 reduces bubble mean diameter by 38.2%. A further increase in discharge ratio from $Q_a/Q_w = 2$ to 3.33, increases the mean bubble diameter by 44.1%. A comparison between single vertical and twin inclined bubble jets shows that the average bubble diameter increases by 10.3%, which indicates that twin inclined jets produce larger bubbles for the same experimental conditions. The proposed formula from the experimental study of Herringe and Davis (1976) on single bubbly jets is also added in Figure 6.6c.

$$x = 0.189d_b^{\frac{1}{2.0229}} \quad (6.1)$$

The experimental study of Herringe and Davis (1976) on air-water mixtures (Eq. 6.1) has shown that the average mean bubble diameter increased with the distance from the nozzle by a maximum value of 34%. The comparison indicates that good agreement between experimental test and the proposed model by Herringe and Davis (1976). Experimental results indicate that average bubble size along the x -axis for the four tested discharge ratios decreased by 50%, 40%, 14%, and 13% as the nozzle configuration changed from single vertical to twin inclined.

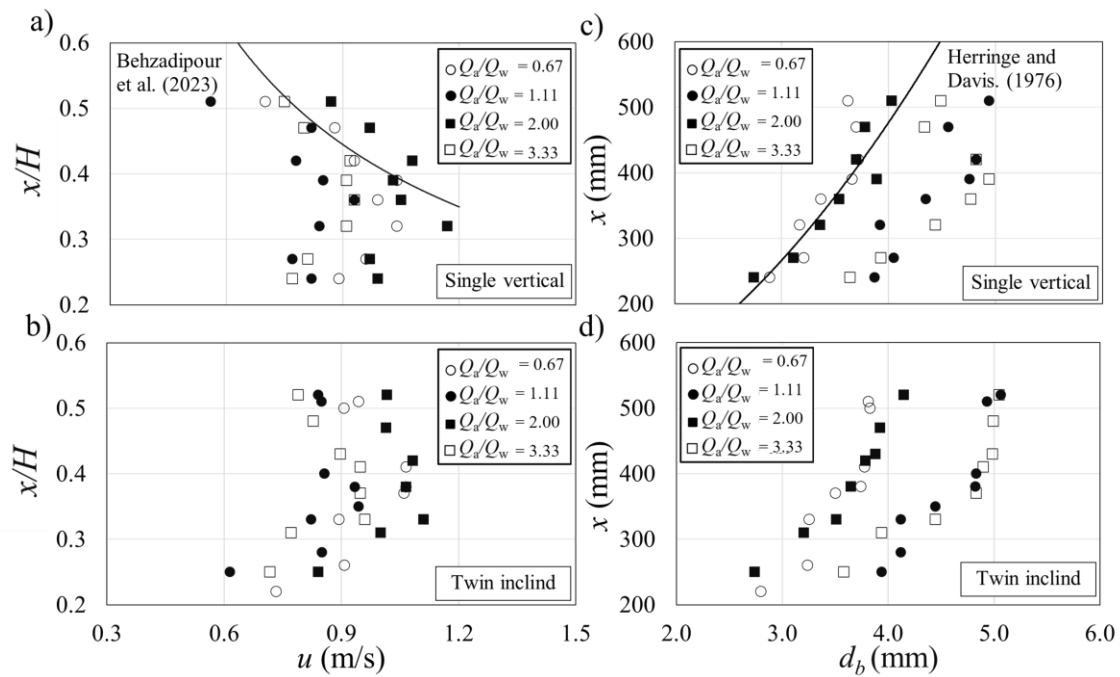


Figure 6. 6: Variations of bubble size and velocity along the vertical axis of bubbly jet with different air-water discharges: a) variations of bubble mean velocity in Single Vertical (SV-Series) bubbly jets; b) variations of bubble mean velocity in Twin Inclined (TI-Series) bubbly jets; c) variations of bubble mean size in Single Vertical (SV-Series) bubbly jets; d) variations of bubble mean velocity in Twin Inclined (TI-Series) bubbly jets.

Figure 6.7 shows the variation of normalized bubble velocity with normalized vertical distance from the nozzle, x/H , for single vertical and twin inclined nozzle configurations. As it can be seen, for the same discharge ratio, Q_a/Q_w , the values of

normalized velocity in twin inclined tests are smaller than the single vertical tests. It is deduced that in twin inclined bubble jets, by increasing the elevation from $x/H = 0.41$ to 0.69 , the normalized vertical velocity reach higher values than the single vertical bubble jets with an average of 5.6%. As can be seen from Figure 6.7a, the peak bubble velocity ranged between 1.02 and 1.2 times of the depth average velocity, and they occur at $x/H = 0.5$. Bubble velocities reduced after the peak and reached to their minimum at the water surface. Similar profile was observed in bubble velocity distribution of twin inclined bubbly jets with smaller peak velocities ranged between 1.0 and 1.1 times of the depth averaged velocity and bubble velocity slightly decreased after the peak.

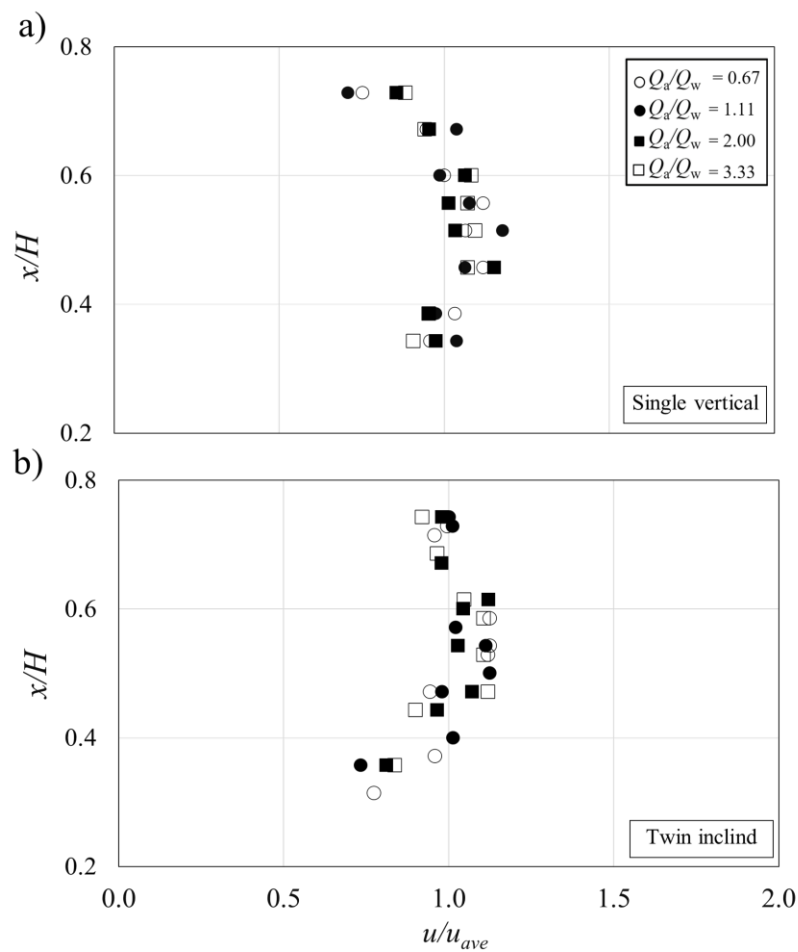


Figure 6. 7: Variations of the normalized bubble velocity with normalized vertical distance from the nozzle in bubble jet with different air–water discharges with same nozzle diameter sizes: a) Single Vertical (SV-Series) bubbly jets; b) Twin Inclined (TI-Series) bubbly jet.

Figure 6.8 illustrates the variations of bubble interfacial area, a , and bubble concentration, C_b , along the vertical axis of bubble jets for both single vertical and twin inclined bubbly jets and for different discharge ratios. The proposed equation for the vertical variations of bubble interfacial area of bubble plume (i.e., $Q_w = 0$ L/min and $Q_a = 6$ L/min, Behzadipour et al., 2023) was added in Figure 6.8a for comparison. A comparison between the present experimental data and proposed equation of Behzadipour et al. (2023) indicated a good agreement in prediction of time-averaged bubble velocity along the axis of the plume and jet.

$$\frac{x}{H} = 0.326a^{-4.046}$$

(6.2)

A comparison between the presented data in Figures 6.8a and 6.8b indicates that increasing the discharge ratio Q_a/Q_w from 0.66 to 1.11, 1.11 to 2, and 2 to 3.33, the bubble interfacial area significantly increases with average values of 1.1%, 42.2%, and 12.1%, respectively (see Figure 6.8a) and for twin nozzle tests reach average values of 2.1%, 45.2% and 14.2%, respectively (see Figure 6.8b). As can be seen from the results, it is concluded that the values of interfacial area for two conditions of single and twin inclined nozzle reach the maximum values of interfacial area for $Q_a/Q_w = 2$.

Figure 6.8c and 6-8d show the variations of bubble concentration in single and twin bubbly jets. As can be seen in Figure 6.8c, increasing the discharge ratio from $Q_a/Q_w = 0.66$ to 1.11, 1.11 to 2, and 2 to 3.33, significantly increased bubble concentration in single vertical bubble jets with average values of 3.2%, 31.4%, and 13.1%, respectively. Figure 6.8d shows similar correlations for twin inclined bubbly jets and increasing discharge ratio increased bubble concentration with average values of 3.1%, 35.3%, and 15.2%, respectively. Comparisons among the experimental tests with different nozzle configurations show that changing nozzle configuration from single vertical to twin inclined reduced bubble concentration by 8.2%. Far from the nozzle, the values of interfacial area and bubble concentration decreased almost linearly and the minimum bubble concentration and interfacial bubble were found to be located at the water surface. The proposed equation of Lime Neto (2015) on single vertical bubble jet with a discharge

ratio (Q_a/Q_w) from 0.5 to 1.5 and nozzle diameter from $d_o = 4$ mm to 9 mm was added in Figure 6.8c for comparison. The proposed model by Lima Neto (2015) is applicable for air and water injection and it is expressed as:

$$\frac{x}{H} = C_b^{-1.25} \quad (6.3)$$

Their result revealed that bubbly jets presented a decay in correlation of C_b with x following a slope of $-5/4$ [i.e., $C_b \sim x^{-5/4}$], which is very close to that of single-phase buoyant jets. Thus, bubbly jets and single-phase buoyant jets with the same values of Fr are expected to present a similar decay rate of C_b with x . A comparison between Eq. (6.3) and experimental results for single vertical bubbly jets indicates a good agreement between experimental test and Lima Neto's proposed equation after modification for discharge ratio. The modified equation is applicable for $0.67 \leq Q_a/Q_w \leq 3.33$ and it is expressed as:

$$\frac{x}{H} = 0.5751 C_b^{-0.716} \quad (6.4)$$

Based on experimental observations, switching from single vertical nozzle to twin inclined nozzle, the highest reduction on the average bubble concentration occurred in $Q_a/Q_w = 0.67$ with 26% reduction and the highest enlargement for average bubble interfacial area happened at $Q_a/Q_w = 3.33$ with 37% enhancement.

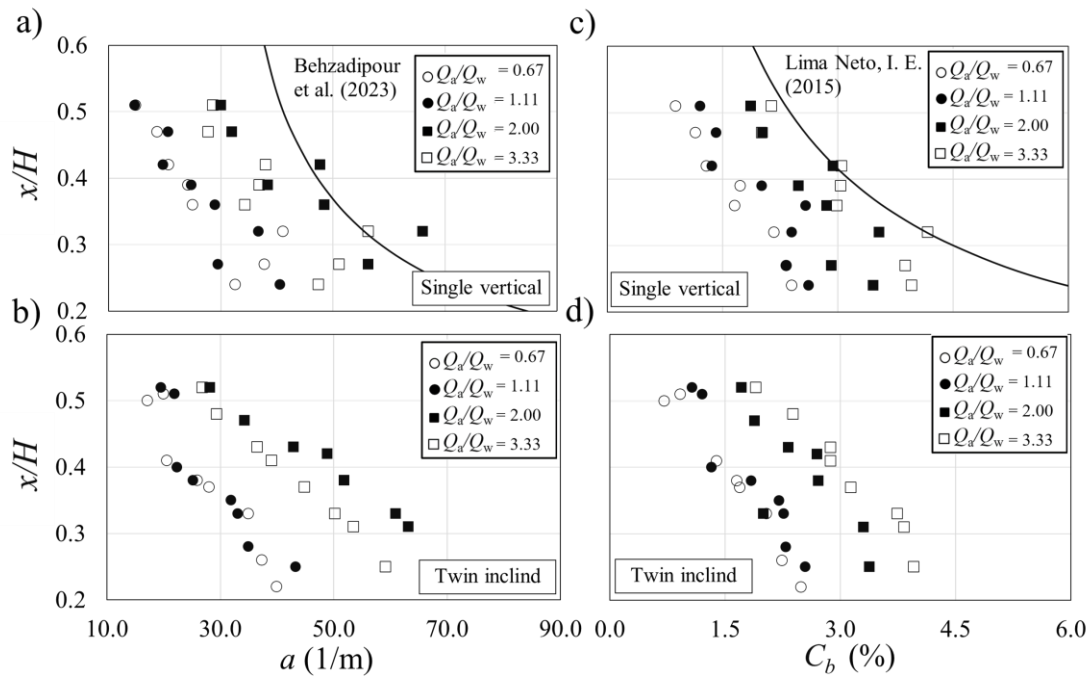


Figure 6. 8: Variations of bubble interfacial area and concentration along the normalized vertical distance of bubbly jet with different air-water discharges: a) variations of bubble mean velocity in Single Vertical (SV-Series) bubbly jets; b) variations of bubble mean velocity in Twin Inclined (TI-Series) bubbly jets; c) variations of bubble mean size in Single Vertical (SV-Series) bubbly jets; d) variations of bubble mean velocity in Twin Inclined (TI-Series) bubbly jets.

6.3.3 Bubble Reynolds number and bubble frequency

Figure 6.9 shows the vertical variations of bubble Reynolds number, Re_b , and bubble frequency, f_b , for single vertical (e.g., Tests No.1 to 4) and twin inclined (e.g., Tests No.13 to 16) bubble jets. As can be seen, the variations of bubble Reynolds number in single vertical and twin inclined nozzle configuration indicate that the maximum bubble Reynolds number occurs at the highest value of discharge ratio (i.e., $Q_a/Q_w = 3.33$). In addition, the maximum bubble Reynolds number occurred at $x/H = 0.41$ which is equivalent to $x/d_o = 137$. Bubble Reynolds number increased significantly as discharge ratio increased from $Q_a/Q_w = 0.66$ to 1.11, 1.11 to 2, and 2 to 3.33 with average values of 4.2%, 6.3%, and 12.2%. A comparison between nozzle configurations with a constant discharge ratio indicates that bubble Reynolds numbers in twin inclined configuration are more than that of single vertical nozzle configuration with an average value of 23.5%.

Figures 6.9c and 6.9d shows the vertical variations of bubble frequency in both nozzle configurations and different discharge ratios. Bubble frequency reached a peak value at approximately $x = 0.3H$ and linearly decreased afterwards. The twin inclined nozzle configuration showed 15.2% reduction on the average values of bubble frequency. Experimental observations expound that the maximum values of bubble frequency are attained in discharge ratio of $Q_a/Q_w = 2$.

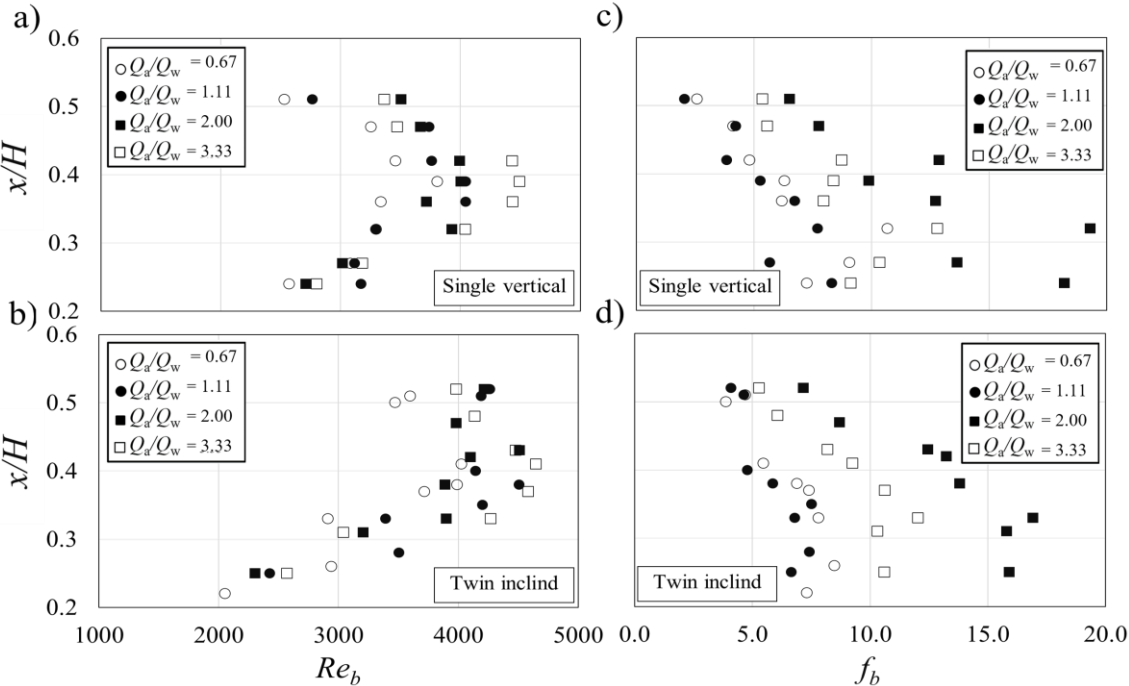


Figure 6. 9: Variations of bubble Reynolds number and bubble frequency along normalized vertical distance of bubbly jet with different air-water discharges: a) variations of bubble mean velocity in Single Vertical (SV-Series) bubbly jets; b) variations of bubble mean velocity in Twin Inclined (TI-Series) bubbly jets; c) variations of bubble mean size in Single Vertical (SV-Series) bubbly jets; d) variations of bubble mean velocity in Twin Inclined (TI-Series) bubbly jets.

6.4 Discussions

One of the operation parameters in reducing bubble velocity and increasing the contact time between bubbles and surrounding ambient is to reduce initial velocity of bubbles by increasing nozzle diameter for the same air and water discharges. Laboratory experiments were repeated with larger nozzle diameters to study the effects of initial

velocity reduction on bubble characteristics for both Single Vertical and Twin Inclined bubbly jets. Figure 6.10 shows the effects nozzle diameter, nozzle configuration, and air-water discharge ratio on variations of bubble velocity profile. Each subplot in Figure 6.10 shows the effect of different air-water discharge ratio, the square symbol shows the results of reduced initial velocity, the open and solid symbols show the SV and IT series, respectively. To analyze the effect of initial velocity reduction, two sets of nozzles for single vertical and twin inclined were considered in which both SV and TI tests have the same cross section area. The benchmark test (i.e., Set 1) has nozzle diameters of $d_o = 2.1$ mm and $d_o = 3$ mm for SV and IT series, respectively. Nozzle diameters increased in Set 2 from $d_o = 2$ mm to 3 mm in single vertical tests and from $d_o = 3$ mm to 4.2 mm for twin inclined tests. The parameter details of all experiments are listed in Table 6.1.

A comparison among the vertical profile of bubble velocity in single vertical nozzle configuration indicated that by decreasing the initial bubble velocity, the vertical velocity of bubbles slightly increased in $Q_a/Q_w = 0.67$. However, the reduction of initial bubble velocity in twin inclined configuration increased bubble velocity by 5%, 13%, 2%, and 4% for $Q_a/Q_w = 0.67, 1.11, 2$ and, 3.33. Also, our results showed that by increasing the nozzle diameter for single vertical from $d_o = 2$ mm to 3 mm, the mean bubble velocity slightly increased by the average of 3 % for all air-water discharge ratio.

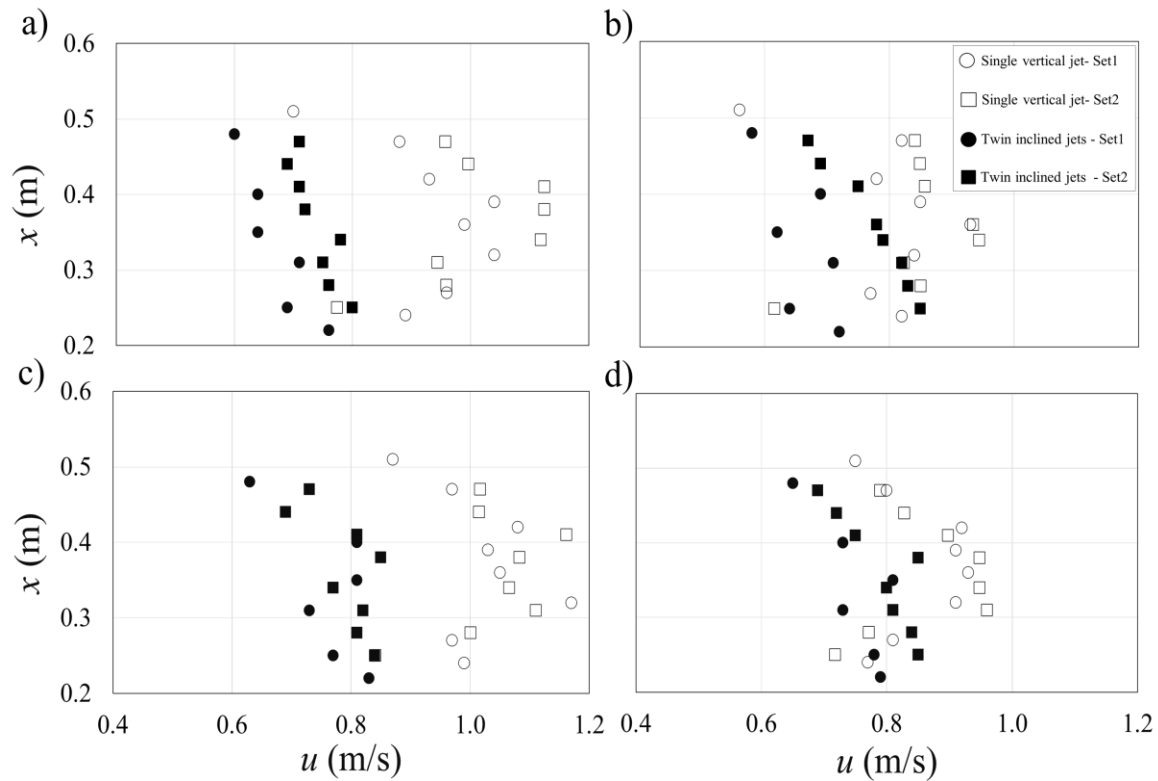


Figure 6. 10: Effects air-water discharge ratio on variations of bubble mean velocity along the vertical axis of Single Vertical and Twin Inclined bubble jets: a) $Q_a/Q_w = 0.67$; b) $Q_a/Q_w = 1.11$; c) $Q_a/Q_w = 2.00$; d) $Q_a/Q_w = 3.33$. Set 1 has a nozzle diameter of $d_o = 2.1$ mm for SV and $d_o = 3$ mm for TI and Set 2 has a nozzle diameter of $d_o = 3$ mm for SV and $d_o = 4.2$ mm for TI.

Figure 6.11 shows the effect of the nozzle diameter size with different type of adjustment of the interfacial area of the jet plume. Figure 6.11a, 6.11b, 6.11c, and 6.11d were plotted for the different ration of the $Q_a / Q_w = 0.66, 1.11, 2$ and, 3.33 , respectively. Comparison among the results of the interfacial area for single vertical nozzle indicated that by increasing the nozzle diameter size, due to raising the $Q_a / Q_w = 0.66, 1.11, 2$ and, 3.33 , change of bubble interfacial area is negligible. On the other hand, Comparison among the results of the interfacial for twin inclined nozzle indicated that by increasing the nozzle diameter size, the values of the interfacial area were increased and due to raising the $Q_a / Q_w = 0.66, 1.11, 2$ and, 3.33 with same experimental conditions, the values of the interfacial area were increased with average of 33.6, 5.5, 9.5, and 6.3 percent. It should be mentioned that this by increasing the values of the fraction $Q_a / Q_w = 0.66$ to 3.33 , the values of the interfacial area are decreased by increasing the elevation from the nozzles position and by

increasing Q_a / Q_w , the slope of this trend is decreased which can be meant that by increasing the ratio of Q_a / Q_w , the interfacial area can reach higher values of the interfacial area at the vicinity of the nozzles for both types of the adjustment.

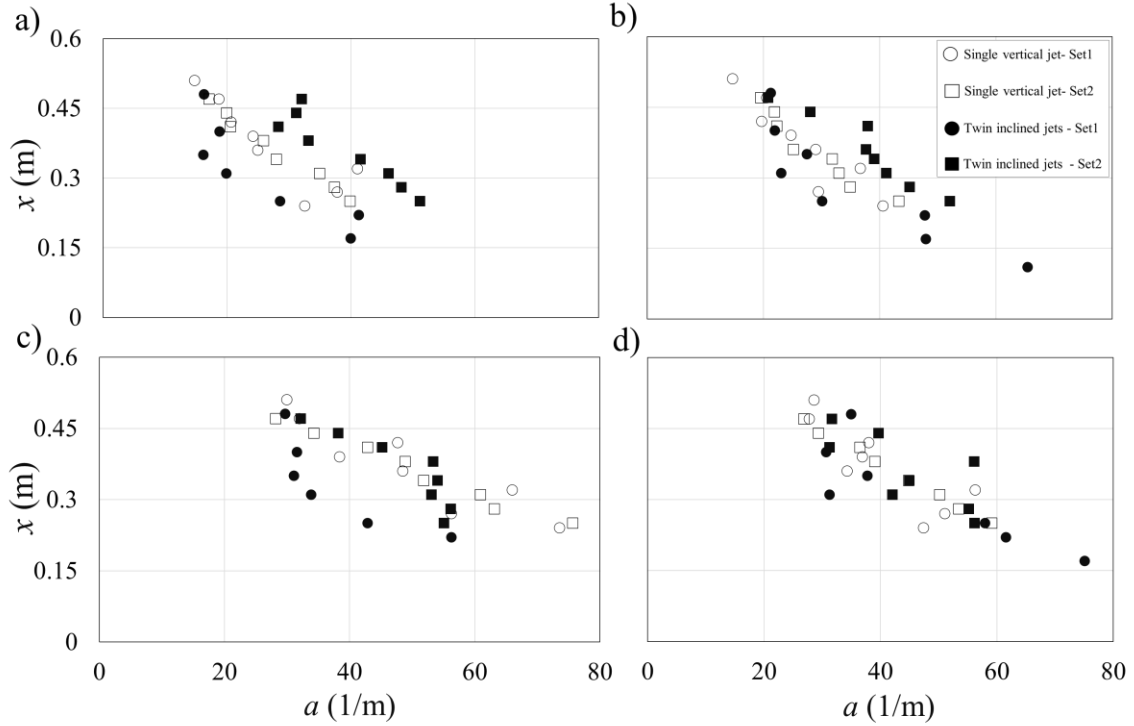


Figure 6. 11: Effects of air-water discharge ratio on variations of bubble interfacial area along vertical axis in both vertical and Inclined on the bubble jet: a) $Q_a / Q_w = 0.67$; b) $Q_a / Q_w = 1.11$; c) $Q_a / Q_w = 2.00$; d) $Q_a / Q_w = 3.33$. Set 1 has a nozzle diameter of $d_o = 2.1$ mm for SV and $d_o = 3$ mm for TI and Set 2 has a nozzle diameter of $d_o = 3$ mm for SV and $d_o = 4.2$ mm for TI.

Figure 6.12 show the variation of the drag coefficient with the values of the bubble Reynolds number for tests with different nozzle types such as single vertical nozzle and twin inclined nozzle. The drag coefficient is calculated by equating the drag force imposed by the bubbles to their buoyancy, as shown in the following equation (Lima Neto et al., 2008b):

$$C_D = \frac{4d_b g \Delta \rho}{3 \rho_w u_b^2} \quad (6.5)$$

where $\Delta\rho = \rho_w - \rho_a$, in which ρ_w and ρ_a are the densities of water and air, respectively. For test with vertical single nozzle by increasing the ratio of Q_a/Q_w from 0.66 to 1.11 the values of the drag coefficient increased marginally with average of 103.2% and by increment of the Q_a/Q_w from 1.11 to 2, the values of the coefficient discharge decreased with average rate of 97.2%. Finally, due to increment of the Q_a / Q_w from 2 to 3.33, the values of the coefficient discharge with increased with average of the 99.2%. It seems that the variation of the coefficient discharge for vertical nozzle is stationary and by increment of the Reynolds bubble number, the variation of the drag coefficients is negligible; however, the variation of the drag coefficients is decreased with slight incline by increment of the Reynolds bubble number for tests with inclined twine nozzles. It is deduced that by switching the vertical single nozzle with inclined twin nozzles, the variation of the drag coefficients are depends two on the Reynolds bubble number which is assumed that had a negligible impact on the variation of the drag coefficients of the vertical single nozzle.

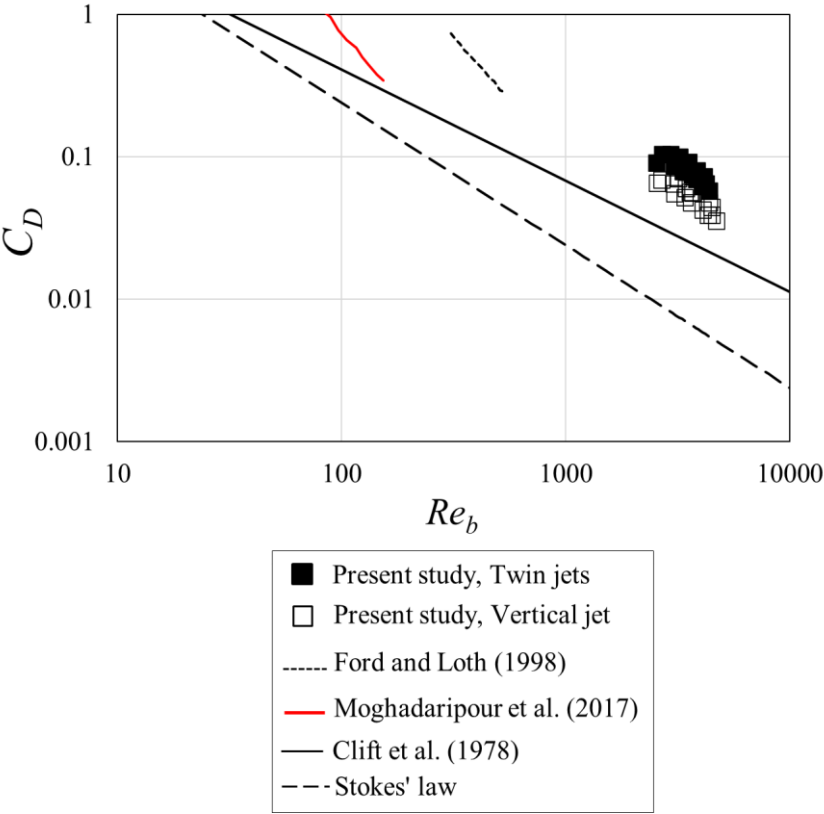


Figure 6. 12: Variation of drag coefficient with bubble Reynolds number: a) Single Vertical bubble jets (SV-Series, Tests No.1 to 4); b) Twin Inclined bubble jets (TI-Series, Tests No.13 to 16).

6.5 Conclusions

A series of laboratory experiments was carried out to study the effects of the effect of different nozzle configuration, including single vertical and two inclined nozzles with same area on the two-phase flow structure of air-water bubbly jets in a still water tank. Hydrodynamics and mass transfer characteristics of jet aeration systems composed of air-water bubbly jets injected vertically and with two inclined nozzles in stagnant water has been studied. The range of air discharge was between 2 L/min and 6 L/min and water discharge were 1.8 L/min and 3 L/min with nozzle diameters were 3 mm for vertical nozzle and 4.2 mm for twin nozzles which formed strong bubble jets. The primary indicators of bubbles such as bubble size, bubble concentration, velocity and bubble Reynolds number were measured along the vertical axis of the jet with a state-of-art RBI bubble probe. Results showed that the diameter size of the bubbles along the vertical ax are increased significantly with average of the 42.3% for $Q_a / Q_w = 0.66$ to 1.11. Also, it was found that by increasing the $Q_a / Q_w = 1.11$ to 2, the average of the bubble diameter sizes is fell marginally with average of 38.2%. Also, due to $Q_a / Q_w = 2$ to 3.33, the average of the bubble diameter sizes is raised with average of 44.1%. Comparing among the experimental test with different number of the nozzle show that due to switching the single nozzle with twin nozzle, the average of the bubble diameter sizes are increased with average of the 10.3% which in turn show that the impaction between the inclined nozzle jets can increase the bubble dimeter size for same experimental conditions. Results showed that not only the average bubble velocity along the x axes from the single vertical jet to twin inclined jet reduced by 32%, 19%. 25% and 11%, but also, the average bubble size decreased by 50%, 40%. 14% and 13%, for air to water discharge ratios of 0.67, 1.11, 2, and 3.33, respectively. Decreasing the bubble velocity and bubble diameter which lead to increase in bubble interfacial area, are the key parameters to enhance the oxygen transfer in bubble jet. Experimental tests with different number of the nozzles showed that due to switching the single nozzle with twin nozzle, the average of the bubble concentration is decreased with average of the 8.2% and by increasing the elevation. Moreover, it was seen that the most reduction in average bubble concentration happened at $Q_a / Q_w = 0.67$ for 26% and the most enlargement for average bubble interfacial area happened at $Q_a / Q_w = 3.33$ for 37%, which both help to increase the rate of oxygen transfer. Finally, results revealed that due to equal

rate of the Q_a / Q_w for single vertical nozzle and twin inclined nozzle, the values of the bubble Reynolds number for twin inclined nozzle are much more than the single nozzle. As a result, twin inclined nozzle could generate the bubble Reynolds number than the single vertical nozzle with average of the 23.5%. Increasing the nozzle diameter from $d_o = 2$ mm to 3 mm in twin inclined configuration increased bubble velocity by 5%, 13%, 2%, and 4% for $Q_a/Q_w = 0.67, 1.11, 2$ and, 3.33. Finally, results indicated that bubble interfacial area increased by average of 33.6, 5.5, 9.5, and 6.3% due to raising the $Q_a / Q_w = 0.66, 1.11, 2$ and, 3.33, when nozzle diameter increased in twin inclined nozzles.

Notation

The following symbols are used in this paper:

a = bubble interfacial area; 1/m

C_b = bubble concentration; vol/vol

C_D = drag coefficient;

D = height of the tank; m

d_b = bubble diameter size; mm

d_o = nozzle diameter; mm

f_b = bubble frequency; Hz

H = height of water, m

L = length of the tank; m

M_{ow} = initial momentum flux of the water phase; m^4/s^2

Q_a = volumetric air discharge; L/min

Q_w = volumetric water discharge; L/min

Re_o = nozzle Reynolds number;

Re_b = bubble Reynolds number;

t = time; s

u = time averaged bubble velocity, m/s

u_{ave} = depth averaged bubble velocity, m/s

u_b = instantaneous bubble velocity; m/s

u_{wo} = initial water velocity; m/s

W = width of the tank; m

x = distance from the nozzle; m

ρ_a = density of air; kg/m^3

ρ_w = density of water; kg/m^3

μ_w = dynamic viscosity of water; kg/m.s.

ν_w = kinematic viscosity of water; m^2/s

Chapter 7

General Conclusions and Recommendations for Future Research

7.1 General Conclusions

In the preceding chapters, comprehensive experimental studies and analyses were presented on the dynamics of bubble plumes and jets. The present chapter provides a general conclusion on the motion of bubbles and proposes some topics for future research.

Detailed laboratory experiments were performed in Chapter 2 to study the effect of grid screen geometry such as grid-screen size and distance from the nozzle on bubble plume hydrodynamics. The experiments were performed in a glass-walled tank of 1.60 m long, 0.85 m wide, and 0.80 m deep. Different airflow rates of $Q_a = 4$ L/min, 6 L/min, and 8 L/min were selected for this study. Experimental results showed that the size of grid-screen and its distance from the nozzle decreased the vertical velocity of bubbles by an average of 38%. Dynamics of bubbles before and after the grid-screen was analyzed and a regime classification was proposed based on variations of the normalized bubble velocity with the distance from the nozzle. The general conclusions on the motion of bubbles passing through a grid-screen are as follow:

- By installing a grid-screen at 0.3 m above the nozzle, the time-averaged bubble concentration increased by 18% and the time-averaged bubble velocity decreased by approximately 31% in comparison with the benchmark test without a grid-screen.
- The size of grid-screen and its distance from the nozzle decreased the vertical velocity of bubbles by an average of 38%.
- The effect of grid-screen on bubble size reduction was more significant in bubble plumes with higher air discharge. Additionally, the experimental results showed that bubble velocity after the grid-screen decreased as the screen opening decreased.
- The bubble size decreased right after the grid-screen. However, it gradually increased as it moved towards the water surface.

- A regime classification was introduced based on the variations of bubble velocity along the axis of the plume.
- Bubble velocity was constant in regime four indicating that the effect of grid-screen was insignificant beyond this position. The distance from the nozzle to a point where bubble velocity reached the equilibrium was defined as a length scale and it was measured for all cases. More detailed information on the conclusions of the proposed chapter can be found in Behzadipour et al. (2022a).

In Chapter 3, the effects of air discharge on bubble dynamics were evaluated by conducting a series of laboratory tests. A pipe with an interior diameter of 3 mm was installed at the bottom of the experimental tank and it was connected to a circular nozzle with a diameter of $d_o = 3$ mm. Different air discharges of $Q_a = 3, 6, 9,$ and 12 L/min were selected. The results showed that bubble characteristics such as bubble interfacial area, bubble frequency, and bubble concentration (also known as gas fraction) significantly varied with the distance from the nozzle and all parameters gradually decreased afterwards. It was found that bubble parameters were independent of air discharge for $x/H < 0.35$, and strong discharge dependency was observed for $x/H \geq 0.35$ where x is the distance from the nozzle and H is the water depth. The general conclusions on the effect of air discharge on bubble dynamics are as follows:

- The most probable bubble size decreased with increasing air discharge, which helped the air (oxygen) transfer with the ambient water.
- Experimental data indicated a direct correlation between air discharge and bubble velocity indicating that the bubble mean velocity increased with increasing discharge.
- The variations of bubble concentration along the vertical axis of the bubble plume indicated that bubble concentration decreased in the plume's centerline due to plume spreading.
- Close to the nozzle, the effect of air discharge on variations of bubble interfacial area was marginal and the interfacial area significantly decreased for $0.24 < x/H < 0.4$.

- The effect of air discharge became significant for $x/H \geq 0.4$ and the interfacial bubble area increased with increasing air discharge indicating a more efficient and stronger mixing with increasing air discharge.
- Bubble frequency increased non-linearly with air discharge and decreased along the vertical axis of the plume. It rapidly decreased at relatively short distance from the nozzle (i.e., $0.25 < x/H < 0.4$) and air discharge came to effect for $x/H \geq 0.4$.

More detailed information on the conclusions of the proposed chapter can be found in Behzadipour et al. (2023).

A series of laboratory experiments was conducted to study the effects of grid-screen and initial plume characteristics on the hydrodynamic forces acting on bubble plume and grid-screen in Chapter 4. Three air discharges of $Q_a = 4, 6, \text{ and } 8 \text{ L/min}$ with two nozzle diameters of $d_o = 1 \text{ mm}$ and 3 mm were tested to form a wide range of bubble Reynolds numbers ranged between 10 and 50. The effects of grid-screen size and its position respect to the nozzle on the primary parameters of bubble plume such as bubble concentration and velocity were evaluated. The general conclusions on the effects of grid-screen and initial plume characteristics on the hydrodynamic forces acting on bubble plumes and grid-screen are as follow:

- An inverse correlation was found between grid-screen size and centerline bubble concentration while the centerline bubble concentration increased with increasing air discharge.
- The direct correlation between bubble concentration and air discharge diminished at the water surface due to bubble coalescence far from the grid-screen. It was found that the effect of nozzle size on bubble concentration is negligible.
- The buoyancy force significantly reduced due to installation of a grid-screen and such reduction increased with increasing air discharge.
- The drag force reduction was found to be correlated with air discharge and it reduced by 18%, 31%, and 53% for $Q_a = 4, 6, \text{ and } 8 \text{ L/min}$, respectively.
- The surface tension forces acting on a grid-screen varied linearly with bubble Reynolds number, Re_b , and the slope of variations was also controlled by Re_b .

- The correlation between surface tension force and Re_b increased by four times in the range of $20 \leq Re_b < 50$.
- The correlation between bubble Reynolds number and the net acting force was defined and an empirical correlation was proposed for proper design of grid-screens.

Detailed laboratory experiments were performed in Chapter 5 to study the effects of sand bed layer in reducing bubble size and increasing the time residence of bubbles in vertically discharged bubble plumes. The larger contact surface between air and water enhances the oxygen transfer between air and water therefore, it is desirable to reduce bubble diameter and velocity to enhance oxygen transfer in bubble plumes. Different airflow discharges were tested as $Q_a = 3$ L/min, 6 L/min, 9 L/min, 12 L/min. To decrease bubble diameter, three sand aggregate sizes were selected ($d_s = 2.76$ mm, 4.76 mm, and 12.5 mm), which were placed to form sand layer thicknesses of $h = 0.10$ m and 0.20 m. The general conclusions on the effects of sand bed layer with different size and thickness on the hydrodynamics of bubbles in vertically discharged bubble plumes are as follow:

- The most probable bubble size was located at the peak of bubble size distribution plot and it decreased from 2.6 mm to 1.1 mm due to the placement of a bed sand. This is approximately equal to 58% reduction in the mean bubble size as the thickness of sand bed increases by 100% (i.e., from $h = 0.10$ m to 0.20 m).
- Increasing sand bed thickness decreased the probability density function of the maximum bubble size by approximately 22.5% as the PDF values decreased from 26.6% to 20.6%.
- A sand bed layer increased the probability of the maximum bubble size by approximately 213%. This indicated the generation of more uniform bubbles in presence of a sand bed layer.
- Increasing the thickness of bed sands from $h = 0.1$ m to $h = 0.2$ m, decreased the mean bubble velocity. For example, at $x/d_o = 67$ and $Q_a = 12$ L/min, the mean

bubble velocity decreased by 26% by increasing the bed sand thickness from 0.10 m to 0.20 m.

- Sand bed increased the averaged bubble concentration by approximately 200%, 262%, and 246% for sand beds with sand diameters of $d_s = 2.38$ mm, 4.76 mm, and 12.5 mm, respectively.
- The interfacial area increased by approximately 32% when air discharge increased from 6 L/min to 12 L/min. It was concluded that, such increase in air discharge enhanced the oxygen transfer rate in bubble plumes.
- It was found that bubble concentration decreased from the nozzle to the water surface by 46% in the case without bed sand when $Q_a = 3$ L/min and $h = 0.10$ m.
- Bubble Reynolds number decreased almost linearly with the distance from the nozzle in bubble plumes without sand bed. The slope of reduction in bubble Reynolds number was found to be $Re_b \sim x/d_o^{-2/3}$.

Chapter 6 presented the results of a series laboratory experiments to study the effects of different nozzle configurations, including single vertical and two inclined nozzles with same cross-sectional area on the two-phase flow structure of air-water bubbly jets in a still water tank. The range of air discharge was between 2 L/min and 6 L/min and water discharge were 1.8 L/min and 3 L/min with nozzle diameters were 3 mm for vertical nozzle and 4.2 mm for twin nozzles, which formed strong bubble jets. The primary indicators of bubbles such as bubble size, bubble concentration, velocity and bubble Reynolds number were measured along the vertical axis of the jet with a state-of-art RBI bubble probe. The general conclusions on the effects of nozzle configuration on the hydrodynamics of bubbles in vertically discharged and twin inclined bubble plumes are as follow:

- The diameter of bubbles along the vertical axis significantly increased with air-water discharge ratio with an averaged value of 42.3% for Q_a/Q_w changing from 0.66 and 1.11.
- By increasing the air-water discharge ratio, Q_a/Q_w from 1.11 to 2, the average bubble diameter marginally decreased with an average value of 38.2%. Also, for

the range of air-water discharge of $Q_a/Q_w = 2$ to 3.33, the average bubble diameter increased with an average value of 44.1%.

- The average bubble velocity along the x -axis from the single vertical jet to twin inclined jet reduced by 32%, 19%, 25%, and 11% for air-water discharge ratios of 0.67, 1.11, 2, and 3.33, respectively.
- The average bubble size decreased by 50%, 40%, 14%, and 13%, for air to water discharge ratios of 0.67, 1.11, 2, and 3.33, respectively.
- A change in nozzle configuration from single vertical nozzle to twin inclined nozzle, decreased the average bubble concentration with an average value of 8.2%.
- The most reduction in the average bubble concentration happened at $Q_a/Q_w = 0.67$ for 26% and the most enlargement for average bubble interfacial area happened at $Q_a/Q_w = 3.33$ for 37%, which both helped to increase the rate of oxygen transfer.
- For equal rate of air-water discharge ratio, Q_a/Q_w , in both single vertical nozzle and twin inclined nozzle, the values of bubble Reynolds number for twin inclined nozzle were found to be much higher than that of the single vertical nozzle.

7.2 Recommendation for Future Research

It is the intention that the findings of current and future work will be integrated to provide knowledge on the performance enhancement of bubble plumes/jets characteristics, in lake management, DAF systems, and in operational wastewater treatment plants. This new and increased knowledge in oxygen transfer process helps to understand how different projects influenced and affected by process variables, which will enable the design and operation of bubble plumes/jets to be optimized. A knowledge on the physical variables and design parameters, such as nozzle configuration, depth of bed sands, grid-screen size and its location, and airflow rate, will enable future investigators to focus on examining the influences of biological and biochemical variables on live respiring systems.

At this interim stage, the following research topics are recommended for future research:

7.2.1 Bubble dynamics in Two-layer domain:

In chapter 3, the effect of different air discharges on the bubble plume hydrodynamics was studied in detail. One of the common methods to mix water with different specifications is the aeration technique. Two-layer flows such as distilled and saline layers can be formed in lakes, ponds, and dam reservoir. Understanding bubble plume characteristics in two-layer flow provides valuable knowledge in this area, which can help for proper design of aerator and validate numerical simulation. For the future studies, it is recommended to employ a series of experimental tests with two layers of water (distilled and saline) to evaluate the mean bubble velocity, bubble size, bubble concentration, and bubble interfacial area along these two layers. Figure 7.1 shows the schematic sketch of the recommended experimental setup to conduct the laboratory tests. Different salinity strength with a wide range of salt concentration is achieved by adding more salt in the water. The average density of ocean water is 1024 kg/m^3 , which the addition of 24 kg in the water density is due to mass of salt. The controlling parameter could be considered by changing the Reynolds number as a combination of nozzle size and initial velocity.

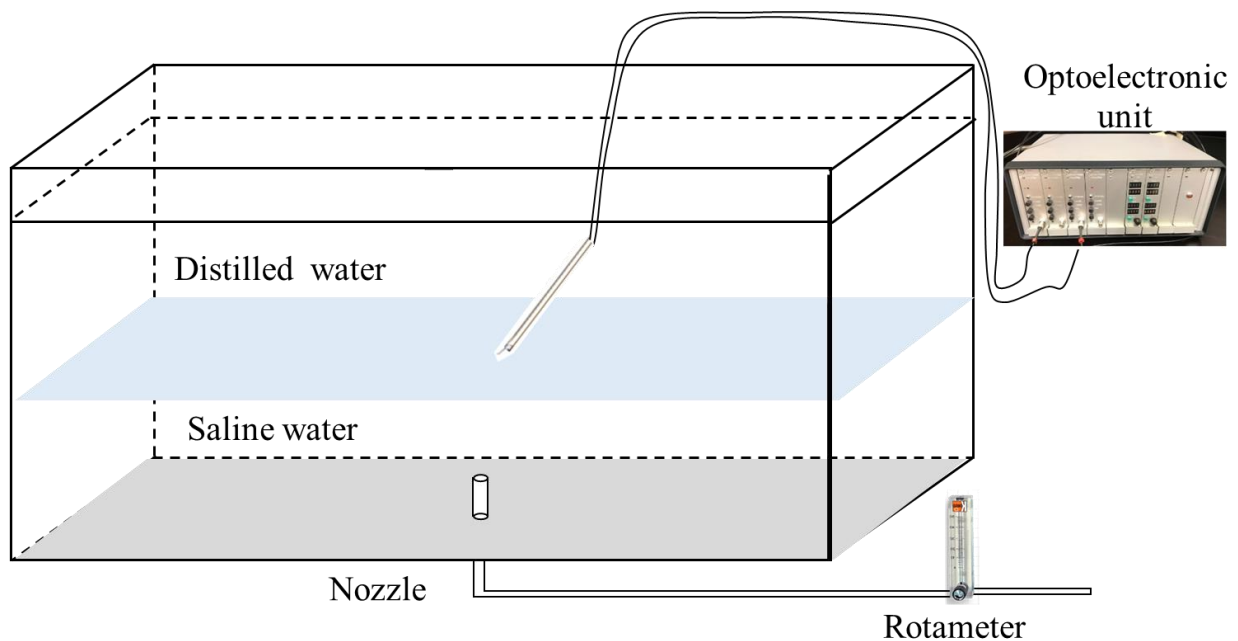


Figure 7. 1: Schematic of the two-layer domain of distilled and saline flow layers in experimental tank and the sketch of the opto-electric unit.

7.2.2 De-stratification in a reservoir mixed by bubble plumes:

Despite all experimental studies in the literature that uses a tank filled up with tap water at room temperature (i.e., $20^{\circ}\text{C} \pm 1^{\circ}\text{C}$), the vertical profile of water density in natural lakes and reservoirs are stratified. During the summer, reservoir stratification negatively affects the quality of water and dissolved oxygen level by preventing natural mixing of water in a daily basis. Strong thermal gradients cause stratification in reservoirs where the surface water temperatures decrease significantly with water depth.

Mixing via bubble plumes has been used in the past as an effective method of de-stratification to reduce the density difference along the depth of reservoirs and natural lakes. Reservoir stratification is formed when there is a temperature gradient within the water column. Thermally stratified water bodies are stable, and mixing is suppressed; these physical effects can have considerable influence on the biological, chemical, and general ecosystem processes of the water body. Correspondingly, summer stratification directly affects the water quality within reservoirs via processes including benthic sediment oxygen demand and decomposition of organic matter, which consume oxygen from the Hypolimnion. Air temperature will increase under future climate change, which will affect stratification; this raises questions over the future applicability of these plumes. Artificial de-stratification (i.e., mixing) is often used in lakes and reservoirs to overcome negative effects of summer stratification. To evaluate bubble-plume performance now and in the future, conducting experiments under different layers of temperature is recommended for reservoir mixing. Thermal stratification results in development of different zones throughout the water column that are segregated by the variations of both density and temperature regimes (Figure 7.2). From the surface down, these zones are referred to as the Epilimnion (in the surface), the Metalimnion (in the middle depth) and the Hypolimnion (in the bottom layer). The Metalimnion contains a sharp temperature gradient known as the Thermocline, which separates the contrasting warm, lower density waters in the Epilimnion and the cold, higher density waters in the Hypolimnion. Thermal stratification, in particular the Metalimnion, acts as a barrier, which limits the natural mixing capabilities of a reservoir.

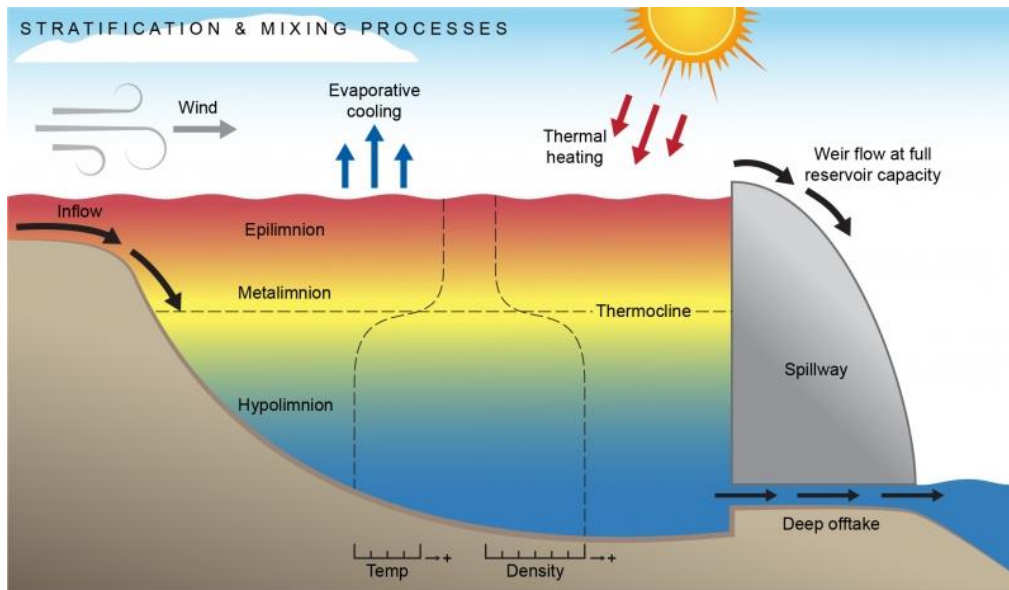


Figure 7. 2: Image of a stratification profile in a reservoir.

<https://www.wrl.unsw.edu.au/sites/wrl/files/uploads/Projects/WRL-TR2021-17-A-review-of-artificial-destratification-techniques-for-cold-water-pollution-mitigation.pdf>

As it can be seen in Figure 7.3 artificial air injection involve pumping compressed air through a pipe network to diffusers typically located in the deepest part of a reservoir.

The main controlling parameters to be measured are as follows:

- Specifications on diffuser design such as nozzle size and geometry, configuration and number of orifices.
- The efficiency of plumes including spacing to optimize interaction between plumes.
- Design optimization of bubble plumes in relation to flowrate.

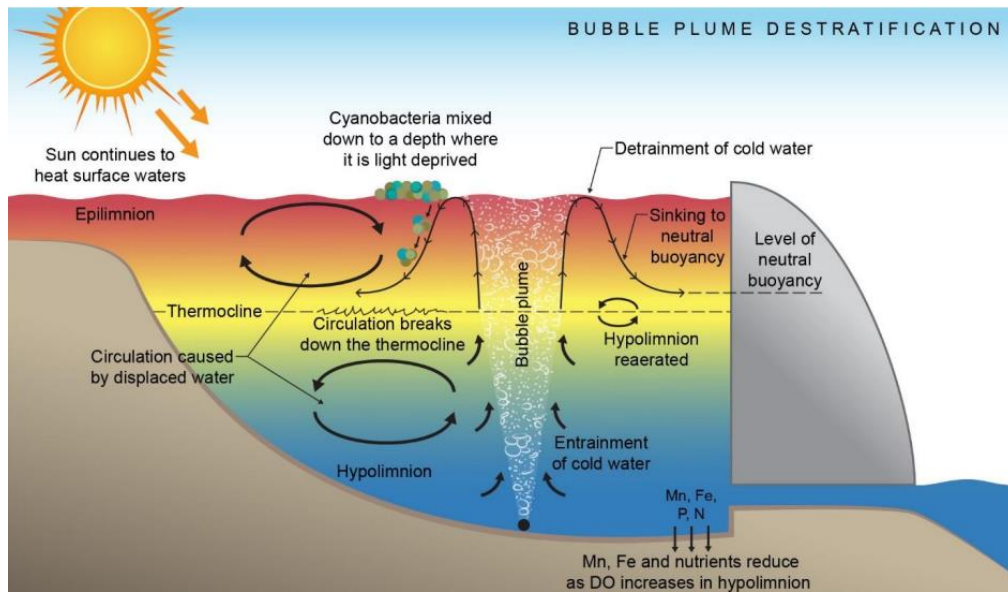


Figure 7. 3: Bubble plume de-stratification in reservoirs.

(<https://www.wrl.unsw.edu.au/sites/wrl/files/uploads/Projects/WRL-TR2021-17-A-review-of-artificial-destratification-techniques-for-cold-water-pollution-mitigation.pdf>)

7.2.3 Numerical simulations of bubble plumes:

Since this research is based on experimental tests, it is suggested to applying numerical models for the purpose of validating experimental results. Physical methods such as implementing grid screen, bed sands, and twin nozzle that has been conducted experimentally in this thesis is helping to enhance oxygen transfer rate and those results could be simulated with the validated numerical models. Grid screens inside a bubble column reactor can serve a number of purposes including the cutting of larger bubbles into smaller ones and thereby increasing the interfacial area (See Figure 7.4). To study the effects of grid-screens on the bubble and liquid hydrodynamics, a new numerical model for cutting of bubbles has been proposed by Jain et al. (2013). They showed that their model is able to predict the hydrodynamic behavior and bubble dynamics, including the cutting of bubbles through wire mesh. It should be noted that they used 49 nozzles with different opening in a confined column reactor, which was completely different from my experimental setup.

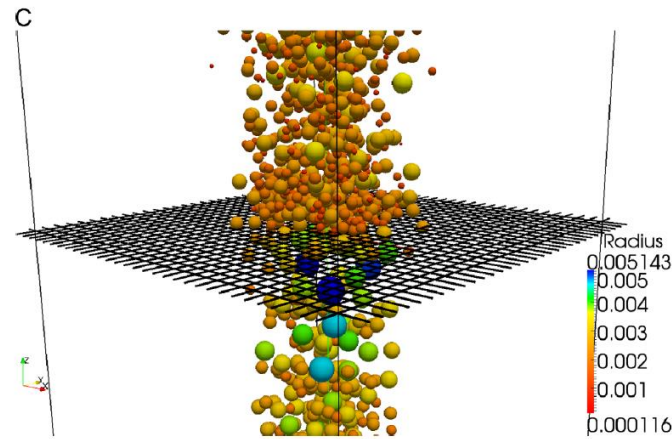


Figure 7. 4: Numerical modeling of grid screen in column reactor by Jain et al. (2013)

An integral model that accounts for most of the physical and chemical processes related to aeration of reservoirs was introduced by Wuest et al. (1992) to facilitate the design for lake restorations. Future study could consider numerical modeling to simulate two-fluid flow by the Computational Fluid Dynamics (CFD) method. Wastewater reservoir aeration involves the simultaneous operation of many bubble plumes. While integral models assume the plume to be isolated, the CFD models are the appropriate tool to study plume–plume, plume–boundary, and plume–crossflow interactions. The two-fluid model can be proposed is based on the general theory of multiphase flows (Drew and Passman, 1998) and has three main components:

- A hydrodynamic component that considers the main physical processes in a free dilute bubbly flow by implementing the increase in effective buoyancy by bubbles, the non-zero slip velocity between the gas and the liquid, and the turbulent dispersion of bubbles.
- A mass transfer component that considers oxygen and nitrogen dissolution from the bubbles and was taken from Wuest et al. (1992).

7.2.4 Bubble dynamics with background turbulence:

Most of the existing laboratory experiments were carried out in stagnant water whereas in reality, bubbles are discharge in an ambient with background turbulence. The background turbulence can be generated by inserting a number of water pumps and generating jet flow with random discharges. Pumping air or air/water from different position in the tank and study the effect of plume/jet turbulence are suggested for future studies. Boundary

conditions such as nozzle geometry, nozzle size and initial air or air-water discharged could be varied to learn bubble plume characteristics. (See Figure 7.5)

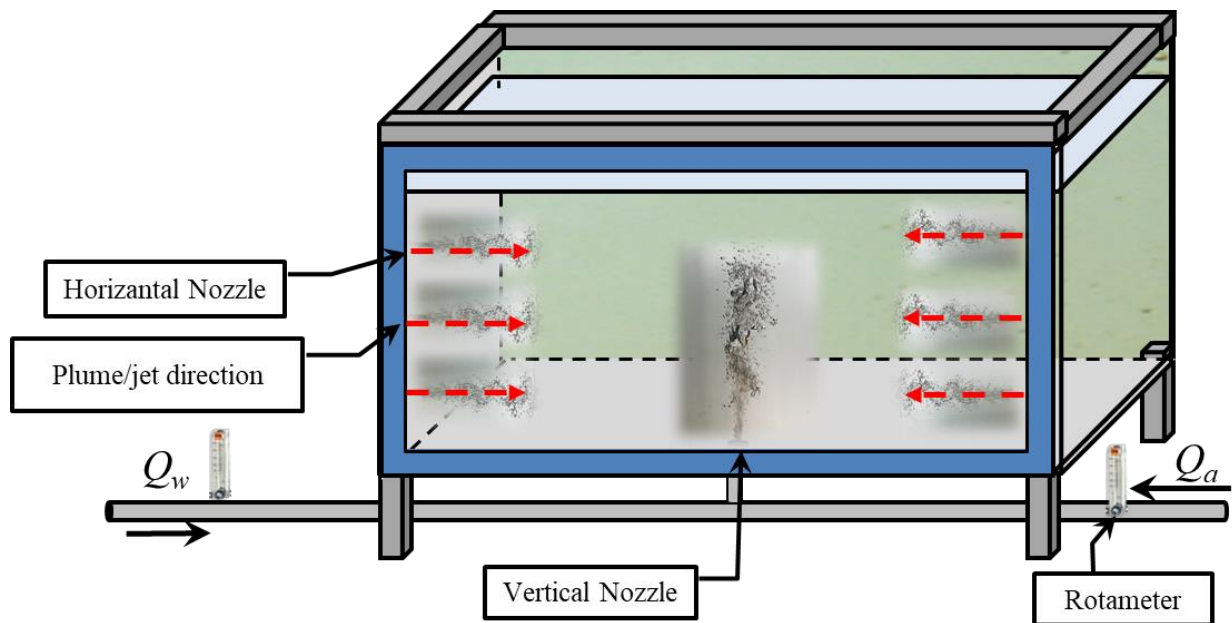


Figure 7. 5: Suggested experimental setup for bubble plume with background turbulence.

Following controlling parameters are suggested to be taken into the account:

- Nozzle size, diameter, configuration, and number orifices.
- Air injection (plume) or air-water injection (jet) with different range of air flow rates and air water ratios.
- Direction of air or air-water injection.
- Position of pumps in the tank.

Appendix 1

Air bubble dynamics in bubble plumes with a grid-screen

1. Introduction

Mixing of air bubbles in ambient water has a lot of applications in industry and environment such as mixing gas and liquid in industrial technologies, natural water reclamation, and water quality improvement. The capacity of bubble plumes to enhance efficient mixing are attained by selecting the governing parameters and optimizing the selected variables in bubble plume. Bubble plumes are considered as multiphase flow and have been recognized as an efficient method of enhancing air/oxygen transfer in lakes, rivers, and wastewater treatment plants. Several studies have been performed to improve the properties of bubble plumes through the water ambient such as using the vertical bubble plume through the shallow lake (Wüest et al., 1992), hydrodynamic of the oscillating bubble plumes (Simiano et al., 2006), and study the effect of ellipsoidal shape of bubbles on airflow mixture through the bubble plumes (Aoyama et al., 2016). The oxygenation of sewage in wastewater treatment plants is also a common application of bubble plumes (Schladow, 1992, 1993). Moreover, air injection into effluent diffusers is an attractive alternative for artificial aeration of water bodies (Lima Neto et al., 2008a). The advantages of bubble plumes over mechanical mixing systems are the simplicity of the design, ease of construction, and acceptable operation cost. Therefore, designing a new structure to improve air injection system in bubble plumes is beneficial and many researchers have promoted the advantages of bubble plume in air and water mixing in comparison to other mechanical mixers (Pacheco and Lima Neto, 2017; Lima and Lima Neto, 2018).

Many geometrical and mechanical parameters in bubble plumes have direct impacts on air-water mixing ratio. Researchers have investigated the effect of bubble plume properties, such as air discharge, nozzle size, initial buoyancy due to density difference between air and water, and turbulent diffusion due to bubble motion (Lima Neto, 2012). The effect of nozzle configuration, single circular nozzle versus a cluster of nozzles, was studied to understand bubble formation in bubbly jets and plumes (Lima and Lima Neto, 2018; Lima

Neto et al., 2008a). Some other aspects of bubble plumes such as the effect of nozzle elevation and air-water mixture ratio (Yapa and Zheng, 1999), the stratification effect on bubble plume properties (Socolofsky and Adams, 2002, 2003), and bubble dynamics in the near field (McGinnis et al., 2004) have been studied in detail. Many research studies have investigated the effect of nozzle diameter and air discharge on the interfacial area of bubbles (Lima Neto et al., 2008a). It was found that an increase in bubble diameter reduced the interfacial area. The relationship between bubble diameter and interfacial area was formulated as $a = 4f_b/u_b$ where f_b is the bubble frequency, and u_b is the bubble velocity (Chanson, 1997). Lima Neto et al. (2008a) found that the radial distribution of specific interfacial area follows a Gaussian distribution while the bubble mean Sauter diameter and velocity distributions are linearly distributed in the radial direction. Moreover, their results indicated that using the porous air-stone instead of a single orifice nozzle increased the interfacial area by approximately 90%.

The present study is motivated by the effect of air stone nozzles in reducing bubble size and increasing the contact area between air and water in buoyancy-driven bubble plumes. The larger contact surfaces between air and water enhance the oxygen transfer in aeration of wastewater treatment plants and improve aerators' efficiency in natural ponds. Due to the presence of small porous media in air-stone nozzles, such nozzles are more susceptible to clogging in wastewater treatment tanks and require frequent backwash and maintenance. To overcome the limitation of air-stone in bubble plumes, a grid-screen is introduced to be placed at fixed distances from a single circular nozzle. The proposed design reduces the maintenance cost due to clogging of air-stones over time. In this study, two grid-screens with different opening dimensions are tested, and the grid-screens are installed at different distances from the nozzle. The variations of bubble size, bubble concentration, and velocity along the vertical axis of bubble plumes are measured for different air discharges to understand how air discharge and screen size alter bubble characteristics and how far air bubbles remain intact after passing through a grid-screen. To test the effects of controlling parameters such as nozzle size, air discharge, grid-screen size, and the distance between grid-screen and nozzle on the efficiency of bubble plume after the grid screen, the variations of bubble characteristics such as bubble size, bubble velocity, and interfacial area with the design parameters are examined. Based on the experimental results, empirical

equations were developed to predict the variations of bubble diameter with different air injection design parameters.

2. Experimental Setup

Figure 1 illustrates the schematic of the experimental tank with an adjusted air injection system and a single circular nozzle. Experiments were carried out in the Multiphase Flow Research Laboratory (MFRL) at Lakehead University. A pipe with a 1-inch interior diameter was installed at the bottom of the tank to inject air with different discharges in the ambient water. The experimental tank was fabricated from glass with dimensions of 1.60 m long, 0.8 m wide, and 0.80 m deep. In order to minimize the impact of temperature, the water temperature in the tank was kept constant at $20 \pm 1^\circ\text{C}$. The depth of water in the tank was 0.70 m and it was constant during the experiments. Different air flowrates of $Q_a = 4$ L/min, 6 L/min, and 8 L/min were set and air discharges were measured with an accurate rotameter (LZM series Zyia OEM, Zhejiang, China) with an accuracy of $\pm 4\%$. In order to investigate the impacts of nozzle diameter on the properties of bubble plumes, two different nozzle diameters of $d_o = 1$ mm and 3 mm were selected. Standard grid-screens with sieve openings of $d_s = 0.841$ mm (i.e., sieve number #20) and $d_s = 2.380$ mm (i.e., sieve number #16) (ASTM, 2007) were selected. The grid-screen was placed above the nozzle and different distances between nozzle and grid-screen were tested. The elevations from the nozzle were $X_s = 0.14$ m, 0.22 m, and 0.30 m. Figure 1 shows the optoelectronic unit (ISO Lite Software, RBI Optical probe, France), the schematic of experimental setup, images of bubble plumes before and after the grid-screen, and the rotameter. The optoelectronic unit measured the bubble characteristics once they passed the two crystal needles of the probe.

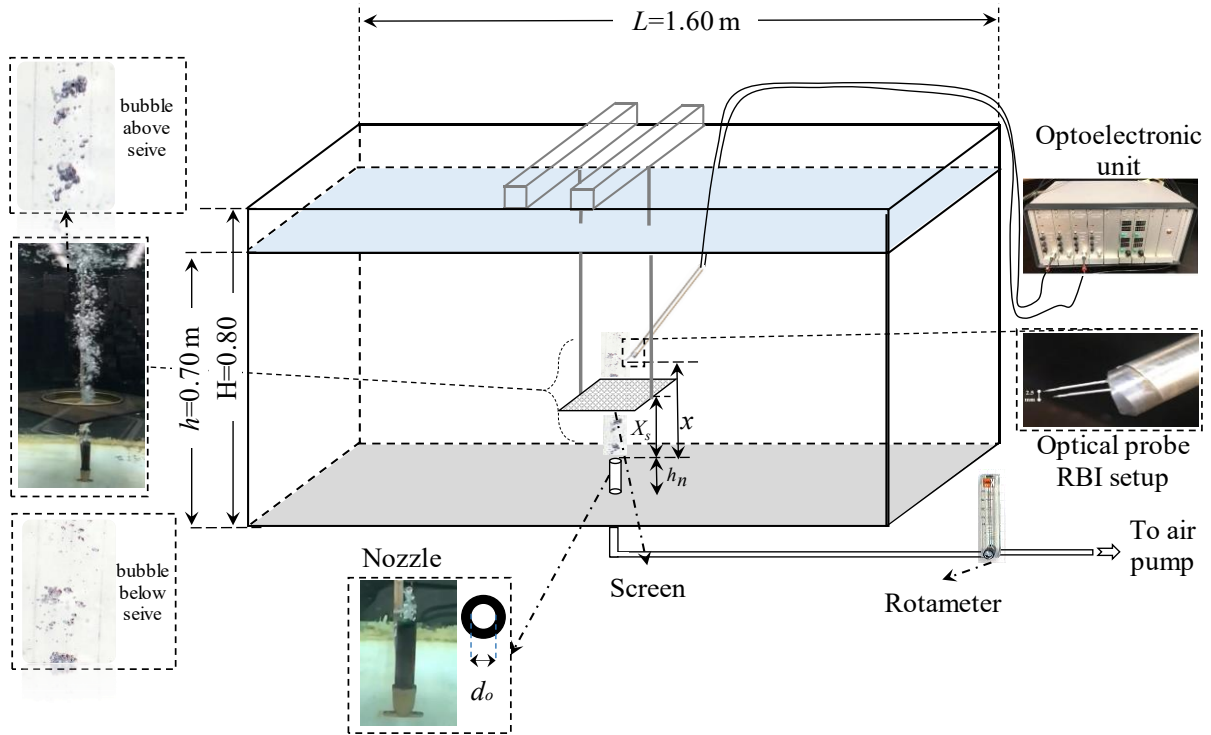


Figure 1: The schematic of experimental setup, image of bubbly plume passing through a grid-screen, the components of an optoelectronic unit and Refractive Bubble Instrument (RBI) optical probe tip.

3. Results and Discussion

Figure 2 shows the snapshot images of bubbles and bubble clouds below and above the grid-screen (e.g., $d_s = 0.841$ mm, and $X_s = 0.14$ m). As shown in Figure 2a, a bubble cloud was created before the grid-screen and due to pressure reduction, the bubble cloud was divided into bubbles with large diameters (see Figure 3.2b). Figure 2c illustrates the bubbles with smaller diameter above the adjusted grid-screen. As can be seen, the impact of grid-screen on bubbles reduced the bubble size. It is assumed that the reduction in bubble diameter is due to the grid-screen effect. Figure 2d shows the bubble plumes far from the grid-screen. As can be seen, bubble sizes were further reduced due to bubble breakup mechanism indicating that the grid-screen can significantly reduce the size of bubbles far from the screen.

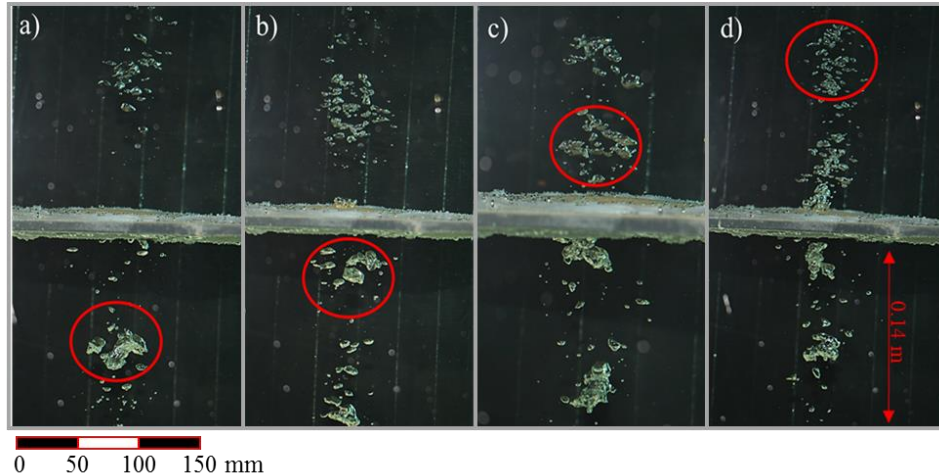


Figure 2: Images of bubble plume variations with time for the plume tests with a grid-screen and for $d_o = 1$ mm, $Q_a = 4$ L/min, $d_s = 0.841$ mm, and $X_s = 0.14$ m. The time step between each image is 0.5 seconds.

The effects of grid-screen on bubble characteristics of bubble plumes were investigated by comparing the variations of bubble size and bubble velocity along the vertical axis of bubble plume. The variations of bubble size along the vertical axis of the plume, x , were measured in the plume's centerline. The results were plotted for bubble plumes with different air discharges (see Figure 3). Figures 3a and 3.3b show the bubble size variations for $Q_a = 4$ L/min, and Figures 3.3c-3.3d and 3e-3f show the bubble size variations for $Q_a = 6$ L/min and 8 L/min, respectively. The left and right columns in Figure3 show the bubble size variations for different nozzle diameters of $d_o = 1$ mm and 3 mm, respectively. Variations of bubble size for a test without grid-screen was also added as a benchmark tests. A comparison between tests with different grid-screen size indicated that adding a grid-screen (e.g., $X_s = 0.14$ m) can significantly decrease the bubble size. However, increasing the grid screen size from $d_s = 0.841$ mm to $d_s = 2.380$ mm did not have a marginal impact on variations of bubble size above the grid-screen. A comparison between tests with different nozzle diameters (e.g., $d_o = 1$ mm and 3 mm) indicated that increasing nozzle diameter reduced the bubble size by an average of 15.8%.

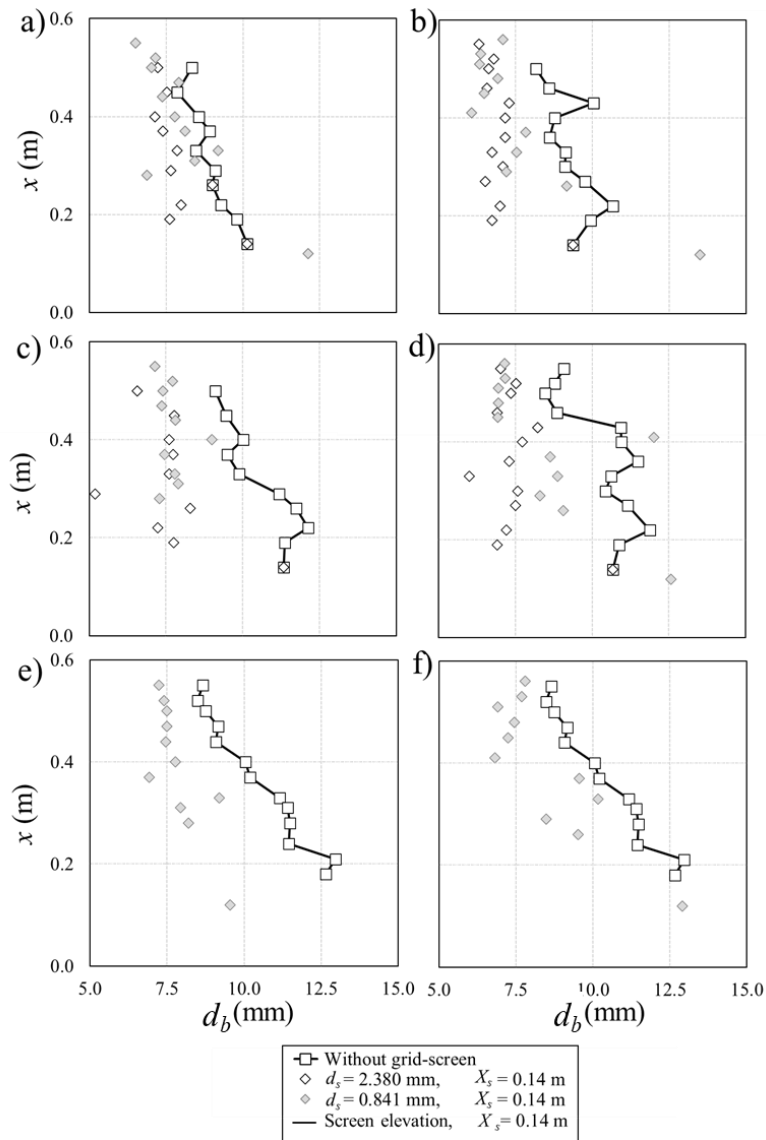


Figure 3: Variations of bubble size along vertical axis of bubble plumes with different air discharges, Q_a , nozzle diameters, d_o , and grid-screen sizes, d_s , for a screen located at $X_s = 0.14$ m: a) $Q_a = 4$ L/min, $d_o = 1$ mm; b) $Q_a = 4$ L/min, $d_o = 3$ mm; c) $Q_a = 6$ L/min, $d_o = 1$ mm; d) $Q_a = 6$ L/min, $d_o = 3$ mm; e) $Q_a = 8$ L/min, $d_o = 1$ mm; f) $Q_a = 8$ L/min, $d_o = 3$ mm.

To study the effect of grid-screen on variation of bubble velocity, the vertical variations of bubble velocity were extracted from RBI probe measurements at the centerline of bubble plume with and without a grid-screen and with different nozzle sizes and air discharges. Figure 4 shows the experimental results of bubble velocity with different air discharges. The variations of bubble velocity along the vertical axis, with the vertical distance from the nozzle, x , were considered. The left and right columns in Figure 3.4 show the bubble

velocities with the nozzle sizes of 1 mm and 3 mm, respectively. The data connected with lines in Figure 4 show the experiments without a grid-screen and with different discharges of $Q_a = 4, 6, \text{ and } 8 \text{ L/min}$. Despite the effect of grid-screen size on bubble size, the effect of grid-screen size on variations of bubble velocity was significant. As can be seen in Figures 3.4a-3.4d, bubble velocity after the grid-screen decreased as the screen opening decreased accordingly. The grid-screen size decreased from 2.38 mm to 0.841 mm, and bubble velocity decreased by 14% and 38% for nozzle sizes of 1 mm and 3 mm, respectively. Such variations showed that increasing the nozzle size caused the air to move through the water with a relatively higher velocity. In this condition, smaller bubbles were formed, and air-water mixing was improved after the grid-screen. Furthermore, Figure 4 shows that by increasing air flow discharge, bubble velocity decreased with increasing the measurement distance from the nozzle. It is assumed that the reduction of double velocity could be intensified by increasing the air discharge.

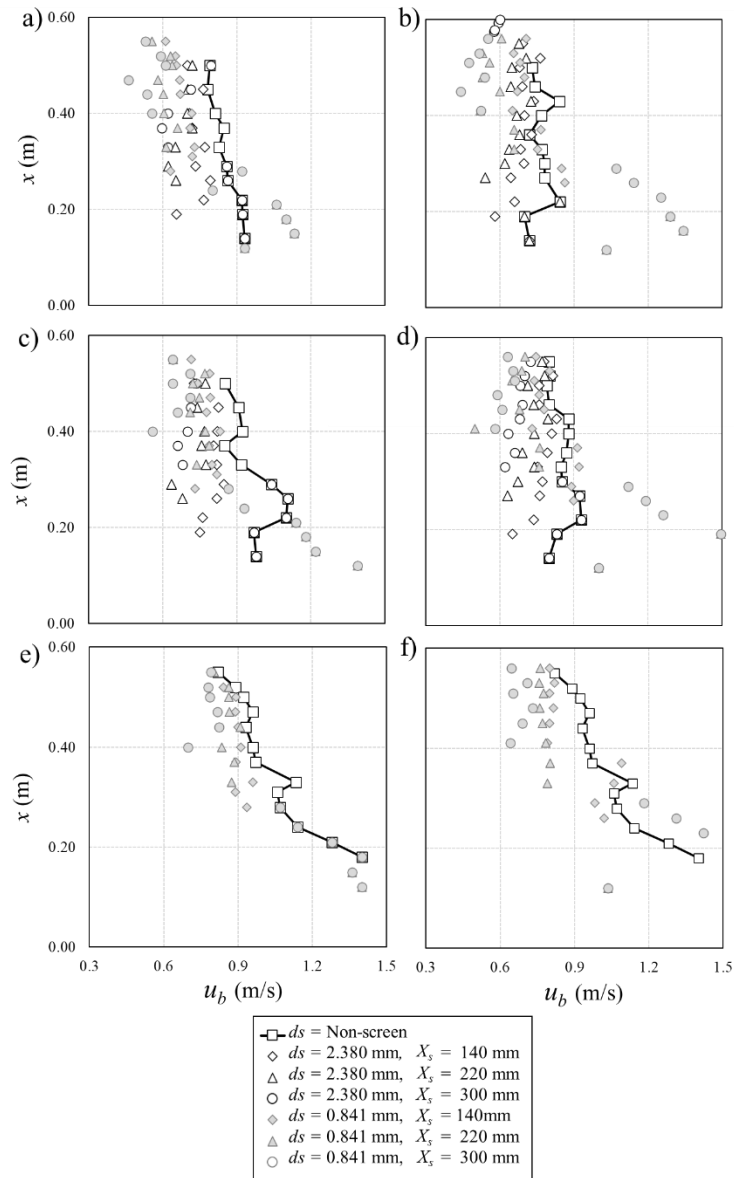


Figure 4: Variations of bubble velocity with vertical distance from the nozzle in bubble plumes with different air discharges, Q_a , nozzle sizes, d_o , and grid-screen sizes, d_s . The grid-screen was located at $X_s = 0.30$ m: a) $Q_a = 4$ L/min, $d_o = 1$ mm; b) $Q_a = 4$ L/min, $d_o = 3$ mm; c) $Q_a = 6$ L/min, $d_o = 1$ mm; d) $Q_a = 6$ L/min, $d_o = 3$ mm; e) $Q_a = 8$ L/min, $d_o = 1$ mm; f) $Q_a = 8$ L/min, $d_o = 3$ mm.

Figure 5 shows the variations of interfacial area along the vertical axis of the plume and in the plume's centerline. The variations of interfacial area along the vertical axis were considered to study the efficiency of grid-screen and to study the effects of nozzle size and air discharge on the mixing efficiency of the plume. The left and right columns in Figure 5

represent the data from $d_o = 1$ mm and 3 mm, respectively. The uncertainty overbars for measuring interfacial area are added in Figure 5. Similar uncertainty ranges with an average value of $\pm 1.5\%$ were found for other tests. The lines in Figure 5 show the location of grid screen. The interfacial area is correlated with the frequency of bubbles and has adverse correlation with bubble velocity. As can be seen, the effect of grid-screen is negligible in low flow rates. As air flow rate increased, the interfacial area increased by 50% above the grid screen. A comparison among the values of interfacial areas at the upstream and downstream of the grid-screen indicated that the values of interfacial area above the grid-screen increased. However, the increment of interfacial area above the grid screen decreased by X_5 . The results indicated that the interfacial area increased by approximately 32% when air discharge increased from 4 L/min to 8 L/min. Our observation is consistence with the observations of Lima Neto et al. (2008a), in which changing air flow rate from 2 L/min to 3 L/min increased the interfacial area by 18%.

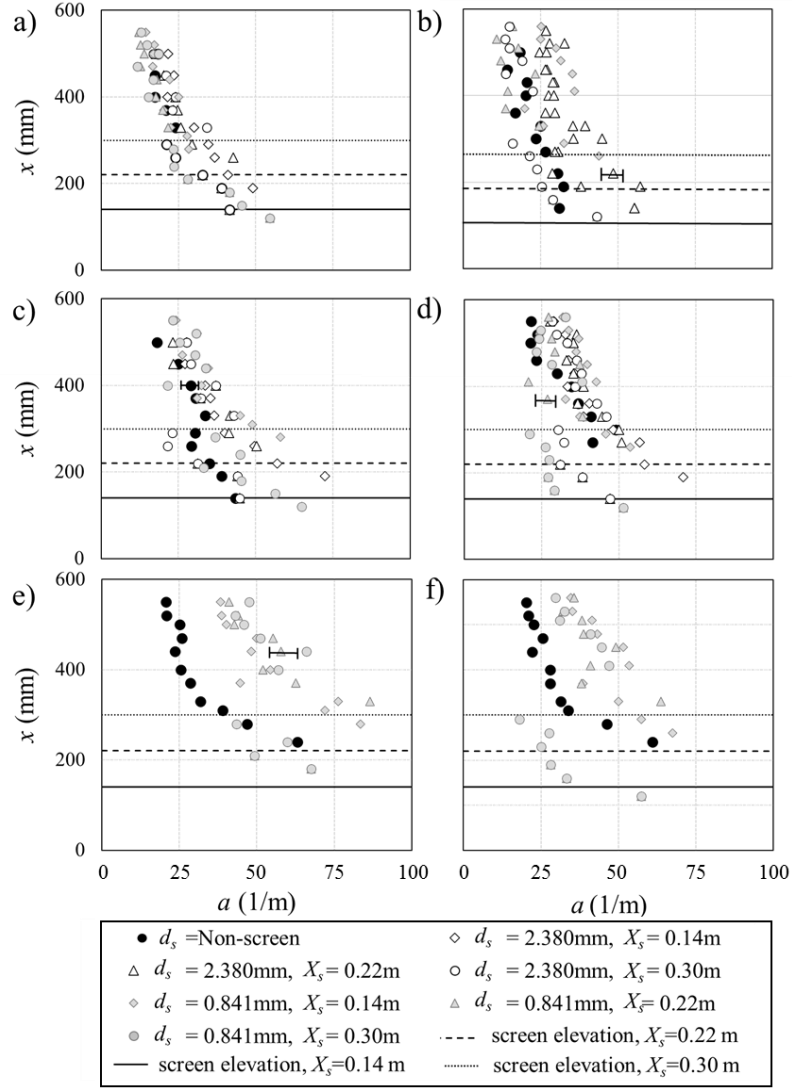


Figure 5: Variations of interfacial area along the vertical axis of bubble plumes with different air discharges, Q_a , nozzle diameters, d_o , and grid-screen sizes, d_s , for a screen located at $X_s = 0.14\text{ m}$, 0.22 m , and 0.30 m : a) $Q_a = 4\text{ L/min}$, $d_o = 1\text{ mm}$; b) $Q_a = 4\text{ L/min}$, $d_o = 3\text{ mm}$; c) $Q_a = 6\text{ L/min}$, $d_o = 1\text{ mm}$; d) $Q_a = 6\text{ L/min}$, $d_o = 3\text{ mm}$; e) $Q_a = 8\text{ L/min}$, $d_o = 1\text{ mm}$; f) $Q_a = 8\text{ L/min}$, $d_o = 3\text{ mm}$.

Eq. (1) shows the contributed parameters to estimate bubble size with grid-screen adjustment.

$$d_b = f_1(d_s, Q_a, g, X_s, x, \rho, u_b, \mu, d_o) \quad (1)$$

where d_b is the bubble diameter size, d_s are the grid screen size, Q_a is the air discharge, g is the gravitational acceleration, X_s is the elevation of the grid-screen from the nozzle, x is the elevation of measurement point, ρ is the density of air, u_b is the bubble velocity, μ is the dynamic viscosity of water, and d_o is the nozzle diameter. Based on dimensional analysis, five dimensionless numbers are formulated as:

$$\Pi_1 = \frac{Q_a}{\sqrt{gX_s}x^{1.5}} \quad \Pi_2 = \frac{\rho u_b d_o}{\mu} \quad \Pi_3 = \frac{d_o}{d_s} \quad \Pi_4 = \frac{x}{X_s} \quad \Pi_5 = \frac{d_b}{d_s} \quad (2)$$

As it can be seen, Π_2 is the Reynolds number of the air at the nozzle. Also, equation (3.3) can be used to estimate the bubble size based on experimental measurements. Eq. (3.3) shows the correlation between normalized bubble size and the related dimensionless numbers.

$$\frac{d_b}{d_s} = f_2\left(\frac{Q_a}{\sqrt{gX_s}x^{1.5}}, \frac{\rho u_b d_o}{\mu}, \frac{x}{X_s}, \frac{d_o}{d_s}\right) \quad (3)$$

The coefficients that connecting the defined parameters with normalized bubble size were extracted from the curve fitting of experimental data. Three equations were introduced as described by:

$$\frac{d_b}{d_s} = 2.07 \text{Log}\left(\frac{Q_a}{\sqrt{gX_s}x^{1.5}}\right) - 1.5 \text{Log}\left(\frac{d_o}{d_s}\right) + 0.8\left(\frac{x}{X_s}\right)^{-1.55} + 0.022\left(\frac{\rho u_b d_o}{\mu}\right)^{0.66}, R^2 = 0.819 \quad (4)$$

$$\frac{d_b}{d_s} = 1.6 \text{Log}\left(\frac{Q_a}{\sqrt{gX_s}x^{1.5}}\right) - 1.45 \text{Log}\left(\frac{d_o}{d_s}\right) + 0.0034\left(\frac{x}{X_s}\right)^{-0.74} \left(\frac{\rho u_b d_o}{\mu}\right)^{0.88}, R^2 = 0.827 \quad (5)$$

$$\frac{d_b}{d_s} = 1.29 \text{Log}\left(\frac{Q_a}{\sqrt{gX_s}x^{1.5}}\right) + 13.77 e^{-6075.3\left(\frac{d_o}{d_s}\right)} - 0.303 \text{Log}\left(\frac{x}{X_s}\right) + 0.326\left(\frac{\rho u_b d_o}{\mu}\right)^{0.45}, R^2 = 0.842 \quad (6)$$

Figure 6 shows the correlation between normalized bubble size and geometry parameters of vertical bubble plumes. Eq. (6) has shown a higher correlation coefficient and is recommended for bubble size prediction.

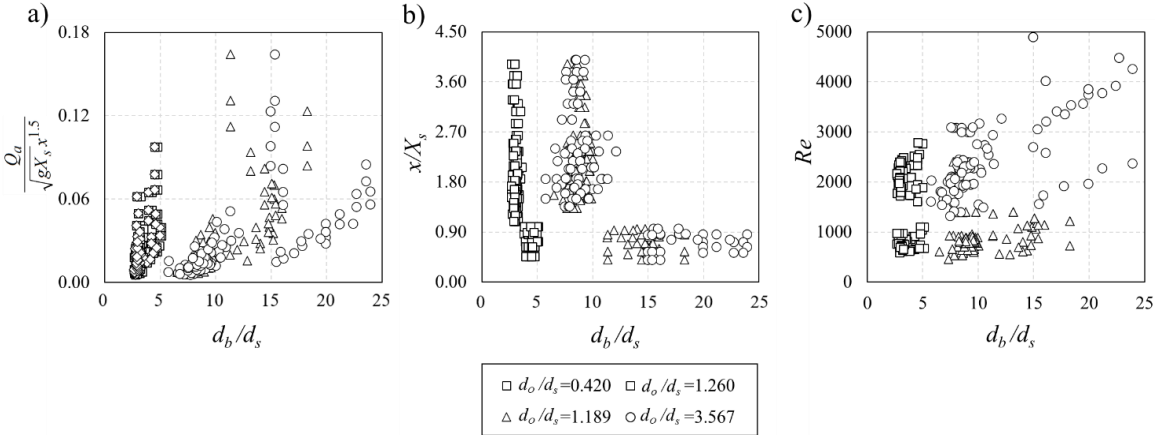


Figure 6: The correlation between normalized bubble size and geometry parameters of vertical bubble plumes: a) variations of normalized bubble size with normalized air discharge; b) variations of normalized bubble size with normalized distance from the nozzle; c) variations of normalized bubble size with Reynolds number.

Figure 7 shows the calculated values of d_b/d_s with prediction of Eq. (6) and the experimental values. As it can be seen, the predicted values of d_b/d_s have an acceptable range of error of $\pm 15\%$, and a good agreement was found between prediction and experimental data.

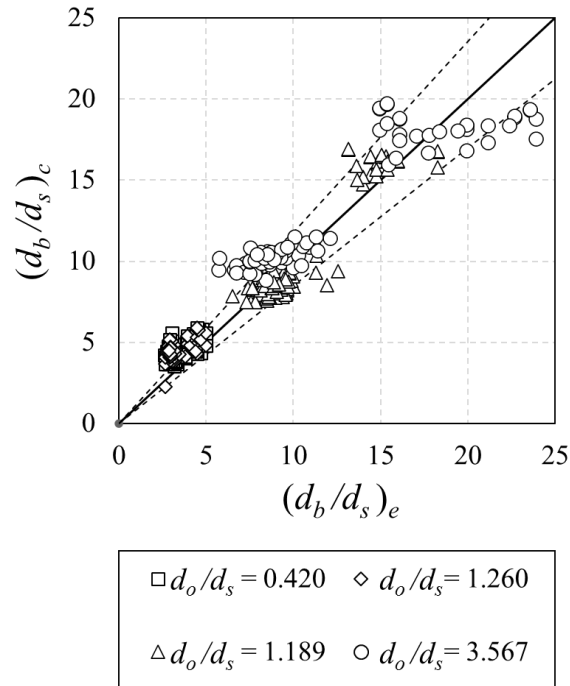


Figure 7: Correlation between measured and predicted normalized bubble size. The dashed lines indicate the $\pm 15\%$ variations from the ideal prediction.

4. Conclusions

The following conclusion remarks were extracted from the present experimental study. A comparison between tests with different grid-screen size indicated that adding a grid-screen (e.g., $X_s = 0.14$ m) can significantly decrease the bubble size. However, increasing the grid screen size from $d_s = 0.841$ mm to $d_s = 2.380$ mm did not have a marginal impact on variations of bubble size above the grid-screen. A comparison between tests with different nozzle diameters (e.g., $d_o = 1$ mm and 3 mm) indicated that increasing nozzle diameter reduced the bubble size by an average of 15.8%. Decreasing the elevation of the grid-screen and its size, formed bubble cloud below the grid-screen and increased the buoyancy forces which accordingly increased bubble velocity. The effect of grid-screen size on variations of bubble velocity was significant and bubble velocity decreased as the screen opening decreased accordingly. As the grid-screen size decreased from 2.38 mm to

0.841 mm, bubble velocity for nozzle sizes of 1 mm and 3 mm decreased by 14% and 38%, respectively.

The comparison between the values of interfacial area above and below the grid-screen indicated that the interfacial areas became less than the benchmark tests. Also, by increasing air discharge in tests with a maximum elevation of the grid-screen (e.g., $X_s = 0.3$ m) the bubble consent was head below the grid-screen which can increased the values of the interfacial are. However, such behavior did not occur for the tests with lower distance from a nozzle to grid screen. Finally, three types of the propose equations based on the dimensionnel less numbers were fitted on the expérimental data. Based on the investigation of the error the propsed equation with higher agriment with experimental data was given to redict the bubble diameter sizes at the center line of the bubble plume with different elevations.

Appendix 2

Suggested guideline for air injection systems in industry

Introduction

In recent years, the utilization of air injection and bubble plume systems has gained significant attention in the field of water management. These systems find extensive application in diverse areas, such as dam and reservoir management, lake management, dissolved air flotation (DAF) systems, and water treatment plants. The efficiency and effectiveness of these systems heavily depend on the parameters of the bubble plume, including mean bubble diameter, mean bubble velocity, bubble Reynolds number, bubble interfacial area, and bubble concentration. To achieve optimal results in each specific application, it is crucial to understand how these parameters impact the performance of air injection and bubble plume systems. Therefore, this thesis presents comprehensive guidelines categorizing the parameters of bubble plume for different areas of application, namely dam and reservoir management, lake management, DAF systems, and water treatment plants. In the realm of dam and reservoir management, the guidelines emphasize the significance of mean bubble diameter, mean bubble velocity, bubble Reynolds number, bubble interfacial area, and bubble concentration. By providing the optimal range of these parameters, the guidelines aim to improve oxygen transfer efficiency, mixing, and destratification within the reservoir. For lake management, the guidelines offer insights into parameter ranges that promote aeration, destratification, and overall water quality enhancement. The impact of mean bubble diameter, mean bubble velocity, bubble Reynolds number, bubble interfacial area, and bubble concentration on achieving the desired outcomes in lake ecosystems is thoroughly explored. Moreover, the thesis delves into the specific requirements of dissolved air flotation (DAF) systems. Understanding the ideal ranges for mean bubble diameter, mean bubble velocity, bubble Reynolds number, bubble interfacial area, and bubble concentration is crucial for effective solid-liquid separation and particle removal in DAF processes. Lastly, the guidelines shed light on the

parameters of bubble plume in the context of water treatment plants. By focusing on mean bubble diameter, mean bubble velocity, bubble Reynolds number, bubble interfacial area, and bubble concentration, the guidelines provide valuable insights into enhancing processes such as mixing, flocculation, and coagulation, thereby improving the overall efficiency of water treatment. It is important to note that these guidelines serve as general recommendations and should be adapted to suit specific system requirements, water characteristics, and management objectives. The development and implementation of efficient air injection and bubble plume systems can greatly contribute to the sustainable management of water resources and the improvement of water quality in various applications. By utilizing the guidelines outlined in this thesis, water management professionals and researchers can make informed decisions regarding the design, operation, and optimization of air injection and bubble plume systems, thereby driving advancements in the field and contributing to the overall sustainable utilization of water resources.

Classification of bubble plume characterize in industry

Air injection and bubble plume systems are widely used in various applications such as dam and reservoir management, lake management, dissolved air flotation (DAF) systems, and water treatment plants. The parameters of bubble plume, including mean bubble diameter, mean bubble velocity, bubble Reynolds number, bubble interfacial area, and bubble concentration, play a crucial role in the efficiency and effectiveness of these systems. Below is a guideline categorizing these parameters for each area of application:

Dam and Réservoir Management:

a. Mean Bubble Diameter:

Optimal range: 1-5 mm

Smaller bubble diameters enhance oxygen transfer efficiency

Larger bubble diameters are suitable for mixing and destratification

b. Mean Bubble Velocity:

Target velocity: Sufficient to reach the desired depth in the reservoir. Velocity should be high enough to prevent bubble coalescence and promote mixing.

c. Bubble Reynolds Number:

Reynolds number range: 100-1000

Low Reynolds numbers favor oxygen transfer, Higher Reynolds numbers promote mixing and destratification

d. Bubble Interfacial Area:

Target range: 100-1000 m^2/m^3

Higher interfacial area enhances oxygen transfer efficiency

Proper mixing and destratification require adequate interfacial area

e. Bubble Concentration:

Concentration range: 1-10% by volume

Concentration should be optimized based on the specific requirements of the reservoir

Lake Management:

a. Mean Bubble Diameter:

Optimal range: 2-10 mm

Larger bubbles are suitable for lake aeration and destratification

b. Mean Bubble Velocity:

Sufficient to reach the desired depth for aeration and mixing purposes

Velocity should be adjusted based on lake characteristics and objectives

c. Bubble Reynolds Number:

Reynolds number range: 100-1000

Low Reynolds numbers are beneficial for oxygen transfer

Higher Reynolds numbers aid in lake mixing and destratification

d. Bubble Interfacial Area:

Target range: 100-1000 m^2/m^3

Higher interfacial area improves oxygen transfer efficiency

Proper mixing and destratification require adequate interfacial area

e. Bubble Concentration:

Concentration range: 1-10% by volume

Concentration should be optimized based on lake conditions and management goals

Dissolved Air Flotation (DAF) Systems:

a. Mean Bubble Diameter:

Optimal range: 20-100 μm

Smaller bubbles enhance flotation efficiency and solid-liquid separation

b. Mean Bubble Velocity:

Sufficient velocity to create upward buoyancy and flotation of particles

Velocity should be adjusted based on the size and characteristics of the particles

c. Bubble Reynolds Number:

Reynolds number range : 10-100

Lower Reynolds numbers favor particle attachment to bubbles for flotation

d. Bubble Interfacial Area :

Target range : 1000-5000 m^2/m^3

Higher interfacial area improves particle-bubble attachment and flotation efficiency

e. Bubble Concentration :

Concentration range : 1-5% by volume

Concentration should be optimized for efficient particle removal and flotation

Water Treatment Plants :

a. Mean Bubble Diameter :

Optimal rang : 100-1000 μm

Larger bubbles are suitable for mixing, flocculation, and coagulation processes

b. Mean Bubble Velocity :

Adequate velocity to facilitate mixing, flocculation, and coagulation

Velocity should be adjusted based on the specific treatment process requirements

c. Bubble Reynolds Number:

Reynolds number range : 10-100

Lower Reynolds numbers favor mixing, flocculation, and coagulation

d. Bubble Interfacial Area:

Target range : 1000-5000 m^2/m^3

Higher interfacial area enhances particle agglomeration and removal efficiency

e. Bubble Concentration :

Concentration range: 1-5% by volume

Concentration should be optimized based on the treatment process and water quality goals

Remember, these guidelines serve as general recommendations, and specific design parameters may vary depending on the system, water characteristics, and desired outcomes. It is essential to consult with experts and conduct pilot studies or simulations to optimize the bubble plume system for each application.

References

- Alumni, P. F. G., & Yimsiri, P. (2001). "Bubble plume". *Department of Chemical Engineering and Biotechnology*. University of Cambridge.
- Aoyama, S., Hayashi, K., Hosokawa, S., & Tomiyama, A. (2016). Shapes of ellipsoidal bubbles in infinite stagnant liquids. *International Journal of Multiphase Flow*, Vol. 79, pp. 23-30.
- ASTM. 2007. Standard test method for particle-size analysis of soils. D422-63 (2007) e2, West Conshohocken, PA.
- Behzadipour, A. and Azimi, A. H. (2022a). "Air Bubble Dynamics in Bubble Plumes with a Grid-screen." *39th IAHR World Congress*, Granada, Spain.
- Behzadipour, A., Azimi, A. H., and Lima Neto, I. E. (2022b). "Effect of grid-screen on bubble characteristics of vertically discharged bubble plumes." *Journal of Chemical Engineering Science*", Volume 253, 117545.
- Behzadipour, A., Azimi, A. H., and Lima Neto, I. E. (2023). "Effects of air discharge on bubble dynamics in vertically discharged bubble plumes." *Journal of Chemical Engineering Science*", Volume 253, 118440, 16 p.
- Besagni, G., & Deen, N. G. (2020). Aspect ratio of bubbles in different liquid media: A novel correlation." *Journal of Chemical Engineering Science*", 215, 115383.
- Besbes, S., Gorrab, I., ElHajem, M., Ben Aissia, H., & Champagne, J. Y. (2020). "Effect of bubble plume on liquid phase flow structures using PIV". *Particulate Science and Technology*, 38(8), pp. 963-972.
- Bombardelli, F. A., Buscaglia, G. C., Rehmann, C. R., Rincón, L. E., & García, M. H. (2007). Modeling and scaling of aeration bubble plumes: A two-phase flow analysis. *Journal of Hydraulic Research*, 45(5), 617-630.
- Boes, R. M., & Hager, W. H. (2003). "Two-phase flow characteristics of stepped spillways." *Journal of Hydraulic Engineering*, Vol. 129, No.9, pp. 661-670.
- Bohne, T., Griebmann, T., & Rolfes, R. (2020). Development of an efficient buoyant jet integral model of a bubble plume coupled with a population dynamics model for bubble

breakup and coalescence to predict the transmission loss of a bubble curtain. *International Journal of Multiphase Flow*, 132, 103436.

Bormans, M., Maršálek, B., and Jančula, D. (2016). “Controlling internal phosphorus loading in lakes by physical methods to reduce cyanobacterial blooms: A review.” *Aquat. Ecol.*, Vol.50, No.3, pp.407–422.

Boyce, F. M., Donelan, M. A., Hamblin, P. F., Murthy, C. R., & Simons, T. J. (1989). Thermal structure and circulation in the Great Lakes. *Atmosphere-ocean*, 27(4), 607-642.

Bryant, D. B., Seol, D. G., & Socolofsky, S. A. (2009). “Quantification of turbulence properties in bubble plumes using vortex identification methods.” *Physics of Fluids*, Vol. 21. No.7, pp. 075101.

Chaumat, H., Billet-Duquenne, A. M., Augier, F., Mathieu, C., & Delmas, H. (2005). “Application of the double optic probe technique to distorted tumbling bubbles in aqueous or organic liquid.” *Chemical Engineering Science*. Vol.60, No. 22, pp.6134-6145.

Chen, G., Zhang, Z., Gao, F., Li, J., & Dong, J. (2021). Effect of Different Configurations on Bubble Cutting and Process Intensification in a Micro-Structured Jet Bubble Column Using Digital Image Analysis. *Processes*, 9(12), 2220.

Chen, L. (2019). An improved correlation of bubble size distribution with the measured acoustic spectrum of a turbulent bubble plume. In Proceedings of *ACOUSTICS* (Vol. 10, No. 13).

Cooke, G. D., & Carlson, R. E. (1989). Reservoir management for water quality and THM precursor control. *AWWA Research Foundation*.

Clift, R., Grace, J. R., and Weber, M. E. (1978). Bubbles, drops and particles, Academic, New York.

Crouse, B. C., Wannamaker, E. J., & Adams, E. E. (2007). “Integral model of a multiphase plume in quiescent stratification.” *Journal of hydraulic engineering*, 133(1), pp. 70-76.

Davidson, L. & Amick, E.H. (1956). “Formation of gas bubbles at horizontal orifices.” *AIChE Journal*, Vol. 2, No.. 3, pp. 337-342.

- Delnoij, E., Lammers, F. A., Kuipers, J. A. M., & van Swaaij, W. P. M. (1997). Dynamic simulation of dispersed gas-liquid two-phase flow using a discrete bubble model. *Chemical engineering science*, 52(9), 1429-1458.
- Díaz, M. E., Montes, F. J., & Galán, M. A. (2006). Influence of aspect ratio and superficial gas velocity on the evolution of unsteady flow structures and flow transitions in a rectangular two-dimensional bubble column. *Industrial & engineering chemistry research*, 45(21), 7301-7312.
- Duan, H., Ren, Y., & Zhang, L. (2018). “Effects of interphase forces on fluid flow in gas-stirred steel ladles using the Eulerian–Lagrangian multiphase approach.” *Multiphase Flows in Materials Processing*, 70 (10), pp. 2128-2138.
- Fannelop, T. K. (1980). “Hydrodynamics of Underwater Blowouts,” Norwegian Maritime Research, Vol. 4, pp. 7-33.
- Fanneløp, T. K., Hirschberg, S., & Küffer, J. (1991). Surface current and recirculating cells generated by bubble curtains and jets. *Journal of Fluid Mechanics*, 229, 629-657.
- Fannelop, T., & Sjoen, K. (1980, January). Hydrodynamics of underwater blowouts. In *18th Aerospace Sciences Meeting* (p. 219).
- Fraga Bugallo, B., Stoesser, T., Lai, C., & Socolofsky, S. (2016). A large-eddy simulation-based Eulerian-Lagrangian approach to predict bubble plume dynamics. *Ocean Modelling*, 97(2016), 27-36.
- Fisher, J. B., & Honda, H. (1979). Branch geometry and effective leaf: a study of terminaua- branching pattern 1. Theoretical trees. *American Journal of Botany*, 66(6), 633-644.
- Felton, K., & Loth, E. (2001). “Spherical bubble motion in a turbulent boundary layer.” *Physics of Fluids*, 13(9), pp. 2564-2577.
- Ford, B., & Loth, E. (1998). “Forces on ellipsoidal bubbles in a turbulent shear layer.” *Physics of Fluids*, 10(1), pp. 178-188.
- Fleck, S., & Rzehak, R. (2019). “Investigation of bubble plume oscillations by Euler-Euler simulation.” *Chemical Engineering Science*, Vol. 207, pp. 853-861.
- Fraga, B., and Stoesser, T. (2016). “Influence of bubble size, diffuser width, and flow rate on the integral behavior of bubble plumes.” *Journal of Geophysical Research: Oceans*, 121(6), pp. 3887-3904.

- Fraga, B., Stoesser, T., Lai, C. C., & Socolofsky, S. A. (2016). A LES-based Eulerian–Lagrangian approach to predict the dynamics of bubble plumes. *Ocean Modelling*, 97, 27-36.
- Funaki, J., Shintani, A., Kawaguchi, R., & Hirata, K. (2009). Basic space structure of bubble-jet plume using consecutive 3D-PTV. *Journal of Fluid Science and Technology*, Vol. 4, No. 2, 348-358.
- Gantzer, P. A., Bryant, L. D., & Little, J. C. (2009). Controlling soluble iron and manganese in a water-supply reservoir using hypolimnetic oxygenation. *Water research*, 43(5), 1285-1294.
- Herringe, R. T., & Davis, M. R. (1976). Structural development of gas-liquid mixture flows. *Journal of Fluid Mechanics*, 73(1), 97-123.
- Hibiki, T., & Ishii, M. (2007). “Lift force in bubbly flow systems.” *Chemical Engineering Science*, 62(22), pp. 6457-6474.
- Ibelings, B. W., Bormans, M., Fastner, J., and Visser, P. M. (2016). “CYANOCOST special issue on cyanobacterial blooms: Synopsis— A critical review of the management options for their prevention, control and mitigation.” *Aquatic Ecol.* Vol.50, No.3, pp.595–605.
- Iamandi, C., & Rouse, H. (1969). Jet-induced circulation and diffusion. *Journal of the Hydraulics Division*, 95(2), 589-602.
- Iguchi, M., Okita, K., & Yamamoto, F. (1998). Mean velocity and turbulence characteristics of water flow in the bubble dispersion region induced by plunging water jet. *International Journal of Multiphase Flow*, 24(4), 523-537.
- Iguchi, M.; Ueda, H., Uemura, T. (1995). “Bubble and liquid flow characteristics in a vertical bubbling jet.” *International Journal of Multiphase Flow*, Vol. 21, pp. 861-873.
- Jirka, G. H., & Harleman, D. R. (1979). Stability and mixing of a vertical plane buoyant jet in confined depth. *Journal of Fluid Mechanics*, 94(2), 275-304.
- Jain, D., Lau, Y. M., Kuipers, J. A. M., & Deen, N. G. (2013). Discrete bubble modeling for a micro-structured bubble column. *Chemical Engineering Science*, 100, 496-505.
- Jain, D., Kuipers, J. A. M., & Deen, N. G. (2014). Numerical study of coalescence and breakup in a bubble column using a hybrid volume of fluid and discrete bubble model approach. *Chemical Engineering Science*, 119, pp. 134-146.

- Kiambi, S. L., Duquenne, A. M., Dupont, J. B., Colin, C., Risso, F., & Delmas, H. (2003). "Measurements of bubble characteristics: comparison between double optical probe and imaging." *The Canadian Journal of Chemical Engineering*. Vol.81, No.3- 4, pp.764-770.
- Kubasch, J. H. (2001). "Bubble hydrodynamics in large pools." *Doctoral dissertation, ETH Zurich*, Nr. 14398, 178 p.
- Kumar, S., Nikitopoulos, D. N., & Michaelides, E. E. (1989). Effect of bubbles on the turbulence near the exit of a liquid jet. *Experiments in fluids*, 7(7), 487-494.
- Lai, C. C., & Socolofsky, S. A. (2019). The turbulent kinetic energy budget in a bubble plume. *Journal of Fluid Mechanics*, 865, 993-1041.
- Laupsien, D., Cockx, A., & Line, A. (2017). Bubble plume oscillations in viscous fluids. *Chemical Engineering & Technology*, 40(8), 1484-1493.
- Laupsien, D., Le Men, C., Cockx, A., & Liné, A. (2021). Effects of liquid viscosity and bubble size distribution on bubble plume hydrodynamics. *Chemical Engineering Research and Design*.
- Liu, L., Yan, H., Ziegenhein, T., Hessenkemper, H., Li, Q., & Lucas, D. (2019). A systematic experimental study and dimensionless analysis of bubble plume oscillations in rectangular bubble columns. *Chemical Engineering Journal*, 372, 352-362.
- Lima, D. D., & Lima Neto, I. E. (2018). "Effect of nozzle design on bubbly jet entrainment and oxygen transfer efficiency." *Journal of Hydraulic Engineering*, Vol.144, No.8, pp. 06018010.
- Lima Neto, I. E. (2012). "Bubble plume modeling with new functional relationships." *Journal of Hydraulic Research*, Vol. 50(1), pp. 134-137.
- Lima Neto, I. E., Zhu, D. Z., Rajaratnam, N., Yu, T., Spafford, M., & McEachern, P. (2007). "Dissolved oxygen downstream of an effluent outfall in an ice-covered river: Natural and artificial aeration." *Journal of Environmental Engineering*, Vol. 133, No.11, pp.1051-1060.
- Lima Neto, I. E., Zhu, D. Z., & Rajaratnam, N. (2008a). Air injection in water with different nozzles. *Journal of Environmental Engineering*, Vol. 134, No. 4, pp. 283-294.
- Lima Neto, I. E. L., Zhu, D. Z., & Rajaratnam, N. (2008b). "Bubbly jets in stagnant water." *International Journal of Multiphase Flow*, Vol. 34, No. 12, pp.1130-1141.
- Lima Neto, I. E., Zhu, D. Z., & Rajaratnam, N. (2008c). "Horizontal injection of gas-liquid mixtures in a water tank." *Journal of Hydraulic Engineering*. 134, No.12, pp. 1722-1731.

Lima Neto, I. E., Cardoso, S. S., & Woods, A. W. (2016). On mixing a density interface by a bubble plume. *Journal of Fluid Mechanics*, Vol. 802.

Leighton, T. (2012). *The acoustic bubble*. Academic Press.

Lima Neto, I. E. L., Cardoso, S. S., & Woods, A. W. (2015). On mixing a density interface by a bubble plume. *Journal of Fluid Mechanics*, Vol. 802.

Lima Neto, I. E. (2015). Self-similarity of vertical bubbly jets. *Brazilian Journal of Chemical Engineering*, 32, 475-487.

Little, J. C., & McGinnis, D. F. (2001). Hypolimnetic oxygenation: predicting performance using a discrete-bubble model. *Water Science and Technology: Water Supply*, 1(4), 185-191.

Leibson, I., Holcomb, E. G., Cacos, A. G., Jacmic, J. J. (1956). "Rate of flow and mechanics of bubble formation from single submerged orifices." *AIChE Journal*, Vol. 2, No. 3, pp. 296-306.

Mantripragada, V. T., Sahu, S., & Sarkar, S. (2021). Morphology and flow behavior of buoyant bubble plumes. *Chemical Engineering Science*, 229, 116098.

McGinnis, D. F., Lorke, A., Wüest, A., Stöckli, A., & Little, J. C. (2004). Interaction between a bubble plume and the near field in a stratified lake. *Water Resources Research*, Vol. 40, No. 10.

Milgram, J. H. (1983). Mean flow in round bubble plumes. *Journal of Fluid Mechanics*, 133, 345-376.

McGinnis, D.F., Greinert, J., Artemov, Y., Beaubien, S.E., Wüest, A. (2006). Fate of rising methane bubbles in stratified waters: how much methane reaches the atmosphere. *J. Geophys. Res. Oceans* 111 (C9), C09007. doi: 10.1029/2005JC003183

Mobley, M., Gantzer, P., Benskin, P., Hannoun, I., McMahon, S., Austin, D., & Scharf, R. (2019). Hypolimnetic oxygenation of water supply reservoirs using bubble plume diffusers. *Lake and Reservoir Management*, 35(3), pp. 247-265.

Moghadaripour, M., Azimi, A.H., Elyasi, S., (2017b). "Experimental study of oblique particle clouds in water." *Int. J. Multiph. Flow*. Vol. 91, pp. 101–119.

Milenković, R.Ž., Sigg, B. and Yadigaroglu, G., 2007. Bubble clustering and trapping in large vortices. Part 1: Triggered bubbly jets investigated by phase-averaging. *International Journal of Multiphase Flow*, 33(10), pp.1088-1110.

- Milgram, J. H., & Van Houten, R. J. (1982). *Plumes from Blowouts and Broken Gas Pipelines*. Massachusetts Institute of Technology, Department of Ocean Engineering.
- Moura, D. S., Lima Neto, I. E., Clemente, A., Oliveira, S., Pestana, C. J., Melo, A., Capelo-Neto, J., 2020. Modeling phosphorus exchange between bottom sediment and water in tropical semiarid reservoirs. *Chemosphere*, Vol. 246. <https://doi.org/10.1016/j.chemosphere.2019.125686>.
- Mueller, J., Boyle, W. C., & Popel, H. J. (2002). *Aeration: Principles and Practice, Volume 11* (Vol. 11). CRC press.
- Murzyn, F., Mouaze, D., & Chaplin, J. R. (2005). "Optical fiber probe measurements of bubbly flow in hydraulic jumps." *International Journal of Multiphase Flow*. Vol. 31, No.1, pp.141-154.
- Morton, B. R., Taylor, G. I., & Turner, J. S. (1956). Turbulent gravitational convection from maintained and instantaneous sources. *Proceedings of the Royal Society of London. Series A. Mathematical and Physical Sciences*, Vol. 234, No. 1196, pp. 1-23.
- Niida, Y., & Watanabe, Y. (2018). Oxygen transfer from bubble-plumes. *Physics of fluids*, 30(10), 107104.
- Oguz, H. N. & Prosperetti, A. (1993). "Dynamics of bubble growth and detachment from a needle." *Journal of Fluid Mechanics*, Vol 257, pp. 111-145
- Pacheco, C. H., & Lima Neto, I. E. (2017). "Effect of artificial circulation on the removal kinetics of cyanobacteria in a hypereutrophic shallow lake." *Journal of Environmental Engineering*. Vol. 143, No.12, pp.06017010.
- Paerl, H. W., and Otten, T. G. (2013). "Harmful cyanobacterial blooms: Causes, consequences, and controls." *Microb. Ecol.* Vol.65, No.4, pp.995–1010.
- Pan, Q., Johansen, S. T., Olsen, J. E., Reed, M., & Saetran, L. R. (2021). On the turbulence modeling of bubble plumes. *Chemical Engineering Science*, 229, 116059.
- Riess, I. R., & Fanneløp, T. K. (1998). Recirculating flow generated by line-source bubble plumes. *Journal of Hydraulic Engineering*, 124(9), 932-940
- Rensen, J., & Roig, V. (2001). "Experimental study of the unsteady structure of a confined bubble plume." *International Journal of Multiphase Flow*. Vol. 27, No.8, pp. 1431-1449.
- Roig, V., & De Tournemine, A. L. (2007). Measurement of interstitial velocity of homogeneous bubbly flows at low to moderate void fraction. *Journal of Fluid Mechanics*, Vol. 572, pp. 87-110.

- Rosso, D., & Stenstrom, M. K. (2006). Surfactant effects on α -factors in aeration systems. *Water research*, 40(7), pp. 1397-1404.
- Sahoo, G. B., and Luketina, D. (2006). Response of a Tropical Reservoir to Bubbler Destratification, ASCE, *Journal of Environmental Engineering*, Vol. 132(7), 736-746.
- Seol, D. G., Bryant, D. B., & Socolofsky, S. A. (2009). Measurement of behavioral properties of entrained ambient water in a stratified bubble plume. *Journal of Hydraulic Engineering*, Vol. 135, No.11, pp. 983-988.
- Simiano, M., Zboray, R., De Cachard, F., Lakehal, D., & Yadigaroglu, G. (2006). Comprehensive experimental investigation of the hydrodynamics of large-scale, 3D, oscillating bubble plumes. *International Journal of Multiphase Flow*, Vol. 32, No.10-11, 1160-1181.
- Singleton, V. L., Gantzer, P., & Little, J. C. (2007). Linear bubble plume model for hypolimnetic oxygenation: Full- scale validation and sensitivity analysis. *Water Resources Research*, 43(2).
- Schladow, S. G. (1992). "Bubble plume dynamics in a stratified medium and the implications for water quality amelioration in lakes." *Water Resources Research*. Vol.28, No.2, pp.313-321
- Schladow, S. G. (1993). "Lake destratification by bubble-plume systems: Design methodology." *Journal of Hydraulic Engineering*. Vol. 119. No.3, pp.350-368.
- Socolofsky, S. A., & Adams, E. E. (2002). Multi-phase plumes in uniform and stratified crossflow. *Journal of Hydraulic Research*, Vol. 40, No. 6, pp. 661-672.
- Socolofsky, S. A., & Adams, E. E. (2003). Liquid volume fluxes in stratified multiphase plumes. *Journal of Hydraulic Engineering*, Vol. 129, No. 11, pp.905-914.
- Soltero, R. A., Sexton, L. M., Ashley, K. I., and McKee, K. O. (1994). "Partial and full lift hypolimnetic aeration of Medical Lake, WA to improve water quality." *Water Res.* Vol.28, No.11, pp. 2297–2308.
- Sujatha, K. T., Meeusen, B. G., Kuipers, J. A. M., & Deen, N. G. (2015). Experimental studies of bubbly flow in a pseudo-2D micro-structured bubble column reactor using digital image analysis. *Chemical Engineering Science*, 130, 18-30.
- Sujatha, K. T. (2016). Cutting bubbles: an experimental and numerical investigation of micro-structured bubble column. PhD Thesis, Technische Universiteit Eindhoven, Netherland, 138 p.

- Schierholz, E. L., Gulliver, J. S., Wilhelms, S. C., & Henneman, H. E. (2006). Gas transfer from air diffusers. *Water research*, 40(5), 1018-1026.
- Schladow, S. G., & Fisher, I. H. (1995). The physical response of temperate lakes to artificial destratification. *Limnology and Oceanography*, 40(2), pp. 359-373.
- Socolofsky, S. A., & Adams, E. E. (2001). "Detrainment fluxes for multiphase plumes in quiescent stratification." In *International Symposium on Environmental Hydraulics (ISEH and IAHR)*.
- Sun, T. Y., & Faeth, G. M. (1986). Structure of turbulent bubbly jets—I. Methods and centerline properties. *International journal of multiphase flow*, 12(1), 99-114.
- Sun, T. Y., & Faeth, G. M. (1986). Structure of turbulent bubbly jets—II. Phase property profiles. *International journal of multiphase flow*, 12(1), 115-126.
- Suñol, F. and González-Cinca, R., 2010. Opposed bubbly jets at different impact angles: Jet structure and bubble properties. *International journal of multiphase flow*, 36(8), pp.682-689.
- Turner, J. S. (1979). *Buoyancy effects in fluids*. Cambridge university press.
- Upadhyay, R. K., Pant, H. J., & Roy, S. (2013). Liquid flow patterns in rectangular air-water bubble column investigated with radioactive particle tracking. *Chemical Engineering Science*, 96, 152-164.
- Vazquez, A., Sanchez, R. M., Salinas-Rodriguez, E., Soria, A., & Manasseh, R. (2005). A look at three measurement techniques for bubble size determination. *Experimental thermal and fluid science*, 30(1), 49-57.
- Varley, J., 1995. Submerged gas-liquid jets: bubble size prediction. *Chemical engineering science*, 50(5), pp.901-905.
- Wang, B., Lai, C. C., & Socolofsky, S. A. (2019). Mean velocity, spreading and entrainment characteristics of weak bubble plumes in unstratified and stationary water. *Journal of Fluid Mechanics*, 874, 102-130.
- Waterhouse, J., Kjeldsen, T., & Bryant, L. (2021). Investigating the effectiveness of bubble-plume destratification systems in a temperate, shallow, drinking water reservoir. In *EGU General Assembly Conference Abstracts* (pp. EGU21-12509).
- Weber, T.C., Mayer, L., Jerram, K., Beaudoin, J., Rzhanov, Y., Lovalvo, D. (2014). Acoustic estimates of methane gas flux from the seabed in a 60 0 0 km(2) region in the northern Gulf of Mexico. *Geochem. Geophys.* 15 (5), pp. 1911–1925.

Wüest, A., Brooks, N. H., & Imboden, D. M. (1992). Bubble plume modeling for lake restoration. *Water Resources Research*, Vol. 28, No. 12, pp. 3235-3250.

Yang, D., Chen, B., Socolofsky, S. A., Chamecki, M., & Meneveau, C. (2016). Large-eddy simulation and parameterization of buoyant plume dynamics in stratified flow. *Journal of Fluid Mechanics*, Vol.794, pp.798-833.

Yapa, P. D., Zheng, L., & Nakata, K. (1999). Modeling underwater oil/gas jets and plumes. *Journal of Hydraulic Engineering*, Vol. 125, No. 5, pp. 481-491.

Zic, K., Stefan, H. G., & Ellis, C. (1992). Laboratory study of water destratification by a bubble plume. *Journal of Hydraulic Research*, 30(1), 7-27.

Ziegenhein, T., & Lucas, D. (2017). Observations on bubble shapes in bubble columns under different flow conditions. *Experimental Thermal and Fluid Science*, 85, 248-256.

Zhang, W., Liu, M., Zhu, D. Z., & Rajaratnam, N. (2014). Mean and turbulent bubble velocities in free hydraulic jumps for small to intermediate Froude numbers. *Journal of Hydraulic Engineering*, 140(11), 04014055.

